Onset of Dynamic Wetting Failure: The Mechanics of High-speed Fluid Displacement

A DISSERTATION
SUBMITTED TO THE FACULTY OF THE GRADUATE SCHOOL
OF THE UNIVERSITY OF MINNESOTA
BY

Eric Allen Vandre

IN PARTIAL FULFILLMENT OF THE REQUIREMENTS
FOR THE DEGREE OF
DOCTOR OF PHILOSOPHY IN CHEMICAL ENGINEERING

MARCIO S. CARVALHO and SATISH KUMAR

July, 2013

Acknowledgements

Reflecting on my years spent at the University of Minnesota, it is undeniable that my achievements, especially this dissertation, would not have been possible without the many contributions from insightful mentors, gracious friends, and supportive family members. Although I cannot hope to repay this sizable debt within a page, I would like to take the next few lines to humbly acknowledge those that have pushed me forward and kept me from drifting astray.

First, I would like to acknowledge my graduate research advisors Professor Satish Kumar and Professor Marcio Carvalho. I cannot imagine a more encouraging research environment than that which is fostered through your collaboration. I thank you for the diversity of projects that you offered me and the patience that you maintained while I tried to navigate my way through the mix. Furthermore, I thank you both for being excellent teachers that generously sharing your expertise with aspiring scientists, such as myself.

I am fortunate to have spent a summer as an undergraduate research assistant to the late Professor H. Ted Davis. Professor Davis' brilliance colored that summer with exciting science and outrageous humor that certainly influenced my decision to continue on to graduate school. Thank you Ted.

I am also grateful to Mikhail L. Pekurovsky and Robert C. Moore for many inspirational discussions over the past five years. Thank you for always asking the tough questions that motivated new and exciting directions in my studies.

In addition, I consider myself lucky to have worked alongside colleagues that are always willing to gather around the chalkboard for a good scientific debate or a needed distraction. I thank current and former members of the Kumar research group, including Dr. Shawn Dodds, Dr. Scott Roberts, Dr. Chunfeng Zhou, Dr. Damien Brewer, Dr.

Changkwon Chung, Dr. Leonardo Espin, Dr. Jeongyong Lee, Aruna Ramkrishnan, Sarit Dutta, Andrew Corbett, Weihua Li, and Chen-Yu Liu.

My family has acted as the stabilizing force during the rough tumble associated with student life. I thank my parents, Rose and Clifton, for convincing me to try the University of Minnesota and providing me with the love and support to carry it through. I am grateful for my siblings, Lisa, Anna, and Alex, for keeping things lighthearted and a little strange. Also, I thank Jenni, Dale, and Claire Shaller for warmly welcoming me into Minnesota and graciously including me into their family.

Finally, I am profoundly grateful to my wife Keely for remaining a pillar of support throughout the entirety of my graduate studies. Whether bolstering my confidence in preparation for a big presentation, or simply reminding me to eat once in a while, you have helped me make it through each day and each step of this program. I love you, and I cannot imagine arriving to this point without you.

Abstract

Dynamic wetting is crucial to processes where a liquid displaces another fluid along a solid surface, such as the deposition of a coating liquid onto a moving substrate. Numerous studies report the failure of dynamic wetting when process speed exceeds some critical value. Typically, wetting failure is a precursor to air entrainment, which produces catastrophic defects in coatings. However, the hydrodynamic factors that influence the transition to wetting failure remain poorly understood from empirical and theoretical perspectives.

This work investigates the fundamentals of wetting failure in a variety of systems that are relevant to industrial coating flows. A hydrodynamic model is developed for planar and axisymmetric geometries where an advancing fluid displaces a receding fluid along a smooth, moving substrate. Numerical solutions predict the onset of wetting failure at a critical substrate speed, which coincides with a turning point in the steady-state solution path for a given set of system parameters. Flow-field analysis reveals a physical mechanism where wetting failure results when capillary forces can no longer support the pressure gradients necessary to steadily displace the receding fluid.

Novel experimental systems are used to measure the substrate speeds and meniscus shapes associated with the onset of air entrainment during wetting failure. Using high-speed visualization techniques, air entrainment is identified by the elongation of triangular air films with system-dependent size. Air films become unstable to thickness perturbations and ultimately rupture, leading to the entrainment of air bubbles. Meniscus confinement in a narrow gap between the substrate and a stationary plate is shown to delay air entrainment to higher speeds for a variety of water/glycerol solutions. In addition, liquid pressurization (relative to ambient air) further postpones air entrainment when the meniscus is located near a sharp corner along the plate. Recorded critical speeds compare well to predictions from the model, supporting the hydrodynamic mechanism for the onset of wetting failure.

Lastly, the common practice of curtain coating is investigated using the hydrodynamic model. Due to the complexity of this system, a new hybrid method is developed to reduce computational cost associated with the numerical analysis. Results show that

the onset of wetting failure varies strongly with the operating conditions of this system. In addition, stresses from the air flow dramatically affect the steady wetting behavior of curtain coating. Ultimately, these findings emphasize the important role of two-fluid displacement mechanics during high-speed wetting. Although this work was motivated by coating flows, it is also relevant to a number of other applications such as microfluidic devices, oil-recovery systems, and splashing droplets.

Contents

List of Tables

List of Figures

Chapter 1

Introduction

Many natural and industrial processes rely on wetting phenomena to form intimate contact between a liquid mass and a solid surface. For instance, the wetting of aqueous films on biological membranes is necessary to initiate cell-cell contact for transport processes in living organisms [3]. Similarly, the petroleum industry depends on wetting behavior to deliver chemical reagents to catalyst surfaces in trickle-bed reactors [4, 5]. The defining characteristic shared by all dynamic wetting systems is the displacement of some fluid (commonly air) initially in contact with a solid surface by the wetting liquid.

Dynamic wetting fails when this displacement process is incomplete, causing non-uniform coverage of the wetting liquid along the solid surface. Depending on the application, the event of wetting failure can produce desirable or detrimental effects. For instance, the lotus leaf contains microstructure that prevents water from completely displacing air layers within small surface features [6]. In this case, wetting failure inhibits the growth of fungi by reducing moisture on the lotus leaf, motivating the development of similar self-cleaning surfaces for implementation in a variety of technologies [7]. As illustrated in Figure 1.1, wetting failure can be catastrophic in coating processes that often must maintain stringent control of coating uniformity to ensure product integrity [8]. Moreover, the onset of wetting failure remains one of the primary obstacles to improving upon current production speeds within the coatings industry [9].

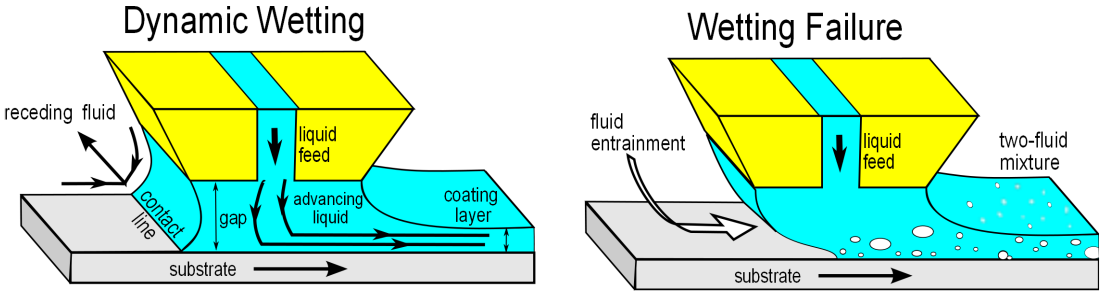

Figure 1.1: Steady dynamic wetting and wetting failure in coating flows.

Although this work is motivated by coating flows, the results presented in the following chapters are relevant to a broad range of other applications. For instance, wetting dynamics are important to microfluidic devices where sub-millimeter scales flows offer efficient and portable fluid processing [10]. In these systems, confined fluid displacement with gas/liquid [11] and liquid/liquid [12] interfaces provides the ability to precisely control chemical separation and reaction [13]. Fluid transport through porous media similarly features multiphase flows in restrictive geometries [14]. In the case of enhanced oil recovery, petroleum yield and process efficiency depend on the mechanics of fluid displacement in porous geological structures [15]. In yet another example of fluid displacement, high-speed wetting plays a significant role during the impact [16] and rapid spreading [17, 18] of drops on solid surfaces. The event of droplet splashing is particularly sensitive to properties of the surrounding air, demonstrating the importance of the two-fluid interaction near the substrate [19, 20].

Even in the simplest of systems, a variety of material properties influence fluid displacement along a solid surface. As is typical of interfacial flows, dynamic wetting is sensitive to parameters that characterize material interactions within the bulk phases (e.g., fluid viscosity μ and density ρ) and along the fluid interface (e.g, surface tension σ). Since the fluid interface meets the solid surface at a three-phase contact line, substrate wettability (related to a balance of interfacial tensions [21]) also influences the mechanics of fluid displacement. Due to this interaction between macroscale (bulk) and microscale (interfacial) physics, the fundamentals of wetting remain under debate [22, 23, 24].

Rather than attack this problem with studies of near-equilibrium behavior, as has been the standard method used within the literature [25], this thesis systematically

investigates the hydrodynamics associated with the onset of dynamic wetting failure. Marking the transition from steady displacement to unsteady fluid entrainment, the onset of wetting failure yields an unambiguous change in flow and interface characteristics (see Section 1.3). Novel experimental and computational techniques are developed in this work to understand the physical mechanism of wetting failure, thereby exposing the fundamental mechanics of high-speed wetting systems. Unlike prior low-speed wetting studies, the results presented here relate to a wide spectrum of real coating systems, which typically operate at high speeds in order to maximize production capacity [2]. This thesis concludes with an analysis of two-fluid displacement in curtain coating, providing insight into the hydrodynamic assist of dynamic wetting [26] that has long been observed in coating flows.

The following sections of this chapter provide a brief survey of the literature relevant to the results presented in this thesis. In addition to the references cited in Sections 1.1 - 1.3, excellent reviews of dynamic wetting [2] and wetting failure [27], including applications to coating flows [28], have been provided elsewhere. Section 1.4 concludes the chapter with an outline of the methods and findings found within this thesis.

1.1 Coating Flows

Coating flows are used to deposit liquid layers that are dried or cured to form solid films with desirable surface properties. Traditionally, coating flows have been a hallmark of industries using decorative paints, audio/video (magnetic) tapes, and paper processing [29, 30]. Recently, high-precision coating processes have become important to the development of a number of emerging thin-film applications found in optical devices, solar cells, and lithium batteries, with each market valued well above $10 billion [31]. Due to the prevalence of coating processes used in a wide range of technologies, it is difficult to assess the total value of the global coatings market. However, heavy investments made toward the research and development of coating processes [31] indicates that the field continues to prosper internationally.

Fluid displacement lies at the heart of a liquid-applied coating process. In order to form intimate contact between the coating and the substrate, air must be completely displaced from the solid surface by the liquid coating flow [32]. Moreover, industrial

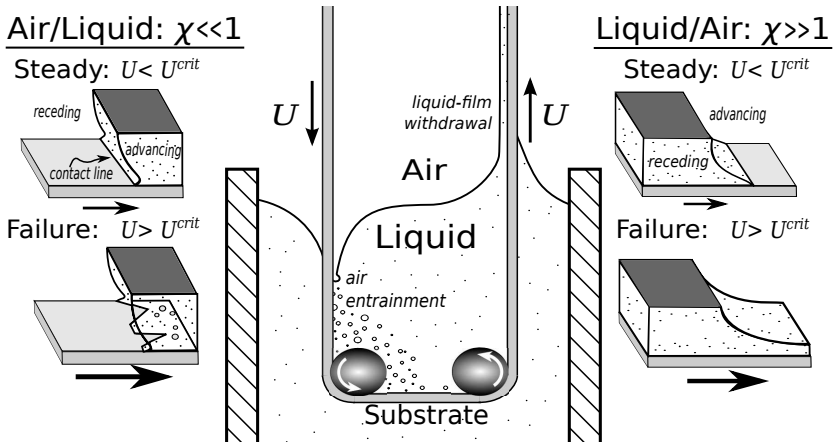

Figure 1.2: Illustration of a typical dip-coating system, where fluid displacement occurs along a substrate moving with speed U. For the purpose of illustration, the fluid interface along the substrate's outer surface exhibits steady displacement, whereas the interior surface shows the effects of wetting failure as the receding phase is entrained along the moving substrate. The bordering panels provide a closer view of interface profiles near the DCL. At the onset of wetting failure, the air/liquid and liquid/air systems transition to states of air entrainment and liquid-film withdrawal, respectively.

coating lines commonly aim to steadily and uniformly deposit liquid coating layers on a substrate moving at speed U, requiring strict control of the dynamic-wetting process.

All such dynamic-wetting systems involve a "receding/advancing" fluid pair, where the advancing fluid with viscosity μ_{adv} displaces the receding fluid with viscosity μ_{rec}. At some critical speed U^{crit}, dynamic wetting fails and the receding fluid becomes entrained within the advancing phase [27]. As shown in Figure 1.2, coating flows transition from "air/liquid" wetting when the coating first contacts the substrate to "liquid/air" displacement during liquid-film deposition (multi-layer coatings may also have a "liquid/liquid" displacement stage). Consequently, displacement flows in coating processes typically span an extremely broad range of viscosity ratio $\chi = \mu_{rec}/\mu_{adv}$, as well as other parameters characterizing the materials and flow geometry. Wetting failure is essential to form a coating layer during the stage of liquid-film withdrawal ($\chi \gg 1$), whereas air entrainment during air/liquid displacement ($\chi \ll 1$) is usually detrimental to coating quality.

In practice, the onset of air entrainment commonly limits production capacity for

a given coating system [8]. Since entrained air bubbles cause voids and irregularities in the solidified layer [33], coating flows must operate at sub-critical speeds to avoid defects in the final product. It is well known that the value of U^{crit} can vary by orders of magnitude depending on the specific coating device and material properties (see Section 1.3.3). However, systematic studies of wetting failure rarely contain the broad spectrum of parameters that are found in a typical industrial coating process [34]. Consequently, methods for delaying air entrainment remain poorly understood, forcing practitioners to resort to trial-and-error techniques when attempting to augment this ceiling on coating speed [21].

Figure 1.3 illustrates several liquid deposition techniques that are found in the coatings industry. There are several key distinction between coating methods that can influence wetting behavior. First, the control on coating thickness is different between premetered and self-metered techniques. In self-metered techniques, an opposing boundary (e.g., blade coating) or force (e.g., air-knife coating) thins the deposited liquid layer to achieve a desired final thickness. Premetered devices (e.g, curtain coating, slide coating, slot coating) control the coating thickness through a balance of the feed flow rate Q and substrate speed U. Generally, dynamic wetting is very sensitive to feed-flow parameters, which strongly influence the interface shape and liquid flow field.

Second, the specific design of each coating system imposes different geometric constraints on the fluid-displacement process. For example, many die coating methods (e.g., slot coating) impose small gaps that confine the fluid interface. As illustrated in Figure 1.3, a local approximation of a meniscus confined between two surfaces can be used to understand the essential fluid-displacement mechanics of these coating flows. Other coating methods have complicated geometries (e.g., curtain coating) or flow fields (e.g., fiber coating) that do not allow for a simple approximation of the dynamic-wetting region.

Curtain-coating flows are particularly challenging to understand because expansive free-surfaces occupy both the upstream and downstream faces of the curtain. These large fluid interfaces allow for massive deformation of the coating domain in response to changes in the operating conditions. Despite this complexity, curtain-coating flows have been studied with computational models using the finite element method (FEM) [35, 36]. Numerical results show that the falling liquid curtain develops high pressures as it makes

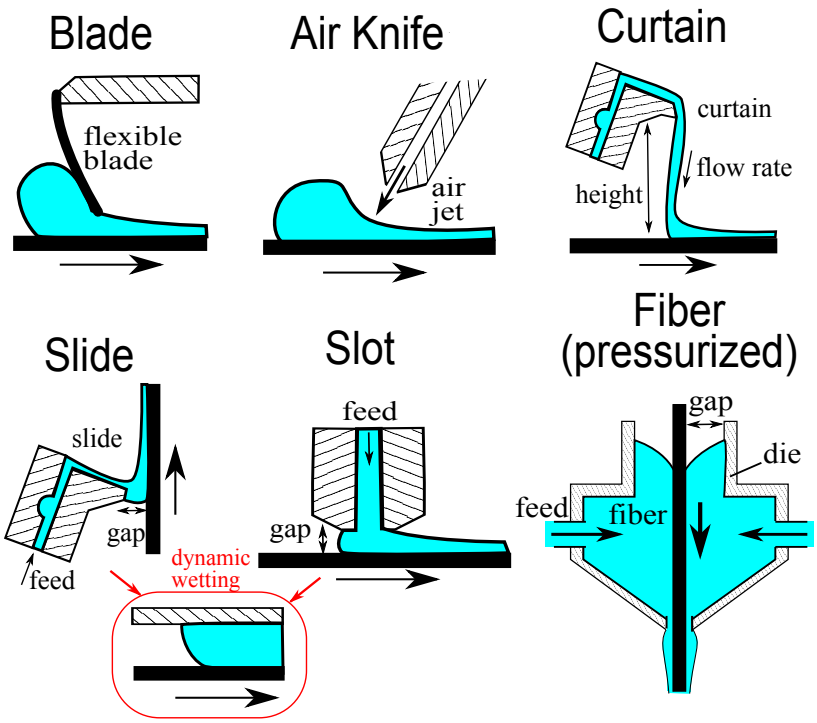

Figure 1.3: Illustration of various liquid coating systems. Note that dip coating is shown in Figure 1.2.

contact with the substrate [37]. This impinging flow near the contact line is thought to assist dynamic wetting, as careful control of the curtain parameters (especially flow rate) can delay air entrainment at fast substrate speeds [26, 38]. Unfortunately, the dynamics of fluid displacement in curtain coating remains only loosely understood. For example, current models cannot accurately describe the variations in interface shape that result from simply adjusting the curtain flow rate [39]. This thesis demonstrates that the air flow, which is a missing ingredient in past models, significantly alters the curtain shape during high-speed wetting (see Chapter 8), explaining prior discrepancies between experiments and theory.

1.2 Wetting Fundamentals

1.2.1 Contact Lines and Dynamic Wetting

The three-phase junction at the wetting front, commonly called the *wetting line* or *contact line*, is of primary importance when discussing dynamic wetting behavior. In a 2D system, the contact line represents the terminal point of the fluid interface separating the receding and advancing fluids at the substrate boundary. Dynamics near this point strongly influence the apparent contact angle θ_M, which is a key parameter characterizing the overall interface profile. A number of reviews have compiled observations that of contact-line dynamics, including the response of the apparent contact angle to wetting speed for diverse material systems [28, 2], wetting with complex fluids and non-ideal substrates [21], and qualitative features of local wetting flows [40, 41]. Despite the breadth of previous work, there remains debate over the factors that influence contact-line behavior, especially for complex flows or fast wetting speeds.

The vast body of experimental evidence suggests the existence of three wetting states: static wetting, steady dynamic wetting, and dynamic wetting failure. As shown by Figure 1.4, the capillary number, $Ca = \mu U/\sigma$, is considered the key dimensionless parameter distinguishing between these fundamental states because it signifies the relative importance of viscous and surface-tension forces acting on the wetting meniscus. Here, U is some characteristic speed associated with interface motion, μ is the liquid viscosity, and σ is the interfacial tension. This thesis considers dynamic wetting along a moving substrate, so U is set by the substrate speed as reflected in Figure 1.4.

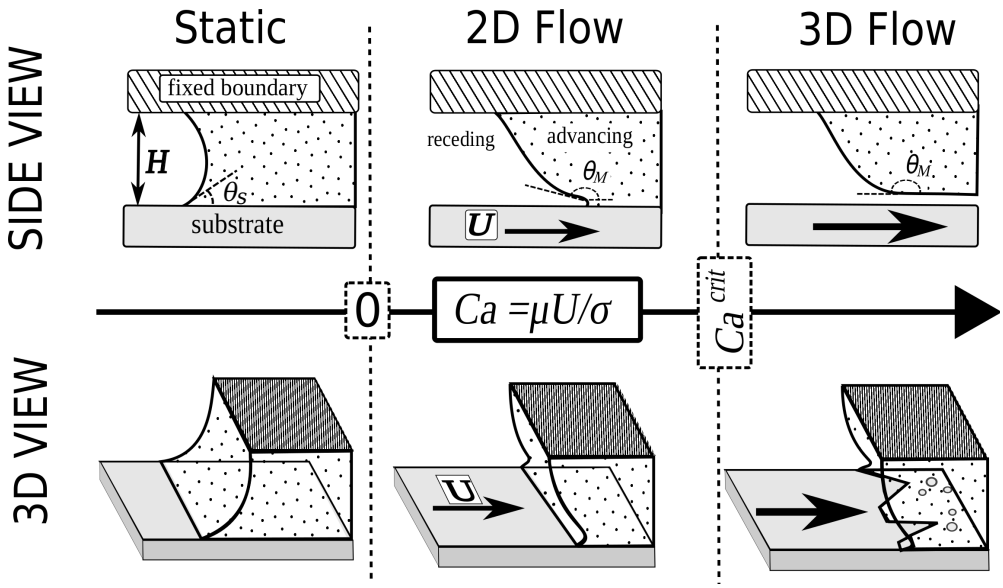

Figure 1.4: Illustration of the fundamental states of wetting as a function of Ca with side and three-dimensional (3D) views. Receding and advancing fluids are separated by a fluid interface, which is characterized by a static contact angle θ_S when $Ca = 0$ and an apparent contact angle θ_M when the substrate moves with velocity U. Wetting failure occurs when the substrate speed exceeds a critical value corresponding to Ca^{crit}. At this point $\theta_M \to 180^o$ and the DCL forms a sawtooth meniscus shape, indicating a local transition to 3D flow.

The first state resides at $Ca \approx 0$, where the wetting system is near equilibrium and can be characterized by a well-defined contact angle, θ_S, which is formed to balance interfacial tensions at the static contact line (SCL). At finite Ca, the substrate moves at some velocity U. During steady fluid displacement, the three-phase junction moves relative to a point on the substrate and is known as a dynamic contact line (DCL). The substrate motion generates 2D fluid flow (for an ideal planar system), which contributes viscous stresses that cause the apparent contact angle θ_M to deviate from the static value. (Note that θ_M is also referred to as a dynamic or macroscopic contact angle.) Numerous experimental studies have demonstrated a monotonic increase of θ_M with Ca [42, 43, 22]. However, steady wetting seems only to exist within a finite Ca range for all physical systems and unsteady, three-dimensional (3D) flow results for $Ca > Ca^{crit}$. Characteristics of this wetting-failure state are discussed in Section 1.3.

The majority of current dynamic wetting theory involves some combination of the

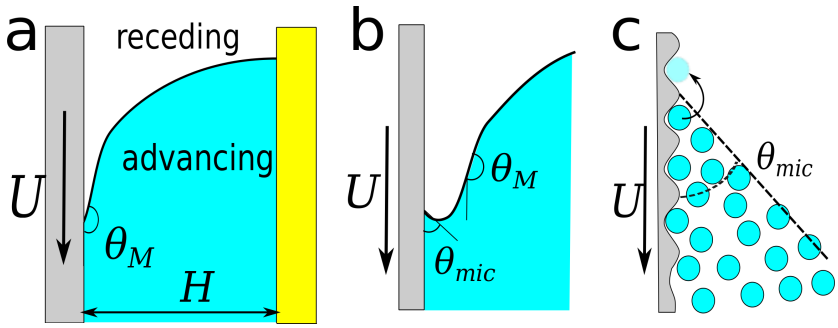

Figure 1.5: Illustration of the apparent and microscopic contact angle along a fluid interface. (a) Outer view of the fluid interface that bends in the direction of substrate motion with apparent contact angle θ_M. (b) Inner view of the interface near the contact line, revealing a microscopic contact angle θ_{mic}. (c) Molecular-level displacement and an interpretation of the "true" contact angle at the contact line.

following physics near the DCL: viscous bending from hydrodynamic theory [44, 45], kinetics of molecular adsorption/desorption [46], disjoining pressures resulting from long-range intermolecular forces [47], molecular transport through a diffuse fluid interface of finite thickness [48], and induced Marangoni effects from arguments of irreversible surface thermodynamics [49]. Sections 1.2.2 - 1.2.4 discuss some of the prominent characteristics of dynamic wetting theory with some comparison to experimental observations. Emphasis is placed on prior results from hydrodynamic theory, as this forms the framework of the wetting model used in this work (see Chapter 2). Broad reviews of dynamic wetting theory are provided by [50], [2], [25], [51], and [40].

1.2.2 Contact Angles

The interface property most commonly used to characterize wetting is the contact angle formed by the intersection of the fluid interface with the substrate surface. (In this work, interface angles θ are always defined with respect to the advancing fluid and the complementary angle is formed in the receding fluid.) Since measurement of the contact angle occurs visually, the microscopic angle θ_{mic} located directly at the contact line cannot be obtained [28]. Instead, the recorded dynamic angle reflects an apparent contact angle θ_M measured at some position along the fluid interface, as illustrated in Figure 1.5. Experimental studies show θ_M to increase with wetting speed [21, 46, 52].

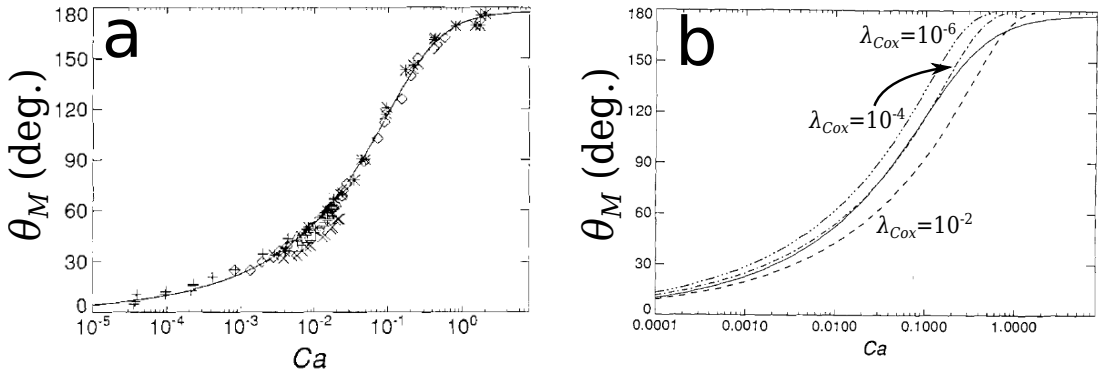

Figure 1.6: (a)Empirical correlation for θ_M measured as a function of Ca taken from [2]. Symbols represent experimental data for various liquids forced through a capillary tube. The liquids cover a viscosity range of $10^3 - 10^6$ cP. The fitted curve is shown expressed by (1.1) [42]. (b) Comparison of the Hoffman correlation (solid line) to the hydrodynamic theory in (1.3) with various values of λ_{Cox} (dashed lines).

This behavior is reflected by the Hoffman correlation [42, 2, 41]:

$$\theta_M = f_H(Ca) = \cos^{-1}\left\{1 - 2\tanh\left(5.16\left[\frac{Ca}{1+1.31Ca^{0.99}}\right]^{0.706}\right)\right\}, \qquad (1.1)$$

which is an empirical fit to θ_M data measured during forced wetting of a liquid in a capillary tube.

Figure 1.6 shows that (1.1) describes contact-angle measurements from various systems in which a viscous liquid advances with air as the receding fluid. This behavior is also captured fairly well by hydrodynamic theory, where the behavior of the apparent contact angle θ_M results from viscous stresses that bend the fluid interface near the DCL:

$$\left.\begin{aligned} &g(\theta_M;\chi) - g(\theta_{mic};\chi) = -Ca\ln(\lambda_{Cox}),\\ &g(\theta;\chi) = \int_0^{\theta} f(\phi;\chi)\,\mathrm{d}\phi,\\ &f(\phi;\chi) = \frac{\chi(\phi^2-\sin^2\phi)[(\pi-\phi)+\sin\phi\cos\phi] + [(\pi-\phi)^2-\sin^2\phi](\phi-\sin\phi\cos\phi)}{2\sin\phi[\chi^2(\phi^2-\sin^2\phi)+2\chi\{\phi(\pi-\phi)+\sin^2\phi\}+\{(\pi-\phi)^2-\sin^2\phi\}]} \end{aligned}\right\} \qquad (1.2)$$

Equation (1.2) is derived using a low-speed asymptotic theory for two-fluid displacement, where χ relates the viscosity of the receding and advancing wetting fluids ($\chi =$

μ_{rec}/μ_{adv}) [44]. Characteristics lengths of the macroscale (H) and microscale (l_{mic}) wetting mechanics are contained in $\lambda_{Cox} = l_{mic}/H$. While θ_M is the apparent contact angle that would typically be observed experimentally, θ_{mic} is the *actual* contact angle formed between the interface and solid surface at the microscopic scale characterized by l_{mic} (refer to Figure 1.5). The value of l_{mic} is typically related to a region of fluid slip near the DCL, as discussed in Section 1.2.3.

The integral function $g(\theta;\chi)$ generally lacks an analytical solution, but can be approximated as $g(\theta;0) \propto \theta^3$ in the limit of small angles and vanishing viscosity of the receding phase [45]. Using this approximation, analytical descriptions for θ_M have been developed through asymptotic analysis (similar to (1.2)) and lubrication theory [53, 54]:

$$\theta_M^3 = \theta_{mic}^3 - 9Ca\ln(\lambda_{Cox}). \tag{1.3}$$

In Equation (1.3), the dependence of θ_M on system parameters is slightly more transparent than in (1.2). In Figure 1.6, λ_{Cox} is treated as a free parameter used to fit (1.2) and (1.3) to the experimental data, but Section 1.2.3 addresses the physical meaning of l_{mic} in detail.

The hydrodynamic description in (1.2) includes θ_{mic}, which is often assumed to be equal to a static contact angle θ_s measured when the three-phase system reaches equilibrium [55, 21]. Figure 1.6 reflects the case where the advancing liquid completely wets the solid at equilibrium ($\theta_s \to 0$). In general, the hydrodynamic theory in (1.2) and (1.3) does not compare as nicely with partial-wetting systems ($\theta_s > 0$) [2]. This is likely due to the fact that θ_M has a stronger dependence on the microscopic angle ($\theta_M \sim \theta_{mic}$) than the wetting speed ($\theta_M \sim Ca^{1/3}$). Contact angle hysteresis is prevalent in real systems, causing θ_s to fluctuate between metastable advancing and receding angles depending on the history of the system [56, 57, 21]. Even with pristine materials, θ_s typically has an uncertainty of at least a few degrees in practice [58], which may impact predictions from (1.2) depending on the treatment of θ_{mic}.

Generally, the microscopic angle may depend on the dynamics of fluid displacement in addition to equilibrium interface properties, such that

$$\theta_{mic} = \theta_{mic}(\theta_s, U, \mu, \sigma, ...). \tag{1.4}$$

Analytical expressions of (1.4) have been developed using arguments for the kinetics of molecular-displacement events near the DCL [59, 46]. Substituting (1.4) into the

hydrodynamic theory in (1.3) tends to improve the agreement of theoretical predictions with experimental data, especially for low viscosity liquids [60]. However, there remains debate over the relative contribution of hydrodynamic and molecular effects near the DCL [25]. Even when attempting to derive the microscopic angle from local force balances, complicated interface shapes near the DCL make it difficult to select the appropriate value of θ_{mic} for use in macroscopic wetting models [61]. Although the exact nature of θ_{mic} remains under investigation, $\theta_{mic} \approx \theta_s$ serves as a good leading-order approximation for many wetting systems [21].

Another factor complicating the interpretation of θ_M is the limited visual resolution available to experimental measurements. Due to curvature of the interface, the interface angle θ varies as a function of the radial distance from the DCL [62, 63]. This variation in θ becomes significant at fast wetting speeds due to large viscous stresses ($\sim \mu U$) that bend the interface [64]. Consequently, the nature of the contact-angle measurement influences the perceived value for θ_M and subsequent comparison with predictions. Moreover, it has been demonstrated that asymptotic hydrodynamic theory (similar to that used in (1.3)) fails to describe interface angle profiles measured during high-speed wetting [64]. This apparent breakdown of hydrodynamic theory is resolved in Section 3.3.4 of this work.

1.2.3 Fluid Slip

Flow fields generated by dynamic wetting systems are challenging to evaluate because viscous stresses diverge near the DCL. If left unchecked, the sharp velocity gradient in the corner flow between the fluid interface and substrate generates an infinite force [65] (also infinite energy dissipation [21]) at the DCL, which prevents a physically meaningful solution to the problem [40]. Another interpretation of this issue is that the fluid velocity must be multi-valued at the DCL in order to simultaneously map onto the velocity functions demanded by boundary conditions at the fluid/fluid interface and the fluid/substrate boundary [66].

In order to avoid a nonintegrable singularity, viscous forces must decay in the vicinity of the DCL. Mathematically, this is achieved by relaxing the no-slip boundary condition (i.e., $u = U$) that is typically postulated at fluid/substrate boundaries. Instead, fluid is allowed to slip near the DCL, adopting some velocity that is different from the substrate.

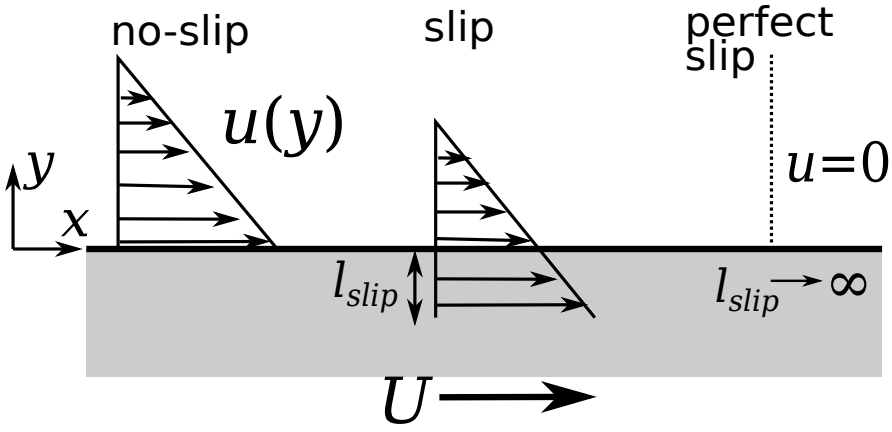

Figure 1.7: Illustration of varying degrees of fluid slip along a moving substrate.

Numerical models for dynamic wetting systems commonly use a Navier condition to describe fluid slip [67, 68, 69]:

$$u - U = l_{slip} \frac{\partial u}{\partial y}. \tag{1.5}$$

Equation (1.5) defines a Navier slip condition for a one-dimensional (1D) flow where u is the fluid velocity and $\frac{\partial u}{\partial y}$ is the shear stress at the substrate (here y is the Cartesian coordinate that points normal to the substrate surface). The slip length l_{slip} typically acts as a coefficient that controls the magnitude of fluid slip.

Fluid-slip conditions, such as (1.5), remove the problem of infinite contact-line force (and infinite energy dissipation) by imposing an *integrable* stress singularity at the DCL [70]. From strictly a mathematical point of view, the DCL singularity can be relieved by any function that causes $u \to 0$ within a distance $\sim l_{slip}$ from the contact line [71]. In fact, when evaluating models for fluid slip, macroscopic properties of wetting systems seem most sensitive to value of the l_{slip}, whereas the exact form of the velocity function has little impact [72]. Therefore, (1.5) is viewed as a fairly generic "slip law" and most effort is spent determining appropriate values for l_{slip} [1].

Many times, the slip length is assumed to be a microscopic length scale that characterizes molecular layers of the wetting fluid ($l_{slip} \sim 0.1$ nm) [2]. More accurately, (1.5) designates l_{slip} as the extrapolated distance that would be needed to recover the no-slip velocity if the liquid domain continued into the substrate, as illustrated in Figure 1.7. Dispute remains over the physical origin of slip [73, 74, 1]. Proposed slip mechanisms

include surface roughness effects [75], flow over entrained gas films [2], and molecular adsorption processes [76]. In addition, l_{slip} has been treated as a friction coefficient that is adjusted to satisfy a global energy balance within a wetting system [77].

Table 1.1: Slip lengths for water on different substrates as measured by various experimental methods. All data is taken from [1]. Note that acronyms are defined as follows: DDS = dimethyldichlorosilane, TMS = trimethylchlorosilane, HTS = hexadecyltrichlorosilane.

Measurement Method	Substrate	l_{slip} (nm)
pressure drop vs. flow rate in channel	silicon	≤ 10
pressure drop vs. flow rate in channel	glass+DDS	~ 1000
pressure drop vs. flow rate in channel	quartz+TMS	30
particle image velocimetry	glass	50
atomic force microscopy	silica/mica	~ 100
atomic force microscopy	borosilicate+HTS	30

Regardless of the physical mechanism, it has become evident that slip is present in a broad variety of experimental systems [74]. Table 1.1 lists typical values of l_{slip} obtained from a range of different experimental techniques. Due to the sensitivity of these types of measurements, there has not yet been direct experimental evidence of slip from the complex dynamics of wetting systems. However, molecular dynamics simulations predict fluid slip very close to the DCL [78] in a manner that is consistent with hydrodynamic theory [79].

Hydrodynamic slip models (i.e., hydrodynamic theory including a slip law near the DCL) predict dynamic wetting flows that present a couple of unresolved problems. First, fluid slip imposes a local stagnation region near the DCL ($u \to 0$), which conflicts with experimentally observed flow kinematics [41, 80]. Second, most slip conditions produce infinite fluid pressures at the DCL. For example, (1.5) relieves the *force* singularity, but still leads to a logarithmic *pressure* singularity at the DCL [71]. A separate "interface-formation" model avoids these issues by adding equations describing surface-tension transport (including several surface-property parameters) to the usual hydrodynamic formulation [40]. However, a recent study demonstrated that the interface-formation model predicts macroscopic wetting behavior that is very similar to results from a hydrodynamic slip model [81]. Therefore, although the consequence of the stagnation point and the diverging fluid pressure at the DCL is not yet clear, slip models may capture the essential microscale wetting mechanics needed to model fluid-displacement processes.

1.2.4 Flow-field Effects

Beyond capillary-number dependence, there is significant evidence that properties of the global flow field influence dynamic wetting [82, 83]. Although numerous studies have investigated the effect of large-scale flow geometry, such as the difference between θ_M measured from Wilhelmy plate and drop spreading techniques (see [84] for further discussion), few experimental studies attempt the challenging task of observing dynamic wetting confined within domains much smaller than the system's capillary length [2].

Figure 1.8 shows data from two low-speed wetting studies that report change of the apparent contact angle through confinement of an air/liquid meniscus between two parallel plates [85] and a liquid/liquid meniscus within a capillary tube [86]. Both data

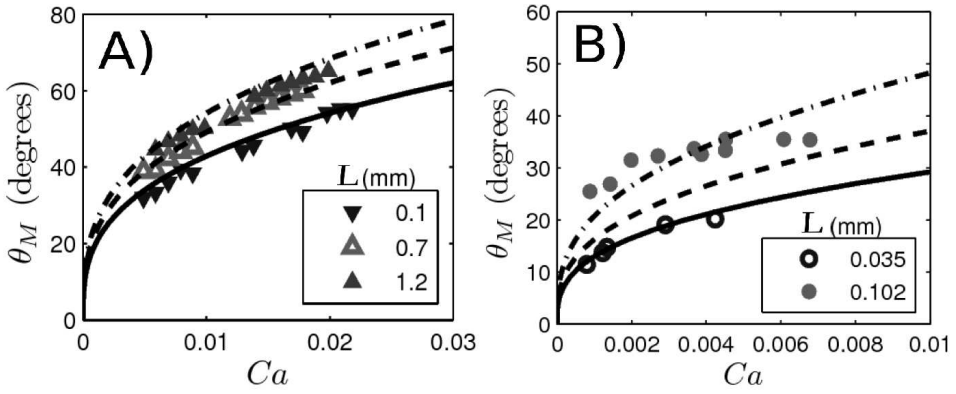

Figure 1.8: The effect of confinement on θ_M at low Ca for (a) an air/liquid meniscus ($\chi \approx 10^{-5}$) between parallel plates and (b) a liquid/liquid meniscus ($\chi \approx 1$) within a capillary tube as reported by [85] and [86], respectively. H reflects measures of (a) the gap between plates and (b) the tube diameter for each experimental system. Curves are constructed using (1.2) with the bold, dashed, and dot-dashed lines representing (a) $\lambda_{Cox} = 10^{-2}, 10^{-3}, 10^{-4}$ and (b) $\lambda_{Cox} = 3 \times 10^{-1}, 10^{-1}, 10^{-2}$, respectively.

sets reflect a decrease in θ_M as the wetting system becomes more confined, i.e., as the characteristic length H decreases. This qualitative trend suggests that dynamic wetting favors confined geometries; however, each study examines too narrow a range of H to properly address the functional dependence of θ_M on geometry. Furthermore, data from these low-speed systems do not exceed dynamic angles of 90^o, making it unwise to deduce anything about high-speed wetting behavior where $\theta_M \to 180^o$.

Previous results from asymptotic analysis of hydrodynamic theory for low Ca [44] or small θ_M [53] support only a logarithmically weak dependence on the characteristic length scale associated with wetting. To compare this prediction with experimental data, the hydrodynamic theory in (1.2) is plotted in Figure 1.8 with various values of $\lambda_{Cox} = l_{mic}/H$. Assuming that l_{mic} is insensitive to the macroscopic geometry, λ_{Cox} should be inversely proportional to the characteristic length used in an experimental system. Although (1.2) captures the trend of the data, there is some ambiguity about curve-fitted values for λ_{Cox} because they do not scale properly with the experimentally measured gaps reported in Figure 1.8. Instead, the available experimental data suggest a stronger dependence of θ_M on confinement than is permitted by (1.2). Yet, the data of Figure 1.8 do not extend to higher wetting speeds ($Ca > 0.1$) where one would expect

an increase of viscous forces and, consequently, more hydrodynamic influence on wetting behavior.

Coating processes provide additional examples of flow-dependent wetting behavior. In fact, some of the most controversial wetting dynamics have been observed during curtain coating. In this coating flow, a liquid curtain falls and impacts a moving substrate at the DCL (refer to Section 1.1). Experimental studies have demonstrated that the liquid curtain height [38], substrate angle [26], and liquid flow rate [82, 83] strongly influence dynamic-wetting behavior. Under the appropriate conditions, curtain coating can operate at exceptionally fast speeds relative to many other coating methods [37]. The flow of the impinging liquid curtain is credited with providing "hydrodynamic assist" that promotes steady dynamic wetting at high speeds [26]. Despite this coined term, the hydrodynamics of this complicated displacement flow are not yet completely understood.

One particular problem that remains unresolved is the flow-rate dependence of the apparent contact angle in curtain coating systems. Experimental studies have demonstrated that θ_M varies with the curtain flow rate while holding Ca fixed, especially during high-speed wetting [82, 83]. Clearly, this behavior is not captured by the asymptotic hydrodynamic theory in (1.2). Furthermore, it has also been demonstrated that a full two-dimensional (2D) hydrodynamic computation cannot reproduce the extreme flow-field dependence of θ_M that is observed during curtain coating [39]. Some authors [82, 39, 87, 25] suggest that flow-dependence of microscopic contact angle θ_{mic} (i.e., (1.4)) is responsible for the curtain-coating results. However, prior computational models only consider the liquid flow while treating the air as a void (zero viscosity) with constant pressure. Findings from this thesis show that *two*-fluid displacement is important to high-speed wetting behavior. Therefore, rather than the functionality of θ_{mic}, the mechanics of the air flow may be the crucial ingredient missing in prior curtain-coating models (see Chapter 8).

1.3 The Onset of Dynamic Wetting Failure

For a given fluid-displacement system, dynamic wetting fails when substrate speed, U, exceeds a critical value, U^{crit} [88, 89, 8, 27]. Consequently, there exists a critical capillary

number $Ca^{crit} = \mu U^{crit}/\sigma$, beyond which steady 2D displacement fails and discrete or continuous regions of the displaced fluid are trapped behind the wetting front [90]. This transition has frequently been reported to coincide with $\theta_M \approx 180^o$, although a more dramatic indicator is the sudden deformation of the DCL in the spanwise direction. At the onset of wetting failure, a "sawtooth meniscus" appears as the DCL becomes inclined (refer to Figure 1.4), forming "vee" shapes that serve as a visual marker for Ca^{crit} [91, 92].

Characteristics of wetting failure depend on properties of the system, especially the fluid-viscosity ratio $\chi = \mu_{rec}/\mu_{adv}$. For cases where the receding fluid is the more viscous fluid ($\chi \geq 1$), the onset of wetting failure marks a transition toward steady liquid-film withdrawal [93]. In contrast, receding air flows ($\chi \ll 1$) typically produce unsteady bubble entrainment during wetting failure [94]. Relative to liquid-film withdrawal ($Ca^{crit} \sim 10^{-3}$), the onset of air entrainment occurs at fast critical speeds ($Ca^{crit} \sim 1$), making experimental visualization more difficult. Consequently, much less is known about the wetting dynamics in the air-entrainment regime (i.e., $\chi \ll 1$). Due to the importance of this phenomena in the coatings industry, the remainder of this thesis attempts a more thorough characterization of air entrainment than has been presented in prior works.

1.3.1 Liquid-film Withdrawal

Wetting failure leading to liquid-film withdrawal has been studied by many experimental and theoretical works, usually considering Newtonian liquids entrained on planar substrates [27]. In these systems, the DCL becomes inclined along the face of the substrate at Ca^{crit}, typically forming a single, broad vee with angle ψ as illustrated in Figure 1.9. As speed increases, the DCL slope becomes steeper with ψ obeying the following relationship:

$$\cos\psi = U^{max}/U. \tag{1.6}$$

Here, $U^{max} \approx U^{crit}$ represents the maximum speed that the contact line can move normal to itself [92]. In other words, (1.6) adjusts ψ in order to keep the velocity normal to the DCL below U^{max}. At some super-critical speed slightly above U^{crit} (also $Ca > Ca^{crit}$), the DCL can no longer remain stationary and instead moves unsteadily in the direction of substrate motion. At this point, a liquid film is withdrawn from the

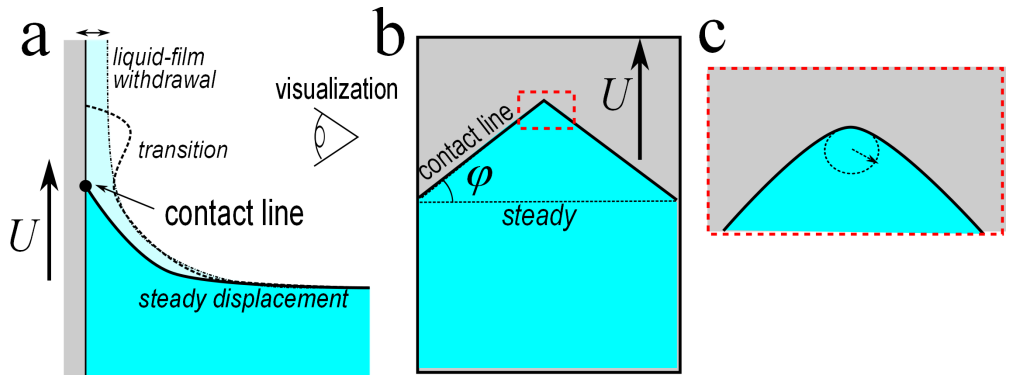

Figure 1.9: The onset of wetting failure leading to liquid-film withdrawal. (a) The side profile of the meniscus shape from steady wetting to liquid-film withdrawal. (b) Front view (typical of experimental visualzation) of the vee-shaped DCL formed at the onset of wetting failure with (c) sharp curvature appearing as a corner at the tip.

bulk liquid, coating the substrate with a thickness determined by a balance of viscous stresses and capillary pressure [95].

Hydrodynamic theory has been used to successfully model the problem of liquid-film withdrawal [96]. It has been found that computational solutions for steady 2D wetting can only be found for $Ca < Ca^{crit}$ when $\chi \geq 1$ [97, 69, 55, 98, 99]. Linear stability analysis shows that the liquid flow is neutrally stable to long-wave perturbations at Ca^{crit} [68]. Numerical results predict that very close to the critical substrate speed (i.e., $Ca \lesssim Ca^{crit}$) a capillary ridge forms from nonlinear effects near the DCL, leading to the quasi-steady elongation of a 2D liquid film [96], as illustrated in Figure 1.9. This behavior has been confirmed experimentally [100], validating the hydrodynamic analysis.

In addition, hydrodynamic models have been used to understand "corners" formed by the DCL at the tail end of liquid drops that slide along a substrate [101]. Hydrodynamic analysis shows that these corners are actually regions of sharp interface curvature (see Figure 1.9c), where the radius of curvature decreases to provide strong capillary forces to balance with increasing viscous stresses as speed increases [102]. Similar to the vees formed prior to liquid-film withdrawal, cornered drops deposit a liquid film on the substrate when sliding faster than some critical speed. Quantitative agreement has been demonstrated between predictions and experimental data for the critical speeds

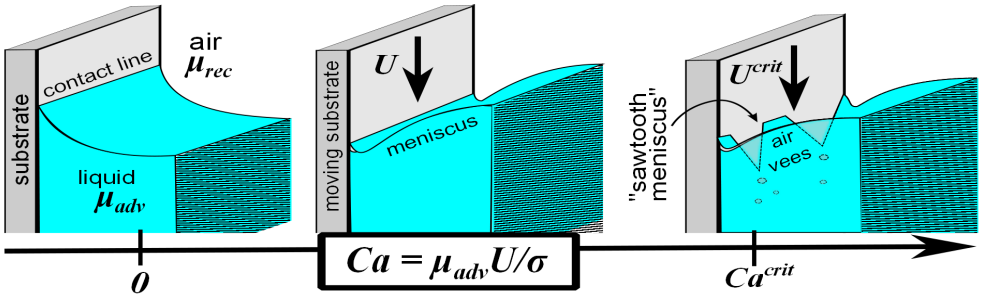

Figure 1.10: The onset of wetting failure leading to air entrainment.

and interface shapes associated with liquid entrainment in these droplet systems [103].

1.3.2 Air Entrainment

The onset of air entrainment typically limits the production capacity of coating operations [8]. Despite the variety of coating flows used in practice (refer to Section 1.1), the literature for air-entrainment phenomena primarily features smooth planar substrates plunging into liquid baths [28]. It is well known that the properties of complex coating flows can have a major effect on wetting failure (see Section 1.3.3). However, lacking a cohesive description for the fluid-displacement mechanics, researchers have struggled to isolate the key hydrodynamic factors that influence critical speeds associated with the onset of air entrainment [34].

A flow transition at Ca^{crit} serves as a precursor to macroscopic air-bubble entrainment. At this substrate speed, flow near the interface becomes three-dimensional (3D) and transient in response to irregular deformation of the DCL, similar to the description in Section 1.3.1. Unlike the case of liquid-film withdrawal, vees formed by the DCL prior to air-entrainment are typically small and appear in a periodic distribution across the width of the substrate [91]. As illustrated by Figure 1.10, this serrated contact-line yields a “sawtooth” meniscus shape that is easily identified in experimental systems . This configuration of the DCL is usually unstable, releasing air bubbles that become entrained within the liquid flow [104, 94].

Only recently have the interface dynamics associated with air-bubble entrainment

been studied systematically. The available experimental evidence suggests that the saw-tooth meniscus causes the elongation of thin ($\sim 1-10$ μm), triangular air films [105, 27]. Apparently, this elongated interface becomes unstable when subjected to disturbances in the two-fluid flow, generating liquid bridges that rupture the air film and produce air bubbles near the DCL [106]. Depending on size and solubility, the air bubbles may then grow, shrink, or dissolve in the surrounding liquid [94]. Observations from high-speed wetting along axisymmetric (fiber) substrates indicate that air entrainment results from tip-streaming phenomena [107]. In this scenario, air bubbles pinch off from an interface cusp at the DCL [108], rather than the film instability discussed above. Yet, the specifics of air entrainment remain debated [82], with little known about the interface dynamics leading to air-bubble entrainment in complex coating flows.

1.3.3 Flow-field Effects

Similar to steady dynamic wetting, parameters of the macroscopic flow field seem to impact wetting failure and the associated Ca^{crit}. For example, numerous experimental systems have demonstrated a power-law relation between the critical speed and liquid viscosity

$$Ca^{crit} \propto \mu^{b} \tag{1.7}$$

where b usually adopts a value near $\frac{1}{4}$ ([28] summarize various prior works where $b \in [0.13, 0.33]$). Other factors involving the feed flow, liquid rheology, and electrostatic effects have been shown to influence Ca^{crit}, though the functional relationships are not yet well-described [34]. These observations have been used by the liquid-applied coatings industry to run production lines at high speeds while resisting the detrimental effects of wetting failure through careful design and control of liquid delivery systems (i.e., coating dies). Figure 1.11 demonstrates that Ca^{crit} can vary by several orders of magnitude depending on the design of specific coating systems. However, the general study of dynamic wetting failure remains largely empirical with little understanding of how specific flow parameters influence Ca^{crit} [2].

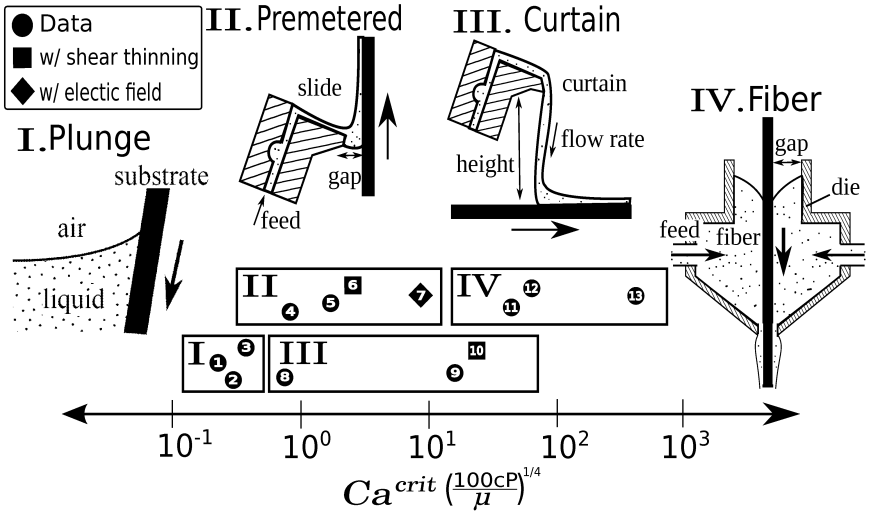

Figure 1.11: Critical capillary numbers found in common industrial coating techniques, including (I) plunge, (II) premetered (e.g., slot and slide) , (III) curtain, and (IV) fiber coating processes. Bold symbols represent estimates of Ca^{crit} from data published within the article and patent literature cited below. To eliminate effects from variable viscosity between the data sources, the axis has been scaled to normalize for a viscosity of 100 cP using (1.7) with $b = 1/4$. Square and diamond symbols indicate studies which include shear-thinning liquids and electrostatic assist, respectively. Data sources: 1.[46] 2.[109] 3.[43] 4.[110] 5.[111] 6.[112] 7.[113] 8.[37] 9.[114] 10.[28] 11.[88] 12.[115] 13.[116]

1.3.4 Theory

From a theoretical perspective, lack of a consensus regarding the physics of steady dynamic wetting has hindered attempts to model the influence of hydrodynamic factors, such as geometry, on the onset of dynamic wetting failure. In its most basic form, a model for wetting failure must include a mechanism that forces the transition from steady wetting to a failure state at some critical wetting speed. As depicted in Figure 1.12, several possible mechanisms exist within current dynamic wetting theories to describe this failure transition. In the case of hydrodynamic analysis (case A), the onset of wetting failure may be imagined as a critical limit in the steady-state solution space arising from one of the following reasons:

(i) steady-state wetting is not permitted by the governing hydrodynamics past some critical speed (i.e., no steady-state exists);

(ii) the dynamic wetting system becomes susceptible to unstable perturbation growth at finite Ca, perhaps even below the critical speed noted above.

Either of these mechanisms may force a steady 2D flow to adopt transient 3D characteristics, which is consistent with experimental observations of the wetting-failure transition. It should also be noted that many authors postulate a wetting-failure condition associated with $\theta_M = 180^o$ when using asymptotic hydrodynamic theories similar to (1.2) [2]; however, there exists no fundamental hydrodynamic principle connecting wetting failure to this geometric constraint and, in fact, numerous experimental studies report critical behavior occurring with $\theta_M < 180^o$ [117, 46, 82].

The second option (case B) features a molecular mechanism for dynamic wetting failure. In this framework, dynamic wetting occurs through the rapid exchange of fluid molecules between adsorption sites near the DCL [25]. Because the adsorption/desorption rates are finite, there exists a critical wetting speed beyond which this molecular displacement process cannot keep pace with the motion of the macroscopic wetting front. Thus, wetting failure originates on the molecular scale of the DCL and incomplete displacement there has macroscopic consequence, including a steep increase of θ_M to 180^o as the critical speed is approached [46].

In the final mechanism (case C), high-speed wetting may be considered a transient process in which a microscopic film of the displaced fluid penetrates past an *apparent*

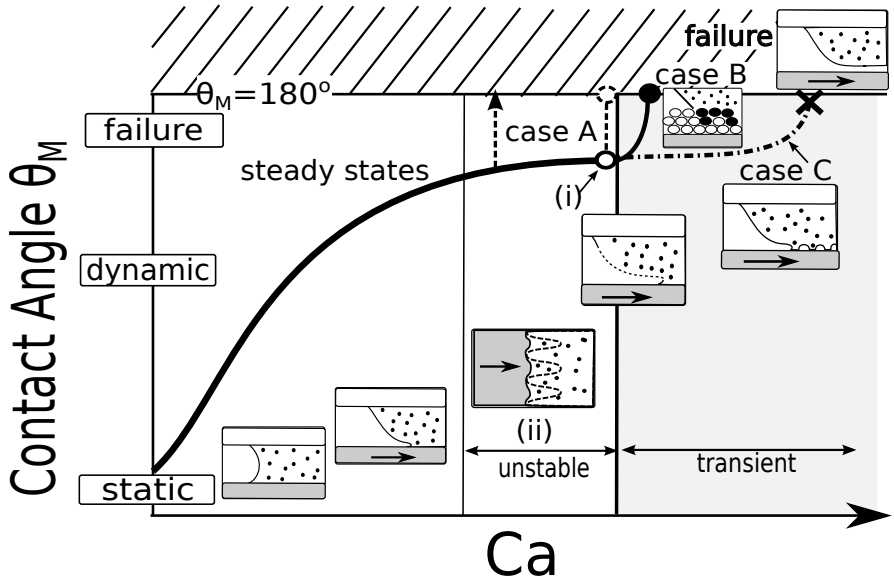

Figure 1.12: The qualitative behavior of θ_M with increasing Ca as suggested by several possible mechanisms for the transition from steady wetting to wetting failure. Case A(i) and A(ii) represent hydrodynamic mechanisms where Ca^{crit} arises from non-existent (open circle) or unstable steady-state solutions. Case B describes a molecular displacement process which forces θ_M to 180^o (filled circle) as wetting fails on a microscopic level. Case C depicts a transient regime where wetting failure ensues when the rate of film entrainment surpasses the rate of wetting nucleation (bold X).

contact line and into the wetting-liquid domain [33]. In order to prevent a "failure" state, this lubricating fluid layer must rupture to allow the nucleation of discrete wetting sites. Thus, the contact line no longer represents a physical line of three-phase contact, but approximates a finite 3D zone where a network of microscopic liquid bridges connect the bulk wetting liquid to the solid surface and resist complete entrainment of the displaced phase. The onset of wetting failure arises at some critical speed when the propensity for film entrainment outweighs the rate of wetting site nucleation, resulting in drastic deformation of the apparent wetting line as it can no longer hold the once steady wetting front.

Each mechanism implies different interface behavior leading up to the onset of wetting failure. For example, while macroscopic geometry is unlikely to greatly impact molecular rate processes, it is expected to play a significant role within a hydrodynamic mechanism. This work explores the onset of wetting failure in different flow conditions, which naturally lends itself to a hydrodynamic description. Specifically, this thesis adopts the perspective of case A(i) from Figure 1.12 and associates Ca^{crit} with critical points in the solution space for 2D steady dynamic wetting. This hydrodynamic wetting-failure approach is validated through comparison with Ca^{crit} data recorded from several experimental wetting systems (see Chapter 4).

1.4 Thesis Overview

In the remainder of this thesis, the onset of wetting failure (particularly in the regime of air entrainment) is systematically investigated using a variety of experimental and theoretical techniques. The following sections provide a brief outline for upcoming chapters.

1.4.1 The Hydrodynamic Model

In Chapter 2, a model is developed to study hydrodynamic effects on fluid-displacement systems operating near the onset of wetting failure. The model postulates that wetting failure arises from a lack of available 2D steady-state solutions when the capillary number exceeds some critical value Ca^{crit}. Unlike prior computational investigations, the model presented here strives to rigorously account for stresses from the two-fluid

flow near the DCL, even when one of the fluids is of much lower viscosity. Due to the complexity of the governing equations, solutions for this model must be determined numerically. Two distinct numerical approaches are presented for a 1D lubrication theory (Section 2.2) and a 2D flow model using FEM (Section 2.3). Both numerical approaches find turning points in steady-state solution paths corresponding to the onset of wetting failure at Ca^{crit}.

1.4.2 Steady Dynamic Wetting

Chapter 3 analyzes steady-state solutions obtained from the fluid-displacement model. Matching the experimental observations discussed in Section 1.2.2, the model predicts that larger apparent contact angles θ_M result as substrate speed increases. Each system with finite receding-fluid viscosity (i.e., $\chi = \mu_{rec}/\mu_{adv} > 0$) reveals a maximum speed of wetting, beyond which 2D steady-state solutions do not exist. This represents a new finding in the hydrodynamics of air/liquid displacement ($\chi \ll 1$), where several prior works predict steady 2D wetting at infinite speeds [53].

Section 3.3 compares numerical approaches to demonstrate that only the 2D flow model satisfactorily solves the governing equations for air/liquid systems. Section 3.4 takes a detailed look at the flow-field characteristics predicted for steady air/liquid displacement using the 2D flow model. Unlike past computational studies (e.g., [73, 118]), the present work exposes features of high-speed wetting near the onset of wetting failure. Results clearly demonstrate the importance of the air flow, which is traditionally neglected when modeling fluid-displacement flows.

1.4.3 The Onset of Wetting Failure

Chapter 4 characterizes the the onset of wetting failure from solutions generated with the 2D flow model. Section 4.3 evaluates the two-fluid flow near the critical substrate speed to understand the physical mechanism for wetting failure. In essence, it is found that receding flow contributes strong pressure gradients that exceed local surface-tension forces at Ca^{crit}, forcing unsteady elongation of the fluid interface. Section 4.4 considers the effects of viscosity, confinement, gravitational forces, wettability, and inertia on Ca^{crit} and also examines axisymmetric geometries. Finally, Section 4.5 demonstrates

that predictions from the model compare well against data from a number of different experimental systems, supporting the proposed wetting-failure mechanism.

1.4.4 Linear Stability Analysis

In Chapter 5, linear stability analysis is used to probe the sensitivity of liquid/liquid displacement to small-amplitude perturbations. In Section 5.2, a numerical model is constructed using a 1D lubrication theory. Solutions presented in Section 5.3 describe the decay or growth of interface perturbations in an equiviscous ($\chi = 1$) displacement system. Ultimately, the linear stability model reveals that steady-states are linearly stable for all tested forms of the small-amplitude perturbation (i.e., various wavelengths in the spanwise direction). This suggests that three-dimensional perturbations do not generally trigger an interface instability at $Ca < Ca^{crit}$. Instead, the onset of wetting failure occurs at $Ca = Ca^{crit}$ as proposed by Chapter 4. Analysis of the perturbation variables provides insight into the unsteady motion of the DCL at Ca^{crit}.

1.4.5 Delaying the Onset of Wetting Failure via Meniscus Confinement

Chapter 6 investigates the effect of system geometry on the onset of wetting failure. Confined geometries are considered where a wetting meniscus is bound between a substrate and another parallel surface, which is characteristic of numerous die-coating processes. To establish a foundation for understanding this problem, a novel experimental apparatus is used to directly compare meniscus characteristics in confined and unconfined wetting systems, as discussed in Section 6.2. Experimental data presented in Section 6.3 demonstrates that confinement postpones the onset of wetting failure to higher substrate speeds relative to an unconfined system. Section 6.4 shows that predictions from the hydrodynamic model match experimentally measured critical speeds as a function of interface confinement. Using results from hydrodynamic theory, Section 6.5 shows that confinement reduces viscous bending of the interface, effectively delaying the onset of wetting failure.

1.4.6 Characteristics of Air Entrainment along a Planar Substrate

In Chapter 7, characteristic substrate speeds and meniscus shapes associated with the onset of air entrainment are studied during dynamic wetting failure along a planar substrate. Section 7.2 describes a new experimental apparatus that uses high-speed video to document the dynamics of air entrainment as a tape substrate is drawn through a bath of a glycerol/water solution. Section 7.3 presents experimentally recorded critical speeds. Meniscus confinement within a narrow gap between the substrate and a stationary plate is shown to delay air entrainment to higher speeds for a wide range of solution viscosity, expanding upon the findings of Chapter 6. Furthermore, liquid pressurization (using compressed air within the experimental apparatus) is found to significantly impact the dynamics of air entrainment when the meniscus is located near a sharp corner, leading to even higher critical speeds. Similar effects have been observed in high-speed fiber coating [115, 88], though to the best of the authors' knowledge, this work presents the first demonstration of air entrainment postponed via liquid pressurization in a planar geometry.

Section 7.4 analyzes visualizations of the air/liquid meniscus recorded at Ca^{crit}. It is shown that operating conditions influence the size of entrained air films, with smaller films appearing in more viscous solutions. Regardless of size, air films become unstable to thickness perturbations and ultimately rupture, leading to the entrainment of air bubbles. Section 7.5 demonstrates that recorded critical speeds and air-film sizes compare well to predictions from a hydrodynamic model for dynamic wetting failure, supporting the wetting-failure mechanism proposed in Chapter 4.

1.4.7 The Hybrid FEM Model: Curtain Coating

This chapter analyzes the problem of fluid displacement in curtain coating using the hydrodynamic model developed in Chapter 2. Unlike prior works that neglect the air flow, this study considers the interaction of *two* viscous fluids. A novel computation technique is developed to reduce the cost associated with the two-fluid calculation. Section 8.2 describes the hybrid FEM technique used to compute the 2D flow of the advancing fluid while approximating receding-flow stresses with one-dimensional (1D) lubrication equations. Section 8.3 discusses numerical details associated with implementation of

the hybrid model in the curtain-coating system. Section 8.4 presents results from the curtain-coating model and makes comparison with parallel-plate solutions from previous chapters (e.g., Chapter 4) to demonstrate similar mechanisms for wetting failure. Although commonly neglected in the literature, air stresses are found to be a crucial ingredient when modeling high-speed curtain coating. Lastly, Section 8.5 summarizes the findings and discusses their implications on the study of curtain coating and other complex wetting behavior.

1.4.8 Conclusion

Chapter 9 summarizes the thesis with three key conclusions that can be drawn from the collective findings of preceding chapters. In addition, Section 9.2 suggests two future research directions that could be approached with the tools and understanding developed in this thesis.

Chapter 2

The Hydrodynamic Model

Although theoretical models are often used to probe mechanisms underlying interfacial phenomena, dynamic wetting systems present a challenge because fundamental questions about the DCL remain unanswered. As described in Section 1.2, both macroscale and microscale dynamics influence contact lines in general. In order to model critical dynamic-wetting behavior (e.g., the onset of wetting failure), it is necessary to define the dominant forces acting near the DCL. Unfortunately, there is no consensus on whether the key contact-line physics are hydrodynamic or molecular in nature. In fact, evidence suggests that the relative contributions of these two regimes may varying depending on specifics of the wetting system [60, 25].

This problem becomes more complicated when attempting to develop a general model for wetting failure. Beyond the issue of DCL fundamentals, there are also several different interpretations for the failure transition that could be incorporated into a model (see Section 1.3.4). Fortunately, a model's efficacy may be determined from comparisons with experimental studies of coating flows, where wetting failure is highly sensitive to a variety of hydrodynamic factors that are usually accessible within a computational framework.

This thesis focuses specifically on describing hydrodynamic effects on dynamic wetting systems near the onset of wetting failure. As discussed in Section 1.3.4, we postulate that wetting failure arises from a lack of available 2D steady-state solutions when the capillary number exceeds some critical value (corresponding to case A(i) in Figure 1.12). Beyond this critical point, the system evolves to transient or higher-dimensional flow,

which is consistent with observations of wetting failure in practice (see Section 1.3).

The theoretical model developed in this chapter features a common hydrodynamic framework for dynamic wetting [44, 55, 21]. Unlike prior investigations, this work strives to rigorously account for stresses from the two-fluid flow near the DCL. Even when the receding phase has relatively low viscosity (e.g., air), it is found that both fluids affect interface dynamics at high wetting speeds, requiring a consistent set of governing mechanics (see Section 2.1) to describe behavior over a wide range of system parameters. Due to the complexity of the governing equations, solutions for this model must be determined numerically. In Sections 2.2 - 2.3, two different numerical approaches are presented with distinct advantages and disadvantages toward the analysis of dynamic wetting problems.

2.1 Governing Equations

This work focuses on dynamic wetting between two immiscible fluids along a smooth, homogeneous substrate. The system we consider is illustrated in Figure 2.1, where an impenetrable fluid interface with surface tension σ resides within a gap H between a stationary boundary (top) and a substrate (bottom) that moves at speed U. A pressure drop ($\Delta P = P_L - P_R$) applied across the length of the channel acts to specify the position of the fluid interface as it balances with drag forces from the moving plate. A schematic of our model wetting system is illustrated in figure 6.6. The steady Navier-Stokes equations govern the fluid velocities $\boldsymbol{v}$ and pressures p:

$$\boldsymbol{\nabla} \cdot \boldsymbol{v} = 0, \quad Re(\boldsymbol{v} \cdot \boldsymbol{\nabla} \boldsymbol{v}) = \nabla^2 \boldsymbol{v} - \boldsymbol{\nabla} p. \tag{2.1}$$

Lengths, velocities and stresses are made dimensionless with H, U, and $\mu U/H$, respectively. The Reynolds number ($Re = \rho U H/\mu$) includes the fluid density ρ and viscosity μ. (Note that subscripts will be used to distinguish between properties of the receding and advancing fluids, e.g., Re_{rec} and Re_{adv}.)

A set of simplifying assumptions may be used when analyzing the confined system depicted in Figure 2.1a:

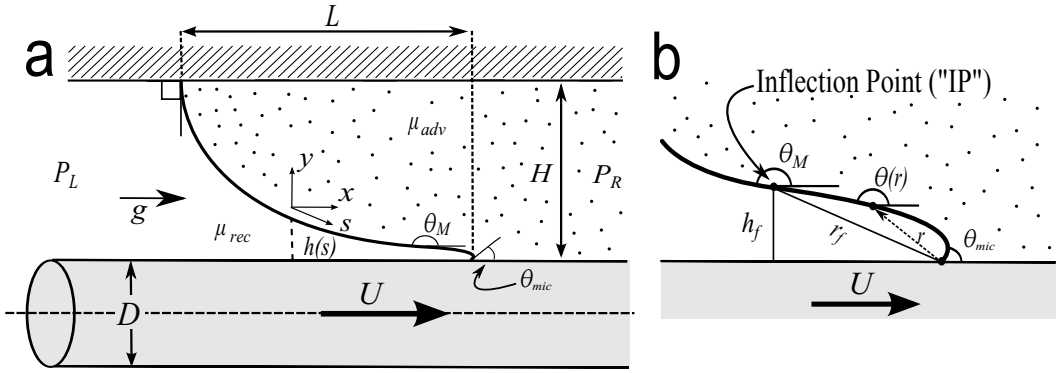

Figure 2.1: Idealization of fluid displacement along a substrate moving with speed U. (a) Outer view of the fluid interface confined within an axisymmetric channel where a fiber substrate of diameter D moves through the center of an annulus with gap H. Note that this system becomes planar when $H/D = 0$. (b) Inner view of the fluid interface where the interface angle θ varies strongly with the radial distance r from the DCL. The maximum interface angle (θ_M) is located at the interface inflection point (IP), which is measured by vertical (h_f) and radial (r_f) distances from the DCL.

(i) viscous stresses dominate over inertial contributions, which results in the creeping-flow equations:

$$\boldsymbol{\nabla} \cdot \boldsymbol{v} = 0, \quad \boldsymbol{\nabla} p = \nabla^2 \boldsymbol{v}; \tag{2.2}$$

(ii) gravitational forces have negligible influence on confined wetting failure.

Although creeping flow neglects inertial effects associated with wetting failure, (2.2) captures the divergent viscous stress that characterizes the DCL in hydrodynamic wetting models [65, 40]. Due to the strength of these viscous effects, finite Re in (2.1) only weakly changes the characteristics of wetting failure relative to the creeping-flow case, as will be demonstrated in Section 4.4.5. While this is true for the confined geometry shown in Figure 2.1a, inertia plays a more significant role in complex coating flows, such as the case of curtain coating explored in Chapter 8.

Approximation (ii) follows from inspection of the characteristic Bond ($Bo = \rho g H^2/\sigma$) and Stokes numbers ($St = \rho g H^2/\mu U$), which are both significantly less than $O(1)$ for confined interfaces ($H < 1$ mm) near the onset of wetting failure. (As a rough estimate, $\mu U^{crit} \sim \sigma \geq 10$ mN/m for most Newtonian liquid considered in this work.) Gravity becomes important as the system becomes unconfined, in which case the capillary length $l_{cap} = \sqrt{\sigma/(\rho g)}$ becomes the important outer length scale (see Section 4.4.3).

The interface shape is determined by the following set of boundary conditions enforced at $y = h(s)$:

$$\boldsymbol{v}|_{rec} = \boldsymbol{v}|_{adv}, \tag{2.3}$$

$$\boldsymbol{n} \cdot \boldsymbol{v} = 0 \tag{2.4}$$

$$\boldsymbol{n} \cdot \boldsymbol{T} \cdot \boldsymbol{t}|_{rec} = \boldsymbol{n} \cdot \boldsymbol{T} \cdot \boldsymbol{t}|_{adv}, \tag{2.5}$$

$$\kappa = Ca\delta(\chi)(\boldsymbol{n} \cdot \boldsymbol{T} \cdot \boldsymbol{n}|_{rec} - \boldsymbol{n} \cdot \boldsymbol{T} \cdot \boldsymbol{n}|_{adv}) + (Bo)x, \tag{2.6}$$

where $\boldsymbol{T}$ is the Newtonian stress tensor, κ is the interface curvature, and u and v are the horizontal (x-coordinate) and vertical (y-coordinate) velocity components, respectively. Normal ($\boldsymbol{n}$) and tangent ($\boldsymbol{t}$) vectors are defined by the interface profile at $y = h(s)$. The stress tensor for the receding fluid contains the viscosity ratio, $\chi = \mu_{rec}/\mu_{adv}$, such that $\boldsymbol{T}|_{rec} = \frac{\chi}{2}[\boldsymbol{\nabla v} + (\boldsymbol{\nabla v})^T]$. The Bond number ($Bo = (\rho_{adv} - \rho_{rec})gH^2/\sigma$) expresses the magnitude of gravitational forces relative to surface-tension forces (the gravity vector has magnitude g and points toward the advancing fluid in Figure 2.1). Note that p includes the pressure head from gravity ρgx (the "modified pressure" in [119]) when assumption (ii) is not invoked ($Bo > 0$).

Following the convention used within the dynamic-wetting literature, Ca (no subscript) represents the capillary number with respect to the most viscous fluid. Consequently, the function $\delta(\chi)$ must be designated to keep (2.6) consistent throughout the entire range of χ:

$$\left.\begin{array}{l} Ca = \mu_{adv}U/\sigma \text{ and } \delta(\chi) = 1 \text{ for } \chi \leq 1; \\ Ca = \mu_{rec}U/\sigma \text{ and } \delta(\chi) = 1/\chi \text{ for } \chi > 1. \end{array}\right\} \tag{2.7}$$

Terminal points of the interface take on special boundary conditions to account for the presence of contact lines. At the fixed plate, the SCL adheres to no-slip and no-penetration along the stationary surface:

$$\boldsymbol{v} = 0. \tag{2.8}$$

Fluid slip must be permitted along the moving boundary to avoid a stress singularity that would otherwise arise at the DCL [65]. A Navier condition relates the fluid velocity to fluid shear stress with the degree of slip characterized by the slip length l_{slip}:

$$\boldsymbol{t_s} \cdot (\boldsymbol{v} - \boldsymbol{U}) = \lambda \left(\frac{\mu_{adv}}{\mu}\right) [\boldsymbol{n}_s \cdot \boldsymbol{T} \cdot \boldsymbol{t_s}]. \tag{2.9}$$

The dimensionless slip length is expressed by $\lambda = l_{slip}/H$, and the substrate's normal, tangent, and velocity vectors are represented by $\boldsymbol{n_s}$, $\boldsymbol{t_s}$, and $\boldsymbol{U}$, respectively. The slip length is assumed to be equal for both fluid phases and (2.9) is applied along the entire substrate in order to have a smooth velocity gradient from the outer "no-slip" region ($\boldsymbol{v} \to \boldsymbol{U}$) to the inner "slip" region ($\boldsymbol{v} \to \boldsymbol{0}$). As illustrated in Figure 2.1, planar and axisymmetric systems are evaluated within this study. In the axisymmetric case, the fiber diameter introduces a second length-scale ratio into the fluid-displacement system, H/D. (Note that $H/D = 0$ recovers the planar system.)

Interface slopes must also be prescribed as a boundary condition at each contact line.

$$\frac{dh}{dx} = \tan\theta_{mic} \tag{2.10}$$

The condition in (2.10) prescribes the microscopic contact angle θ_{mic}, which can be interpreted as the substrate wettability and is sometimes assumed to be equal to the static contact angle [55, 21]. Smaller values of θ_{mic} promote more contact between the advancing fluid and substrate in Figure 2.1. Though neglected by this study, the influence of flow field [39, 83] and molecular interactions [61, 18] on θ_{mic} remain active areas of research. Section 4.4.4 briefly discusses the selection of the substrate's microscopic contact angle, θ_{mic}, and its impact on predictions from the hydrodynamic model.

A notable implication of our θ_{mic} assumption is that any observed change in dynamic angle results from an *apparent* contact angle θ_M. Figure 2.1b emphasizes that the prescribed microscopic angle is distinct from the dynamic angle θ_M, which arises from viscous bending at some distance away from the moving contact line. In this work, θ_M is defined as the maximum interface angle, although the details of specific experimental approaches (e.g., resolution of visualization techniques) would influence the definition of θ_M in practice. The location of θ_M marks an inflection point (IP) along the interface with vertical and radial distances from the DCL of h_f and r_f, respectively (see Figure 2.1b).

The creeping-flow equations and associated boundary conditions generate a highly nonlinear free-boundary problem. We analyze the resulting equation set through two different approaches:

(i) a non-uniform finite difference method to evaluate a 1D lubrication-type approximation of the governing equations,

(ii) a Galerkin finite element method (FEM) with elliptic mesh generation to evaluate the full 2D free-boundary problem,

Our first approach results from the observation that the fluid interface in the vicinity of the moving wetting line will tend toward parallel alignment with the substrate as the meniscus deforms and elongates. This "quasi-parallel" (QP) assumption simplifies the governing equations to represent a wetting dynamics dominated by horizontal flow near the meniscus. The second approach uses FEM to solve for the 2D flow field and interface position simultaneously. Although this approach is clearly more rigorous in its treatment of the hydrodynamics, it also carries the penalty of being very computationally taxing. Further benefits and drawbacks to each approach are exposed within the following sections.

2.2 Quasi-parallel Approach

Lubrication-theory-based models commonly provide insight into the mechanics of complex flows with a major reduction in computational effort in comparison to full 2D or 3D calculations [120]. In principle, lubrication theory is restricted to long, slender fluid domains (e.g., $\theta(r) \to 180^o$) with slowly varying boundaries ($|\partial\theta/\partial x| \ll 1|$) [67]. However, lubrication-theory-based models sometimes work well even outside of this regime [120]. For instance, a quasi-parallel (QP) flow model was shown to compare favorably to full 2D models for liquid/liquid displacement over a wide range of contact angles ($\theta_{mic} \in [30^o, 150^o]$) [98]. Results therein reveal the natural appearance of Ca^{crit} from turning points in families of steady-state solutions. To date, the QP approach has proven valuable for analyzing wetting flows with a viscous receding phase [98, 99], but its performance has not been characterized for systems with an advancing phase that is significantly more viscous than the receding. The remainder of this section considers an adaptation of the QP approach for general fluid pairs, as defined by the full range of the viscosity ratio χ.

2.2.1 Quasi-parallel Flow Approximation

The formulation of the QP approach follows closely to descriptions provided in prior works [98, 99]. The creeping-flow equations (2.2) simplify to a one-dimensional momentum balance when considering nearly parallel flow generated in the direction of the substrate motion. Integration of the momentum balance results in a velocity profile of the following form:

$$u = a_1(x) + a_2(x)y + \frac{1}{2}\frac{\mathrm{d}p}{\mathrm{d}x}y^2 \tag{2.11}$$

The unknown variable coefficients $a_1(x)$ and $a_2(x)$, and the pressure gradient become specified in terms of $h(s)$ for each fluid after applying the velocity boundary conditions.

First, a slip condition is derived from (2.9) for parallel flow near the substrate at $h = 0$:

$$u - 1 = \lambda\frac{du}{dy}. \tag{2.12}$$

In the spirit of the original formulation of the QP approach [98], the top plate has oppositely-directed velocity in comparison to the substrate (bottom plate), as shown in Figure 2.2. Since the top plate moves with speed U_T, a slip condition similar to (2.12) is required near the contact line at $h = 1$:

$$u + \omega = -\lambda\frac{du}{dy}, \tag{2.13}$$

where the dimensionless top-plate speed is defined by $\omega = U_T/U$. Note that (2.13) reduces to $u = 0$ as $\omega \to 0$ because of weak velocity gradients near the top plate as U_T decreases.

Next, a tangential stress balance is derived from (2.5) in the limit of parallel flow:

$$\frac{\partial u}{\partial y}|_{adv} = \chi\frac{\partial u}{\partial y}|_{rec}. \tag{2.14}$$

Due to the dominance of the horizontal velocity, only one velocity gradient contributes significant stress with each fluid. These tangential stress are weighted by the viscosity ratio $\chi = \mu_{rec}/\mu_{adv}$. Both fluids generate equivalent stresses in the special case that $\omega = 1$ and $\chi = 1$ (the "symmetric case"), which has been studied previously [98, 99].

Lastly, the kinematic condition (2.15) enforces zero mass flux across the fluid interface, expressed as

$$\int_0^h u_{rec}\,dy = 0; \quad \int_h^1 u_{adv}\,dy = 0 \tag{2.15}$$

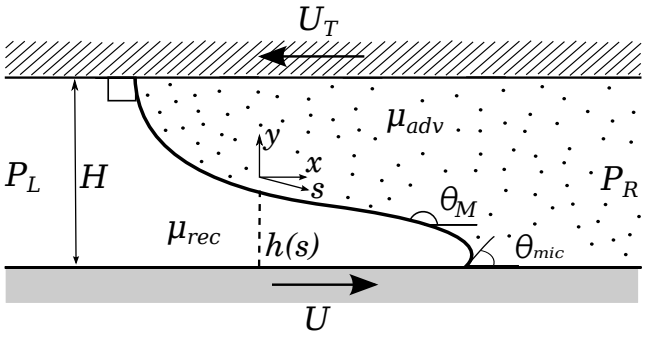

Figure 2.2: Schematic representation of the QP approach. The fluid interface, $h(s)$, separates two immiscible fluids in a gap H with top and bottom plates moving at velocities U_T and U, respectively. The interface is characterized by contact angles θ_{mic} at the DCL and a maximum interface angle θ_M.

when combined with the continuity constraint in (2.1). Incorporating equations (2.11) - (2.15) with the normal-stress condition (2.6) develops a well-posed equation system for the QP approach.

Normally, solving this system is difficult due to the non-linear partial differential equation introduced by the curvature term κ in (2.6):

$$\kappa = \frac{\partial^2 h}{\partial x^2}\left[1 + \left(\frac{\partial h}{\partial x}\right)^2\right]^{-\frac{3}{2}}. \tag{2.16}$$

The QP approach removes this problem with an approximation of the arc length: $ds \approx dx$. Using this approximation and the differentiation of (2.6), the normal stress balance becomes

$$\frac{d\kappa}{ds} = Ca\delta(\chi)\left(\frac{dp}{dx}|_{adv} - \frac{dp}{dx}|_{rec}\right) = F(h(s); Ca, \lambda, \chi, \omega). \tag{2.17}$$

In (2.17), curvature gradients along the interface arc length s balance with local normal forces (pressure gradients in the parallel flow limit) exerted by the fluid flow. This expression implies that differential steps along s and x are equivalent, which is consistent with the lubrication approximation and becomes more rigorous as the interface elongates in the approach to wetting failure. Since (2.17) features a differential form of the normal stress balance, absolute fluid pressures may be prescribed by an arbitrary pressure drop across the channel ($\Delta P = P_L - P_R$), though ΔP is not a necessary input of the QP approach.

A set of geometric identities relate the interface curvature, angle, and Cartesian position (x, $h(s)$) to the arc-length domain:

$$\kappa = \frac{\mathrm{d}\theta}{\mathrm{d}s}, \quad \frac{\mathrm{d}h}{\mathrm{d}s} = -\sin\theta, \quad \frac{\mathrm{d}x}{\mathrm{d}s} = -\cos\theta. \tag{2.18}$$

Therefore, (2.17) may be solved as function of s without integrating in x, avoiding the hassle of solving (2.16) directly. Note that curvature remains rigorously defined in (2.18) for arbitrary interface profiles. Thus, the QP approach is not completely self-consistent within the lubrication limit.

2.2.2 Comparison to Lubrication Theory

The *ad hoc* modifications discussed above provide the QP approach with several benefits that are not available to conventional lubrication analysis. Qualitatively, the QP approach allows for interface profiles to be double-valued in the x-domain, as shown in Figure 2.2 where the interface must bend back sharply near the bottom plate to meet the small θ_{mic}. Conventionally, lubrication analysis uses a 1D interface height function $h = h(x)$, which only allows a single values of h for each position along the x-coordinate. Consequently, profiles with a large disparity between θ_M and θ_{mic} cannot be addressed with strict lubrication theory.

More significantly, the QP approach maintains the full curvature κ in (2.17). In contrast, lubrication analysis requires that $|\frac{dh}{dx}| \ll 1$, which results in an asymptotic form of the curvature, κ_{lube}:

$$\kappa_{lube} = \frac{d^2h}{dx^2} = (\sec^3\theta)\kappa. \tag{2.19}$$

Equation (2.19) uses the identity $\sec(\theta) = \sqrt{1 + (\frac{dh}{dx})^2}$ (recall that $\frac{dh}{dx} = \tan(\theta)$ from (2.18)).

Substituting (2.19) into (2.6) and differentiating with respect to x produces the normal stress balance in the lubrication limit:

$$\frac{d\kappa}{dx} - 3\kappa\tan(\theta)\frac{d\theta}{dx} = Ca\delta(\chi)\cos^3(\theta)\left(\frac{dp}{dx}|_{adv} - \frac{dp}{dx}|_{rec}\right) \tag{2.20}$$

A quick asymptotic analysis of this expression shows that as $\theta \to 90^o$ the interface angle becomes constant $\left(\frac{d\theta}{dx} \to 0\right)$. In other words, lubrication analysis predicts that the

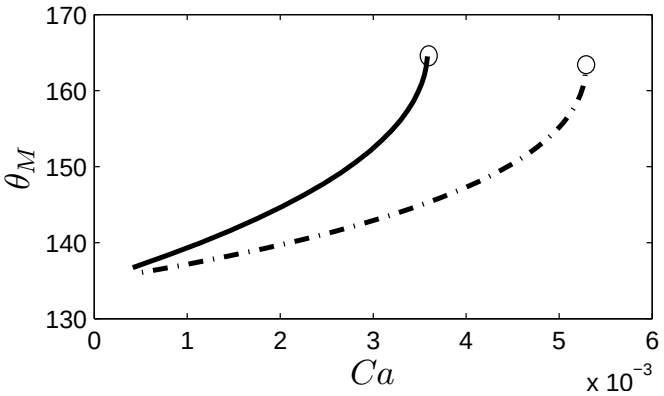

Figure 2.3: Comparison of solutions obtained with the QP approach (solid) and lubrication theory (dashed). Each solution path is generated for symmetric case ($\chi = 1$ and $\omega = 1$) with $\theta_{mic} = 135^o$ and $\lambda = 10^{-3}$. The curves show that lubrication theory overestimates the amount of viscous force relative to surface tension (i.e., Ca) needed to change the interface angle. Turning points are denoted by open circles.

viscous forcing term $\left(\frac{dp}{dx}|_{adv} - \frac{dp}{dx}|_{rec}\right)$ must become enormous to deform interfaces characterized by angles much less than 180^o. If this were true, dynamic angles would only advance from 90^o toward 180^o as $Ca \to \infty$, which is in clear conflict with experimental data shown in Section 1.2.2. Thus, lubrication analysis generally overestimates the Ca needed to deform the 2D fluid interface. This is conveyed by a comparison between lubrication and QP approach in Figure 2.3.

Instead of altering the curvature term, the QP approach modifies the normal stress balance by invoking $ds \approx dx$, as reflected in (2.17). The arc-length dependence can be removed from the balance using the definition for $\frac{dx}{ds}$ in (2.18), resulting in the following:

$$\frac{d\kappa}{dx} = Ca\delta(\chi)J_{QP}(\theta)\left(\frac{dp}{dx}|_{adv} - \frac{dp}{dx}|_{rec}\right)$$

$$J_{QP}(\theta) = \sec(\theta) \tag{2.21}$$

Equation (2.21) shows that a factor of $\sec(\theta)$ appears in the normal stress balance for the QP approach. This can be seen as viscous correction factor, $J(\theta)$, needed to compensate for the parallel flow approximation used to reduce the system to a 1D flow field. In fact, a similar form of the normal stress balance results when looking at a higher-order expansion of lubrication theory that includes systems without slender

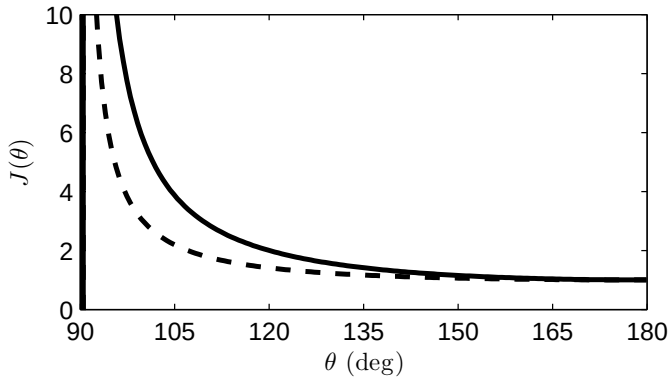

Figure 2.4: Comparison of viscous correction factors $J(\theta)$. Solid and dashed line plot the correction factors from the QP approach in (2.21) and higher-order lubrication theory in (2.22), respectively. Note that both curves become unbounded at $\theta \to 90^o$ and equal unity at $\theta \to 180^o$. The latter asymptote reflects convergence to the true (small-angle) lubrication limit. Lubrication analysis cannot proceed for $\theta < 90^o$ because the interface is double-value on the x-domain.

slopes [121]. Specifically, the full curvature is maintained in κ and a correction factor $J_S(\theta)$ augments the viscous forcing term:

$$\frac{d\kappa}{dx} = Ca\delta(\chi)J_S(\theta)\left(\frac{dp}{dx}|_{adv} - \frac{dp}{dx}|_{rec}\right)$$

$$J_S(\theta) = \frac{\cos(\pi-\theta)\sin^2(\pi-\theta)}{\pi-\theta-\sin(\pi-\theta)\cos(\pi-\theta)} \tag{2.22}$$

The viscous correction factors from (2.21) and (2.22) are compared in Figure 2.4. Both curves match well for angles greater than 135^o, but $J(\theta)$ increases at a greater rate as $\theta \to 90^o$. Nevertheless, the similarity between the curves suggests that the arc-length approximation ($dx \approx ds$) used in the QP approach effectively augments viscous forces in a manner that that is consistent with high-order lubrication theory. In total, the use of complete curvature ($\kappa = d\theta/ds$) and a viscous correction factor $J(\theta) = \sec(\theta)$ makes the QP approach more successful than classical lubrication analysis (see Figure 2.3) for the study of dynamic wetting failure.

2.2.3 Numerical Method

Numerical analysis is required to solve the ODE system described in Section 2.2.1. In order to resolve sharp interface curvature near the DCL [98], a centered finite-difference

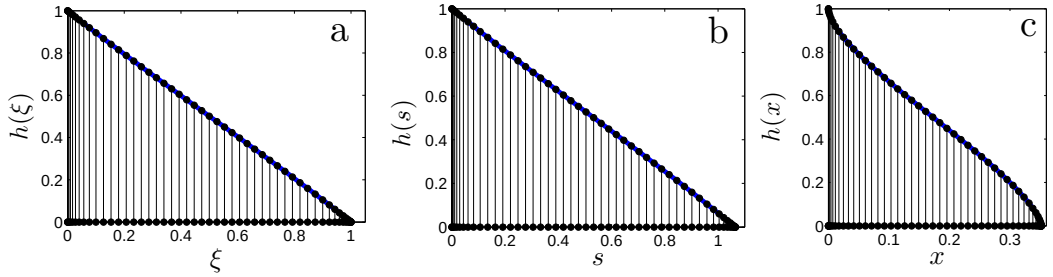

Figure 2.5: Transformation of the interface profile between the (a) computational coordinate ξ, (b) arc-length coordinate s , and (c) Cartesian coordinate x used in the QP approach. The bold blue line denotes the interface profile in each panel for the symmetric case ($\omega = 1$ and $\chi = 1$) with $\theta_{mic} = 90^o$, $\lambda = 0.01$, and $Ca = 0.03$ (more shown in Figure 2.7). Schematic comparison of numerical methods applied to the quasi-parallel model. Filled circles and connected lines mark the node positions with $N = 50$.

method is implemented along a nonuniform grid [122] where nodes are concentrated near the contact lines. Since the interface shape in not known *a priori*, the governing equations are mapped to a computational domain where the domain boundaries are defined by $\xi \in [0, 1]$. Thus, the position of the DCL in the arc-length domain ($s = L$) becomes an additional unknown which is included in the mapping relation $\xi = s/L$. The following finite-difference expressions are applied to each computational node i:

$$\left.\begin{aligned} \frac{\theta_{i+1} - \theta_i}{\Delta\xi_i[(\Delta\xi_i + \Delta\xi_{i-1})/2]} - \frac{\theta_i - \theta_{i-1}}{\Delta\xi_{i-1}[(\Delta\xi_i + \Delta\xi_{i-1})/2]} &= L^2 F(h_i; Ca, \lambda, \chi, \omega), \\ \frac{h_{i+1} - h_{i-1}}{\Delta\xi_i + \Delta\xi_{i-1}} &= L \sin\theta_i, \end{aligned}\right\} \tag{2.23}$$

where $F(h_i; Ca, \lambda, \chi, \omega)$ represents the functional form of the pressure gradients in (2.17). The nonuniform grid influences (2.23) through the node spacings $\Delta\xi_{i-1} = \xi_i - \xi_{i-1}$ and $\Delta\xi_i = \xi_{i+1} - \xi_i$. Figure 2.5 demonstrates the nonuniform grid used to calculate the interface profile with the computational (ξ) and physical (s, and x) coordinate systems used in the QP approach.

Near the DCL, the pressure gradient (represented by $F(h_i; Ca, \lambda, \chi, \omega)$) becomes very large in magnitude, diverging as $h \to 0$. The slip condition in (2.1) makes this singularity integrable, allowing the interface to converge to the prescribed microscopic angle very close to the DCL ($\theta \to \theta_{mic}$ as $h \to 0$). Imposing boundary conditions slightly away from the substrate avoids numerical problems associated with the pressure singularity,

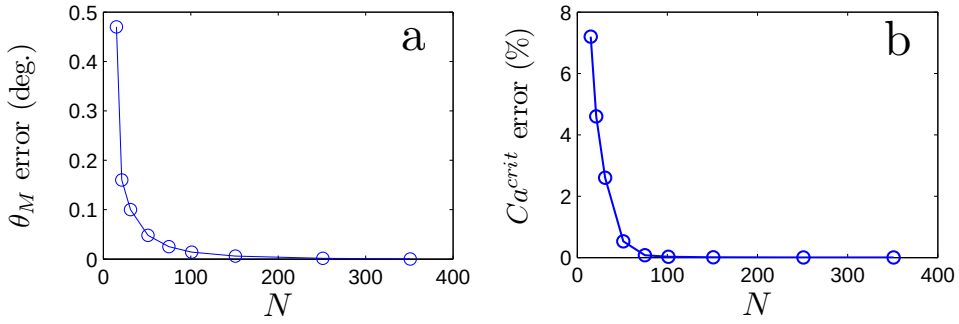

Figure 2.6: Error associated with (a) θ_M and (b) Ca^{crit} calculated with the finite-difference method as a function of the number of nodes N. Solutions are compared to the symmetric case ($\omega = 1$ and $\chi = 1$) of [98] with $\theta_{mic} = 90^o$, and $\lambda = 0.01$ (more shown in Figure 2.7). As N increases, the solutions converge to $\theta_M = 114.29^o$ (at $Ca = 0.03$) and $Ca^{crit} = 0.048$.

while still resolving the essence of the microscopic interface profile (i.e., θ_{mic}). More specifically, the terminal nodes ($i = 1$ and $i = N$) of the interface are placed a distance ϵ_s away from the contact lines, such that

$$\theta_i = \begin{cases} 90^o & i = 1 \\ \theta_{mic} & i = N \end{cases} \quad ; \quad h_i = \begin{cases} 1 - \epsilon_s & i = 1 \\ \epsilon_s & i = N. \end{cases} \tag{2.24}$$

Solutions are insensitive to the choice of ϵ_s as long as it is two orders of magnitude smaller than the slip length λ. As a conservative measure, $\epsilon_s \leq \lambda \times 10^{-3}$ for all QP results reported here.

It should be noted that two boundary conditions appear for h in (2.24) although the height function is governed by a first-order differential equation in (2.23). The boundary condition at $i = 1$ is strongly imposed (substituting for (2.23)), while the boundary condition at $i = N$ is used as a constraint that specifies the unknown interface length L. To satisfy the first-order ODE, the backward-difference approximation ($(h_i - h_{i-1})/\Delta\xi_{i-1} = L \sin\theta_i$ is applied at $i = N$ instead of the centered-difference form of (2.23).

The finite-difference approach is validated against solutions for the symmetric case ($\omega = 1$ and $\chi = 1$) that has been verified in previous works [98, 99]. Computed interface angles (e.g., θ_M) and critical capillary numbers Ca^{crit} are highly sensitive to numerical resolution. Figure 2.6 demonstrates that numerical error decays exponentially as the

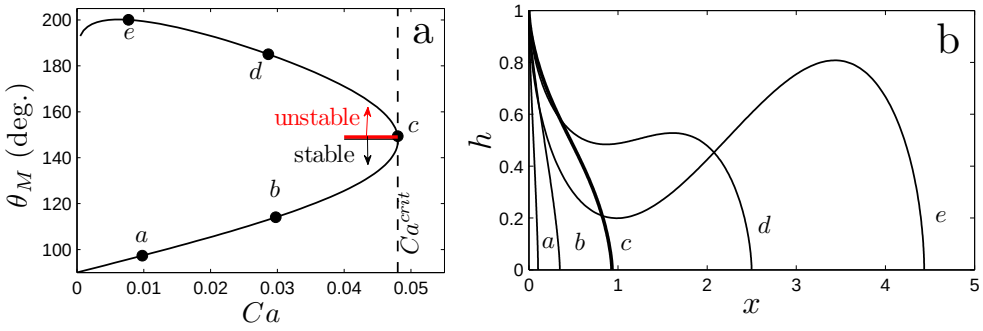

Figure 2.7: Demonstration of a turning point in the QP solution path for the symmetric case ($\omega = 1$ and $\chi = 1$) with $\theta_{mic} = 90^o$ and $\lambda = 0.01$. (a) The maximum interface angle θ_M is plotted as a function of Ca. (b) Interface profiles corresponding to points along the solution path in (a) are shown with corresponding letter labels. The bold line marks the critical interface at $Ca^{crit} = 0.048$.

number of nodes N increases in the finite-difference method. When $N > 150$, errors are typically less than 0.1% for both θ_M and Ca^{crit}. (Note that this error varies with λ, which sets the smallest length scale in the system.) To ensure convergence, 351 nodes are used for all of the QP computations presented throughout the remainder of this work. Nodes are concentrated at the ends of the ξ-domain with node spacing proportional to the cube of the distance from the nearest contact line. Solutions to the QP approach seem insensitive to the functional form of the node distribution (e.g., polynomial vs. hyperbolic [123]), so long as $\Delta\xi_i \sim \epsilon_s$ near the contact line.

2.2.4 Solution Paths

The critical capillary number Ca^{crit} is determined by tracing a steady-state solution path to increasing Ca for a given set of system parameters (i.e., θ_{mic}, χ, ω, and λ) until locating a critical point where the method fails to converge to a solution. This critical point represents a bifurcation which separates stable and unstable branches of steady-state solutions [98, 99, 68]. In this work, a pseudo-arclength continuation scheme [124] is used to trace past bifurcation points and obtain complete steady-state solution trajectories. Results from the QP approach have been validated against solution paths for the symmetric case ($\omega = 1$ and $\chi = 1$) presented in [98].

Figure 2.7 plots solutions that are typical of the QP approach. The solution path

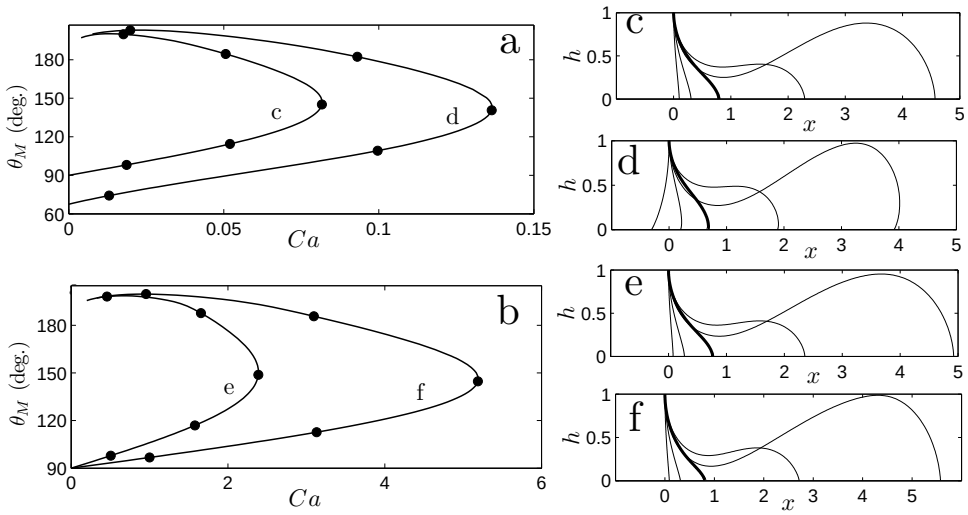

Figure 2.8: QP solutions for various system parameters. Solution paths (panels a and b) and corresponding interface profiles (panels c-f) are plotted in similar fashion to Figure 2.7. (a) Solution paths are shown for different substrate wettabilities: $\theta_{mic} = 90^o$ (curve c) and $\theta_{mic} = 45^o$ (curve d). The following parameters are the same for both curves: $\omega = 0$, $\chi = 1$, and $\lambda = 0.01$. (b) Solutions paths are plotted with different values of the slip length: $\lambda = 10^{-2}$ (curve e) and $\lambda = 10^{-4}$ (curve f). The following parameters are the same for both curves: $\omega = 0$, $\chi = 0.01$, and $\theta_{mic} = 90^o$. Each panel c-f corresponds to the solution path labeled with the matching letter.

(Figure 2.7a) shows that θ_M starts near θ_{mic} at low speed ($Ca \to 0$) and moves toward 180^o as Ca increases. However, the solution path encounters a turning point at Ca^{crit} well before θ_M is able to achieve 180^o. Moving around the turning point, the solution path proceeds along an unstable branch [98, 99], where θ_M continues to increase as Ca decreases. The interface elongates dramatically along the unstable branch (see Figure 2.7b), forming a thick ridge as fluid builds near the contact line. As Ca decreases, the interface ridge grows until it begins to interact with the opposing solid surface as $Ca \to 0$ (shown more clearly in Figure 2.8c-f, as discussed below).

System parameters only weakly influence the qualitative features of solution paths from the QP approach. For instance, solutions for various parameter values (ω, χ, λ, and θ_{mic}) are shown in Figure 2.8. Despite differences in the material properties, each solution path (Figure 2.8a-b) proceeds through the same characteristic trajectory outline above for Figure 2.7. Furthermore, each solution path produces remarkably similar interface profiles (Figure 2.8c-f) with noticeable differences only arising when changes are

made to the substrate wettability (especially at low speed where θ_{mic} strongly impacts the interface shape). In each case, the interface reaches an angle of $\theta_M \approx 150^o$ near the turning point (Ca^{crit}) and then proceeds to form a thick film of the receding fluid along the unstable branch.

Although interface predictions seem consistent with observations of liquid-film withdrawal [96], the results severely conflict with evidence from the regime of air entrainment ($\chi \ll 1$), where very thin air films [105] are observed at the DCL when $\theta_M \approx 180^o$ [43]. This conflict suggests that assumptions of the QP approach may not be valid for the entire range of viscosity ratio χ. Results from a 2D numerical approach (method description in Section 2.3) confirm that the advancing liquid flow violates the quasi-parallel approximation implemented within this section. Therefore, the QP approach only satisfactorily approximates the governing mechanics of the hydrodynamic model when viscous effects of the advancing fluid are small compared to the receding flow (i.e, $\chi \geq 1$). Results from the QP approach are discussed further in Section 3.3.

2.3 2D Flow Model

The second computational approach uses a Galerkin finite element method (FEM) to evaluate the full 2D set of equations outlined in Section 2.1. The theory and implementation of FEM has been discussed in a number of prior works [35, 125, 126, 127]. Therefore, this section focuses on details of FEM that are needed to treat dynamic wetting in the 2D flow model. The reader is encouraged to consult reference [128] for a broader perspective of FEM applied to free-boundary problems.

The utility of FEM has been demonstrated for the analysis of complicated interface dynamics [129] and two-fluid coating flows [130]. Since the interface position is coupled to the flow field, domain boundaries for the physical problem are unknown. Thus, the 2D system is mapped to a fictitious, computational domain where the dynamic boundary conditions are implemented. Within this computational domain, coordinates for the physical domain are retained as unknowns that are solved simultaneously with the flow variables. The free-boundaries (fluid interfaces) of the physical domain deform in response to the global flow field. The mapping function that connects the physical and computational domain satisfies the elliptic mesh generation equations as follows:

$$\boldsymbol{\nabla} \cdot (D_\xi \boldsymbol{\nabla} \xi) = 0, \quad \boldsymbol{\nabla} \cdot (D_\eta \boldsymbol{\nabla} \eta) = 0. \tag{2.25}$$

These equations effectively map the computational coordinates ξ and η back to the physical domain represented within 2D Cartesian coordinates. The elliptic character of the mapping equation preserves mesh quality by smoothly distributing elements within the physical domain as controlled by the diffusion coefficients D_η and D_ξ [125].

The primary objective of FEM is to solve the governing fluid equations through the minimization of weighted residuals resulting from the differential equations. Each flow variable is approximated by an expansion of polynomial basis functions. The analysis presented within this work uses quadrilateral elements with continuous biquadratic basis functions to describe position and velocity variables, and linear discontinuous basis functions for pressure. A typical mesh used for the FEM computations is illustrated in figure 2.9.

Similar to the QP approach (see Section 2.2.4), the critical capillary number is determined by tracing steady-state solutions as a function of Ca. Solution paths from the 2D flow model reveal a turning point that corresponds to Ca^{crit} and some critical

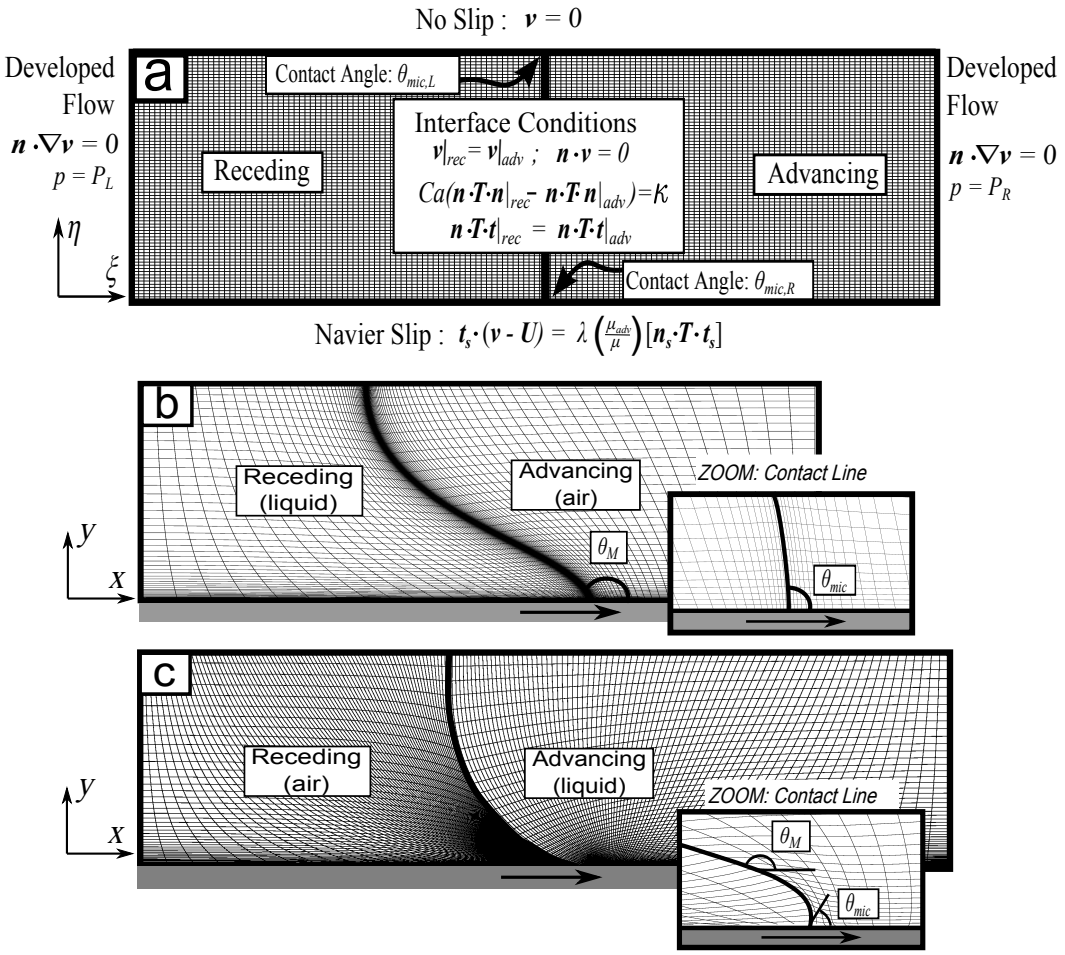

Figure 2.9: Meshes used with FEM. (a) The mesh in computational coordinates with boundary conditions denoted at the domain boundaries and fluid interface. (b-c) Solutions mapped mapped back to the physical domain for (b) $\chi \geq 1$ and (c) $\chi < 1$. Solutions are shown at $Ca \approx Ca^{crit}$ for each case. A coarser mesh (5000 elements) is used in (b) because liquid/air and liquid/liquid interfaces primarily bend on a macroscopic scale, as illustrated by magnification ($10^2\times$) of the contact line. Finer mesh (16000 elements) is used in (b) with the smallest element height $\sim 10^{-6}$. Magnification ($10^4\times$) of the contact line reveals sharp interface bending that separates θ_M and θ_{mic} along the air/liquid interface. Parameter values: $\lambda = 10^{-2}, \theta_{mic} = 90^o, Re = 0$ with (b) $\chi = 10^3$ and (c) $\chi = 1.5 \times 10^{-4}$.

interface angle θ_M^{crit}. Following the turning point, the path continues along an unstable solution branch, where θ_M increases as Ca decreases. Unlike the QP approach, where the entire unstable branch is easily recovered (e.g., Figure 2.7), the 2D flow model tends to fail as the macroscopic angle increases a few degrees beyond θ_M^{crit}. Numerical error from mesh distortion appears to alter the convergence of the 2D flow solver along the unstable branch (as $\theta_M \to 180^o$).

Computations become very sensitive to mesh conditions as Ca nears Ca^{crit} and the interface becomes highly deformed. As a measure of mesh control, the DCL position x_0 is artificially fixed to be approximately centered along the substrate length. This constraint preserves element size and distribution by resisting the tendency for interface migration with increasing Ca. Iterative adjustment of the pressure drop ($\Delta P = P_L - P_R$) sets θ_{mic} to the desired substrate contact angle for each Ca. Equivalent results may be obtained by specifying a contact angle (θ_{mic}) and then solving for ΔP to place the interface at some desired position. However, the fixed-DCL method avoids convergence issues that arise near Ca^{crit} with the alternate approach.

Once Ca^{crit} is located on the solution path, the free parameter ΔP is used to continue onto the unstable branch. In this portion of the continuation method, solutions are found by searching for Ca that will satisfy the contact angle constraint (θ_{mic}) while holding ΔP fixed. Using this technique, the solution path is traced around the critical point ($Ca < Ca^{crit}$ and $\theta_M > \theta_M^{crit}$) as the magnitude of ΔP increases. A first-order continuation technique is used with ΔP to develop the unstable branch.

The computational mesh must be refined near the DCL to resolve interface deformation associated with viscous bending. Consequently, many prior FEM models have been limited to low-Ca ranges ($Ca < 0.1$) where interface deformation is not as severe [73, 118]. This issue is discussed by [127] with recommendations made for optimizing mesh and momentum conditions near the DCL. Figure 2.10 provides an example of the flow field close to the DCL for the 2D flow model. Velocity (u) and pressure (p) profiles illustrate the necessity for high mesh resolution due to the formation of steep gradients approaching the wetting line ($x \to x_0$). After conducting numerous studies, it is determined that the elements adjacent to the DCL must be significantly smaller than the slip length λ to achieve mesh independent solutions for the wetting systems in this study.

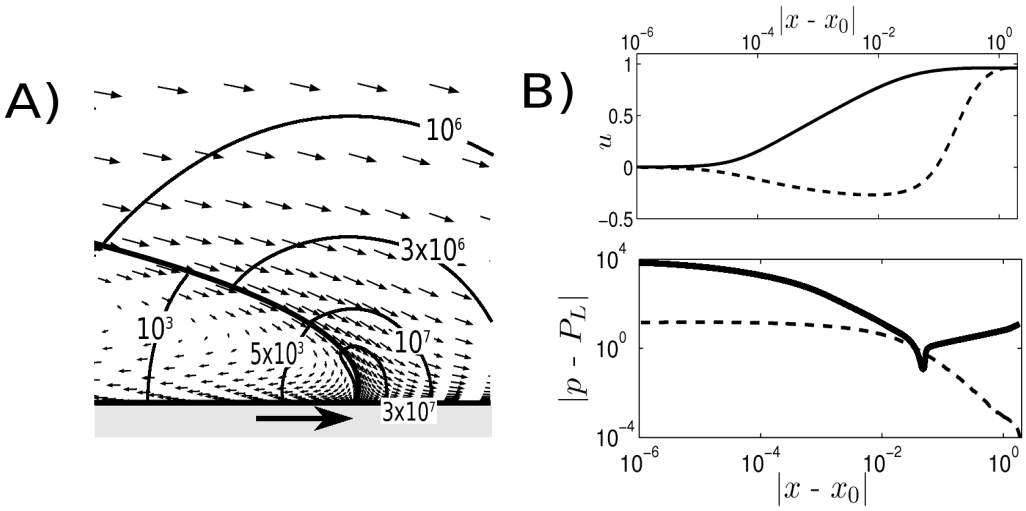

Figure 2.10: Illustration of the flow field near the DCL obtained from the 2D flow model. System parameters are consistent with those used in Figure 2.9 for air/liquid displacement. (A) Magnified view ($10^4\times$) of the velocity field near the DCL. Contour lines for $|\boldsymbol{\nabla} p|$ are shown in both the air (left phase) and liquid (right phase). (B) Plots of x-velocity and pressure (relative to P_L) along the substrate ($y \approx 0$) as a function of distance from the DCL. The solid and dashed lines represent data from the liquid and air, respectively.

Numerical error is reduced by adaptively refining the mesh near the DCL as solution paths are traced to higher Ca. The following constraint governs mesh resolution at each step in the continuation method:

$$|\theta_{ele} - \theta_{mic}| \leq 0.1^o \quad \text{and} \quad \frac{|x_{cl} - y_{cl}|}{\min(x_{cl}, y_{cl})} \leq 1. \tag{2.26}$$

Here, θ_{ele} is the angle measured from the corner node of the element adjacent to the contact line. The horizontal and vertical lengths of the element are represented by x_{cl} and y_{cl}, respectively. In essence, (2.26) ensures that the fluid interface has converged to the microscopic contact angle and reduces numerical error associated with element deformation at the contact line. Typically, $y_{cl} < \lambda \times 10^{-2}$ satisfies (2.26) at high substrate speeds near Ca^{crit}. Although systematic tests were not conducted for all of the data presented within this work, mesh studies for selected parameter sets reflect less than 1% error in Ca^{crit} when (2.26) is satisfied. Since the value of Ca^{crit} is highly sensitive to numerical errors, precision within 1% indicates that the 2D flow results presented here are practically mesh independent, as demonstrated in Appendix B.

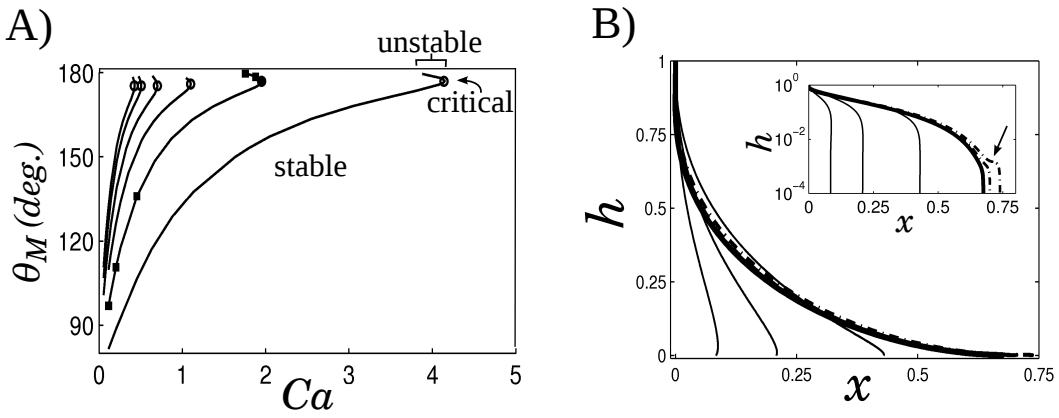

Figure 2.11: Steady-state solutions for $\chi = 1.5 \times 10^{-4}$ obtained with the 2D flow model. (a) Solution families show the change in θ_M with Ca for different values of λ. Going left to right, each curve increases in λ with values of $2 \times 10^{-6}, 10^{-5}, 10^{-4}, 10^{-3}, 10^{-2}$, and 10^{-1}, respectively. Open circles indicate the critical point for each curve. (b) Interface profiles correspond to square symbols along the $\lambda = 10^{-2}$ solution family in (a). The solid and dot-dashed lines represent stable and unstable steady-state profiles, respectively. The inset figure shows profiles on semi-log axes. An arrow denotes the location of thin air-film entrainment along the interface profile.

Figure 2.11a shows mesh-independent solution paths for the 2D flow model with $\chi = 1.5 \times 10^{-4}$ and various values of λ. Each curve exhibits an increase in the apparent contact angle with capillary number until reaching a critical point near $\theta_M = 177^o$. Unstable solution branches exist for a narrow Ca range before the solution path reaches $\theta_M = 180^o$. Near the critical point ($Ca \approx Ca^{crit}$), interface profiles (Figure 2.11b) elongate rapidly on small scales near the DCL. Unlike results from the 1D approximation used in the QP approach (see $\chi = 0.01$ in Figure 2.8), the 2D flow captures qualitative features associated with the onset of air entrainment, such as thin air-film elongation when $\theta_M^{crit} \approx 180^o$ (see Section 1.3). This comparison suggests that 2D flow crucially impacts the dynamics of wetting when advancing liquids displace gases ($\chi \ll 1$). Further discussions of 2D flow results are provided in Chapter 3 and Chapter 4.

Chapter 3

Steady 2D Wetting

3.1 Introduction

The three-phase junction at a moving wetting front, commonly called the dynamic contact line (DCL), plays a primary role during fluid displacement along a solid surface. In a 2D system, the DCL represents the terminal point of the fluid interface separating the advancing and receding fluids at the substrate boundary. Fluid stresses near this point strongly influence the apparent contact angle θ_M. As illustrated in Figure 3.1, simply changing the fluid viscsosity ratio ($\chi = \mu_{rec}/\mu_{adv}$) offers a spectrum of different wetting behavior. A number of reviews have been published on the topic of dynamic wetting [41, 50, 28, 2, 21, 40]. Despite the breadth of previous work, the fundamentals of dynamic wetting remain debated, especially in high-speed displacement processes.

The hydrodynamic model presented in Chapter 2 describes steady 2D fluid displacement along a smooth, homogeneous substrate that moves with speed U. Matching experimental findings (refer to Section 1.2), the hydrodynamic model predicts that larger

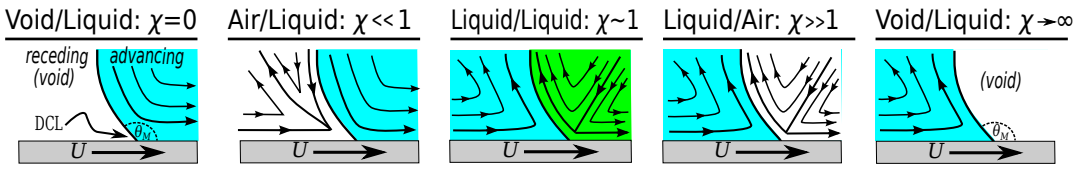

Figure 3.1: Illustration of the different two-fluid displacement systems.

dynamic angles θ_M result as substrate speed increases. Each system with finite receding-fluid viscosity (i.e., $\chi = \mu_{rec}/\mu_{adv} > 0$) reveals a maximum speed of wetting, beyond which the hydrodynamic model cannot produce steady-state solutions. Therefore, the system must transition to a transient or 3D flow state at any higher speed, matching observations of fluid entrainment during wetting failure. This chapter examines the characteristics of steady wetting near the transition to fluid entrainment, setting the stage for later analysis into the physical mechanism underlying the onset of wetting failure (see Chapter 4).

Section 3.3 compares solutions obtained from two different computational methods: the QP approach (see Section 2.2) and 2D flow model (see Section 2.3). Although computationally efficient, the QP approach is shown to only satisfactorily approximate the 2D flow solution when the receding fluid is of equal or greater viscosity than the advancing fluid. In contrast, asymptotic theory from a prior work [44] matches 2D flow solutions surprisingly well, except for very close to the critical substrate speed associated with the onset of wetting failure.

Section 3.4 takes a detailed look at solutions obtained from the 2D flow model. Unlike past computational works that were typically limited to moderate substrate speed [73, 118], the present work exposes features of steady, high-speed wetting near the onset of wetting failure. Moreover, flow fields from both the receding and advancing fluids are analyzed for a wide range of viscosity ratio χ. Results clearly demonstrate the importance of the receding flow, even when this fluid is a low-viscosity gas. In contrast to the common neglect of air dynamics in wetting models (i.e., "void/liquid" models), the present work shows that viscous effects from the air flow crucially impact high-speed wetting behavior near the limit of air entrainment.

3.2 Methods

Chapter 2 presents a hydrodynamic model for fluid displacement along a moving substrate. The Navier-Stokes equations and associated boundary conditions (see Section 2.1) generate a highly nonlinear free-boundary problem. The model is evaluated with three distinct approaches: (i) the low-speed asymptotic theory from [44], (ii) a one-dimensional (1D) lubrication approach and (iii) a two-dimensional (2D) flow model

solved with the Galerkin finite element method (FEM). These approaches are briefly described in Sections 3.2.1 - 3.2.3.

3.2.1 Asymptotic theory

Asymptotic methods have previously been applied to the free-boundary problem associated with moving contact lines [131, 44, 55]. For example, Cox developed a theory describing the behavior of the "apparent" contact angle, θ_{ap}, during two-phase displacement [44]:

$$\left.\begin{aligned} &g(\theta_{mic};\chi) - g(\theta_{ap};\chi) = Ca\log(\lambda_{Cox}),\\ &g(\theta;\chi) = \int_0^{\theta} \frac{\chi(x^2-\sin^2 x)[(\pi-x)+\sin x\cos x] + [(\pi-x)^2-\sin^2 x](x-\sin x\cos x)}{2\sin x[\chi^2(x^2-\sin^2 x) + 2\chi\{x(\pi-x)+\sin^2 x\} + \{(\pi-x)^2-\sin^2 x\}]}\,\mathrm{d}x. \end{aligned}\right\} \tag{3.1}$$

Equation (3.1) is derived for a system of arbitrary geometry and general slip law characterized by lengths l_M and l_{mic}, respectively. Therefore, the length-scale ratio $\lambda_{Cox} = l_{mic}/l_M$ is related to the dimensionless slip length from the Navier slip law in (2.9), but does not necessarily equal λ. Similarly, θ_{ap} generally is not identical to the maximum interface angle, θ_M [132].

The integral function $g(\theta;\chi)$ generally lacks an analytical solution, but simplifies considerably in the limit of vanishing χ [45, 53]:

$$g_0(\theta) = \int_0^{\theta} \frac{x - \cos x\sin x}{2\sin x}\,\mathrm{d}x \approx \frac{\theta^3}{9}, \tag{3.2}$$

where the right-hand side of (3.2) reasonably approximates $g_0(\theta)$ when $\theta < 135^o$ [45]. Even when solved numerically, (3.1) and (3.2) should be limited to relatively low-speed dynamic wetting ($Ca \ll 1$, $Ca|\log\lambda_{Cox}| \sim 1$, and $Ca|\partial\theta/\partial x| \ll 1$) because the theory neglects inertial effects and only accounts for leading-order Ca contributions [44]. Although (3.1) has been compared to contact-angle measurements from many experimental studies, the accuracy and applicability of the Cox theory remains debated [133, 134, 135, 25].

To avoid ambiguity inherent to contact-angle measurements, asymptotic theory has also been compared against experimentally measured interface profiles near moving contact lines. While remaining near the contact line but outside of the microscopic region

(such that $l_M \gg r \gg l_{mic}$), the interface angle can be described free of microscopic parameters [62, 64, 136]:

$$\theta(r) = g_0^{-1}(g_0(\theta_{ap}) + Ca \log r) + f(r; \theta_{ap}) - \theta_{ap}. \tag{3.3}$$

The apparent angle θ_{ap} serves as the lone fitting parameter for (3.3). Extrapolating from the axisymmetric formula in Chen *et al.* (1995) [64], the geometry-dependent function $f(r, \theta_{ap})$ is derived for interfaces in contact with planar substrates:

$$f(r, \theta_{ap}) = \theta_{ap} + 2r \sin\left(\frac{90^o - \theta_{ap}}{2}\right) - \frac{r^2}{2}\sin(90^o - \theta_{ap}). \tag{3.4}$$

Interface profiles predicted from (3.3) have compared favorably with experimental data for $Ca \leq 0.1$ and 20 μm $< r <$ 400 μm . Numerous assumptions underlying the derivation of (3.3) could lead to the "breakdown" of this hydrodynamic theory at high speeds ($Ca > 0.1$) [64]. Alternative theories are needed to improve upon the limitations of (3.1) and (3.3).

3.2.2 QP approach

In principle, lubrication theory is restricted to long, slender fluid domains (e.g., $\theta(r) \rightarrow 180^o$) with slowly varying boundaries ($|\partial\theta/\partial x| \ll 1|$) [67]. However, lubrication-theory-based models sometimes work well even outside of this regime [120]. For instance, a quasi-parallel (QP) flow model was shown to compare favorably to full 2D models for liquid/liquid displacement over a wide range of contact angles ($\theta_{mic} \in [30^o, 150^o]$) [98]. Simply stated, the QP approach uses lubrication theory to reduce (2.1) - (2.9) to the following expression [98, 99]:

$$\frac{\mathrm{d}^2\theta}{\mathrm{d}s^2} = Ca\delta(\chi)(\frac{\mathrm{d}p}{\mathrm{d}x}|_{adv} - \frac{\mathrm{d}p}{\mathrm{d}x}|_{rec}) = F(h(s); Ca, \lambda, \chi), \tag{3.5}$$

where $F(h(s); Ca, \lambda, \chi)$ describes local normal forces (pressure gradients) exerted by the fluid flow. Unlike most lubrication theories, (3.5) maintains the full curvature term (i.e., $\kappa = d\theta/ds$) and equates curvature gradients along s to pressure gradients in the x-direction [98]. Interface profiles result from numerical integration of (3.5) and use of the following geometric relationships:

$$\frac{dh}{ds} = -\sin\theta; \quad \frac{dx}{ds} = -\cos\theta; \quad r = \sqrt{x^2 + h^2}. \tag{3.6}$$

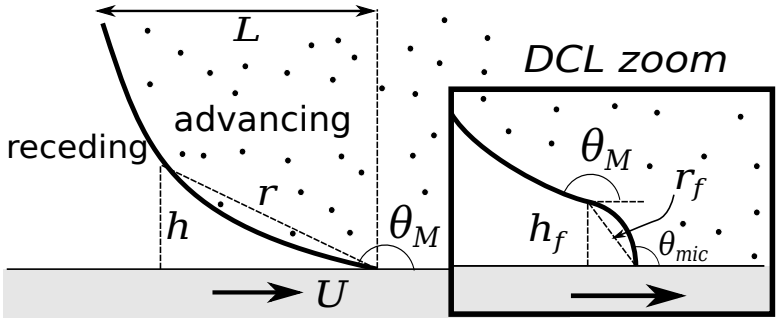

Figure 3.2: The macroscopic appearance of the air/liquid interface with an apparent contact angle θ_M. Magnification near the DCL reveals an inflection point (IP) in the inner interface profile. The IP position is measured from vertical (h_f) and radial (r_f) distances from the DCL.

Here, the origin for the coordinate system is located at the substrate such that r measures the radial distance of a point along the interface from the DCL (see Figure 3.2). A more complete description of the QP approach is provided in Section 3.2.2.

3.2.3 2D flow model

We also apply the Galerkin finite element method [128, 130] to evaluate the full 2D set of equations outlined in Section 2.1. Since the interface position is coupled to the flow field, coordinates for the physical domain (x and y) are retained as unknowns that are solved simultaneously with the flow variables ($\boldsymbol{v}$ and p). Using elliptic mesh generation [125], the physical system is mapped to a fictitious, computational domain where the dynamic boundary conditions are implemented. Details of our method and meshing procedure are discussed in Section 2.3.

3.3 Comparison of Numerical Approaches

3.3.1 Solution Paths

Qualitatively, each numerical approach used to solve the hydrodynamic model (see Chapter 2) predicts similar behavior for the maximum interface angle θ_M, shown schematically in Figure 3.2. At low substrate speed ($Ca \approx 0$), θ_M approximately matches the microscopic angle θ_{mic}. The capillary number Ca increases with higher speeds, causing larger values of θ_M due to greater viscous bending of the interface . Figure 3.3 reflects

these trends in solution paths obtained with the QP approach (Section 3.2.2 and the 2D flow model (Section 2.3). To demonstrate the impact of χ, Figures 3.3a, 3.3b and 3.3c compare solutions for cases of liquid/air ($\chi \gg 1$), liquid/liquid ($\chi \sim 1$), and air/liquid displacement ($\chi \ll 1$), respectively. Solution paths are also compared against asymptotic theory developed in a prior work [44]. The asymptotic theory predicts apparent contact angles θ_{ap} of the form

$$g(\theta_{ap}, \chi) = g(\theta_{mic}, \chi) + Ca \ln(\lambda_{Cox}), \tag{3.7}$$

where $g(\theta, \chi)$ is the integral function defined in (3.1). (Further discussion of the asymptotic theory is provided in Section 1.2).

Collectively, the plots of Figure 3.3 demonstrate that the asymptotic theory (3.1) qualitatively matches stable-solution branches from the 2D flow model through the entire χ range, assuming that the apparent angle equals the maximum interface angle (i.e., $\theta_{ap} = \theta_M$). Similar to a recent comparison of asymptotic theory and numerical solutions for droplet spreading [132], we find the best quantitative agreement between the 2D flow model and (3.1) when $\lambda_{Cox} \sim 10\lambda$.

In contrast, the QP approach only approximates the 2D flow model well when $\chi \geq 1$. As illustrated by Figure 3.3b, QP solutions severely overestimate the Ca range available for steady wetting when the advancing liquid is more viscous than the receding fluid (e.g., $\chi = 0.1$), becoming increasingly inaccurate as $\chi \to 0$ (for this reason the QP approach is omitted from Figure 3.3c). Reasons for the failure of the QP approach are discussed later in this section.

3.3.2 Turning Points and Unstable Solution Branches

Figure 3.3a illustrates that the asymptotic theory diverges from QP and 2D flow solutions near Ca^{crit}, where turning points characterize the onset of wetting failure. Asymptotic theory fails to predict the turning points shown for the other two solution methods due to the fact that (3.1) is a single-valued function of Ca for $\theta_M \in [0^o, 180^o]$. Monotonic solution paths are only recovered for the "void/liquid" case plotted in Figure 3.3c, where the receding viscosity vanishes ($\chi = 0$), and both the 2D flow solution and asymptotic theory approach the asymptote $\theta_M \to 180^o$ as $Ca \to \infty$. Even the low-viscosity flow of receding air produces a turning point in the 2D flow solution at some critical speed

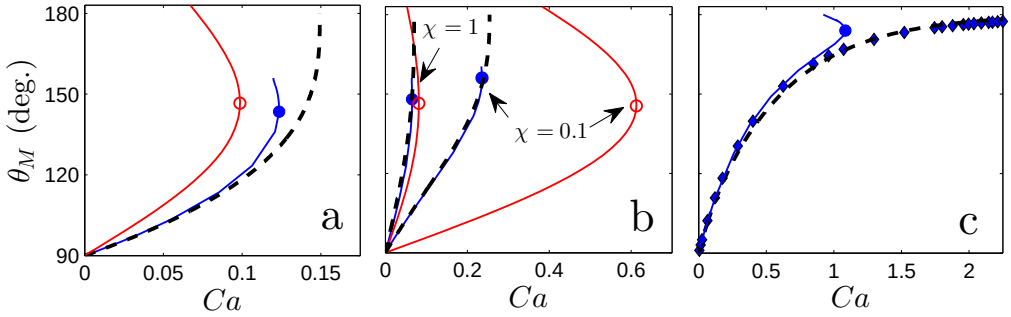

Figure 3.3: Solution families obtained with the 2D flow model (curves with closed symbols), the QP approach (curves with open symbols), and asymptotic theory (dashed lines). The macroscopic contact angle θ_M is plotted as a function of Ca for various χ values: (a) $\chi = 10^3$ for all curves; (b) χ values labeled; (c) $\chi = 10^{-3}$ for the 2D flow model (solid line) and $\chi = 0$ for the 2D flow model (diamonds) and asymptotic theory (dashed line). Symbols mark the turning point for solution curves where $\chi > 0$. Dashed lines are produced from (3.1) assuming $\lambda_{Cox} = 0.07$ and $\theta_M = \theta_{ap}$. Additional parameter values: $\lambda = 10^{-2}$, $\theta_{mic} = 90^o$, $Bo = 0$, $Re = 0$ and $H/D = 0$.

(e.g., $\chi = 10^{-3}$ curve in Figure 3.3c). This means that in the absence of a receding fluid an advancing liquid may steadily wet a substrate at infinite speed, whereas finite Ca^{crit} is predicted when $\chi > 0$.

Figure 3.4 shows interface behavior as the solution path moves around the turning point at Ca^{crit} for liquid/air (Figure 3.4a-b) and air/liquid (Figure 3.4c-e) displacement. In both systems, interface elongation accompanies increasing θ_M values along the unstable branch as solutions move toward a state of film entrainment. For the case of liquid/air displacement, the entire interface stretches horizontally by a factor of L (see Figure 3.2) as a thick liquid film grows along the substrate (see inset of Figure 3.4b). In comparison, air/liquid profiles shown in Figure 3.4d are characterized by increasing deformation near the contact line rather than uniform stretching of the interface. Plotting the air/liquid profiles on semi-log axes in Figure 3.4e reveals small-scale interface elongation consistent with thin-film air entrainment. Although the QP approach approximates the 2D flow solution in the regime of liquid-film withdrawal, QP solutions fail to capture the interface behavior preceding air entrainment. (Note the discrepancy in Ca and θ_M values associated with the air/liquid turning points shown in Figure 3.4c.) Interface profiles plotted in Figure 3.4d and 3.4e illustrate that the QP approach misses

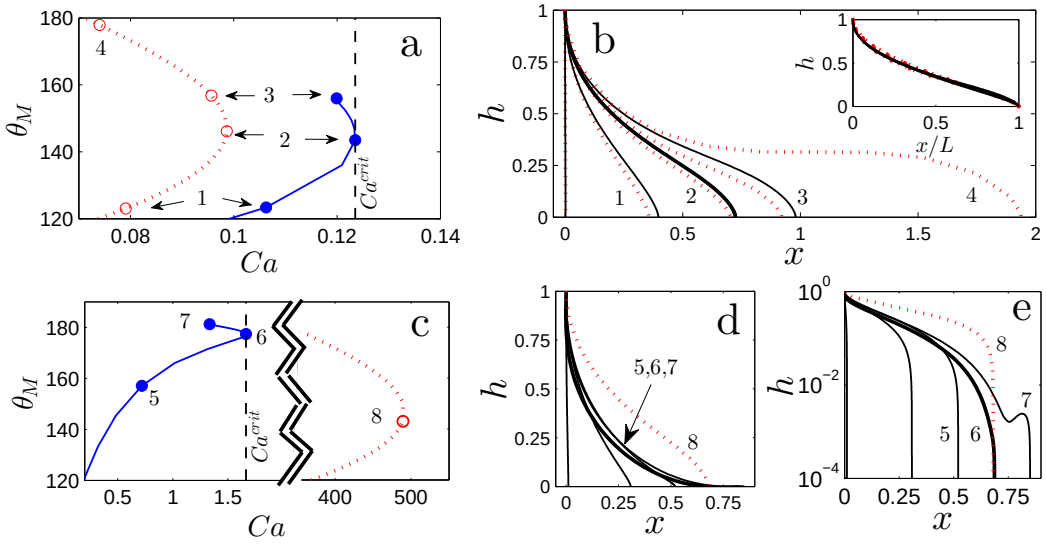

Figure 3.4: Interface profiles and corresponding solution paths near Ca^{crit} for (a-b) liquid/air displacement with $\chi = 10^3$ and (c-e) air/liquid displacement with $\chi = 10^{-4}$. Panels (a) and (c) plot θ_M as a function of Ca with Ca^{crit} marked by a dashed line. Interface profiles plotted in panels (b), (d), and (e) are numbered to denote the corresponding point along each solution path. Solid and dotted lines represent solutions from the 2D flow model and the QP approach, respectively. (b) *Inset*: Liquid/air interface profiles (1 - 3) plotted with the x coordinate scaled by the interface length L. Additional parameter values: $\lambda = 10^{-2}$, $\theta_{mic} = 90^o$, $Bo = 0$, $Re = 0$ and $H/D = 0$

the "thinning" of the receding-fluid domain that occurs at high Ca during air/liquid displacement (discussed further below).

One drawback of the 2D flow model is that elongation of the interface leads to global mesh distortion, which causes the method to diverge when the interface length is approximately equal to the gap ($L \approx 1$). For this reason, the 2D flow model has fewer solutions along the unstable branch relative to the QP approach. Even with the limited data, there is evidence that the receding fluid forms a capillary ridge ($\theta_M > 180^o$) as the interface continues to elongate (see Figure 3.4e).

3.3.3 The Interface Inflection Point (IP)

Figure 3.5 illustrates the change of interfacial length scales with Ca for various viscosity ratios. For instance, Figure 3.5a shows that the interface inflection point (IP) moves consistently closer to the contact line (decreasing r_f and h_f; see Figure 3.2) with

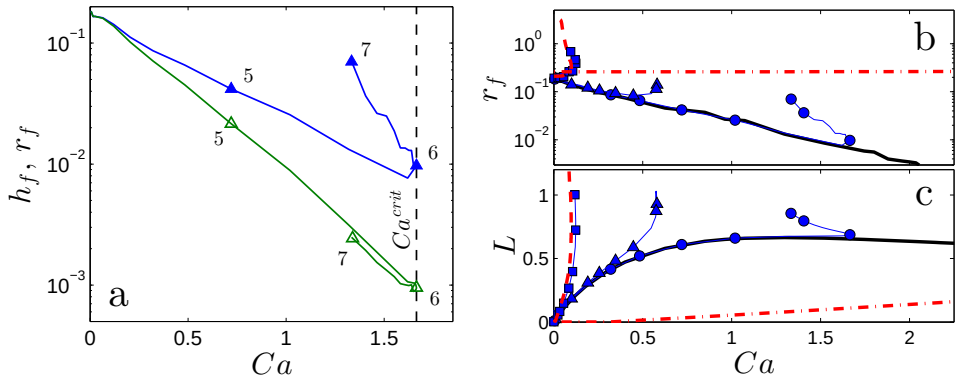

Figure 3.5: Interfacial length scales measured as a function of Ca. (a) The inflection-point positions r_f (closed symbols) and h_f (open symbols) are plotted corresponding to the air/liquid interfaces shown in Figure 3.4 (see numbered curves in Figure 3.4e). (b) Inflection point position r_f and (c) interface length L plotted against Ca for various χ. Solid lines denote 2D flow solutions for $\chi = 0$ (bold curve), 10^{-4} (circles), 10^{-2} (triangles), and $\chi \to \infty$ (squares). Broken lines represent QP solutions for $\chi \to \infty$ (dash) and $\chi = 10^{-2}$ (dot-dash). Additional parameter values: $\theta_{mic} = 90^o$, $Bo = 0$, $Re = 0$, $H/D = 0$, and $\lambda = 0.01$.

increasing Ca during air/liquid displacement. In other words, faster substrate speeds increase interface deformation, thinning the air domain near the DCL. Only at speeds near Ca^{crit} does the air layer begin to elongate, resulting in a significant increase in r_f. Figure 3.5b illustrates this IP behavior for a wide range of χ. Due to the lack of Ca^{crit} for the void/liquid ($\chi = 0$) case, r_f seems to decrease indefinitely with Ca, even after the interface length (plotted in Figure 3.5c) becomes nearly constant at faster speeds. In fact, the 2D flow solutions for all air/liquid systems fall along the same curve in Figure 3.5b until reaching their respective turning points at Ca^{crit}, where r_f abruptly increases with the elongation of a thin air film. This overlap between the air/liquid and void/liquid curves suggests that the IP location is completely controlled by the advancing liquid until $Ca \approx Ca^{crit}$.

Closer inspection of predicted interface profiles reveals that the QP approach and asymptotic theory fail to match 2D flow solutions for air/liquid systems. For example, Figure 3.5b demonstrates that the QP solution inaccurately describes the IP location r_f as a function of Ca when $\chi = 0.01$. Similarly, interface profiles generated from asymptotic theory fail to accurately track IP behavior predicted from the 2D flow model,

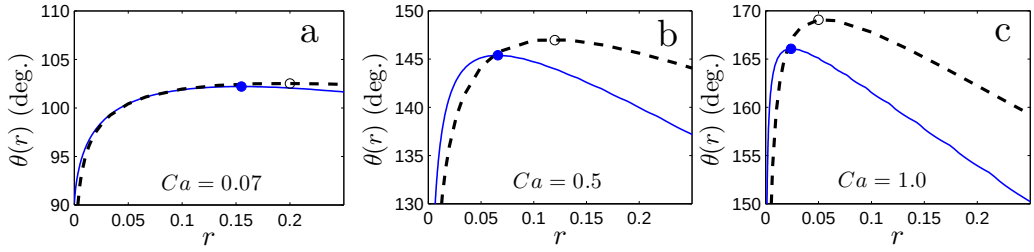

Figure 3.6: Interface angle profiles obtained near the contact line for air/liquid displacement. Solid curves represent solutions from the 2D flow model for (a) $Ca = 0.07$, (b) $Ca = 0.5$, and (c) $Ca = 1.0$. Dashed curves are obtained by fitting (3.3) to the 2D flow solution at each value of Ca. Symbols mark the IP position for each case. Additional parameter values: $\chi = 10^{-4}$, $\theta_{mic} = 90^o$, $Bo = 0$, $Re = 0$, $H/D = 0$, and $\lambda = 10^{-2}$.

as demonstrated below.

3.3.4 On the Breakdown of Asymptotic Theory

In Figure 3.6, the asymptotic theory expressed by (3.3) is fitted to solutions from the 2D flow model in the spirit of Chen *et al.* (1995) [64]. As Ca increases, curves from the 2D flow model reflect the migration of the inflection point toward the contact line (refer to Figure 3.5a) to a degree than cannot be duplicated with the asymptotic theory. The overall fit between profiles becomes poor for $Ca > 0.1$. Qualitatively, this discrepancy between solution curves in Figure 3.6b and 3.6c is strikingly similar to that observed when comparing asymptotic theory to experimentally measured interface profiles [64]. Therefore, the IP behavior may be the ingredient missing from (3.3) that has been attributed to the "breakdown" of asymptotic hydrodynamic analysis at high Ca.

3.3.5 Failure of the QP Approach

To obtain a qualitative appreciation for the failure of the QP approach, flow fields near the fluid interface are plotted in Figure 3.7. Here, comparison is made between QP and 2D flow solutions at the turning point (Ca^{crit}) predicted for air/liquid displacement with $\chi = 1.5 \times 10^{-4}$ (corresponding to liquid viscosity of approximately 120 cP). In the QP result, the air phase controls the interface velocity as it is pumped away from the DCL by strong pressure gradients in order to conserve mass and preserve the zero-flux

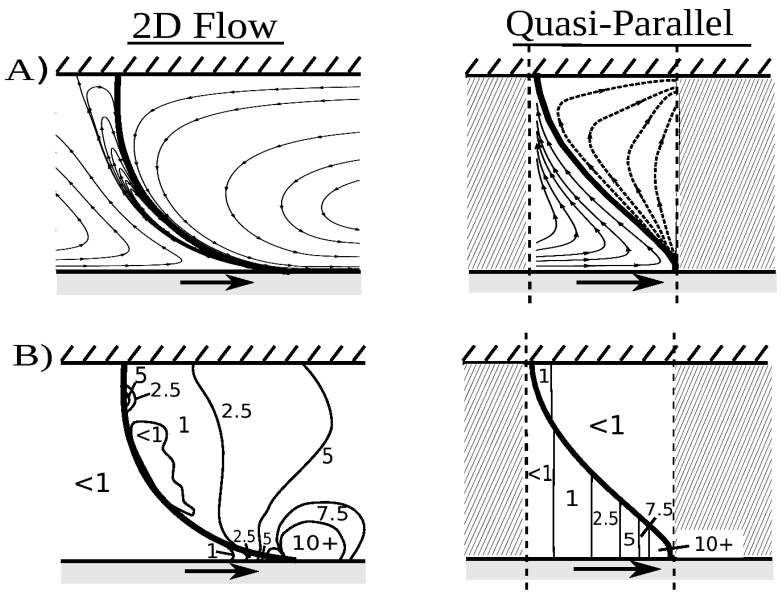

Figure 3.7: Comparison of (A) streamlines and (B) $|\nabla p|$ contours obtained from the QP and 2D flow models for an air/liquid wetting system with $\chi = 1.5 \times 10^{-4}$ and $\lambda = 10^{-2}$. Flow fields are extracted at Ca^{crit} for each model. The fluid interface is represented by a bold line which separates the advancing glycerol (right phase) from the receding air (left phase). The flow domain of the QP approach appears truncated as it is only defined within the bounds of the fluid interface.

condition at the fluid interface. In contrast, the 2D flow model depicts a dominant liquid flow field which directs interface velocity toward the DCL. Consequently, the air phase adopts a recirculation flow near the interface and develops weak pressure gradients relative to the liquid phase. In both models, low pressure gradients found within the subservient phase contribute negligibly to the macroscopic interface shape. Thus, air flow provides the primary driving force for interface deformation with the QP approach, whereas the 2D flow result shows liquid-side pressure gradients to dominate a majority of the interface shape with the impact of air flow felt only very close to the DCL.

The two models clearly conflict over the flow features and stress fields relevant to air/liquid displacement. The flow field obtained from 2D flow model agrees qualitatively with flow visualization of past dynamic wetting studies [66, 137]. Results from the QP approach oppose basic intuition that substrate drag should generate liquid flow which will contribute stresses that deform the fluid interface. Furthermore, the highly two-dimensional flow field shown in Figure 3.7 invalidates the lubrication assumption

at the foundation of the QP approach. Consequently, the QP approach severely overestimates Ca associated with the dynamic wetting behavior of air-liquid systems because it neglects liquid stresses that should develop within the advancing fluid. The QP approach is a good approximation for the 2D flow model only when viscous stress within the receding fluid dominates the interface behavior (i.e., cases where $\chi \geq 1$ in Figures 3.3 - 3.5).

3.4 Analysis of 2D Flow Solutions

In 2D flow model, interface profiles are determined by fluid stresses that contribute to interface bending through the normal stress balance (2.6). Figure 3.8 plots characteristic flow fields that shape the liquid/air, liquid/liquid, and air/liquid interfaces near the onset of wetting failure (refer to solution paths in Figure 3.3). In each case, the dominant (typically more viscous) fluid exhibits a "rolling flow" pattern with parallel streamlines along the interface and substrate, whereas the secondary (typically less viscous) fluid has a splitting streamline near the contact line that causes flow recirculation near the interface. In the air/liquid system, the rolling motion of the liquid is formed by "suction" (rapidly decreasing pressure) near the contact line that drives liquid from the outer interface toward the moving substrate. Due to the low viscosity of the receding phase, the flow field of the air generates negligible stress relative to the liquid. Thus, strong velocity gradients can form in the air, and these accompany the thin recirculation region near the interface without much consequence for the interface shape. Air pressures only become significant when $Ca \approx Ca^{crit}$ because strong adverse pressure gradients are needed to pump air out of the slender wedge formed by the interface ($\theta_M \sim 180^o$) near the contact line (see magnified image in Figure 3.8). As discussed in Chapter 4, the magnitude of these pressure gradients exceeds that of the local capillary forces, leading to the onset of wetting failure at Ca^{crit}.

In contrast, the liquid/liquid and liquid/air systems ($\chi \geq 1$) in Figure 3.8 illustrate flow fields dominated by the receding liquid. Here the characteristic rolling-flow pattern appears in the receding phase and the advancing phase adopts the splitting streamline near the contact line. Since the splitting streamline drives fluid back toward the substrate along a broad recirculation path (i.e., low velocity gradients), the advancing flow

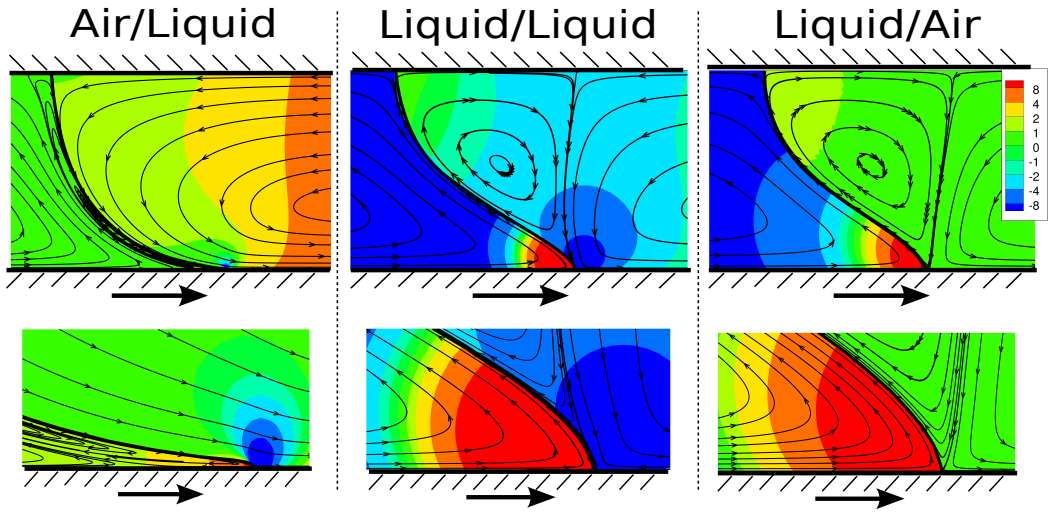

Figure 3.8: Comparison of the flow fields obtained at Ca^{crit} with the 2D flow model. Streamlines and pressure contours are shown for air/liquid ($\chi = 10^{-3}$), liquid/liquid ($\chi = 1$), and liquid/air ($\chi = 10^{3}$) displacement. The bottom images show approximately 10× magnification of the flow field near the contact line. Values of the system parameters: $\lambda = 0.01$, $\theta_{mic} = 90^{o}$, $Bo = 0$, $Re = 0$ and $H/D = 0$.

contributes weak interfacial stresses (even when $\chi = 1$) relative to the receding flow. Consequently, viscous bending arises primarily from pressure gradients related to the pumping mechanism in the receding phase in these systems.

Since this thesis aims to characterize wetting failure leading to air entrainment, the following sections take a close look at flow fields associated with fluid diplacement when $\chi \ll 1$. Specificaly, the cases of void/liquid ($\chi = 0$) and air/liquid ($0 < \chi \ll 1$) displacement are examined in detail. As substrate speed increases, interface behavior near the DCL varies between these two systems. For simplicity, creeping flow ($Re = 0$) is considered in a planer geometry ($H/D = 0$) with only the value of the viscosity ratio (χ) changing between Sections 3.5 - 3.6. Other parameters remain fixed ($Bo = 0$, $\theta_{mic} = 90^{0}$, and $\lambda = 0.01$) unless otherwise noted.

3.5 2D Flow: The Void/Liquid System

The void/liquid system always achieves steady 2D wetting because the void does not provide any viscous resistance toward the advancing liquid ($\chi = 0$). Interface characteristics of each steady state are determined by the balance of forces within the liquid (i.e., an equilibrium between capillary and viscous stresses) that satisfy the microscopic wetting conditions in (2.9) for a given set of material parameters. As illustrated by Figure 3.9, the interface shape and neighboring flow field depend strongly on the value of Ca for the system. Due to the normal stress balance (2.6), the interface becomes more curved as viscous force increases relative to surface tension (increasing Ca). Interface bending lengthens the interface, increasing the distance between the contact lines (i.e, SCL and DCL). Figure 3.9 demonstrates that large regions of slow moving fluid reside near the SCL when the DCL moves downstream due to interface bending. This in turn affects the stress field along the length of the interface, leading to complicated interface behavior as Ca increases.

3.5.1 Characteristics of the Outer Interface

Figure 3.10 idealizes the characteristic regions of the void/liquid interface: (Figure 3.10a) the outer interface region of constant curvature and apparent contact angle θ_M; (Figure 3.10b) the IP region that connects the outer and inner profiles at $h = h_f$; (Figure 3.10c) the inner region containing fluid slip and the microscopic contact angle θ_{mic}. At low speeds, the interface deforms macroscopically when viscous effects intensify via larger Ca values. Pressure gradients remain weak near the outer interface, allowing the interface to bend evenly above the IP. Using simple geometric arguments (refer to Figure 3.10a), the outer interface curvature κ_M and length L are related to the apparent contact angle θ_M as follows:

$$\kappa_M \approx \cos\theta_M; \quad L \approx \frac{1-\sin\theta_M}{\cos\theta_M}. \tag{3.8}$$

Here, the interface is assumed to have constant curvature κ_M between SCL and IP (interface curvature becomes convex at the IP, as illustrated in Figure 3.10b). In actuality, curvature is not completely uniform along the outer interface, so κ_M may be approximated by the mean curvature $\left(\int_{h_f}^{1} \kappa dh\right)/(1-h_f)$, or the curvature at the interface midpoint ($h = 0.5$).

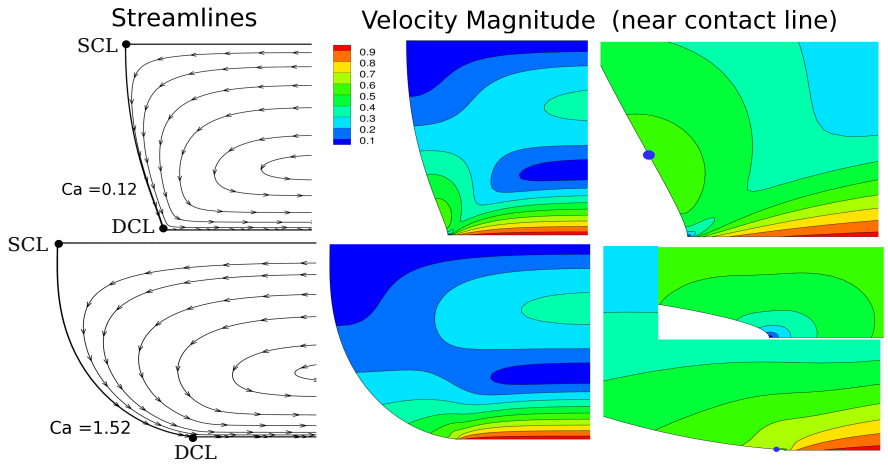

Figure 3.9: Flow fields obtained for the void/liquid system for $Ca = 0.12$ (top) and $Ca = 1.25$ (bottom). Streamlines (first column) and velocity-magnitude contours (second column) are plotted for both cases. Ten-fold magnification is used (third column) to show the strong velocity gradients near the contact line. Further magnification ($\approx 100\times$) is used in the inset for $Ca = 1.25$ (bottom right panel). Blue circles mark the inflection point for each interface. All values for velocity contours correspond to the legend shown in the center panel.

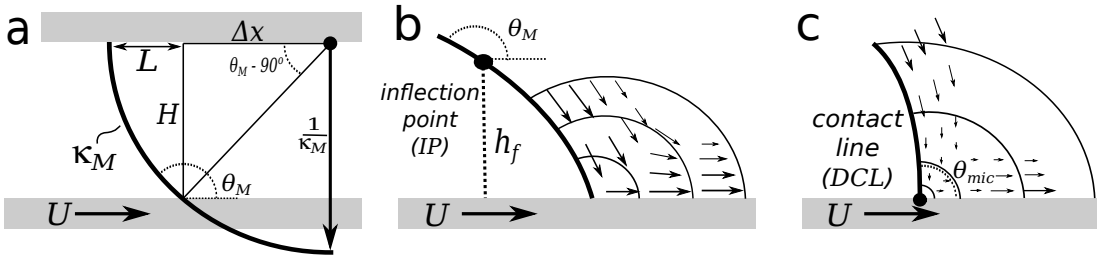

Figure 3.10: Idealization of the different regions of void/liquid interface dynamics. (a) The outer interface shape with nearly constant curvature, κ_M. The interface appears as an arc (bold line) with radius $1/\kappa_M$ that intersects the substrate at an angle θ_M. The interface length L is related to θ_M by (3.8). (b) Region (i) of the inner interface where suction ($p \sim 1/r$ as illustrated by contour lines) pulls liquid toward the substrate similar to classical flow in a corner. (c) Region (ii) of the inner interface where pressure gradients weaken ($p \sim \log r$) due to low liquid velocity from fluid slip very near the contact line. (Note: $\theta_{mic} = 90^o$ for all systems in this report)

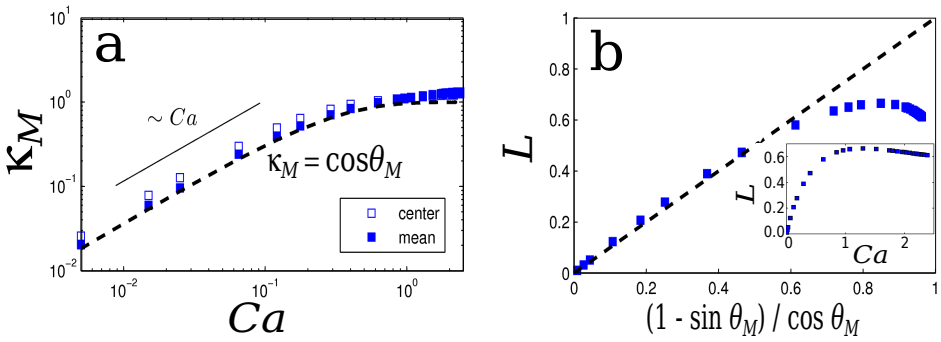

Figure 3.11: Characteristics of the outer interface profile for the void/liquid system. (a) The mean curvature ($\int \kappa dx/L$) and the point value at the center of the interface ($h = 0.5$) are plotted against Ca and compared with (3.8), where θ_M is found from the data in Figure 3.3. (b) The interface length L is plotted against the function predicted from geometric arguments assuming uniform interface curvature. Symbols represent values obtained from FEM solutions and the dashed line is the prediction from (3.8). *Inset*: The data from (b) for L replotted as a function of Ca.

Figure 3.11 compares the geometric approximations in (3.8) to results from the void/liquid system. At low speeds, the outer interface curvature increases proportionally with Ca, causing θ_M to increase according to (3.8), as shown in Figure 3.11a. Liquid stresses are insensitive to Ca in the low-speed regime and, therefore, the outer interface must bend to match capillary pressure with the increasing viscous stress (i.e., $\kappa \sim Ca$ because $[\boldsymbol{n} \cdot \boldsymbol{T} \cdot \boldsymbol{n}]_{adv}$ remains constant in (2.6)). Since θ_M asymptotically approaches 180^o at high substrate speed, (3.8) predicts the asymptote $\kappa_M \to 1$ as $Ca \to \infty$, which is consistent with numerical results.

Although the interface steadily elongates at low speeds, L remains nearly constant as $\theta_M \to 180^o$ (for $\theta_M > 150^o$ in Figure 3.11b and $Ca \sim 1$ in the inset plot). This shift in interface behavior is important to note because many experimental studies estimate θ_M using some measurement of L and a geometric argument similar to (3.8) [2]. Figure 3.11b shows that these types of indirect measurements may underestimate θ_M as Ca increases because L values lie below the curved generated by (3.8) for $\theta_M > 150^o$.

3.5.2 Corner Flow near the DCL

Fluid stresses near the DCL are crucial to high-speed wetting behavior. Figures 3.10b and 3.10c illustrate two flow regimes that are present near the DCL ($r \leq r_f$) for all Ca:

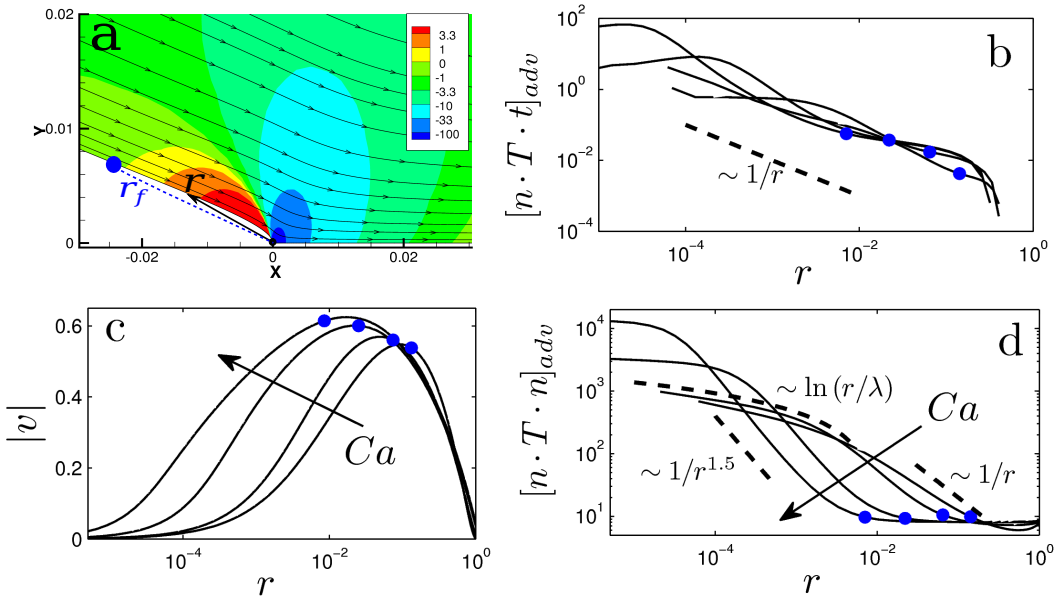

Figure 3.12: (a) Advancing liquid flow field near the DCL with $\lambda = 0.01$ and $Ca = 1.07$. (b) Magnitude of tangential stress exerted by the liquid onto the interface as a function of the radial distance from the DCL. (c) Velocity magnitude along the void/liquid interface. (d) Magnitude of normal stress exerted by the liquid onto the interface. Solutions are shown for $Ca = 0.12, 0.40, 1.07$ and 1.52 in panel (b) - (d). Blue circles correspond to values measured at the inflection point (r_f) for each profile.

(i) a region that resembles viscous flow in a corner and (ii) a near-stagnation zone caused by fluid slip. Figure 3.12 plots liquid stresses and velocities associated with these two regions. In region (i), strong suction draws liquid from the outer field to replace fluid drawn away with the moving substrate. Suction is generated from rapidly decreasing liquid pressure in the corner flow near the DCL (see note in Appendix C.1.1). The pressure divergence weakens in region (ii) due to fluid slip. In essence, fluid slip results from strong shear stress as the liquid flow changes directions at the DCL (refer to the Navier-slip condition (2.9)). Consequently, as $r \to 0$, the interfacial velocity decays to zero and the normal stress approaches a weak singularity ($p \sim \log r$) relative to the corner flow case ($p \sim r^{-1}$).

The stress field changes as Ca increases and $\theta_M \to 180^o$. As shown in Figure 3.12, normal-stress gradients become steeper in the high-speed regime because the interface

velocity near the DCL decays slowly in comparison to the low-speed case (this is also true for velocity along the substrate, as shown in Appendix C.1.2). Large interface angles direct streamlines to be nearly parallel with the substrate, weakening local liquid shear along the substrate. Consequently, fluid slip is less effective in reducing interface velocity (Figure 3.12c) and mitigating the pressure divergence that originates in the corner-flow region (note that $p \sim 1/r^{1.5}$ when $Ca > 1$ in Figure 3.12d).

3.5.3 Position of the IP along the Interface

Interface curvature becomes convex at the IP, marking the beginning of the corner-flow region. (Note that each curve in Figure 3.12d reflects the corner-flow divergence $[\boldsymbol{n} \cdot \boldsymbol{T} \cdot \boldsymbol{n}] \sim 1/r$ near the IP.) The IP position along the interface ($h = h_f$) is set by the balance of viscous stress $\left(\int \mu U/h \; dh\right)$ and capillary pressure $\left(\int \sigma/h \; dh\right)$ in this region, as approximated by the following expression:

$$\ln(h_f) \sim Ca \ln \lambda. \tag{3.9}$$

The logarithmic term on the right-hand side considers the integration of viscous stress up to the slip region ($h \sim \lambda$), where viscous effects decay. Since the interface must bend from θ_M to θ_{mic} in the distance between the IP and SCL, sharper curvature results when this distance is decreased (smaller h_f), as reflected by the left-hand side of (3.9). Ultimately, higher interface curvature increases the capillary pressure that balances against the viscous term weighted with the capillary number.

Equation (3.9) predicts exponential decay for h_f as Ca increases, which explains the importance of this effect in the high-speed regime. Physically, constant curvature in the outer domain (refer to Figure 3.11a) forces the interface to become more curved on small scales to satisfy the normal-stress balance at high Ca. Decreasing h_f allows for high *inner*-region curvature ($\kappa \sim 1/h_f$), while keeping relatively low *outer* curvature ($\kappa_M \sim 1$) as specified from (3.8).

Figure 3.13 plots the logarithm of the IP position as a function of the capillary number for various slip lengths. Each case results in a linear plot with slope proportional to $\ln \lambda$, as predicted from (3.9) (see additional plots in C.1.3). Intercepts from linear fits of the data in Figure 3.13 are approximately equal to $\log\left(|\log \lambda|^{-1}\right)$, which signifies the location of overlap between inner and outer regions in asymptotic theory for $Ca \to 0$

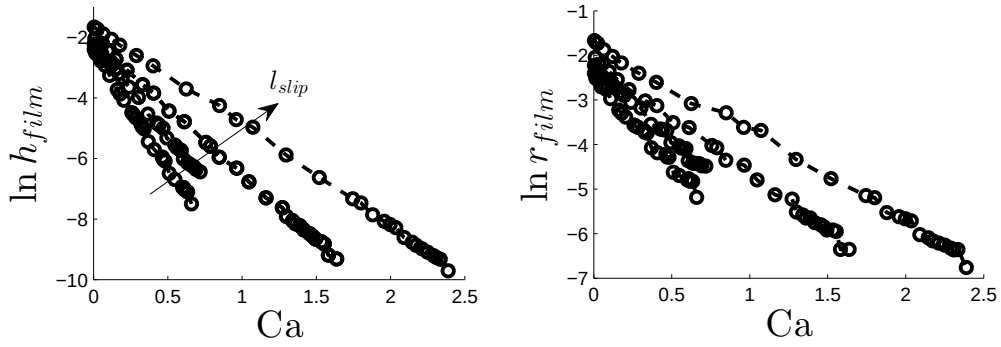

Figure 3.13: Inflection-point position for various values of λ. Curves are shown for $\lambda = 10^{-2}, 10^{-3}10^{-4}$, and 10^{-5}.

[44]. Similarly, the fitted slopes, which coincide with (3.9), can be interpreted as the matching condition for the "intermediate" region that arises when $Ca \ln \lambda \to 1$ [44]. (In the terminology of the present work, the intermediate region of [44] would be located within the inner-interface domain near the IP.)

Ultimately, the IP migrates closer to the DCL to keep capillary pressure on par with viscous stresses as Ca increase. Lacking this behavior, the interface would be unable to satisfy the normal stress balance because the outer interface does not support strong curvature gradients, but instead adheres to the geometric constraints of (3.8). Therefore, the IP behavior is key to maintaining steady 2D wetting as $Ca \to \infty$ in the void/liquid system.

3.6 2D Flow: The Air/Liquid System

Unlike the void/liquid case, steady states are limited to finite speed ($Ca \leq Ca^{crit}$) for all air/liquid systems. Clearly, the void/liquid case lacks viscous effects from the receding phase (air) that may influence interface behavior in air/liquid systems. In practice, the air/liquid viscosity ratio is very small ($\chi =\leq 0.01$), which usually limits air to a passive role in comparison to the advancing liquid flow. This statement does not always hold true close to the DCL, where air pressure is sensitive to substrate speed and *interface shape*. The latter dependence can lead to high stresses as the interface becomes more curved and the air flow is confined within a slender wedge. The remainder

of this section will discuss when these air stresses become significant, how they alter the interface shape, and what conditions cause the critical behavior (turning point) associated with the onset of wetting failure.

3.6.1 Characteristics of the Outer Flow

At low speeds, viscous effects from the air phase are negligible and the interface is determined by the balance of liquid stresses and capillary pressure, as detailed in Section 3.5 determines the interface shape (see normal stress profiles in Appendix C.2). Fluid velocity near the interface is controlled by the liquid flowing from the outer domain toward the moving substrate. Due to the low viscosity of the air, a thin velocity boundary layer forms at the inteface with an adjacent zone of slowly recirculating air. Outside of the recirculation zone, the air shows the characteristics of wedge flow where substrate drag brings fluid toward the contact line and strong pressure gradients pump the air away to conserve mass. Figure 3.14 provides plots of the streamlines and velocity contours associated with the air/liquid flow field. (Note that liquid flow fields are practically identical to the void/liquid examples shown in Figure 3.9.)

3.6.2 Air Flow within a Thin Wedge

As speeds increase, the interface becomes more curved and elongated due to viscous stress that develops in the liquid flow (refer to Section 3.5). Consequently, the air becomes confined to a long, slender wedge near the DCL. Figure 3.15 plots the air pressure measured at the IP as the air wedge thins at higher substrate speeds. As demonstrated by Figure 3.15a, air pressure gradients become nearly one-dimensional within this region and can be approximated from lubrication theory as follows (in dimensionless form):

$$\frac{dp}{dx} \sim \frac{\chi}{h^2}. \tag{3.10}$$

Figure 3.15a confirms that (3.10) describes the increase in the air pressure gradients due to local thinning (decreasing h_f) of the air flow. (Pressure-gradient profiles along the full extent of the air/liquid interface also match the scaling of (3.10), as demonstrated in Appendix C.3.) Air pressure in the outer domain changes very little in response to interface shape (i.e., the outer air pressure remains "ambient"), which means that

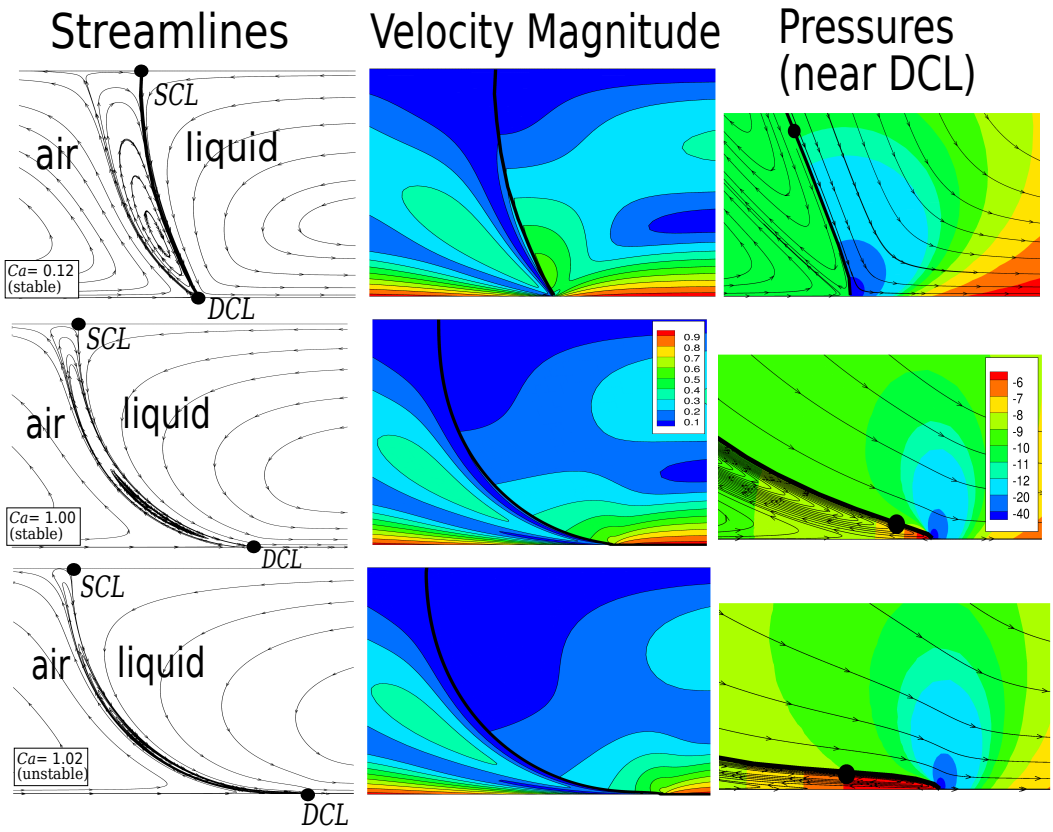

Figure 3.14: Flow fields obtained for the air/liquid system with $\chi = 0.001$ for $Ca = 0.12$ (stable), 1.00 (stable) and 1.02 (unstable). Streamlines (first column) and velocity-magnitude contours (second column) are plotted for the both cases. Ten-fold magnification (third column) is used to show the pressure contours for air and liquid near the contact line. Black circles mark the SCL and DCL in the first column, and the IP position in the third column. Velocity and pressure values correspond to the legends shown in plots for $Ca = 1.00$.

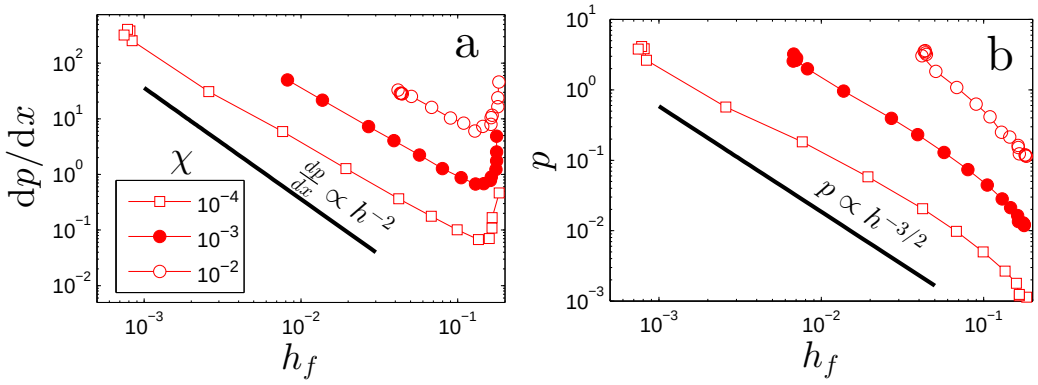

Figure 3.15: Air pressure gradient at the IP ($y = h_f$) for various values of the viscosity ratio χ (see legend). The bold line shows the expected slope corresponding to the lubrication scaling for in (3.10). Also note that each curve is shifted by an order of magnitude along the vertical coordinate, which corresponds to changes in χ in (3.10). (b) Air pressures measured at the IP for various values of χ (see legend in (a)). The bold shows an empirical fit to power-law behavior of the curves.

higher values of $\mathrm{d}p/\mathrm{d}x$ lead to large air pressures near the DCL (see right panels of Figure 3.14). In fact, Figure 3.15b demonstrates that air pressures near the IP also increase steeply as h_f decreases. Since the interface beings to bend sharply near the IP, the local dimensionless curvature is on the order of unity ($\kappa \sim \partial^2 h/\partial x^2 \sim 1$), making the interface height vary strongly along horizontal coordinate ($h \sim x^2$). Therefore, integration of pressure gradient predicted in (3.10) yields $p \sim 1/h^{3/2}$, which accurately describes the build of air pressure near the IP for various values of χ plotted in Figure 3.15b.

Interface behavior deviates from the void/liquid case only when the air pressures near the IP exceed liquid pressures along the outer interface. As discussed in Section 3.5, the outer interface has nearly uniform curvature, which yields constant liquid pressure in the outer domain that is related to θ_M by the geometric approximation in (3.8) and the normal stress balance in (2.6). Although liquid pressure decreases steeply near the DCL (dut to suction forces from the corner flow), liquid stresses at the IP nearly match those along the outer interface (note the slow variation in normal stress as $r \to 1$ in Figure 3.12d). In contrast, the large pressure gradients needed to pump air away from the DCL lead to large air pressures near the IP as substrate speed increases. Since normal stresses from the air and liquid must be equal at the IP (where the interface

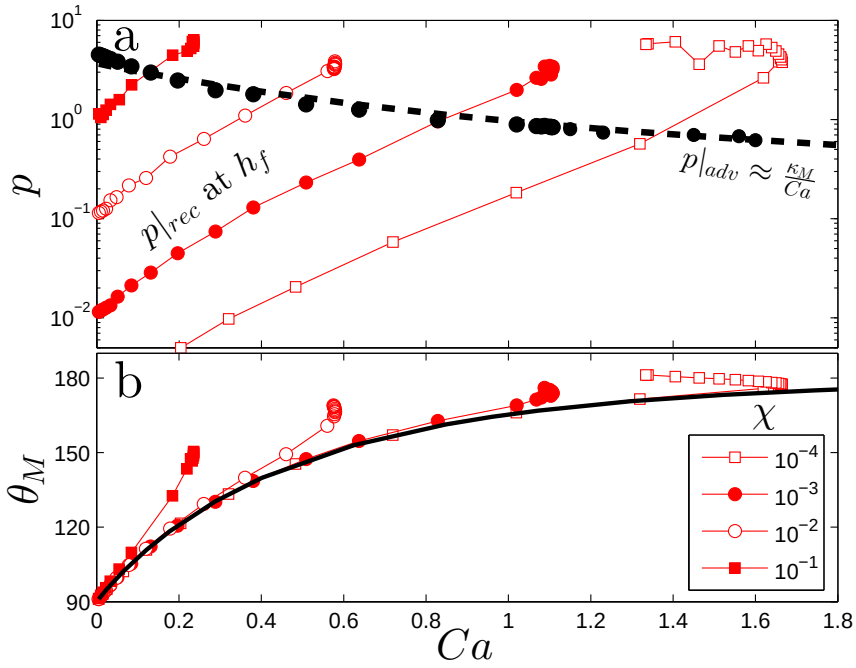

Figure 3.16: The increase of air pressure at the inflection point h_f as a function of Ca for various values of χ (see legend). Circles mark the mean normal stress within the outer domain ($r \geq r_f$) of the liquid for $\chi = 0$. The dashed line approximates the outer liquid pressure from an assumption of constant curvature, κ_0, using (3.8) and θ_M values from Figure 3.3. The bottom panel demonstrates that solution paths deviated from the $chi = 0$ case (bold curve) when air pressures (symbols) exceed the outer liquid pressure (dashed curve) in the upper panel.

has zero curvature), high air pressures at h_f necessitate the increase of liquid stresses along the outer interface. Therefore, air stresses developed in the thin wedge flow during high-speed wetting dominate local interface dynamics instead of the balance of liquid stresses and capillary pressure discussed in Section 3.5.

Figure 3.16a plots the outer liquid pressure ($p|_{adv}$ measured at $h = 0.8$) and the building air pressure ($p|_{rec}$) at h_f as Ca increases for different viscosity ratios. The capillary number where the air and liquid pressures match is identical to the point where void/liquid and air/liquid solution paths diverge, as shown in Figure 3.16b. Collectively, the panels of Figure 3.16 clearly demonstrate that growing air pressures at the IP significantly impact interface behavior as substrate speed increases.

3.6.3 Air-film Elongation

Approaching the onset of wetting failure, air stresses force the interface to elongate near the DCL. The mechanism of interface elongation during high-speed wetting can be interpreted at least two different ways.

(i) The resistance toward further constriction of the air wedge ($p \sim 1/h^{3/2}$; Figure 3.15b) is greater than the driving suction forces ($p \sim 1/r$; Figure 3.12d) from liquid flow in the corner near the DCL.

(ii) Capillary forces can no longer pump air away from the DCL at increasing substrate speed with a fixed interface length. Consequently, the interface elongates to facilitate higher pressure gradients to drive out the impinging air flow.

The first statement essentially argues that the air wedge builds enough pressure to support itself against the compressive action of the viscous liquid flow that tends to decrease h_f as Ca increases (refer to Section 3.5). Instead, excessive pressures needed to pump air away from the DCL form a thin air film that will become entrained within the liquid flow. Therefore, the unstable branch associated with air-film growth coincides with the Ca range where air pressures at h_f match or exceed the outer liquid pressure (this is approximately $Ca \in [1.3, 1.6]$ for $\chi = 10^{-4}$, as shown in Figure 3.16b).

The second argument follows from analysis of gradients in interface curvature, as plotted in Figure 3.17. Curvature gradients translate into adverse pressure gradients that counteract substrate drag in the receding flow. Therefore, integration of the curvature gradient ($\int \partial\kappa/\partial x \, dx$) along the outer interface (SCL to IP) provides a measure of the interface's ability to pump air away from the DCL. Figure 3.17 shows that although this integrated quantity depends strongly on the specific air/liquid system (χ value), the *mean* curvature gradient ($[\int \partial\kappa/\partial x \, dx]/L$) can be universally described for all air/liquid systems as a function of Ca. (Substrate wettability likely influences the curve in Figure 3.17b, although the effect of θ_{mic} is not explored here). Physically, this means that the interface can only support a finite stress gradient per interface length (on average) for a given substrate speed relative to the speed of interface relaxation σ/μ_{adv}. (Note that the mean curvature gradient can be predicted simply from results of the void/liquid system, which further supports the argument as a general characteristic

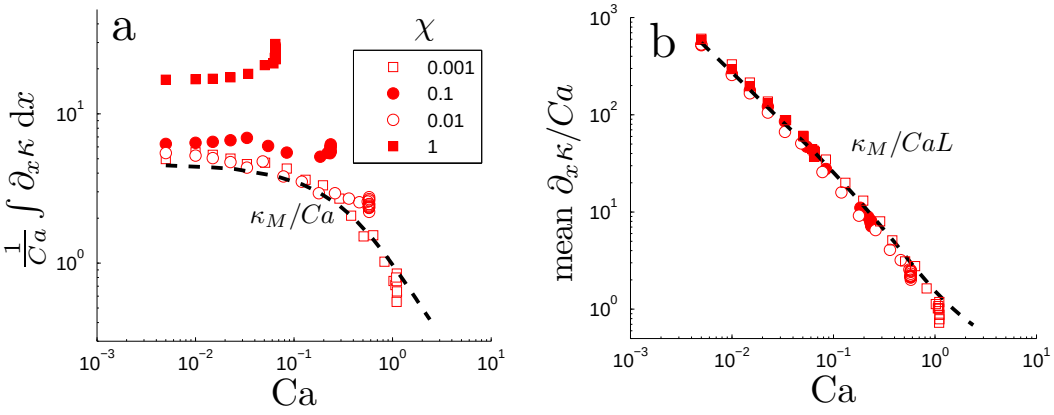

Figure 3.17: Integrated (a) and mean (b) curvature gradients provide along the air/liquid interface plotted as a function of Ca. Values are divided by Ca to provide the effective pumping action from the capillary stresses. Different viscosity ratios χ with corresponding symbols are listed within the legend. The dashed-line is plotted using the geometric argument (3.8) and the θ_M values shown in Figure 3.3 for the void/liquid case $\chi = 0$. All curves collapse to a master curve in (b) using the mean curvature gradient.

of the interface.) Thus, as substrate speed increases, requiring more air to be removed by pumping action, the interface must elongate to distribute stresses more evenly.

3.6.4 Loss of Steady 2D Wetting at Ca^{crit}

Lastly, the turning point at Ca^{crit} arises from strong air stresses acting on the interface near the IP. At this critical speed, the local pressure gradient at $h \approx h_f$ becomes too strong for the interface to remain stationary, resulting in wetting failure. In other words, the interface curvature gradient (note $\partial_x \kappa/Ca = \partial_x p$) can no longer pump air away from the DCL and simultaneously support the suction needed to draw liquid toward the moving substrate. Similar to the preceding discussion about interface elongation, Figure 3.18 shows that this critical curvature gradient is a function of Ca that can be approximated from solutions for the void/liquid system. One may anticipate this result because the same visco-capillary balance governs interface curvature, regardless of whether there is viscous flow from one (void/liquid) or two (air/liquid) fluids. As demonstrated by Figure 3.18, the pressure gradient in the air grows exponentially with

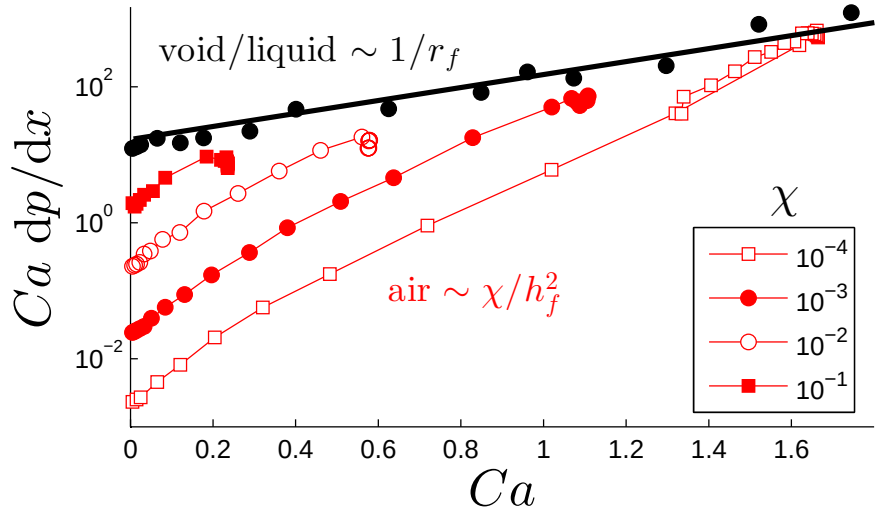

Figure 3.18: Pressure gradients from air flow and capillary forces at the IP (r_f) as a function of Ca. Air pressure gradients are shown for various values of χ (see legend). Capillary-stress gradients (filled circles) are shown from the void/liquid results. The bold line denotes $dp/dx \sim 1/r_f$, where r_f is obtained from void/liquid ($\chi = 0$) results in Figure 3.5.

Ca, while the curvature gradient set by the void/liquid force balance only scales approximately as $1/r_f$. Consequently, growing pressure gradients in the air flow overcome surface tension forces at Ca^{crit}, leading to transient behavior, such as air entrainment, at any super-critical substrate speed. This mechanism for wetting failure is explored in more depth in Chapter 4.

Chapter 4

The Onset of Wetting Failure

4.1 Introduction

The liquid-applied coatings industry commonly aims to steadily and uniformly wet a substrate moving at speed U with a particular liquid. All such dynamic-wetting systems involve a "receding/advancing" fluid pair, where the advancing phase with viscosity μ_{adv} displaces the receding phase with viscosity μ_{rec}. At some critical speed U^{crit}, dynamic wetting fails and the receding fluid becomes entrained within the advancing phase [27]. As discussed in Section 1.1, coating flows transition from "air/liquid" wetting when the coating first contacts the substrate to "liquid/air" displacement during liquid-film deposition (multi-layer coatings may also have a "liquid/liquid" displacement stage). Consequently, displacement flows in coating processes typically span an extremely broad range of viscosity ratio $\chi = \mu_{rec}/\mu_{adv}$, as well as other parameters characterizing the materials and flow geometry. Wetting failure is essential to form a coating layer during the stage of liquid-film withdrawal ($\chi \gg 1$), whereas air entrainment during air/liquid displacement ($\chi \ll 1$) is usually detrimental to coating quality. Despite the importance of wetting failure in coating applications, the influence of various system parameters remains poorly understood [34].

As demonstrated in Chapter 3, the hydrodynamic model predicts the onset of wetting failure at a critical speed corresponding to Ca^{crit} for each wetting system with a receding fluid of finite viscosity (i.e., $\chi = \mu_{rec}/\mu_{adv} > 0$). The examined numerical approaches fail to find solutions for steady 2D wetting at substrate speeds exceeding

Ca^{crit}. Instead, solution paths encounter a turning point where the interface continues to deform (typically producing larger apparent contact angles θ_M) as substrate speed decreases ($Ca < Ca^{crit}$). Prior studies of liquid/air systems have demonstrated that the solution branch following the turning point at Ca^{crit} is unstable [98, 68, 99], leading to unsteady elongation of the interface. Predicted interface profiles and critical speeds match experimental measurements made during liquid-film withdrawal [100, 96], confirming the connection between the onset of wetting failure and the turning point at Ca^{crit}.

The results presented in this chapter build upon prior work in two important ways. First, the 2D model is used to consider the influence of viscosity ratio, gravitational forces, wettability, and inertia on Ca^{crit}, and also examine axisymmetric geometries. Surprisingly, the trends obtained from the 2D model are matched by predictions from asymptotic theory, even outside of the low-speed regime where the theory is typically viewed to be valid. Second, a wetting-failure mechanism is proposed in which strong pressure gradients pump the receding fluid away from the contact line. Indeed, it is demonstrated that Ca^{crit} coincides with the substrate speed at which these pressure gradients equal the local capillary forces, signifying that the interface cannot steadily displace the receding phase at any faster rate. Predictions from the 2D flow model compare favorably to values measured in experimental air-entrainment studies, supporting the proposed wetting-failure mechanism.

The following sections characterize the onset of wetting failure from solutions generated with the 2D flow model. Section 4.2 briefly reviews the hydrodynamic model and numerical approaches. Section 4.3 evaluates flow fields near the interface inflection point (IP) and proposes a mechanism for wetting failure based on a local stress balance near the DCL. Section 4.4 considers the effects of viscosity, confinement, gravitational forces, wettability, and inertia on Ca^{crit} and also examines axisymmetric geometries. Finally, Section 4.5 compares predictions from the parametric study with experimental data published within the literature. Since the phenomenon of air entrainment remains poorly understood [34] in comparison to cases of liquid-film withdrawal [27], each section focuses on results from air/liquid systems ($\chi \ll 1$).

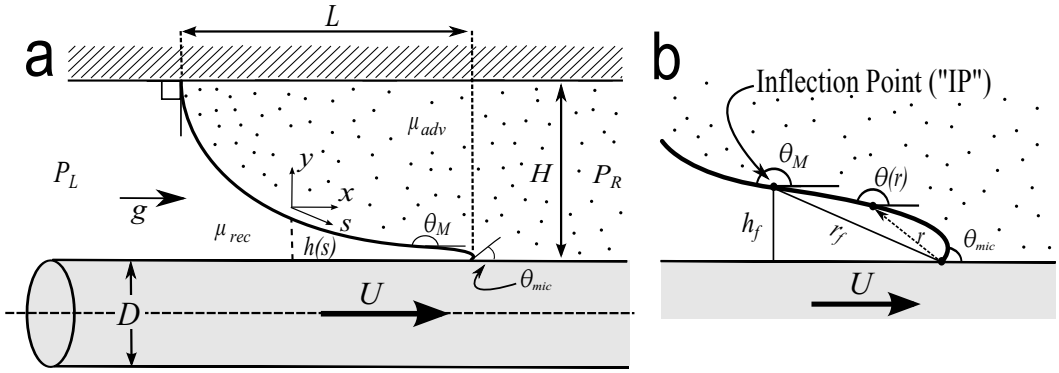

Figure 4.1: Idealization of fluid displacement along a substrate moving with speed U. (a) Outer view of the fluid interface confined within an axisymmetric channel where a fiber substrate of diameter D moves through the center of an annulus with gap H. Note that this system becomes planar when $H/D = 0$. (b) Inner view of the fluid interface where the interface angle θ varies strongly with the radial distance r from the DCL. The maximum interface angle (θ_M) is located at the interface inflection point (IP), which is measured by vertical (h_f) and radial (r_f) distances from the DCL.

4.2 Methods

Chapter 2 presents a hydrodynamic model for fluid displacement along a moving substrate as illustrated by Figure 4.1. The Navier-Stokes equations and associated boundary conditions (see Section 2.1) generate a highly nonlinear free-boundary problem. The model is evaluated with three distinct approaches: (i) the low-speed asymptotic theory of Cox [44], (ii) a one-dimensional (1D) lubrication approach and (iii) a two-dimensional (2D) flow model solved with the Galerkin finite element method (FEM). These approaches are briefly described in Sections 3.2.1 - 3.2.3 and detailed derivations are provided in Sections 2.2 - 2.3.

4.2.1 Determining Ca^{crit}

The critical capillary number, $Ca^{crit} = Ca^{crit}(\chi, \lambda, \theta_{mic}, Re_{adv}, Re_{rec}, Bo, H/D)$, is determined for each method described in sections 3.2.1 - 3.2.3 by tracing steady-state solution families as a function of Ca until locating a point beyond which 2D steady-state solutions cannot be found. For the asymptotic theory, this critical point corresponds to $\theta_{ap} = 180^o$, and Ca^{crit} can be defined by substituting this apparent angle into (1.2):

$$Ca^{crit} = \frac{1}{\delta(\chi)} \left(\frac{g(\theta_{mic}; \chi) - g(180^o; \chi)}{\log(\lambda_{Cox})} \right). \tag{4.1}$$

Solution families from the QP and 2D flow models reveal a turning point that corresponds to Ca^{crit} and some critical interface angle θ_M^{crit} (see Section 4.4.1). Following the turning point, the solution path continues to higher θ_M, but returns to $Ca < Ca^{crit}$. As discussed in prior work [98, 68, 99], this bifurcation at Ca^{crit} separates stable and unstable branches of steady-state solutions. Solution trajectories are traced around the turning point (onto the unstable branch) using a pseudo-arclength continuation scheme [124] for the QP approach and by switching to a continuation method using the channel's pressure drop $\Delta P = P_R - P_L$ (refer to Figure 4.1a) for the 2D flow model [138]. The entire unstable branch is easily recovered for the QP approach, whereas the 2D flow model tends to fail as the macroscopic angle increases a few degrees beyond θ_M^{crit}. Numerical error from mesh distortion appears to alter the convergence of the 2D flow solver along the unstable branch (as $\theta_M \to 180^o$).

4.3 The Wetting-failure Mechanism

The onset of wetting failure corresponds to a critical capillary number Ca^{crit} (see definition in (2.7)), suggesting that the competition of viscous and surface-tension forces is crucial to the loss of steady 2D wetting. In each displacement system, the interface bends in order to balance capillary pressure with stresses produced in the fluid flow. Interface curvature is especially sharp near the DCL, where strong stresses result from viscous flow in a corner. Due to the effects of slip near the DCL, the interface curvature diverges as $\kappa \sim \ln r$ [27] rather than the $\sim 1/r$ singularity found in viscous corner flow with no-slip boundary conditions [65]. Therefore, the capillary-stress gradient at the IP is characterized by

$$\frac{1}{Ca} \left| \frac{\partial \kappa}{\partial x} \right| \sim \frac{1}{Ca} \left(\frac{1}{r_f} \right). \tag{4.2}$$

Lubrication theory predicts the magnitude of the pressure gradient needed to pump the receding phase away from the contact line:

$$\left| \frac{\partial p}{\partial x} \right| = 6\chi \left[\frac{2\lambda v_f + h_f(1 + v_f)}{(h_f)^2(h_f + 4\lambda)} \right] \tag{4.3}$$

where v_f is the horizontal component of the velocity at the IP. To maintain steady fluid displacement, the IP must be positioned such that the capillary-stress gradient is larger than the pressure gradient demanded by the receding flow. Therefore, the onset of wetting failure would be expected when (4.2) equals (4.3) such that

$$\left.\begin{aligned} &Ca^{crit} \sim M(h_f, r_f; \chi, \lambda, ...) \quad \text{and} \\ &M(h_f, r_f; \chi, \lambda, ...) = \frac{2}{r_f}\left[\frac{5}{6\chi}\left(\frac{h_f^3 + 4\lambda h_f^2}{4\lambda + 7h_f}\right)\right], \end{aligned}\right\} \tag{4.4}$$

where $M(h_f, r_f; \chi, \lambda, ...)$ represents the magnitude of the curvature gradient divided by the receding-fluid pressure gradient (i.e., $|\partial_x \kappa / \partial_x p|$) measured at the IP. Since this ratio is most sensitive to the IP position, the notation $M(h_f, r_f)$ will be used from this point forward, although other parameters (e.g., λ and χ) may also influence this visco-capillary balance in general.

The form of $M(h_f, r_f)$ expressed in (4.4) assumes a prefactor of two in (4.2), which is justified later in this section when comparing (4.2) to 2D flow solutions. Also, since interface velocity weakly affects the pressure gradient in (4.3) relative to h_f, (4.4) assumes that $v_f \approx 0.4$, which tends to be within 20% of the true value when $\lambda \ll 1$ and $Re = 0$ (velocity values will be discussed further in Section 4.4.5). In the simplest case, (4.4) obeys the following scaling

$$Ca^{crit} \sim \frac{(h_f)^2}{r_f}, \tag{4.5}$$

which is valid for systems where χ is fixed and $h_f \gg \lambda$.

Figure 4.2 plots stress gradients taken near the IP of 2D flow solutions for liquid/air and air/liquid displacement. Figure 4.2a demonstrates that the capillary-stress gradient of the liquid/air interface decreases with Ca, as described by (4.2) using a prefactor of two. The onset of wetting failure occurs once the capillary-stress gradient matches the pressure gradient predicted by (4.3). Furthermore, the inset of figure 4.2a shows that the visco-capillary balance summarized by (4.5) determines Ca^{crit} for liquid/air systems with a variety of contact-line properties (i.e, different values of λ and θ_{mic}).

Similar arguments can be made for air/liquid systems, where the impact of the receding air flow is clearly seen in Figure 4.2b. Although the air pressure remains ambient along the outer interface, strong pressure gradients arise near the inflection

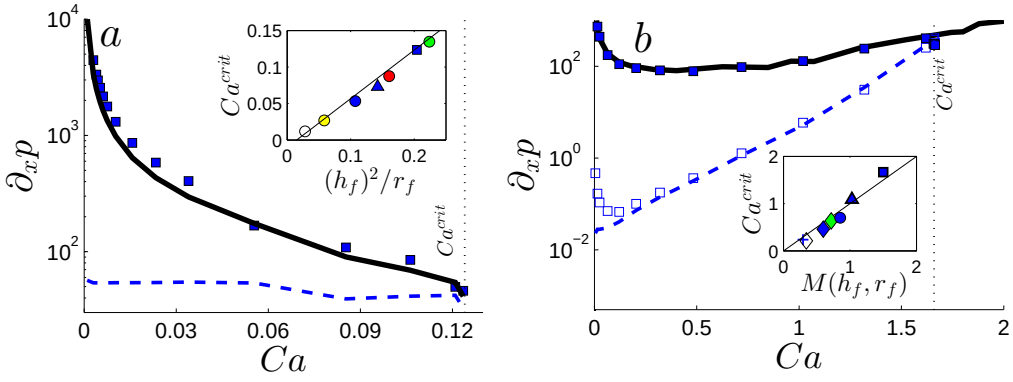

Figure 4.2: Normal-stress gradients at the IP for (a) liquid/air with $\chi \to \infty$ and (b) air/liquid displacement systems with $\chi = 10^{-4}$. Data points are obtained from the 2D flow model for the capillary-stress gradient (filled symbols) and receding-fluid pressure gradient (open symbols) at various values of Ca with Ca^{crit} marked by the vertical dotted line. Dashed lines represent (4.3) using values of h_f obtained from each data set. Bold lines are plotted from (4.2) using a prefactor of two and r_f data from (a) $\chi \to \infty$ and (b) $\chi = 0$ (refer to Figure 3.5b). Additional parameter values: $\lambda = 10^{-2}$, $\theta_{mic} = 90^o$, $Bo = 0$, $Re = 0$ and $H/D = 0$. *Insets*: Ca^{crit} values from 2D flow results for various systems plotted against the visco-capillary balance in (4.4) and (4.5). Solid lines provide a linear fit of the data. Unless listed in the following, parameter values for the inset figures are the same as main panel they occupy: $\lambda = 10^{-2}$ (squares, diamonds, and cross), 10^{-3} (triangles), 10^{-4} (circles); $\theta_{mic} = 50^o$ (green) 70^o (red), 90^o (blue), 110^o (yellow), 130^o (white); (a) $\chi \to \infty$ and (b) $\chi = 0.1$ (cross), 0.02 (diamonds), 10^{-4} (others).

point (refer to Figure 3.8) in order to pump air away from the contact line during steady 2D displacement. At low Ca, stresses from liquid suction control the interface curvature and pressure gradients in the air remain relatively weak. However, the air flow becomes confined to a thin wedge as the interface deforms at high Ca ($h_f \rightarrow 0$ as $\theta_M \rightarrow 180^o$), which dramatically increases pressure gradients within the air. Figure 4.2b shows that the air-pressure gradient (open symbols) grows with Ca at a faster rate than the capillary-pressure gradient (filled symbols) at the interface inflection point. Steady-state solutions cease to exist when the air-pressure gradient equals the capillary-stress gradient observed near r_f. Since characteristics of the air/liquid and void/liquid interfaces are nearly identical prior to Ca^{crit} (refer to Figures 3.3c and 3.5b), the bold curve in Figure 4.2b approximates the interface's pumping capability due to capillary forces as a function of Ca. Extrapolating to $Ca > Ca^{crit}$, these 2D capillary forces would be exceeded by the air-pressure gradient (crossover of dashed and bold lines in Figure 4.2b) at super-critical substrate speeds, leading to transient or three-dimensional interface behavior which is indicative of air entrainment.

Unlike the critical speeds for liquid-film withdrawal shown in Figure 4.2a, Ca^{crit} values associated with air entrainment generally do not follow the simple scaling of (4.5). Specifically, the assumption that $h_f \gg \lambda$ often fails for air/liquid systems because h_f decays exponentially with Ca (refer to Figure 3.5a). Therefore, the full form of the visco-capillary balance (i.e., (4.4)) must be used predict the onset of air entrainment. The inset of Figure 4.2b confirms that (4.4) matches Ca^{crit} for air/liquid systems with various values of λ, θ_{mic}, and χ.

Collectively, the panels of Figure 4.2 demonstrate that the phenomena of liquid-film withdrawal and air entrainment arise from the stress balances outlined by (4.2) - (4.5). Wetting failure results from large pressure gradients required to pump the receding fluid away from the contact line, even when the advancing liquid outweighs the air viscosity by several orders of magnitude ($\chi \ll 1$). Using this insight into the underlying wetting-failure mechanism, the following section systematically investigates the effects of system parameters on Ca^{crit}.

4.4 Parametric Study of Ca^{crit}

4.4.1 Viscosity

The viscosity ratio χ controls the relative strength of viscous stresses within the receding and advancing fluids. Figure 4.3 compares the onset of wetting failure predicted from asymptotic theory, the QP approach, and the 2D flow model while varying the value of χ. Given the wetting-failure mechanism discussed in Section 4.3, one may anticipate the result in Figure 4.3a that Ca^{crit} increases when lowering the receding-fluid viscosity (decreasing χ in (4.4)). Although the lowest Ca^{crit} value coincides with liquid/liquid displacement ($\chi = 1$), lessening the viscosity of the advancing phase in liquid/air displacement does not dramatically change the critical capillary number. Simply stated, this means that the receding phase is crucial to the onset of wetting failure, while the advancing fluid plays a secondary role that only becomes important when $\chi < 1$. Consequently, the receding fluid must have non-zero viscosity ($\chi > 0$) for wetting failure to occur at finite Ca^{crit}. Furthermore, the inset of Figure 4.3a illustrates that the visco-capillary balance in (4.4) matches critical speeds obtained with the 2D flow model, confirming that the onset of wetting failure is driven by pressure gradients that pump the receding flow away from the contact line.

Surprisingly, the asymptotic theory qualitatively matches 2D flow results through the entire range of χ. Since the asymptotic theory does not predict turning points along steady-state solution paths (refer to Figure 3.3), this comparison is made by assuming that the onset of wetting failure corresponds to $\theta_M = 180^o$ in (4.1). Figure 4.3b shows that the critical dynamic angle θ_M^{crit} (measured at $Ca = Ca^{crit}$) is actually always less than 180^o and only converges to the *ad hoc* constraint used for (4.1) in the limit of vanishing receding-fluid viscosity ($\theta_M^{crit} \to 180^o$ as $\chi \to 0$). However, asymptotic theory predicts that θ_M increases rapidly with faster substrate speeds as $Ca \to Ca^{crit}$, which makes (4.1) insensitive to the dynamic angle, so long as $\theta_M^{crit} \sim 180^o$.

Unlike the asymptotic theory, the QP approach only approximates the 2D flow solution well when $\chi \geq 1$. Figure 4.3 shows that the discrepancy in Ca^{crit} is minor for the case of liquid/air displacement, but becomes considerable within the air/liquid regime. As previously discussed in Section 3.3.5, the QP approach does not accurately account for fluid stresses within the advancing flow when $\chi < 1$ [138]. Consequently,

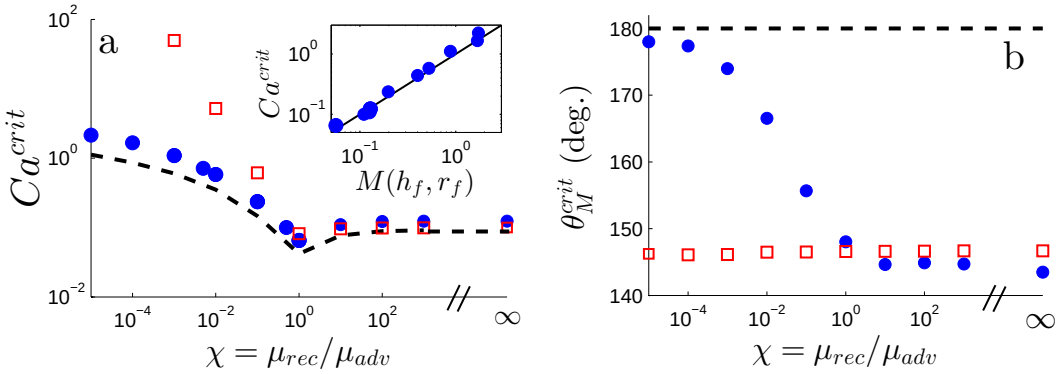

Figure 4.3: (a) The critical capillary number and (b) critical macroscopic angle plotted as a function of the viscosity ratio. Comparison is made between the 2D flow model (circle), QP approach (square), and asymptotic theory (dashed line). *Inset*: Ca^{crit} values from the 2D flow data replotted against the visco-capillary balance in (4.4). Note that to remain consistent with the definition of Ca in (2.7), the viscosity ratio is omitted from $M(h_f, r_f)$ when $\chi \geq 1$. Solid lines provide a linear fit of the data. Additional parameter values: $\lambda = 0.01$, $\theta_{mic} = 90^o$, $Bo = 0$, $Re = 0$ and $H/D = 0$.

QP results reflect improper behavior of the IP during air/liquid displacement (refer to Figure 3.5b), leading to errors in the visco-capillary balance (4.4) that ultimately determines the magnitude of Ca^{crit}. The following parametric studies focus on wetting failure in the air-entrainment limit, which has not been as thoroughly characterized by numerical models as the liquid-withdrawal case [97, 69, 98, 55, 68, 99, 139, 140]. Therefore, the QP approach will be omitted from the remainder of this paper due to its failure within the air/liquid viscosity regime ($\chi < 1$).

4.4.2 Confinement

Changes made to the characteristic length of the problem geometry, H, influence the relative importance of outer (viscous) and inner (slip) mechanics. Our prior work has demonstrated that confinement reduces the action of viscous bending during air/liquid displacement within parallel-plate geometries, allowing Ca^{crit} to increase as H decreases [138]. This trend is reflected in the following scaling obtained from asymptotic theory (i.e, (4.1)):

$$Ca^{crit} \propto [\log (l_M/l_{slip})]^{-1}. \tag{4.6}$$

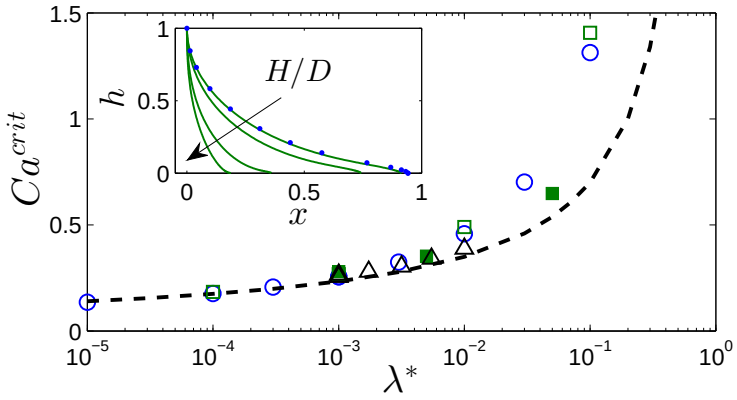

Figure 4.4: The critical capillary numbers plotted as a function of the generic confinement ratio λ^* (defined in text) for air/liquid displacement. Open circles and squares denote 2D flow results where λ varies and $H/D = 0$ and 0.5, respectively. Filled symbols represent the case where $\lambda = 10^{-3}$ and H/D varies (i.e., $H/D = 0.5$, 5, and 50). Triangle data points are taken from Figure 4.7a and discussed in the text of Section 4.4.3. The dashed line shows a fit from the confinement scaling (4.6). *Inset*: Solid lines show interface profiles at Ca^{crit} for $H/D = 0$, 0.5, 5, and 50 with $\lambda = 10^{-3}$. Circles denote the critical profile for $\lambda = 10^{-2}$ and $H/D = 0$. Additional parameter values: $\chi = 0.02$, $\theta_{mic} = 90^o$, $Bo = 0$, and $Re = 0$.

For the purpose of generality, l_M represents some macroscopic length scale associated with viscous effects (e.g., $l_M = H$ in the parallel-plate example) and $\lambda^* = l_{slip}/l_M$ is a generic confinement ratio. As systems become more confined, the inner and outer length scales approach the same order of magnitude ($\lambda^* \to 1$), which yields larger Ca^{crit} values in (4.6).

In the current work, interface confinement is extended to the axisymmetric geometry shown in Figure 4.1a. The axisymmetric system contains azimuthal curvature as the interface bends around the fiber circumference, in addition to the usual interface deformation in the flow direction. Therefore, viscous bending is influenced by two macroscopic lengths within the axisymmetric geometry: the annulus gap (H) and the fiber diameter (D).

Figure 4.4 compares the confinement effect for air/liquid displacement in axisymmetric and parallel-plate systems. Interestingly, the data computed from the 2D flow model collapse to a single curve when plotting Ca^{crit} against $\lambda^* = l_{slip}/l_M$ in Figure 4.4, where l_M is the *smallest* macroscopic length within the system. (For example, $l_M = D$

when the fiber diameter is thinner than the gap such that $H/D > 1$). Confinement reduces viscous effects relative to the impact of fluid slip near the contact line ($\uparrow \lambda^*$), leading to higher Ca^{crit} values as described by the scaling relationship (4.6). (Note that asymptotic theory systematically underpredicts the 2D flow data as $\lambda^* \to 1$.) Although the axisymmetric case may not be intuitive, the inset of Figure 4.4 illustrates that thinner fiber substrates do, in fact, reduce viscous bending of the interface, leading to the apparent "contraction" of profiles with increasing H/D. In contrast, critical interface shapes simply scale with H for planar systems ($H/D = 0$), appearing independent of the degree of confinement (i.e, λ) when plotted with dimensionless coordinates h and x.

Figure 4.5 takes a closer look at properties of the axisymmetric air/liquid interface for different fiber diameters. Due to axisymmetry, the interface bends around the circumference of the fiber in addition to the usual flow-direction curvature seen in planar systems. Since the interface is deflected in the direction of the fiber motion, the azimuthal curvature increases in concavity (with respect to the receding fluid) while approaching the contact line, as illustrated by Figure 4.5a and 4.5c for $H/D = 0.5$ and 5, respectively. This curvature contributes capillary-stress gradients that intensify as the fiber diameter decreases, while capillary forces in the flow-direction are analogous to the planar system discussed in Section 4.3 (e.g., (4.2)). Contributions from the two curvature gradients can be approximated at the IP as

$$\left|\frac{\partial \kappa}{\partial x}\right|_{fd} \approx 2/r_f \quad \text{and} \quad \left|\frac{\partial \kappa}{\partial x}\right|_{az} \approx \frac{\partial}{\partial x}\left(\frac{1}{h_f + \frac{1}{2}(H/D)^{-1}}\right), \tag{4.7}$$

where subscripts "fd" and "az" denote the flow-direction and azimuthal terms, respectively.

Figure 4.5b and 4.5d plot the contributions of (4.7) at Ca^{crit} for fibers of diameter $H/D = 0.5$ and 5, respectively. The azimuthal contribution increases considerably as the fiber diameter decreases, becoming significant when $H/D > 1$. Using (4.2) and the fact that $\partial_x \kappa|_{az} \sim H/D$, the following expression approximates the capillary-stress gradient at the IP for systems where $H/D \geq 1$:

$$\frac{1}{Ca}\left|\frac{\partial \kappa}{\partial x}\right| \sim \frac{1}{Ca}\left(\frac{H/D}{r_f}\right). \tag{4.8}$$

Equation (4.8) states that increasing H/D strengthens capillary forces acting near the IP. Consequently, higher Ca^{crit} values are obtained for fluid displacement along thin

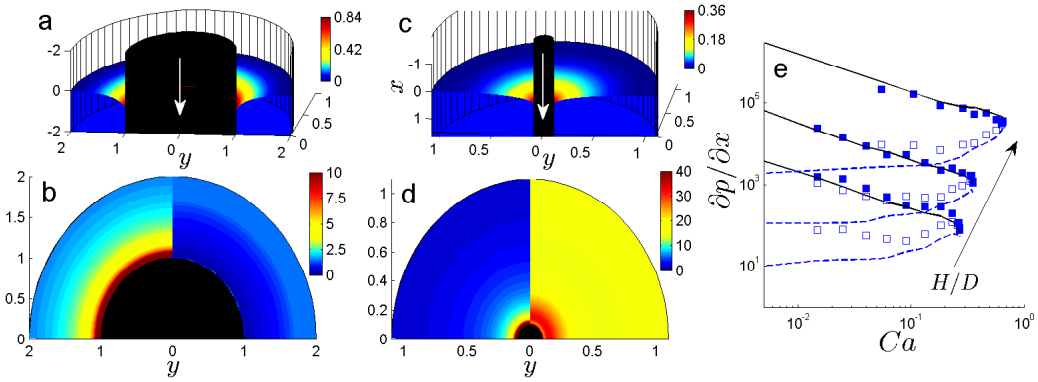

Figure 4.5: Interface properties obtained with the 2D flow model for axisymmetric air/liquid systems for various values of H/D. Panels (a) and (c) plot interface profiles along a downward moving fiber (black) with $H/D = 0.5$ and 5, respectively. Color contours indicate the interface deflection (vertical position) following the fiber motion. Panels (b) and (d) show curvature gradients computed from the interface profiles of (a) and (c), respectively, using (4.7). Color contours of the left and right halves of each image reflect the flow-direction ($\partial_x \kappa|_{fd}$) and azimuthal ($\partial_x \kappa|_{az}$) contributions, respectively. (e) Normal-stress gradients measured at the IP as a function of Ca for $H/D = 0.5$, 5, and 50. Data points are obtained from the 2D flow model for the capillary-stress gradient (filled symbols) and receding-fluid pressure (open symbols). Dashed and solid lines represent (4.3) and (4.8) using values of h_f and r_f obtained from each data set. Additional parameter values: $\chi = 0.02$, $\lambda = 10^{-3}$, $\theta_{mic} = 90^o$, $Bo = 0$, and $Re = 0$

fibers because the azimuthal curvature assists in pumping the receding phase away from the contact line. These axisymmetric confinement effects likely contribute to the high-speed wetting processes that have become a trademark of the fiber coating industry [115, 141, 88].

Figure 4.5e plots stress gradients measured at the IP for air/liquid interfaces in axisymmetric geometries with varying H/D values. For each case, the capillary-stress gradient is matched by (4.8). The receding-fluid pressure gradient is fairly well described by the planar lubrication theory (4.3), especially near Ca^{crit} where the air film is typically much thinner than the fiber diameter (i.e., $h_f \ll (H/D)^{-1}$). Therefore, the appropriate visco-capillary balance for axisymmetric systems with $H/D \geq 1$ is

$$M(h_f, r_f) = \frac{2H/D}{r_f}\left[\frac{5}{6\chi}\left(\frac{h_f^3 + 4\lambda h_f^2}{4\lambda + 7h_f}\right)\right], \tag{4.9}$$

which predicts the onset of wetting failure as discussed in the derivation of (4.4). Figure 4.6 collapses Ca^{crit} data for air/liquid systems with various degrees of confinement using functions of the IP position. In Figure 4.6, critical speeds follow the visco-capillary balance for planar and axisymmetric geometries using $M(h_f, r_f)$ defined in (4.4) and (4.9), respectively. This once again confirms that pressure gradients in the receding flow are crucial to initiate wetting failure.

4.4.3 Body Force

Body force effects, such as the action of gravity, may become important as H increases ($\lambda \to 0$). Figure 4.7 demonstrates the impact of gravity on the onset of wetting failure for air/liquid displacement (note that the gravity vector points toward the advancing liquid as illustrated in Figure 4.1a). In Figure 4.7a, the strength of the body force increases with Bo while all other parameters are held constant. Physically, this could correspond to a scenario where the liquid density is increased to strengthen gravitational action during fluid displacement. Data from the 2D flow model illustrate that Ca^{crit} increases with $\sqrt{Bo}$ in this case.

In practice, system geometry usually determines the magnitude of Bo because liquid densities rarely vary by more than a factor of two. Figure 4.7b reflects the effect of increasing Bo by widening the gap H in the air/liquid system such that $\lambda \propto 1/\sqrt{Bo}$

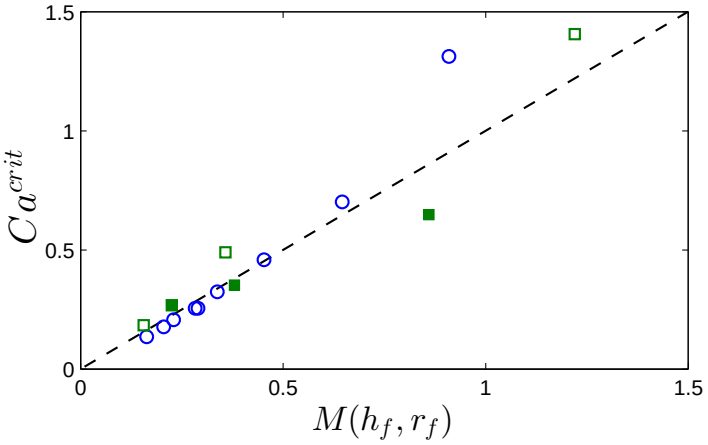

Figure 4.6: Critical capillary number data from Figure 4.4 replotted as a function of the visco-capillary balance. The dashed line represents Ca^{crit} values predicted from (4.4) using a prefactor of unity in both cases. Note that $M(h_f, r_f)$ is calculated using (4.9) when $H/D \geq 1$. Refer to Figure 4.4 for parameter values associated with circle and square symbols.

(since $\lambda = l_{slip}/H$ and $Bo \sim H^2$). Two distinct limits can be observed from the Ca^{crit} data plotted in Figure 4.7b. First, at low values of Bo the interface remains confined to small gaps (relatively large values of λ), which increase Ca^{crit} as predicted by (4.6). Second, the 2D flow model gradually deviates from the confinement scaling as the gap widens and Bo exceeds unity. Unlike Figure 4.7a, Ca^{crit} tends toward a constant value as gravitational forces increase such that $Bo \gg 1$.

Despite the different behaviors of Ca^{crit}, the inset of Figure 4.7b illustrates that Bo controls the intensity of the gravitational forces (relative to surface-tension forces), leveling the fluid interface in both of the cases discussed above. Gravity dominates the interface shape away from the substrate at distances greater than the capillary length $l_{cap} = \sqrt{\sigma/\rho g}$. Viscous effects deform the interface closer to the contact line, making l_{cap} the appropriate viscous length scale (i.e., l_M) when gravity levels the outer interface. In terms of the Bond number, $l_M = H/\sqrt{Bo}$ (note that $H/\sqrt{Bo} = \sqrt{\sigma/\rho g}$) for systems where $Bo > 1$. Increasing Bo while fixing all other parameters effectively reduces viscous bending relative to slip, as reflected by an increase in the generic confinement ratio $\lambda^* = l_{slip}\sqrt{Bo}/H$ (see Section 4.4.2). Using this definition for λ^*, data from Figure 4.7a are plotted alongside the confinement study in Figure 4.4 to demonstrate

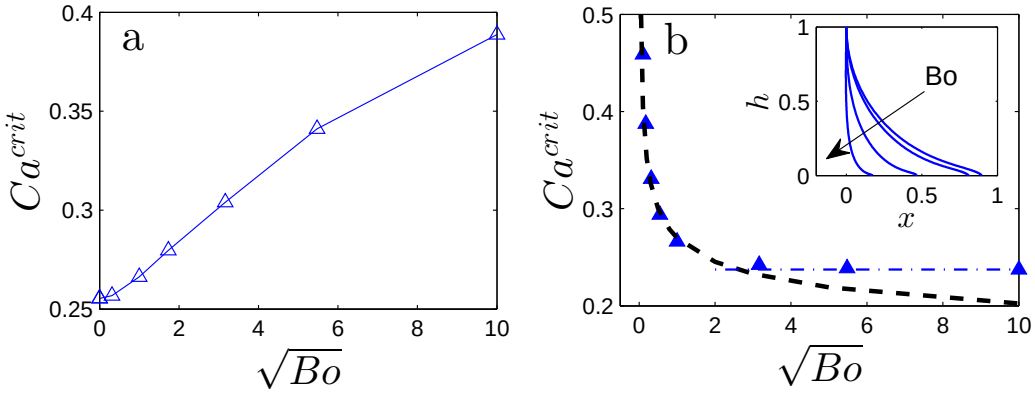

Figure 4.7: The effect of body forces on Ca^{crit} for air/liquid displacement. (a) The Bond number increases while fixing the gap to $\lambda = 10^{-3}$. Symbols are obtained from 2D flow solutions and the solid line is included to guide the eye. (b) The Bond number increases with larger gaps such that $\lambda = 10^{-3}/\sqrt{Bo}$. Symbols are obtained from the 2D flow model and the dash-dot line marks a constant critical speed $Ca^{crit} = 0.24$. The dashed line represents the confinement scaling expressed in (4.6). *Inset*: Interface profiles at Ca^{crit} for $Bo = 0$, 1, 10, and 100. Additional parameter values: $\chi = 0.02$, $\theta_{mic} = 90^o$, $H/D = 0$, and $Re = 0$.

that physical boundaries (decreasing H) and body forces (increasing Bo) increase Ca^{crit} analogously through effective confinement of the interface.

In contrast, increasing Bo by widening the gap (i.e., $l_{slip}/H \propto 1/\sqrt{Bo}$) exactly counteracts this effective confinement from gravitational leveling (i.e., $\lambda^* =$ constant). Consequently, the relative impact of viscous bending and fluid slip does not change for $Bo \gg 1$ in Figure 4.7b. As has been shown experimentally, Ca^{crit} remains constant for relatively unconfined systems ($Bo > 1$), regardless of the exact size of the outer geometry [138].

4.4.4 Wettability

Substrate wettability is modeled with a microscopic contact angle, θ_{mic}, that prescribes the interface slope at the dynamic contact line through (2.9). Figure 4.8a shows the effect of θ_{mic} on Ca^{crit} for air/liquid displacement with $\lambda = 0.01$. Matching intuition, the data show that increasing substrate wettability (smaller θ_{mic}) allows for steady wetting at faster speeds (larger Ca^{crit}). The inset figure confirms that this result holds for various values of λ. In fact, all tested cases show a similar sensitivity of Ca^{crit} to

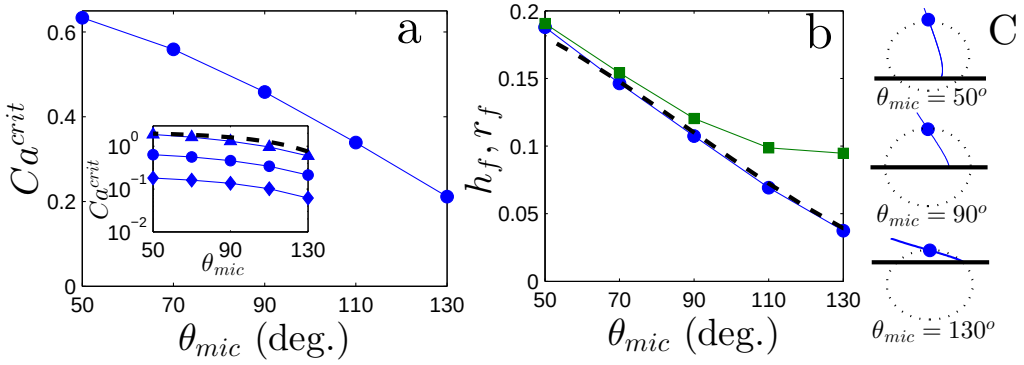

Figure 4.8: (a) The critical capillary number obtained from 2D flow solutions plotted as a function of substrate wettability for air/liquid displacement with $\lambda = 10^{-2}$. *Inset*: Ca^{crit} values plotted against θ_{mic} for $\lambda = 10^{-1}$ (triangles), 10^{-2} (circles), and 10^{-5} (diamonds). Symbols represent 2D flow solutions and the dashed line is obtained from the asymptotic theory expressed in (4.10) with a prefactor of unity. (b) The IP location plotted as a function of θ_{mic} for $\lambda = 0.01$ and fixed substrate speed $Ca = 0.1$. Symbols are taken from 2D flow data for h_f (circle) and r_f (square). Dashed lines are plotted from (4.11). (c) Inner interface profiles from 2D flow solutions (IP position marked with symbol) are compared against the spherical-cap approximation used to derive (4.11). Note that $R_c = 0.11$ is used in (4.11) for both (b) and (c). Additional parameter values: $\chi = 0.02$, $Bo = 0$, $Re = 0$, and $H/D = 0$

θ_{mic} that is well described by asymptotic theory

$$Ca^{crit} \sim \frac{\pi}{6} \ln \chi - \frac{\theta_{mic}^3}{9}, \tag{4.10}$$

which results from (4.1) when χ and λ are assumed to be much less than unity (here θ_{mic} is reported in radians) [44]. Surprisingly, this means that the impact of θ_{mic} is independent of the relative scale of the contact-line region (i.e., λ) where microscopic mechanics control the interface shape. Note that the use of a structured mesh composed of quadrilateral elements restricts the 2D flow model to $\theta_{mic} \in [50^o, 130^o]$, as reflected by the data in Figure 4.8. With this limitation, the 2D flow cannot directly model the highly wetting fluids commonly used in experimental studies due to their small equilibrium contact angles ($\theta_{mic} \to 0^o$).

The microscopic contact angle primarily influences displacement through changes to the interfacial length scales. For example, Figure 4.8b shows that increasing θ_{mic} causes the inflection point to move closer to the contact line. Figure 4.8c demonstrates that this IP behavior can be understood by idealizing the inner interface region (shown

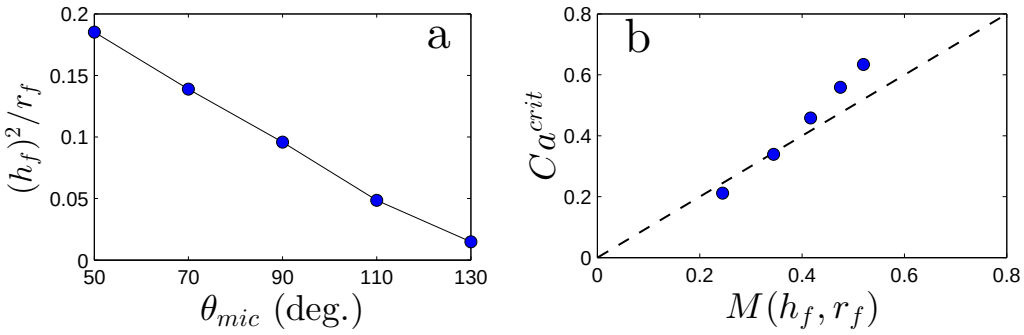

Figure 4.9: (a) The influence of θ_{mic} on the IP function used in the scaling (4.5) and (b) corresponding critical speeds plotted against the visco-capillary balance (4.4). The dashed line represents (4.4) using a prefactor of unity. Symbols denote 2D flow data taken from Figures 4.8a and 4.8b with the following parameter values: $\lambda = 0.01$, $\chi = 0.02$, $Bo = 0$, $Re = 0$, and $H/D = 0$.

in Figure 4.1b) as a spherical cap with height h_f and a complementary contact angle $(180 - \theta_{mic})$ at the substrate. The height of the spherical cap depends on θ_{mic} through the geometric approximation

$$h_f = R_c(1 + \cos\theta_{mic}), \tag{4.11}$$

where R_c is the radius of curvature. Although a constant-curvature cap does not accurately represent the inner interface shape (recall that $\kappa \sim \ln r$ as $r \to 0$), Figure 4.8b-c affirms that (4.11) is sufficient to capture the geometric effect of θ_{mic} on h_f at fixed substrate speed.

Figure 4.9 connects substrate wettability to the wetting-failure mechanism discussed in Section 4.3. For instance, Figure 4.9a illustrates that less wettable substrates decrease the value of $(h_f)^2/r_f$, which reflects building larger air pressure gradients ($\sim 1/(h_f)^2$) without commensurate increases to the local capillary forces ($\sim 1/r_f$) as higher values of θ_{mic} thin the air film near the contact line. These large air stresses are responsible for the decrease in Ca^{crit} as θ_{mic} increases in Figure 4.8a. Although the visco-capillary balance in Section 3 does not explicitly account for substrate wettability, Figure 4.9b shows that (4.4) matches the trend of the Ca^{crit} data for various θ_{mic}, suggesting that the onset of wetting failure is more sensitive to stresses near the IP than interface characteristics very close to the contact line.

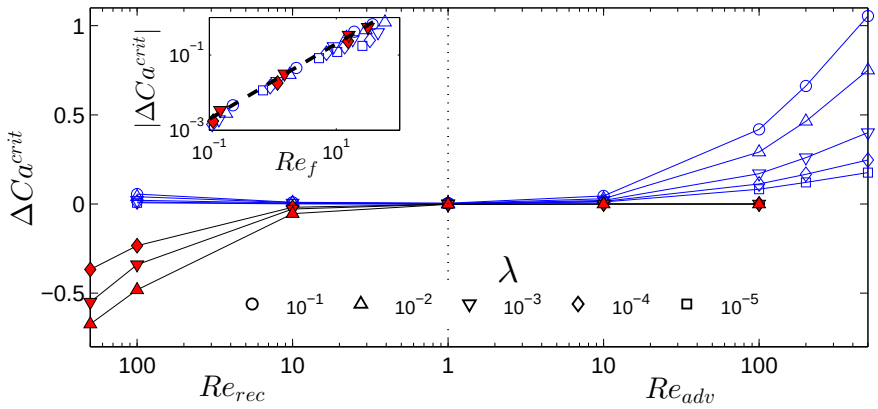

Figure 4.10: The fractional difference in Ca^{crit} due to the influence of fluid inertia at various values of Re (relative to the creeping-flow limit $Re = 0$). Data points are obtained from the 2D flow model for liquid/air (filled) and air/liquid (open) displacement with various values of λ, as listed in the legend at bottom. *Inset*: ΔCa^{crit} data from the main figure are replotted against the local Reynolds number $Re_f = Re \times h_f$. Additional parameter values: $\chi = 10^{-3}$ (open) and 10^3 (filled), $\theta_{mic} = 90^o$, $Bo = 0$, and $H/D = 0$.

4.4.5 Inertia

Results shown up to this point have neglected inertial effects, which may become important at sufficiently high substrate speeds. To probe the impact of fluid inertia on wetting failure, Ca^{crit} values are computed for $Re \in [1, 500]$, and the fractional difference with respect to the creeping-flow result ($Re = 0$) is plotted in Figure 4.10 . Since it is not readily apparent how inertia will impact each phase, the Reynolds number is *independently* varied for the receding (Re_{rec}) and advancing fluids (Re_{adv}) of the air/liquid system. (For example, $Re_{rec} = 0$ when varying Re_{adv} along the right-side of Figure 4.10, and vice versa.) Data are also plotted for liquid/air displacement to demonstrate the symmetry between cases of air entrainment and liquid withdrawal.

Figure 4.10 shows that Re_{adv} and Re_{rec} have a relatively weak impact on Ca^{crit}. Even for $Re \sim 10$, the critical capillary number remains within 10% of the creeping-flow results. Data points in Figure 4.10 only become distinct from the creeping-flow limit when $Re \sim 100$. Here, it can be seen that inertial effects are primarily felt from the more viscous phase. In other words, Re_{adv} and Re_{rec} are important for air/liquid and liquid/air displacement, respectively. In both cases, inertia "assists" the flow of liquid

toward the substrate. As shown by the behavior of Ca^{crit} in Figure 4.10, inertia of the advancing liquid (Re_{adv}) aids the displacement of the air phase, leading to steady wetting at higher speeds. In contrast, Re_{rec} resists displacement by "assisting" the motion of the receding fluid, promoting wetting failure at lower Ca^{crit}. The fractional change in the critical speed (ΔCa^{crit}) increases weakly with λ due to changes in the local Reynolds number (see inset of Figure 4.10), as discussed in more detail later in this section.

The momentum balance of (2.1) suggests that inertia may alter the fluid-stress gradients that bend the fluid interface:

$$\nabla p = \nabla^2 \boldsymbol{v} - Re(\boldsymbol{v} \cdot \nabla \boldsymbol{v}). \tag{4.12}$$

To demonstrate the role of inertia in the receding flow, Figure 4.11 plots liquid/air flow fields with various values of Re. When $Re_{rec} \gg 1$, the adverse pressure gradient intensifies (i.e., $|\partial_x p|_{rec}$ increases relative to the estimate of (4.3)) in order to resist the receding fluid's inertia and then pump the fluid away from the contact line. This is reflected by higher receding-fluid pressures observed near the contact line when liquid inertia is significant (Figure 4.11a) compared to the $Re_{rec} = 0$ case (Figure 4.11b). Thus, increasing Re_{rec} effectively makes the receding liquid more difficult to displace, requiring larger values of $|\partial_x p|$ and, ultimately, promoting wetting failure at lower substrate speeds (refer to Figure 4.10). In contrast, Re_{adv} has negligible effect on the flow fields (Figure 4.11c) and Ca^{crit} values associated with the onset of liquid-film withdrawal because the receding liquid dominates the interface behavior in this viscosity regime.

Figure 4.12 explores the impact of liquid inertia on air/liquid displacement. Relative to creeping flow, liquid inertia localizes velocity gradients in a thin boundary layer near the substrate, as revealed by a comparison of the flow fields shown in Figure 4.12a and 4.12b. Away from the substrate the liquid remains nearly stagnant when $Re_{adv} \gg 1$. Holding other parameters fixed (including Ca), increasing liquid inertia reduces interface deformation, as shown in Figure 4.12c. Figure 4.12d demonstrates that large values of Re_{adv} slow the fluid flow along the interface, reducing liquid stresses that would bend the interface in the creeping-flow limit. Consequently, larger values of Re_{adv} allow for steady air/liquid displacement at higher Ca before interface deformation restricts the air flow to a thin wedge, leading to the onset of wetting failure.

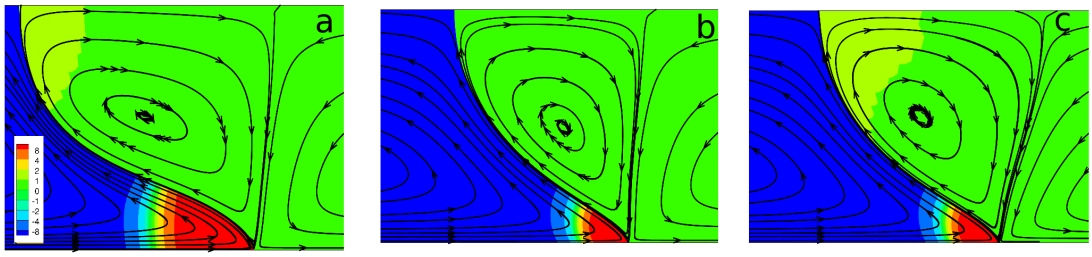

Figure 4.11: Comparison of the flow fields obtained at Ca^{crit} with the 2D flow model for liquid/air displacement. Streamlines and pressure contours are shown at various Re: (a) $Re_{rec} = 100$ and $Re_{adv} = 0$; (b) $Re_{rec} = 0$ and $Re_{adv} = 0$; (c) $Re_{rec} = 0$ and $Re_{adv} = 100$. Values of the other system parameters are listed in the following: $\chi = 10^3, \lambda = 0.01, \theta_{mic} = 90^o, Bo = 0$ and $H/D = 0$.

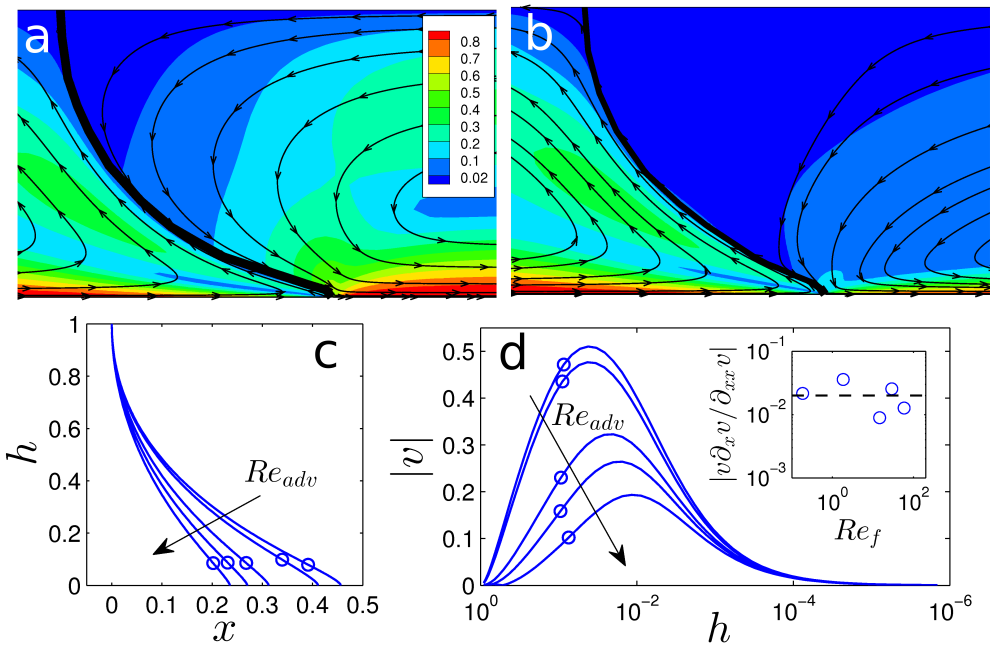

Figure 4.12: The effect of Re_{adv} on the velocity field and interface shape obtained from 2D flow solutions for air/liquid displacement. (a-b) Velocity magnitude contours and streamlines are shown at Ca^{crit} for (a) $Re_{adv} = 0$ and (b) $Re_{adv} = 500$ ($Re_{rec} = 0$ in all panels) . The legend in panel (a) lists velocity magnitude values associated with each contour color. (c) Interface profiles are plotted for $Re_{adv} = 0, 10, 100, 200$, and 500 at fixed $Ca = 0.25$. (d) Fluid velocity profiles are measured along the interfaces plotted in panel (c). Symbols denote values at the IP for each curve. *Inset*: The ratio of inertial and viscous effects from velocity gradients measured at the IP. The dashed line marks $|v\partial_x v/\partial_{xx} v| = 0.02$. Additional system parameters: $\chi = 0.02$, $\lambda = 0.001$, $\theta_{mic} = 90^o$, $Bo = 0$, and $H/D = 0$.

Since stresses near h_f are key to the wetting-failure mechanism of Section 4.3, the local Reynolds number is best suited to characterize inertial effects near the onset of fluid entrainment. In fact, the inset of Figure 4.10 demonstrates that data points for liquid/air and air/liquid displacement nearly collapse to a single curve based on Re_f:

$$\Delta Ca^{crit} \approx 0.02 Re_f. \tag{4.13}$$

Equation (4.13) states that inertial contributions additively modify the critical speeds calculated from creeping-flow analysis by a factor that is proportional to Re_f. Unlike the bulk Reynolds number which is insensitive to microscopic parameters, Re_f accounts for contact-line conditions (e.g., λ) through their influence on h_f. Therefore, the curves plotted in Figure 4.10 for various λ conform to (4.13) without explicitly accounting for differences in slip length. The prefactor in (4.13) reflects the fact that velocity gradients near the IP tend to favor viscous effects ($\partial_{xx} v$) over inertial contributions ($v \partial_x v$) by approximately two orders of magnitude (see inset in Figure 4.12d). Since the impact of inertia at the IP is weighted by the ratio $|v\partial_x v / \partial_{xx} v| \approx 0.02$, large Reynolds numbers are needed to significantly change Ca^{crit} relative to the creeping-flow limit.

4.5 Discussion

Collectively, the preceding sections demonstrate that the onset of wetting failure coincides with a steady-state bifurcation at some critical substrate speed, which is sensitive to characteristics of the displacement flow and interface shape. Unlike past studies that have typically been limited to a relatively narrow range of fluid properties [98, 99, 68, 97, 69, 138], this investigation spans a much larger parameter space and also includes inertial effects. However, results presented in the preceding sections suggest that viscous effects influence the onset of wetting failure most strongly, even when $Re \gg 1$. As detailed in section 4.3, steady displacement fails when capillary forces can no longer support the adverse pressure gradient required to pump the receding fluid away from the contact line. To overcome viscous resistance within the receding fluid, this pressure gradient increases as the substrate moves faster until wetting failure occurs at some critical speed. Viscous effects are even important when air is the receding fluid ($\chi \ll 1$) because the advancing liquid contributes stresses that deform the interface and

restrict the air to a very thin wedge. Consequently, the magnitude of Ca^{crit} primarily depends on the viscosity ratio χ and the location of the IP (i.e., h_f and r_f), which characterizes the size of the "wedge" near the contact line.

4.5.1 Comparison of Numerical Approaches

As discussed in Section 3.3, only the 2D flow model accurately describes the position of the IP during air/liquid displacement. Approximate solutions from asymptotic theory (Section 3.3.4) and the QP approach (Section 3.3.5) do not correctly reflect the rapid migration of the IP toward the contact line as Ca increases. This failure leads to particularly large errors in Ca^{crit} values obtained from QP solutions when $\chi < 1$. Asymptotic theory improves upon the estimates of the QP approach in the air/liquid regime, but inaccurately describes interface profiles near the contact line when $Ca > 0.1$, similar to the findings of Chen *et al.* (1995) [64]. Our results suggest that this apparent breakdown of asymptotic theory can be attributed to its failure to describe the IP behavior during high-speed wetting.

Surprisingly, asymptotic theory captures many trends related to the onset of wetting failure. To illustrate this point, Figure 4.13 compares critical speeds obtained from the 2D flow model and asymptotic theory. Figure 4.13a demonstrates that all Ca^{crit} data from the 2D flow parameter studies (Sections 4.4.1 - 4.4.5) match the prediction of asymptotic theory when modifying (4.1) to account for the inertial effects described in (4.13). Figure 4.13a also uses the generic confinement ratio $\lambda^* = l_{slip}/l_M$, where l_M is the most restrictive macroscopic length scale within the system geometry, as discussed in Section 4.4.2. Recall that l_M typically equals the channel gap H, except in axisymmetric systems with thin fibers such that $H/D > 1$ and $l_M = D$. Also, $l_M = H/\sqrt{Bo}$ when $Bo > 1$ because gravity levels the interface as discussed in Section 4.4.3. Although the wetting-failure mechanism based on IP location (refer to Section 4.3) most accurately represents the Ca^{crit} trends shown in Section 4.4, asymptotic theory offers a useful tool that could be used to estimate critical speeds without a 2D numerical solution. Even for inertial systems, the need for IP data can be eliminated by using $Re_f \approx Re/\log\lambda^*$ (note that $h_f \sim 1/\log\lambda^*$ in the inset of Figure 4.13a), allowing critical speeds to be predicted *a priori* given values for the system parameters.

Although asymptotic theory matches trends for Ca^{crit}, 2D flow solutions provide

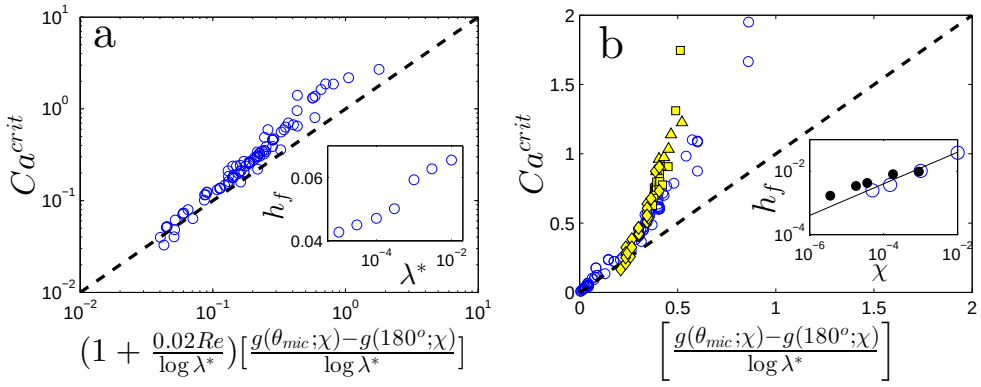

Figure 4.13: Comparison of Ca^{crit} values from the 2D flow model (open circles) and asymptotic theory (dashed line) expressed in (4.1). (a) All 2D flow results from Section 4.4 are plotted against asymptotic theory modified for a generic system geometry ($\lambda = \lambda^*$) and finite Re using (4.13) with $Re_f \approx Re/\log\lambda^*$, as described in the text. *Inset*: IP location measured as a function of λ^* with $Re = 0$, $Bo = 0$, $H/D = 0$, $\theta_{mic} = 90^0$ and $\chi = 0.02$. (b) 2D flow results from the creeping-flow regime ($Re = 0$) are fitted with a cubic interpolating function (bold line) to aid the eye. Filled symbols represent experimental data for various (diamonds) liquid viscosities [104], (squares) effective gas viscosities [142], and (triangles) confinement gaps [138]. For each experimental data point, $g(\theta;\chi)$ is calculated from (1.2) assuming $\theta_{mic} = \theta_s$ and $\lambda = 10^{-5}$, and using reported viscosities for χ. (Note that $\lambda \in [10^{-5}, 10^{-3}]$ depending on the gap corresponding to each green data point.) *Inset*: Comparison of h_f values at various χ obtained from the model at Ca^{crit} with $\lambda = 10^{-4}$ (open), experimental measurement of air entrainment [105] (filled), and $h_f \propto \chi^{1/2}$ (line).

useful insight into wetting failure that is not readily accessible from theory even within the creeping-flow regime. Figure 4.13b illustrates that the critical capillary numbers predicted from (4.1) systematically underestimate values obtained from the 2D flow model for air/liquid displacement. Both model and theory reflect the trend of increasing Ca^{crit} for lower relative air viscosities (χ decreases; Section 4.4.1), more wettable substrates (θ_{mic} decreases; Section 4.4.4), and greater interface confinement (λ^* increases; Section 4.4.2); however, 2D flow solutions exhibit stronger sensitivity to these hydrodynamic factors.

4.5.2 Comparison with Experimental Data

Similar to the 2D flow results, experimental measurements systematically deviate from the predictions of asymptotic theory as Ca^{crit} increases in Figure 4.13b. Critical speeds are shown for experimental air/liquid studies with unconfined, plunge-type systems where liquid [104] and effective air viscosities [142] are varied by several orders of magnitude. In addition, data from our experimental study presented in Chapter 6 reflect the effect of interface confinement by decreasing the gap H. The abscissa in Figure 4.13b is computed for each experimental data set using the definition of $g(\theta;\chi)$ in (4.1), reported fluid viscosities for χ ($\mu_{air} = 0.018$ cP when not reported), and the assumption that θ_{mic} is equal to the reported static contact angle. The slip length acts as a fitting parameter within the model. For simplicity, it assumed that $l_{slip} \sim 10$ nm ($\lambda = 10^{-5}$ for the unconfined studies) in agreement with the findings of our experimental study (see Chapter 6). The model matches the trend of the experimental data over a wide parameter range ($\theta_{mic} \in [50^o, 130^o], \chi \in [10^{-5}, 10^3]$ and $\lambda \in [10^{-5}, 10^{-1}]$ for the model), improving considerably upon the performance of the asymptotic theory (4.1). Non-ideal substrates [138] and gas-density effects [105] may account for the slight underprediction of experimental data when $Ca^{crit} > 1$, although the impact of these factors is not yet known within the context of the hydrodynamic model.

In addition, the 2D flow model provides information about the air-film shape at the onset of wetting failure in air/liquid systems. Interface profiles in Figure 3.4d demonstrate that thin air films form at the contact line as a precursor to air entrainment. Consequently, the IP height h_f at Ca^{crit} can be used to characterize the size of the entrained air layer. The inset of Figure 4.13b compares predicted air-film thickness

obtained at Ca^{crit} to experimental measurements for air entrainment when a silicon wafer plunges into silicon oils of various viscosities [105]. Similar to the findings of Marchand *et al.* [105], the 2D flow results show that highly viscous liquids decrease h_f, leading to thinner entrained air films (data appear to follow a weak power-law trend, e.g., $h_f \sim \chi^{1/2}$). Furthermore, predictions from the 2D flow model come within a factor of two of the experimentally measured air-film thicknesses.

Solutions from the 2D flow model also suggest that the elongated air film may form a capillary ridge prior to entrainment. Although these solutions lie along the unstable solution branch (see Figure 3.4c-e), similar interface features have been experimentally observed during the onset of liquid-film withdrawal [100]. In the case of air entrainment, one possibility is that the capillary ridge may become unstable in the transverse direction, as it does in related thin-film problems [143, 144, 145]. The transient dynamics of air-film entrainment are explored experimentally in Chapter 7.

Chapter 5

Linear Stability Analysis

5.1 Introduction

Systems with moving contact lines are often susceptible to interface instabilities that can be triggered by small perturbations to the steady flow state. Prior works have demonstrated these instabilities in the case where a liquid mass (surrounded by ambient air) spreads or translates along a substrate through a two-dimensional (2D) flow [143, 146, 145, 147, 148]. Flow disturbances along the width of the substrate ("spanwise" direction) cause the interface to become unstable, forming three-dimensional (3D) liquid fingers that elongate in the primary flow direction ("streamwise" direction). Many researchers have used linear stability (LS) analysis to model the onset of such phenomena, predicting the growth rate α and wavenumber k associated with dynamic contact line (DCL) instabilities. Furthermore, LS analysis can expose underlying physical mechanisms that influence the stability characteristics of dynamic wetting systems.

This chapter probes the stability of a liquid/liquid displacement system that is subjected to small-amplitude perturbations. An equiviscous ($\chi = 1$) system is considered where both receding and advancing fluid stresses influence interface dynamics, making this analysis distinct from prior works (e.g.,[68]) that only consider a viscous receding liquid. A numerical model is constructed by performing LS analysis with the QP approach developed in Section 2.2. (Note that although the QP approach fails when $\chi < 1$, QP solutions approximate 2D flow results well when $\chi \geq 1$, as demonstrated in Chapter 3). Solutions to the resulting linear stability model (LS model) describe

the rate α corresponding to exponential decay or growth of interface perturbations. In addition, the perturbation wavelength $(1/k)$ in the spanwise direction is varied to test the system's sensitivity to three-dimensional (3D) disturbances.

Ultimately, the LS model reveals that base states from stable solution branches of the QP model are linearly stable for all tested values of the wavenumber k. As anticipated, solutions become unstable to small disturbances as the solution path moves around the turning point at Ca^{crit}. The largest growth rate α is found when $k = 0$, indicating that liquid/liquid displacement is most sensitive to long-wave perturbations. This suggests that the onset of wetting failure occurs at $Ca = Ca^{crit}$ and may initially proceed (while perturbations remain small) through the unsteady elongation of a 2D liquid film.

The remainder of the chapter is organized by the following sections. Section 5.2 derives the LS model and discusses numerical techniques used for the analysis. Section 5.3 presents growth rates for different values of the wavenumber along base-state solution paths. In addition, analysis of the perturbation variables provides insight into the flow characteristics within different stability regimes. Section 5.4 summarizes results from the LS model and discusses the physical implications of the findings.

5.2 Methods

5.2.1 Governing Equations

The QP approach uses lubrication theory to reduce the 2D governing mechanics for fluid displacement (see Section 2.1) to a set of 1D differential equations. Essentially, steady-state solutions are produced from the QP approach through numerical integration of the following expression [98, 99]:

$$\frac{\mathrm{d}^2\theta}{\mathrm{d}s^2} = Ca\left(\frac{\mathrm{d}p}{\mathrm{d}x}|_{adv} - \frac{\mathrm{d}p}{\mathrm{d}x}|_{rec}\right) = F(h(s); Ca, \lambda), \tag{5.1}$$

where $F(h(s); Ca, \lambda)$ describes local normal forces pressure gradients) exerted by the fluid flow on the interface. Although Section 3.3.5 demonstrates that the QP approach fails to describe air/liquid systems, (5.1) compares favorably to full 2D models for liquid/liquid displacement over a wide range of system properties [98, 99]. Therefore, this chapter focuses on the case of equiviscous liquid displacement ($\chi = 1$), where the QP approach remains a good approximation of the 2D hydrodynamic model. (Note

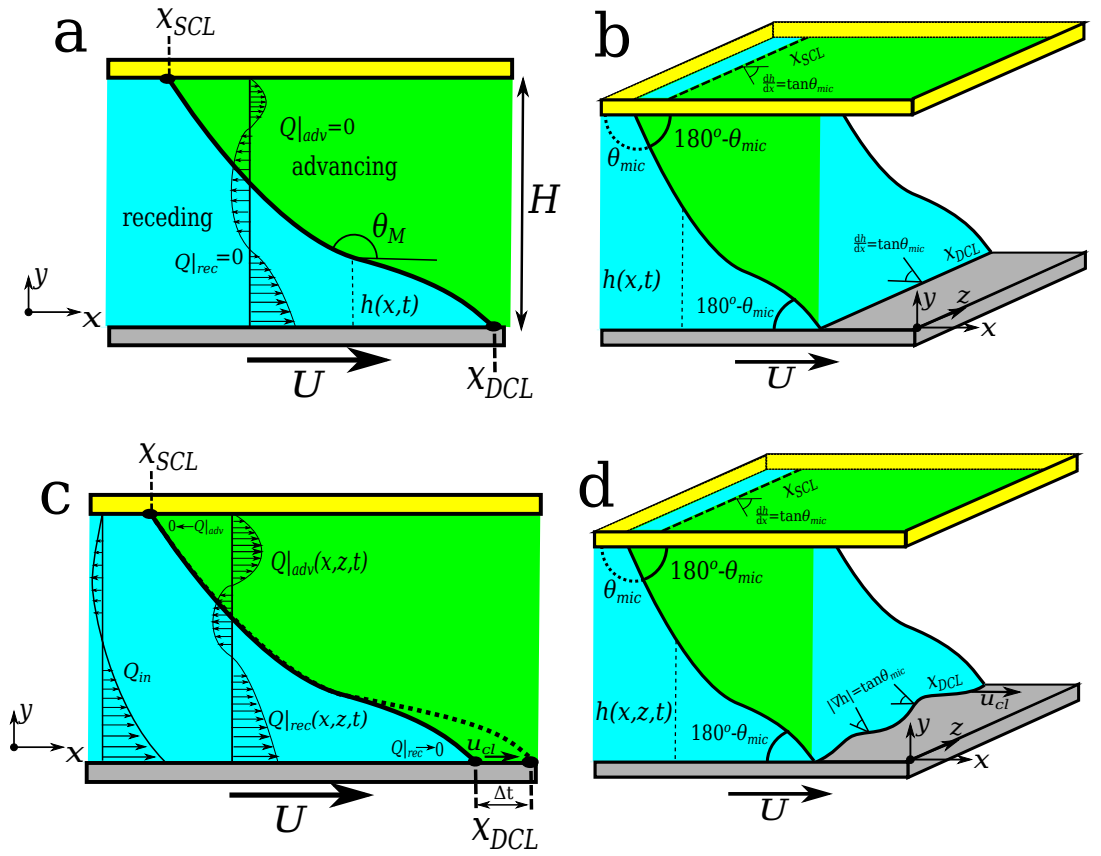

Figure 5.1: Schematic of equiviscous liquid/liquid displacement in a parallel-plate geometry with gap H. Two-dimensional (a) and three-dimensional (b) views are shown for the case of steady wetting. At the onset of wetting failure, the interface becomes unsteady and may elongate two-dimensionally (c) with contact-line speed u_{cl}, or through the growth of three-dimensional (d) perturbations at the DCL.

that (5.1) results from the general expression for he QP approach by substituting $\chi = 1$ in (2.17).)

The goal of the LS model is to probe whether or not small flow disturbance cause steady-state solutions from the QP approach to become unstable. This linear stability analysis includes perturbations in the spanwise direction z, which may cause the flow state to become three dimensional (3D). Anticipating a transition to unsteady liquid entrainment, the LS model must allow for motion of the dynamic contact line (DCL) and subsequent elongation of the fluid interface, as illustrated in Figure 5.1. Interface perturbations can significantly alter the size of the arc-length domain s, complicating the

numerical integration of (5.1). To avoid this complication, (5.1) can be rewritten solely as a function of Cartesian coordinates (using x instead of s as the independent variable) since small interface perturbations should minimally influence locations of the SCL ($\{x_{SCL}, 1, z\}$) and DCL ($\{x_{DCL}, 0, z\}$) until the system reaches a state of entrainment. The governing equations for the LS model are derived in this manner below.

Extending (5.1) to include the spanwise direction z, the governing equations for the QP approach can be expressed as follows:

$$\partial_x \kappa = \sec(\theta) Ca \left(\partial_x p|_{adv} - \partial_x p|_{rec} \right); \tag{5.2}$$

$$\partial_y \kappa = Ca \left(\partial_y p|_{adv} - \partial_y p|_{rec} \right). \tag{5.3}$$

Consistent with the derivation of the QP approach (see Section 2.2.1), the left-hand sides of (5.2) and (5.3) use the full (3D) curvature of the fluid interface using the height function $h(x, z, t)$:

$$\kappa = \frac{(\partial_x h^2 + 1)\partial_{zz} h - 2\partial_x h(\partial_{xz} h)\partial_{xx} h + (\partial_z h^2 + 1)\partial_z h}{(1 + \partial_x h^2 + \partial_z h^2)^{3/2}}, \tag{5.4}$$

where subscripts indicate the coordinates of differentiation (e.g., $\partial_x h = \frac{\partial h}{\partial x}$ and $\partial_{xx} h = \frac{\partial^2 h}{\partial x^2}$).

Similar to the steady QP formulation in (5.1), θ is defined as the interface angle formed in the xy-plane

$$\partial_x h = \tan(\theta). \tag{5.5}$$

Note that $\sec(\theta)$ augments the viscous-forcing term (right-hand side) in (5.2) because of the approximation $\partial x \approx \partial s$ used in the formulation of the QP approach. This *ad hoc* approximation is discussed in more detail in Section 2.2.1.

Pressure gradients differ from the steady case in (5.1) because interface perturbations trigger transient flow within the receding and advancing fluids, producing non-zero flow rates $Q|_{rec}$ and $Q|_{adv}$ defined by integration of the streamwise velocity u:

$$\int_0^h u_{rec} \mathrm{d}y = Q|_{rec}; \quad \int_h^1 u_{adv} \mathrm{d}y = Q|_{adv}. \tag{5.6}$$

The flow rates may vary as a function of space and time (i.e., $Q(x, z, t)$), but ultimately decay to zero if the system returns to a steady state. Therefore, (5.6) replaces the

zero-flux condition (2.15) used in the steady QP formulation. The remaining conditions applied to u_{adv} and u_{rec} are consistent with the steady QP approach derived in Section 2.2.1, where the velocity profile is specified in the lubrication limit by standard interface conditions at $y = h$, no-slip at $y = 1$, and Navier-slip along the substrate at $y = 0$.

Spanwise flow is governed by conditions that are analogous to the lubrication analysis for the streamwise velocity. First, both fluids adopt the familiar lubrication velocity profile

$$w = b_1(x, z, t) + b_2(x, z, t)y + \partial_z p \frac{y^2}{2}, \tag{5.7}$$

where b_1 and b_2 are variable coefficients that are specified by boundary conditions on w. Matching the conditions for u, the fluid is allowed to slip along the substrate ($y = 0$)

$$w = \lambda \partial_y w, \tag{5.8}$$

but obeys the no-slip postulate ($w = 0$) at the top plate ($y = 1$). (Note that this work only considers substrate velocity in the x direction.) Also, velocities and shear stresses are equal at the interface ($y = h$):

$$w_{adv} = w_{rec}; \quad \partial_y w_{adv} = \partial_y w_{rec}. \tag{5.9}$$

Similar to (5.6), non-zero flow rates $W|_{rec}$ and $W|_{adv}$ are permitted from the integration of spanwise velocity:

$$\int_0^h w_{rec} \mathrm{d}y = W|_{rec}; \quad \int_h^1 w_{adv} \mathrm{d}y = W|_{adv}. \tag{5.10}$$

Arguments involving mass conservation specify three of the four flow rates in (5.6) and (5.10). Since the substrate only moves in the x direction, it is assumed that there is zero net flux in the spanwise direction:

$$W|_{rec} + W|_{adv} = 0. \tag{5.11}$$

In contrast to (5.11), the streamwise flow is only restricted to a *constant* net flux:

$$\partial_x Q|_{rec} + \partial_x Q|_{adv} = 0. \tag{5.12}$$

Equation (5.12) allows for entrainment of the receding fluid following the substrate motion without demanding mass flux within the advancing fluid. More specifically,

Q_{rec} may be nonzero (Q_{rec} = constant) while $Q_{adv} = 0$, which would not be permitted by a constraint similar to (5.11).

Spanwise and streamwise velocities are coupled through the interface evolution equation

$$\partial_t h + \partial_x Q|_{rec} + \partial_z W|_{rec} = 0. \tag{5.13}$$

This expression guarantees that fluid mass does not cross through the interface at $y = h$. Instead the interface height evolves dynamically in response to spatial gradients in the receding flow rates. (Note that (5.13) could equivalently be written in terms of the advancing-fluid flow using (5.11) and (5.12).)

To specify the interface shape, boundary conditions must be applied at the static and dynamic contact line at x_{SCL} and x_{DCL}, respectively. At the DCL, a microscopic contact angle θ_{mic} is set by long-range intermolecular forces that interact with the fluid interface. Since the DCL may bend in response to flow disturbances, θ_{mic} is prescribed to the interface angle that is locally normal to the DCL shape:

$$|\nabla h| = \tan(\theta_{mic}) \ , \ h = 0 \text{ at } x = x_{DCL}. \tag{5.14}$$

When the DCL is straight and perpendicular to the substrate motion, (5.14) recovers the boundary condition used in the steady QP approach (i.e., substitution of θ_{mic} in (5.5)). For simplicity, it is assumed that the SCL remains uniformly straight with the same microscopic angle:

$$\partial_x h = \tan(\theta_{mic}) \ , \ h = 1 \text{ at } x = x_{SCL}. \tag{5.15}$$

Equations (5.14) and (5.15) contain four boundary conditions for $h(x, z, t)$. Although (5.2) produces a third-order partial differential equation (with respect to x), the extra condition is needed because the DCL may move, making x_{DCL} an additional unknown. (Periodic boundary conditions are assumed in the spanwise direction to integrate (5.3) with respect to z.)

Lastly, boundary conditions must be applied to the streamwise flow rates in (5.12). To ensure that mass is not transported through the contact lines, the following conditions must be satisfied:

$$Q|_{adv} \to 0 \text{ as } x \to x_{SCL}; \quad Q|_{rec} \to 0 \text{ as } x \to x_{DCL}. \tag{5.16}$$

Using the receding flow as an example, (5.16) allows for finite liquid flux entering the interface region (at x_{SCL}), so long as the Q_{rec} decays at x_{DCL}. Therefore, a liquid film may elongate and accumulate mass without permitting transport through the DCL.

5.2.2 Linear Stability Analysis

Linear stability analysis is conducted by assuming a small perturbation ϵ to the base-state solution from the QP approach. Variables describing the interface shape and fluid flow rates are expanded according to a normal-mode perturbation:

$$\begin{aligned} h(x,z,t) &\sim h_0(x) + \epsilon h_1(x) e^{\alpha t + ikz}; \\ \theta(x,z,t) &\sim \theta_0(x) + \epsilon \theta_1(x) e^{\alpha t + ikz}; \\ Q|_{rec}(x,z,t) &\sim \epsilon Q|_{rec,1}(x) e^{\alpha t + ikz}; \\ Q|_{adv}(x,z,t) &\sim \epsilon Q|_{adv,1}(x) e^{\alpha t + ikz}; \\ W|_{rec}(x,z,t) &\sim \epsilon W|_{rec,1}(x) e^{\alpha t + ikz}; \\ W|_{adv}(x,z,t) &\sim \epsilon W|_{adv,1}(x) e^{\alpha t + ikz}. \end{aligned} \tag{5.17}$$

Here, k is the wavenumber assigned to the spanwise perturbation and α is the exponential growth rate. The expansions in (5.17) are truncated to only include the base-state interface profile (e.g., $h_0(x)$) and $O(\epsilon)$ terms (e.g., $\epsilon h_1(x) e^{\alpha t + ikz}$). Note that all fluxes are equal to zero during steady displacement, which is the reason why base-state terms do not appear in the flow-rate expansions.

To proceed with the stability analysis, the expansion listed in (5.17) are inserted into the governing equations described in Section 5.2.1. To evaluate asymptotic behavior of the dynamics, each resulting expression is linearized to only keep leading order ($\sim \epsilon$) contributions from the perturbation. Although linearization greatly simplifies the differential equations, the analysis remains tedious and is outlined schematically in Figure 5.2. Note that the variable $\theta' = \partial_x \theta$ is introduced in Figure 5.2 in order to remove third-order derivatives (i.e., $\partial_{xxx} h$) from the analysis. This substitution is preferable because numerical errors increase with higher-order derivatives, as discussed in Section 5.2.3.

Ultimately, the linearized set of equations produces an ordinary differential equation

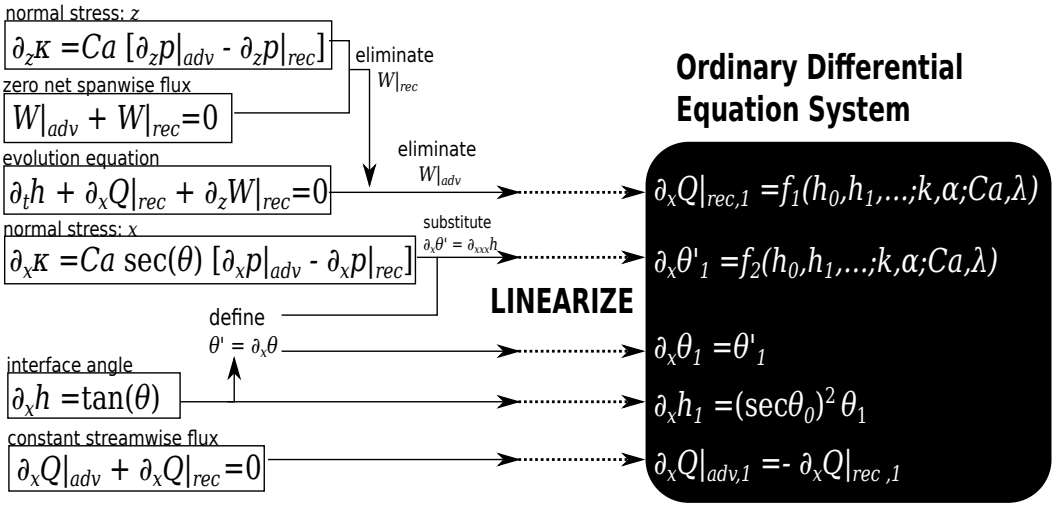

Figure 5.2: Schematic of procedure used to linearize governing equations for the LS model. The end result (black box) is set of first-order ordinary differential equations.

system that can be expressed as

$$\frac{\mathrm{d}\boldsymbol{X}}{\mathrm{d}x} = \boldsymbol{A}\boldsymbol{X}, \tag{5.18}$$

where $\boldsymbol{X} = \{Q|_{rec,1}\ \theta_1'\ \theta_1\ h_1\ Q|_{adv,1}\}^T$ and $\boldsymbol{A}$ is a 5×5 matrix with component entries A_{ij}. The non-zero entries are listed below:

$$\begin{aligned}
A_{11} &= -\frac{3Ca(-1 - h_0 + 2h_0^2 - 6\lambda)(1 + 2\lambda)\sec^2(\theta_0)}{(-1 + h_0)h_0^2[-h_0(1 + 2\lambda) + h_0^2(1 + 2\lambda) - 3\lambda(1 + 4\lambda)]};\\
A_{22} &= \theta_0' \tan(\theta_0);\\
A_{12} &= -A_{52} = -\frac{(-1 + h_0)^2 h_0^2(h_0 + 2h_0\lambda - h_0^2(1 + 2\lambda) + 3\lambda(1 + 4\lambda))k^2\cos(\theta_0)}{3Ca(1 + 8\lambda + 12\lambda^2)};\\
A_{13} &= -A_{53} = -\frac{\theta_0'(-1 + h_0)^2 h_0^2(-h_0(1 + 2\lambda) + h_0^2(1 + 2\lambda) - 3\lambda(1 + 4\lambda))k^2\sin(\theta_0)}{3Ca(1 + 8\lambda + 12\lambda^2)};\\
A_{14} &= -A_{54} = -\alpha + \frac{(-1 + h_0)^2 h_0^2(h_0 + 2h_0\lambda - h_0^2(1 + 2\lambda) + 3\lambda(1 + 4\lambda))k^4\cos(\theta_0)}{3Ca(1 + 8\lambda + 12\lambda^2)};
\end{aligned} \tag{5.19}$$

$$\begin{aligned}
A_{23} &= \sec^2(\theta_0)\{k^2 - (\theta_0')^2[-2 + \cos(2\theta_0)] - 9(\theta_0')^2\sin^2(\theta_0) - \partial_x\theta_0'\sin(2\theta_0)\\
&+ \frac{\tan(\theta_0)[3Ca(-1 + h_0 - 4\lambda + 2h_0\lambda) + (-h_0 + h_0^2)((h_0^2 - h_0)(1 + 2\lambda) - 3\lambda - 12\lambda^2)]}{(-h_0 + h_0^2)((h_0^2 - h_0)(1 + 2\lambda) - 3\lambda - 12\lambda^2}\\
&+ 3\cos(\theta_0)\sin(\theta_0)[\partial_x\theta_0' + 2(\theta_0')^2\tan(\theta_0)]\};
\end{aligned}$$

$$A_{24} = -3Ca\sec^2(\theta_0)\left[\frac{3h_0^4(1+2\lambda)^2 - 3\lambda(1+4\lambda)^2 - 8h_0^3(1+5\lambda+6\lambda^2)}{(-1+h_0)^2h_0^2(h_0+2h_0\lambda - h_0^2(1+2\lambda)+3\lambda(1+4\lambda))^2)}\right]$$
$$- 3Ca\sec^2(\theta_0)\left[\frac{h_0^2(7+37\lambda+34\lambda^2-24\lambda^3)+h_0(-2-6\lambda+32\lambda^2+96\lambda^3)}{(-1+h_0)^2h_0^2(h_0+2h_0\lambda - h_0^2(1+2\lambda)+3\lambda(1+4\lambda))^2)}\right];$$
$$- \frac{1}{2}\tan(\theta_0)\left[2\theta_0' k^2\right];$$

$$A_{25} = -\frac{3Ca(-3h_0+2h_0^2-6\lambda)(1+2\lambda)\sec(\theta_0)^2}{(-1+h_0)^2h_0[-h_0(1+2\lambda)+h_0^2(1+2\lambda)-3\lambda(1+4\lambda)]};$$
$$A_{32} = 1;$$
$$A_{43} = \sec^2(\theta_0);$$

Boundary conditions (5.14) - (5.16) must be used in order to integrate (5.18). In problems with moving interfaces, boundary conditions are commonly linearized around the location of the base-state interface when performing linear stability analysis. In this case, the DCL may freely move, which changes the location (x_{DCL}) of the boundary conditions in (5.14) and (5.16). Linearizing the conditions in (5.14) around the base-state position $x_{DCL,0}$ produces the following condition:

$$h_1 = \left(\frac{\partial_x h_0}{\partial_{xx} h_0}\right)\partial_x h_1. \tag{5.20}$$

Equation (5.20) essentially describes the relationship between interface height and slope (at $x_{DCL,0}$) that is necessary to preserve the microscopic angle θ_{mic} as the DCL moves a small distance away from its base-state position [146].

The remaining boundary conditions are homogeneous. Linearization of (5.16) around $x_{DCL,0}$ produces an equivalent condition:

$$Q_{rec,1} = 0 \text{ at } x = x_{DCL,0}. \tag{5.21}$$

Lastly, the conditions at the static contact line (see (5.16) and (5.15)) are satisfied by the base-state solution, leaving

$$Q_{adv,1} = 0,\ h_1 = 0,\ \theta_1 = 0 \text{ at } x = x_{SCL,0}. \tag{5.22}$$

5.2.3 Numerical Method

Integration of (5.18) is nontrivial, requiring a number of problem-specific techniques to obtain a meaningful solution. This section outlines the numerical procedure used to acquire the solutions presented in Section 5.3.

Since boundary conditions are applied at both ends of the domain (x_{SCL} and x_{DCL}), it would be convenient to treat (5.18) as a boundary-value problem (BVP) with a finite-difference solver. However, preliminary tests with the non-uniform finite difference method described in Section 2.2.3 showed solutions to be very sensitive to errors in the numerical differentiation of the base-state functions (specifically $\partial_x \theta_o' = \partial_{xx} \theta_o$). Since interface curvature becomes singular near the contact lines, high-order derivatives of the height function (recall that $\tan(\theta) = \partial_x h$) are susceptible to large errors that cause the BVP solver to diverge.

Instead, a shooting method is used to solve (5.18) in the manner of an initial value problem (IVP). IVP solvers integrate while taking sequential steps along the domain of the independent variable (x in this case), allowing for high resolution of system gradients with relatively low effort. In this work, a 4th-order Runge-Kutta method is used with adaptive stepping [149] to reduce numerical errors associated with steep interface gradients near the contact lines. Since errors primarily arise from derivatives of the base-state functions, the Runge-Kutta algorithm resolves the steady QP expression in (5.1) while adaptively stepping in x. Using this approach, the components of $\boldsymbol{A}$ in (5.19) may be accurately evaluated at each node along the interface. The shooting method typically uses ≥ 2000 with step size $\Delta x < 10^{-8}$ near the DCL, as demonstrated in Figure 5.3.

Integration of (5.18) begins at the SCL ($x = x_{SCL,0}$) and proceeds toward the DCL ($x = x_{DCL,0}$). However, a complete set of conditions for $\boldsymbol{X}$ are not known at the SCL. Therefore, a "shooting" procedure searches for boundary values at $x_{SCL,0}$ that will satisfy the known conditions at $x_{DCL,0}$ following integration of (5.18). The shooting method used for the LS model iteratively adjusts Q_{in}, which denotes the receding-fluid flow rate at $x = x_{SCL}$ (refer to Figure 5.1). The growth rate α is an additional unknown in (5.19) that is iterated simultaneously with Q_{in} (using a two-parameter secant method [149]) to satisfy boundary conditions (5.20) and (5.21) at the DCL. This method typically converges quadratically to a tolerance of 10^{-7}.

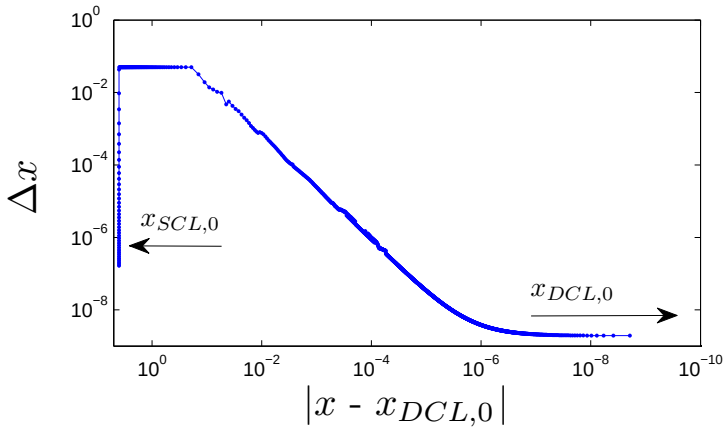

Figure 5.3: Discretization of the x-domain using the adaptive stepping with the shooting method.

Spanwise disturbances enter (5.18) through a small change to the interface curvature (recall that $\theta' = \partial_x \theta$) at the SCL

$$\theta_1' = \delta, \tag{5.23}$$

where δ acts as an arbitrary constant that scales the eigenfunction X. Using (5.22), (5.23), and Q_{in}, the boundary conditions at the SCL can be written as follows:

$$\boldsymbol{X} = \{Q_{in}\ \delta\ 0\ 0\ 0\}^T \tag{5.24}$$

Note that when $\delta = 0$ the LS model recovers the homogeneous solution: $\boldsymbol{X} = \boldsymbol{0}$ (including $Q_{in} = 0$) and $\alpha = 0$.

5.3 Results

5.3.1 Base-state Solutions

Steady-state solution paths are calculated using the QP approach described in Section 2.2. As an example, Figure 5.4 shows the solution path for equiviscous liquid displacement with $\theta_{mic} = 120^o$. The maximum interface angle θ_M increases with Ca until a turning point is reached at Ca^{crit}. At this point, the solution path transitions to an unstable branch where θ_M continues to increase, but at lower Ca. Interface profiles (see inset of Figure 5.4) reflect the macroscopic elongation of the interface as θ_M increases.

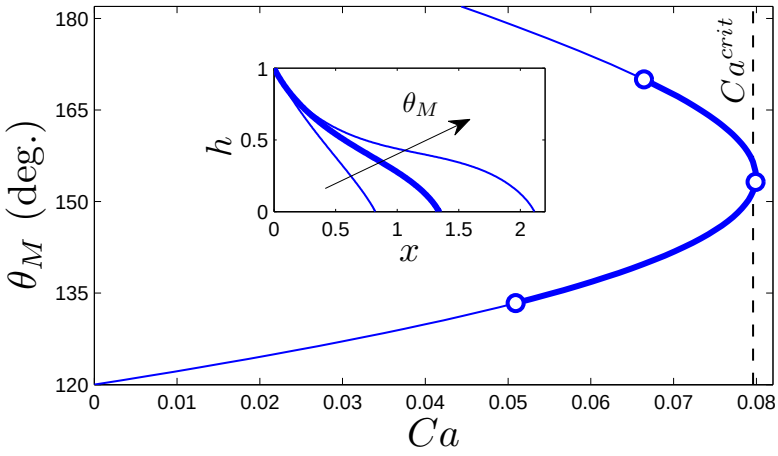

Figure 5.4: Base-state solution path for steady wetting obtained from the QP approach with $\theta_{mic} = 120^o$ and $\lambda = 10^{-1}$. The bold portion of the curve is evaluated with the LS model below.

The slip length λ and substrate wettability θ_{mic} influence the value of Ca^{crit}, but do not change the qualitative characteristics of the solution path shown in Figure 5.4. In each system, θ_M reaches 180^0 as the interface lengthens along the unstable branch, suggesting the transition from steady liquid displacement to unsteady liquid-film entrainment. Perturbations may trigger this transition prematurely, causing the system to jump between stable (lower branch) and unstable solutions (upper branch) at $Ca < Ca^{crit}$. The following section considers this possibility for small-amplitude perturbations using the LS model derived in Section 5.2.

5.3.2 The Dispersion Relation

Figure 5.5 plots the dispersion relation using the LS model and the base-state solution shown in Figure 5.4. Each curve represents the growth rate α as a function of Ca for different values of the wavenumber k. According to the normal-mode expansion in (5.17), $\alpha > 0$ leads to unstable growth of $O(\epsilon)$-amplitude perturbations. However, each curve reflects the stable decay of perturbations ($\alpha < 0$) along the stable branch, until the turning point at Ca^{crit}. Therefore, as postulated in Section 2.2.4, the turning point does indeed mark a change in the stability of liquid displacement.

Interestingly, Figure 5.5 shows that higher wavenumbers produce negative growth

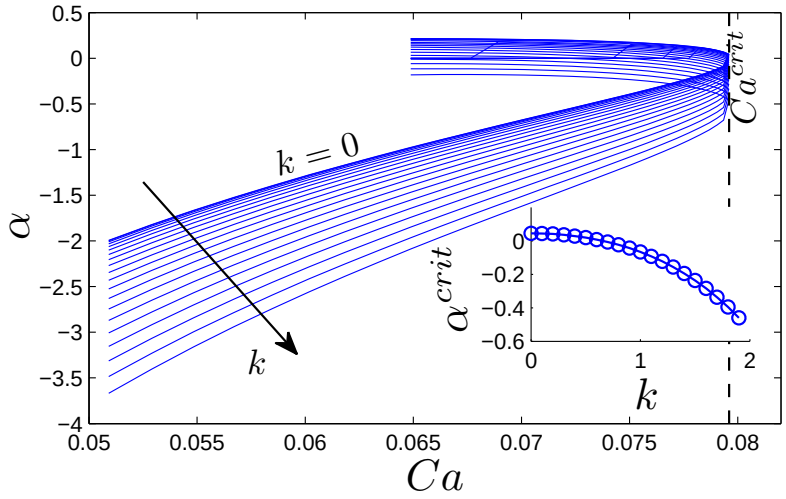

Figure 5.5: Dispersion relation obtained from the LS model for equiviscous liquid displacement using the base-state solution in Figure 5.4. Each curve represents a different perturbation wavenumber k. The inset figure plots the growth rate measured at $Ca \approx Ca^{crit}$ as a function of k.

rates with larger magnitudes. This means that spanwise perturbations with short wavelength ($1/k \to 0$) decay faster than long-wave perturbations ($k \to 0$). In fact, even solutions at Ca^{crit} and along the unstable branch become stable when $k \sim 1$. For instance, the inset of Figure 5.5 shows that the growth rate α^{crit} measured at Ca^{crit} decreases monotonically with increasing k.

Figure 5.6 plots the dispersion relation for different values of λ and θ_{mic}. Similar to the case discussed above, the curves in Figure 5.6 only reflect unstable perturbation growth along the unstable branch. Furthermore, smaller-wavelength disturbances are more stable in each case ($k = 0$). Overall, the stability characteristics of equiviscous displacement appear insensitive to changes in slip length and substrate wettability.

5.3.3 Physical Interpretation

As expected, perturbations to solutions along the unstable branch cause unsteady growth of a liquid film near the contact line. Figure 5.7 plots interface profiles obtained from the LS model assuming $\delta = 0.1$ in (5.22). Figure 5.7a-b show that the

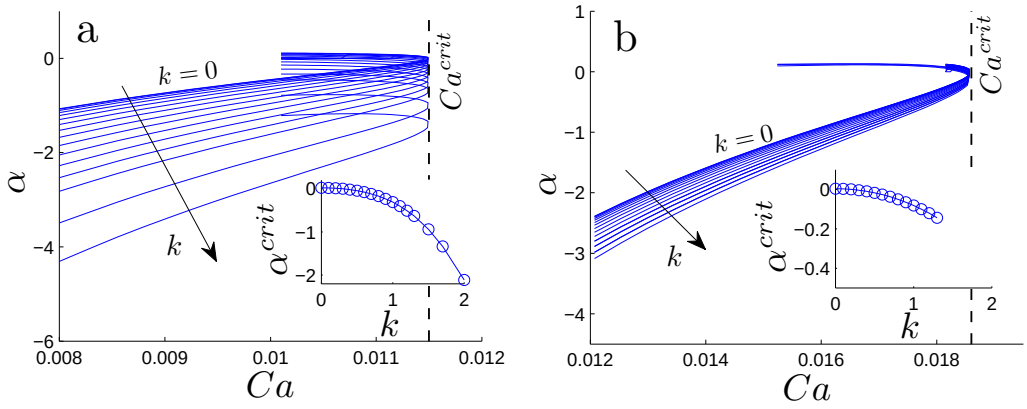

Figure 5.6: Demonstration of the insensitivity of the dispersion relation to different values of the slip length and substrate wettability: (a) $\lambda = 0.1$ and $\theta_{mic} = 150^o$; (b) $\lambda = 0.001$ and $\theta_{mic} = 120^o$. Each panel has analogous form to Figure 5.5.

interface disturbance h_1 becomes more pronounced near the DCL with the lengthening of the interface as $Ca \to Ca^{crit}$. This trend continues along part of the unstable branch, but h_1 changes suddenly signs once the interface becomes grossly elongated, as illustrated in Figure 5.7c.

Figure 5.8 plots flow characteristics corresponding the liquid displacement system shown in Figure 5.7. (Note that the solution path is plotted in Figure 5.8a). Interface behavior can be understood from an inspection of the x-component of fluid velocity at the DCL. Although perturbations typically move the DCL outside of the LS domain ($x_{DCL} > x_{DCL,0}$), the contact-line velocity u_{cl} can be estimated from linearization of the DCL boundary conditions that yield (5.20):

$$u_{cl} \approx -\alpha h_1 / \tan(\theta_0). \tag{5.25}$$

Figure 5.8b shows that u_{cl} becomes positive at the turning point, corresponding to movement of the DCL in the direction of substrate motion. Figure 5.8c illustrates that a positive mass flux ($Q_{in} > 0$) enters the receding-fluid domain at $x = x_{SCL,0}$ in order to support the growth of a liquid film with the downstream migration of the DCL. Therefore, the receding liquid transitions to a state of unsteady film elongation at Ca^{crit}, corresponding to the onset of wetting failure (note that $\alpha > 0$ near Ca^{crit} in Figure 5.8d.)

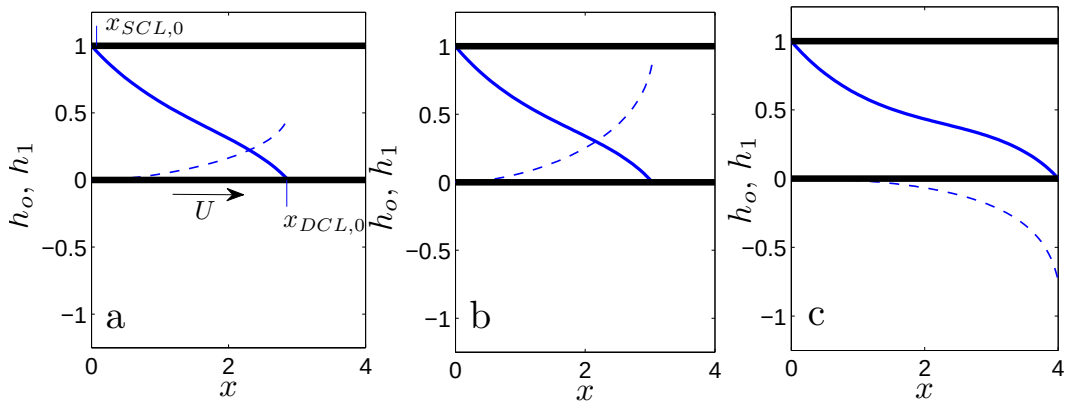

Figure 5.7: Interface profiles for the perturbed liquid/liquid interface at $t = 0$. Curves correspond to the base state h_0 (solid) and the $O(\epsilon)$ perturbation h_1 (dashed). Bold lines mark the solid surfaces in the domain. Profiles are plotted for (a) $Ca = 0.008$ on the stable branch, (b) $Ca = Ca^{crit}$, and (c) $Ca = 0.01$ on the unstable branch (see solution path in Figure 5.8a).

Surprisingly, the contact-line velocity diverges at some substrate speed corresponding to Ca^f (bold line in Figure 5.8), where $Ca^f \lesssim Ca^{crit}$. Consequently, small interface perturbations at this point lead to rapid motion of the DCL and growth of the liquid film. This result is similar to prior findings for the case of film deposition along a plate that is withdrawn from an infinite liquid bath. In these systems, steady liquid deposition (i.e., the Landau-Levich transition) occurs when the plate is withdrawn from the bath at some critical speed that is slightly less than Ca^{crit} [93, 96, 140]. In the liquid/liquid case studied here, the DCL has the strongest tendency to move along the substrate at Ca^f (see Figure 5.8d), suggesting that this point may correspond with a rapid transition from steady displacement to steady liquid deposition. Presumably, large-amplitude perturbations or non-normal transient modes could drive a displacement system onto the unstable branch at Ca^f, spurring nearly instantaneous film entrainment associated with the diverging contact-line speed.

Rather than the interface-elongation mechanism discussed above, perturbations cause unstable *retraction* of the fluid interface when $Ca < Ca^f$. Due to the relationship in (5.25), negative values of the interface perturbation function (h_1 in Figure 5.7c) produce contact-line velocity that opposes the substrate velocity. In fact, Figure 5.8 shows that both u_{cl} and Q_{in} are negative in the $Ca < Ca^f$ regime along the unstable solution

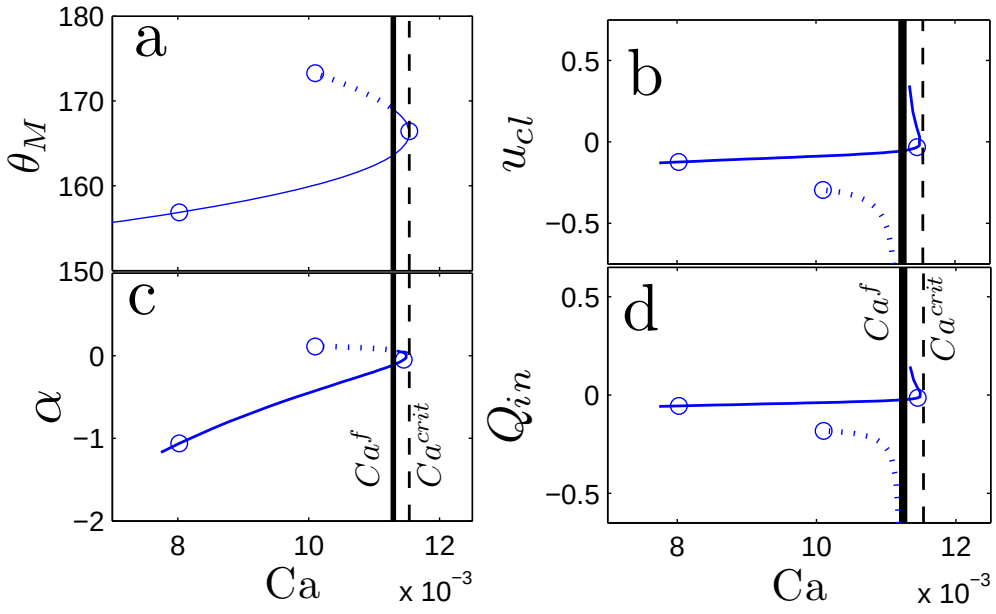

Figure 5.8: Characteristics of the perturbed liquid flow plotted as a function of Ca with $\lambda = 0.1$ and $\theta_{mic} = 150^o$. The base-state solution path (a) and values of the growth rate for $k = 0$ perturbation (c) are plotted against Ca. Corresponding values of the contact-line speeds (b) and receding-fluid flow rates (d) at the time of the initial perturbation ($t = 0$) are also shown. Dashed lines denote the regime of contact-line retraction, as discussed in the text. Symbols mark the location of solutions used to construct the interface profiles in Figure 5.7. The bold line indicates the capillary number Ca_f corresponding to diverging contact-line speed.

branch (indicated by dashed lines in Figure 5.8). Since $Ca < Ca^f$, capillary forces are strong enough to pull the DCL backward, resisting drag from the substrate. Although the LS method cannot fully predict this transient behavior, it remains possible that this interface retraction may return the system to the stable solution branch. Qualitatively, surface-tension forces act would act to stabilize the elongated interface in Figure 5.7c, causing the interface to evolve toward a steady-state displacement configuration similar to the profile shown in Figure 5.7a. Further investigation is needed to fully realize the transient dynamics in these liquid displacement systems.

Along the lower "stable" solution branch (see Figure 5.4), the liquid/liquid interface

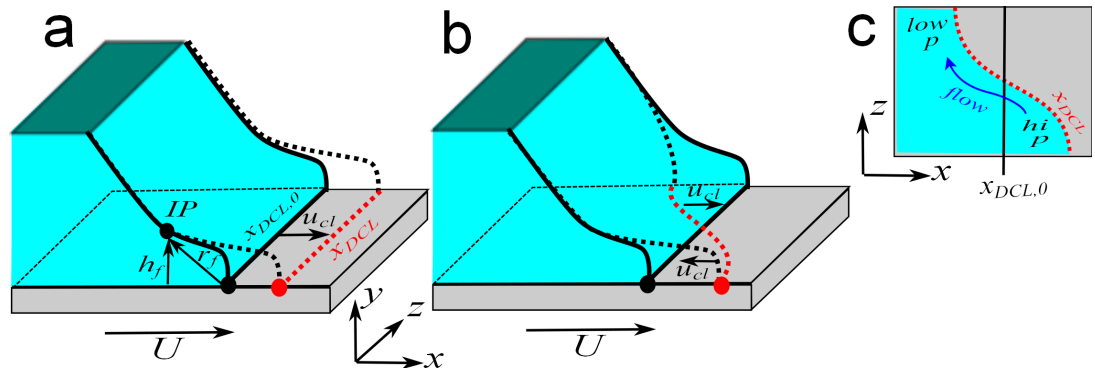

Figure 5.9: Illustration of (a) uniform and (b) periodic motion of the DCL. Panel (c) illustrates that capillary pressure drives flow to counteract the growth of periodic disturbances near the DCL.

remains linearly stable with respect to small periodic disturbances in the spanwise direction. In fact, perturbations decay more quickly as the spanwise disturbance increases in wavenumber k. Even the solutions along the "unstable" branch remain steady ($\alpha < 0$ in Figure 5.5). when the perturbation wavelength ($1/k$) is on the order or small than the interface length ($k \geq 1$). This result can be understood using the schematic in Figure 5.9 and the mechanism for dynamic wetting failure developed in Chapter 4. Crucial dynamics occur near the interface inflection point (IP) labeled in Figure 5.9a, where the local pressure gradient must scale as $1/h_f^2$ in order to pump the receding fluid away from the DCL. However, capillary-stress gradients near the DCL have a weaker dependence ($\sim 1/r_f$) on the IP location. As the interface uniformly elongates in response to perturbation of the DCL position (Figure 5.9a), the required pressure gradient exceeds the local capillary forces due to the changing IP position (i.e., $r_f/h_f^2 > 1$ in (4.5) in Section 4.2), ultimately leading to unstable growth of the liquid film.

Spanwise disturbances change this essential force balance near the DCL. Due to the periodic perturbations assumed in the LS model, the DCL becomes corrugated symmetrically around its base-state position $x_{DCL,0}$, as illustrated in Figure 5.9b. This generates sinusoidal curvature as the interface bends back and forth in the spanwise direction. Figure 5.9c illustrates a cross-section of the interface in the plane formed by the spanwise (z) and streamwise (x) coordinate near the DCL. Regions of concave curvature generate higher pressures than the convex regions, pumping liquid out of the "hills" and into the "valleys" formed by the DCL corrugation. This flow effectively

stabilizes the interface, returning the DCL to its base-state configuration at $x_{DCL,0}$

5.4 Conclusion

In this chapter, a linear stability (LS) model was developed to address the effect of small-amplitude perturbations on equiviscous liquid displacement along a moving substrate. Expanding upon the framework of the QP approach (see Section 2.2), the LS model accounts for the three-dimensional (3D), time-dependent displacement mechanics of two fluid phases. Linearization of the governing equations presents a challenging ordinary differential equation system that must be integrated numerically to determine the system's response to disturbances. Although comparable analysis has been conducted for similar systems with a single viscous fluid [143, 146, 68], this may be the first work to look at a LS model with two-fluid flow near a dynamic contact line (DCL).

Numerical results reveal that there is a linearly stable base-state solution branch corresponding to substrate speeds less than some critical value ($Ca < Ca^{crit}$). Normal-mode perturbations decay in this regime in a manner that is very similar to a prior theoretical work that considered the linear stability of a film deposited on a plate that is withdrawn from a liquid bath [68]. This work shows a consistent result for the case of liquid/liquid displacement and finds the dispersion relation to be fairly insensitive to wetting parameters, such as the slip length λ and microscopic contact angle θ_{mic}.

At a critical capillary number Ca^{crit}, the base-state solution path encounters a turning point and progresses onto an unstable branch, where the interface becomes unsteady when exposed to infinitesimal perturbations. Growth rates α are positive in this regime for long-wave perturbations (i.e., $k \to 0$ where wavelength $= 1/k$), resulting in unstable motion of the DCL. The liquid interface tends to be more stable to perturbations with shorter wavelength ($k > 1$). In this case, spanwise curvature of the interface produces capillary forces that efficiently pump the receding fluid away from the DCL. Consequently, short wavelength disturbances decay ($\alpha < 0$) near the DCL, even for base-state solutions that lie on the unstable branch.

At $Ca = Ca^{crit}$, long-wave perturbations ($k \to 0$) cause unsteady movement of the DCL in the direction of the substrate velocity, elongating a film of the receding film as it becomes entrained along the substrate. This suggests that wetting failure

during liquid/liquid displacement may proceed initially (while perturbations remain small) through the unsteady elongation of a 2D liquid film. While remaining on the unstable solution branch, the contact-line velocity diverges at some critical capillary number Ca^f that is just slightly less than Ca^{crit}, predicting instantaneous growth of the liquid film that might indicate a rapid transition to steady 2D film deposition [93, 96, 140]. At $Ca < Ca^f$, the DCL retracts unsteadily against the motion of the substrate. While retracting, the interface may reach a configuration consistent with a solution along the stable branch (at equivalent Ca), effectively stabilizing the displacement process. (Note that this final state would represent a different steady solution than the base state from the unstable branch.)

The transient characteristics of liquid/liquid displacement flows may be influenced by additional factors that lie beyond the analysis presented here. For instance, small interface perturbation can become amplified at the DCL during relatively short time intervals, exciting nonlinearities from the growth of non-normal eigenfunctions that are missed by classical (asymptotic) linear stability theory [145, 147]. However, further investigation is needed to determine whether or not the linearized problem developed in this chapter is non-normal in nature. Ultimately, a detailed analysis of the transient interface dynamics may require 3D simulations of unsteady liquid/liquid displacement [148].

Despite the similarity between liquid-film withdrawal ($\chi = \mu_{rec}/\mu_{adv} \gg 1$; [68]) and liquid/liquid displacement ($\chi \sim 1$; this work), experimental evidence indicates that air/liquid displacement ($\chi \ll 1$) may have very different stability properties. For instance, air entrainment is preceded by a 3D flow transition in which triangular air films grow from the DCL. We have shown in a novel experimental study (see Chapter 7) that entrained air-films appear to have a periodic distribution with size that is dependent on the system parameters (e.g, χ). Due to the very thin air flow near the DCL, air/liquid systems may be more sensitive to spanwise perturbations than the equiviscous-displacement case analyzed in this chapter. On the other hand, air/liquid displacement could still be linearly stable to spanwise disturbances, suggesting that air films are initially 2D (see Figure 5.9a) and become susceptible to 3D effects during transient film growth. Since the QP approach fails in the air/liquid regime ($\chi < 1$), linear stability analysis will need to be performed with the 2D flow model to resolve this

speculation. Similar stability analysis has been conducted with free-surface flows [150], although the presence of contact lines and two-fluid flow will likely make this a non-trivial computation. Reduced-order models, such as the 1D/2D hybrid FEM technique developed in Chapter 8, may be a useful tool for such analysis in future studies.

Chapter 6

Delaying the Onset of Wetting Failure via Meniscus Confinement

6.1 Introduction

Dynamic wetting is a prominent feature of many natural and industrial processes. Examples range from the everyday task of filling a glass of water to the complex processes of liquid coating deposition. The defining characteristic shared by dynamic wetting systems is the displacement of some fluid initially in contact with a solid surface by the wetting liquid. Dynamic wetting fails when this displacement process is incomplete, causing non-uniform coverage of the wetting liquid along the solid surface. The event of wetting failure can be catastrophic for coating processes which often must maintain stringent control of coating uniformity to ensure product integrity [8]. Moreover, the onset of wetting failure remains one of the primary obstacles to improving upon current production speeds within the coatings industry [9]. Despite the insights gained from industrial practice and our everyday experience with wetting behavior, questions persist about the fundamentals of dynamic wetting and the influence of global flow fields on the onset of wetting failure.

This chapter investigates the effect of system geometry on the onset of wetting failure. [i] Specifically, we are interested in confined systems where a wetting meniscus

[i] The results in this chapter were originally published in E. Vandre, M. S. Carvalho, and S. Kumar *Journal of Fluid Mechanics* 707 (2012) 496-520.

is bound between a substrate and another parallel surface, which is characteristic of numerous die-coating processes. In practice, the coating gap, H, is typically less than the capillary length ($H \sim 100$ μm) and should therefore influence the meniscus profile. However, there has yet to be a systematic study revealing how such spatial restrictions influence wetting behavior (e.g., wetting failure). To establish a foundation for understanding this problem, we devise a novel experimental apparatus that allows for direct visual comparison of confined and unconfined wetting systems. Using this apparatus, we show that confinement postpones the onset of wetting failure to higher substrate speeds, U, relative to an unconfined system. In an attempt to broaden our understanding of this phenomenon and its implications, we develop a hydrodynamic wetting model. Analysis conducted both with lubrication theory and application of the finite element method (FEM) demonstrate the success of the hydrodynamic model in capturing the observed confinement trends.

The remainder of the chapter is organized as follows. In section 2, we briefly review relevant background material. Our experimental methods and procedures are outlined in section 3. In section 4, we present our measured data and discuss experimental trends. Theoretical models are developed in section 5 using lubrication theory (§5.1) and two-dimensional (2D) two-phase flow solved using FEM (§5.2). Results from our experimental and theoretical work are discussed in section 6. In section 7, we summarize our results and discuss the implications of our findings for dynamic wetting theory.

6.2 Experimental Methods

6.2.1 Confinement System

Our experimental investigation of dynamic wetting failure was conducted with the laboratory-scale coating apparatus depicted schematically in figure 6.1. This system consists of two rolls stationed within a reservoir of the wetting liquid with exposure to an ambient air environment. The front roll functions as a continuous plunging substrate as it rotates into the liquid bath. The back (metering) roll acts in series with a squeegee to dry the substrate surface upstream of the wetting meniscus. Each roll is a chrome-plated steel cylinder (American Roller Company) that measures 50 cm in length and 20 cm in diameter with surfaces characterized by a roll run-out of 1 μm. A variable-speed

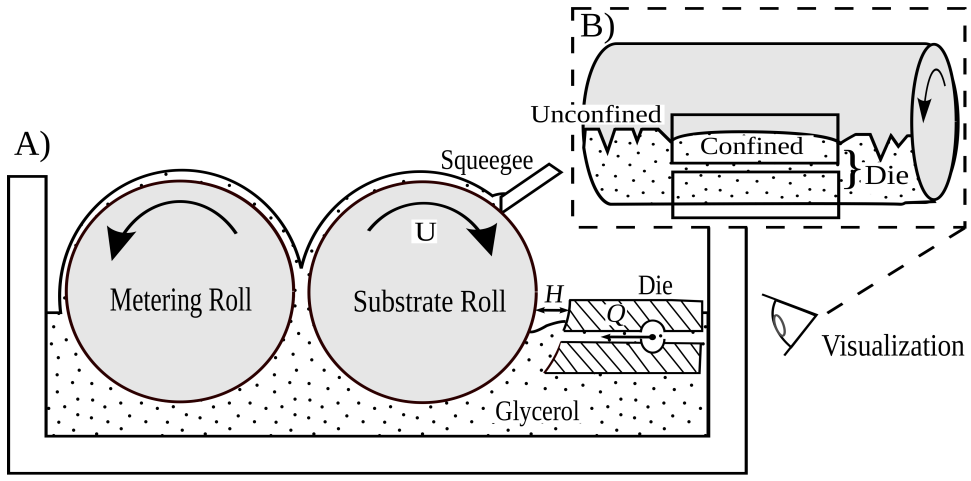

Figure 6.1: Schematic of the experimental coating apparatus. The side view (A) shows the substrate roll dried by the metering roll and squeegee as it rotates at speed U into the glycerol bath. A coating die provides a confinement gap, H, and feed flow rate Q along a portion of the substrate length. The visualization field (B) simultaneously includes the confined and unconfined wetting regions.

DC motor (Pacific-Scientific) controls the rotation speed to increments of 3 mm s^{-1}.

A coating die sits in close proximity to the roll to provide meniscus confinement along a portion of the wetting line. To allow for flow visualization and geometric flexibility, the die construction features a mobile upper block and a stationary base cast from transparent acrylic blocks. The die face matches the curvature of the roll to provide a nearly uniform gap between the confinement surface (die face) and roll surface. Clamps attached to the outer tank walls secure the position of the stationary base to prevent the die from moving during operation of the rolls. The mobile upper block allows the confinement gap (H) to be easily adjusted between runs without compromising the overall alignment of the die with respect to the roll surface. The approximate length and height of the assembled die are 15 cm and 5 cm, respectively, and this forms a confinement region that covers under 10% of the roll circumference and less than half of its length.

In addition to confining a local region of the wetting meniscus, the coating die also provides a feed flow (Q) to aid in positioning the confined wetting meniscus between the roll and the upper die block. As noted by [151],[8], and [88], the flow within the small gap generates large drag forces that pull the meniscus in the direction of the substrate

μ_{liq}(cP)	σ(mN m^{-1})	$\theta_{s,roll}$(deg.)	$\theta_{s,die}$(deg.)	ρ(kg m^{-3})
120 ± 10	64 ± 1	70 ± 10	87 ± 2	1200

Table 6.1: Physical properties for glycerol. A Brookfield viscometer (DV-II) and Krüss digital tensiometer (K10ST) are used to measure μ_{liq} and σ, respectively. A Kruss goniometer (DSA) is used to measure static wetting angles on the die surface ($\theta_{s,die}$). Digital photographs of glycerol droplets resting on top of the substrate roll are analyzed with ImageJ software [153] to estimate $\theta_{s,roll}$. Density is approximated from [152].

motion. In our system, this amounts to the disappearance of the meniscus from our visualization field as it is displaced to the exit of the confinement channel toward the underside of the plunging roll. The supplementary die feed, which we control with a gear pump (Nichols Zenith), serves to replenish liquid within this confined wetting region and stabilize the position of the confined wetting meniscus.

6.2.2 Material Properties

Glycerol was selected as the wetting liquid for this study because of its Newtonian behavior and low vapor pressure at room temperature. These favorable properties eliminate the effects of complex rheology and evaporation. In addition, glycerol's viscosity is easily adjusted through dilution with deionized water or concentration with 99.7 % pure glycerin. By controlling the glycerol composition, we are able to compensate for any changes in ambient temperature or humidity to maintain our liquid viscosity within 10% of 120 cP as measured by a Brookfield viscometer. A summary of the measured material properties of glycerol is reported in table 6.1. (Note: we assume the glycerol density $\rho \approx 1200$ kg m^{-3} [152] when estimating the capillary length, $l_{cap} = \sqrt{\sigma/\rho g}$).

6.2.3 Operating Procedure

Our experimental procedure follows a tiered structure in which an experimental series is composed of multiple runs that are defined by the same governing steps. This process is designed to minimize errors that may accrue from some of the crude aspects of the system design. The following outline highlights some of the key components of our procedure:

- **Experimental series**: Shims are used to find parallel alignment between the stationary die base and the substrate roll. Clamps are applied to fix the base position and the shims are removed. Approximately 15 confinement runs (one per confinement gap) are conducted before resetting the die alignment.

- **Confinement run**:

  (i) A confinement gap is chosen at random from 15 possibilities spanning $H \in$ [0.1 mm, 10 mm]. The gap is measured between the upper die block and the substrate surface using shims for $H < 2$ mm and a ruler for larger gaps. Clamps hold the upper block in position and prevent the gap from widening during operation.

  (ii) Glycerol is added to the reservoir until the die is submerged (approximately 16 L). The glycerol is mixed for approximately 30 minutes within the tank to eliminate any density gradients within the reservoir.

  (iii) Data acquisition begins at low roll speed (≈ 13 $\mathrm{cm\,s^{-1}}$). Feed flow from the die is adjusted to place the confined wetting meniscus at a desired position between the roll and the upper die block. After observing steady-state for at least 3 minutes, the roll speed is incremented in 1 $\mathrm{cm\,s^{-1}}$ steps. The die flow rate is increased in parallel with roll speed to maintain a constant meniscus position. While waiting for steady-state, the confined and unconfined wetting lines are observed simultaneously for the characteristic air vees associated with wetting failure.

  (iv) The critical speed U^{crit} is recorded once the wetting line spontaneously forms a sawtooth meniscus. This critical point is observed at distinct speeds for both the unconfined and confined wetting regions, yielding two critical capillary numbers (Ca_u^{crit} and Ca_c^{crit} , respectively) recorded for each run. Following wetting failure, the roll speed is reduced to a sub-critical value and then slowly ramped toward wetting failure to test for hysteresis and repeatability of the critical speed. Less than 1% uncertainty is reported for values of Ca_c^{crit} during each run.

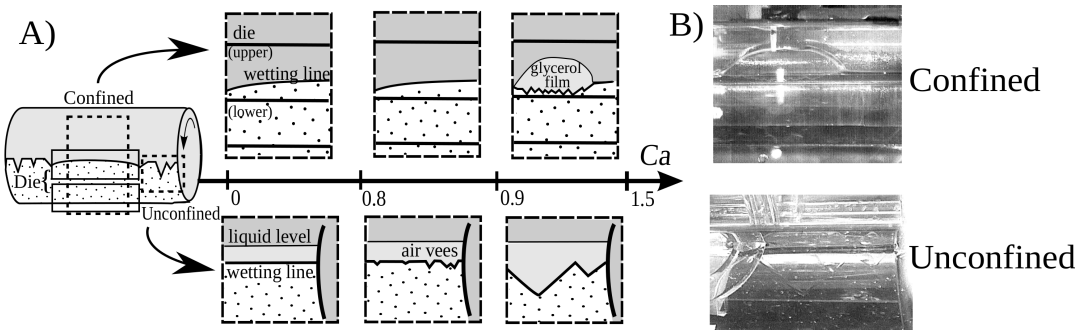

Figure 6.2: Visualization data comparing confined and unconfined wetting. (A) Sketches illustrate meniscus behavior as a function of Ca. At low Ca, both wetting lines appear smooth. The unconfined region adopts a sawtooth meniscus characteristic of wetting failure at $Ca \approx 0.84$ (see figure 6.3 for Ca_u^{crit} data). Confined wetting failure generally occurs at higher speeds ($Ca_c^{crit} \geq Ca_u^{crit}$) and a glycerol film outlines the resulting sawtooth meniscus. Photographs (B) are shown for each wetting failure state.

The experimental series was repeated three times to obtain a suitable sample of critical speeds at the various confinements.

6.3 Experimental results

6.3.1 Unconfined wetting failure

The unconfined wetting region displays a sharp transition to wetting failure at some critical speed of the substrate. At this speed, triangular serrations form with periodic distribution along the wetting line. The resulting air vees vary in dimension with a trend toward elongation as substrate speed exceeds the critical point. In this study, we focus on the macroscopic event of wetting failure and, therefore, associate Ca_u^{crit} with the point at which air vees are clearly visible (on the order of 1 mm) and form a prominent sawtooth meniscus along the entire wetting line, as shown in figure 6.2. Disparity between the appearance of the first air vee (usually nucleated near the roll edge) and our definition of macroscopic wetting failure accounts for less than 1% uncertainty in Ca_u^{crit}.

Values of Ca_u^{crit} vary from day to day due to imperfect control of liquid viscosity, μ_{liq}, and ambient conditions (e.g., temperature and humidity). During our confinement runs, we adjust the glycerol composition to tolerate 10% uncertainty for μ_{liq}, which

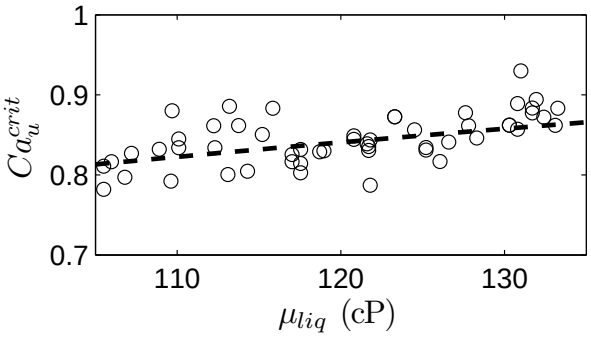

Figure 6.3: The dependence of Ca_u^{crit}on glycerol viscosity, μ_{liq}. Each symbol represents a critical speed recorded during a distinct confinement run. The dashed line is fitted from (1.7) using $b = \frac{1}{4}$ and matching the mean critical capillary number ($Ca_u^{crit} = 0.84$) at $\mu_{liq} = 120$ cP.

generates a narrow distribution of fluid properties tested over the entirety of the study. In Figure 6.3, our recorded critical speeds are well described by the correlation in (1.7). This agreement suggests that the slight variability in μ_{liq} is primarily responsible for any run-to-run variation seen in critical speed. Note that any effects from variable fluid properties are effectively removed from our analysis because comparisons are made only between confined and unconfined data observed during the *same* run.

6.3.2 Confined wetting failure

In addition to the unconfined region, the wetting meniscus also exists within a confined region between the die and the substrate that spans approximately half of the total length of the wetting line. Feed flow from the die is used to locate the confined meniscus at a steady position while roll speed is increased toward the limit of wetting failure. It is found that Q must increase proportionally with Ca to counteract the increasing drag generated by the moving substrate, as is case for the upstream bead of a slot-coating flow [151]. Figure 6.4 demonstrates the linear correlation between flow rate and Ca while holding a constant meniscus position.

Similar to results from the unconfined wetting region, a single critical capillary number, Ca_c^{crit}, characterizes the onset of wetting failure for a given confinement. Upon breaching this threshold, the previously uniform and smooth wetting line spontaneously deforms to yield the sawtooth structure shown in figure 6.2. This transition commonly

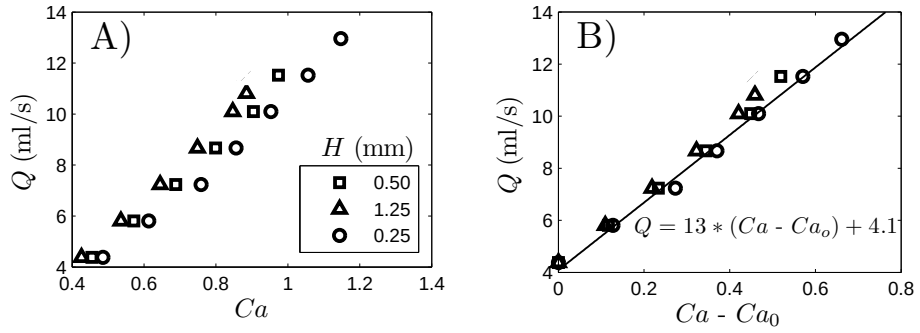

Figure 6.4: Feed flow rate as a function of Ca needed to maintain steady a meniscus position (approximately 1 cm above the feed slot). Plot (A) shows the raw data, while (B) shifts the data along the horizontal axis by Ca_o, the capillary number corresponding to $Q \approx 4.1$ for each data set. The inset equation provides the linear fit of the shifted data.

occurs on the order of 5 seconds after reaching the critical speed and can easily be visualized by eye. In fact, the presence of the confinement die emphasizes the resulting sawtooth meniscus as a thin film of glycerol is displaced from the wetting line and forced back against the die surface to form a circular outline around the site of wetting failure.

Confined critical speeds display marginal hysteresis when approaching the wetting-failure transition from speeds above and below Ca_c^{crit}. However, hysteretic behavior proved difficult to reproduce within our system and usually resulted in less than 1% change in Ca_c^{crit}values. Therefore, wetting failure in our system appears to have mild path dependence in comparison to the reports of [114]. Within the remainder of work, we account for this hysteresis in the experimental uncertainty associated with Ca_c^{crit}.

Despite the importance of feed flow for locating the wetting meniscus, adjustments to feed rate are ineffective in preventing or reversing the transition to wetting failure. This means that the birth of a sawtooth meniscus occurs at a single critical speed independent of the flow rate applied just prior to deformation of the steady wetting meniscus. Furthermore, manipulation of the feed rate following wetting failure does not alter the presence or scale of the air vees, but only displaces the sawtooth meniscus position along the substrate. As a corollary to this observation, the meniscus position within our confinement gap has negligible influence on Ca_c^{crit}. Therefore, feed flow influences only the position of the meniscus, implying that confinement alone is responsible for

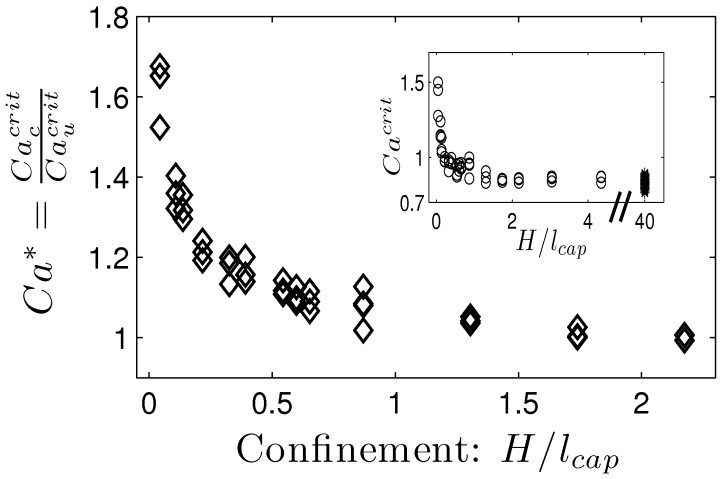

Figure 6.5: The critical speeds of wetting failure as a function of dimensionless confinement gap. Ca^* is calculated from Ca_c^{crit} and Ca_u^{crit} data recorded during the same confinement run. Each diamond symbol represents a distinct run. The inset figure displays the comprehensive set of Ca^{crit} data points obtained from the confined (circles) and unconfined (asterisks) wetting regions.

any effect on wetting failure (relative to the unconfined region).

Wetting failure within the confined region consistently occurs at equal or greater speeds than that observed along the unconfined portion of the roll, as demonstrated qualitatively by the illustrations of figure 6.2. Since data were obtained from unconfined and confined wetting failure simultaneously, it is convenient to define an enhancement factor, Ca^*, by the ratio of Ca_c^{crit} and Ca_u^{crit} taken from the same run. Figure 6.5 clearly shows this fractional increase in critical speed due to confinement becomes significant as the gap (H) between the die and substrate decreases. Furthermore, upon inspection of the data one may imagine a trend of diverging Ca^* as $H \to 0$. However, due to uncertainty associated with setting gaps with very thin shims, we are not able to reliably decrease H beyond a nominal gap of 100 μm . Even with these limitations we observe a 70% increase in critical speed at our smallest gaps. As the gap is widened to the order of the capillary length ($l_{cap} = \sqrt{\sigma/\rho g} \approx 2.3$ mm), the confinement effect diminishes and Ca^* approaches unity. Gaps in excess of twice l_{cap} produce Ca_c^{crit} which are not statistically distinct from Ca_u^{crit}, reflecting an effectively unconfined system along the entire length of the roll.

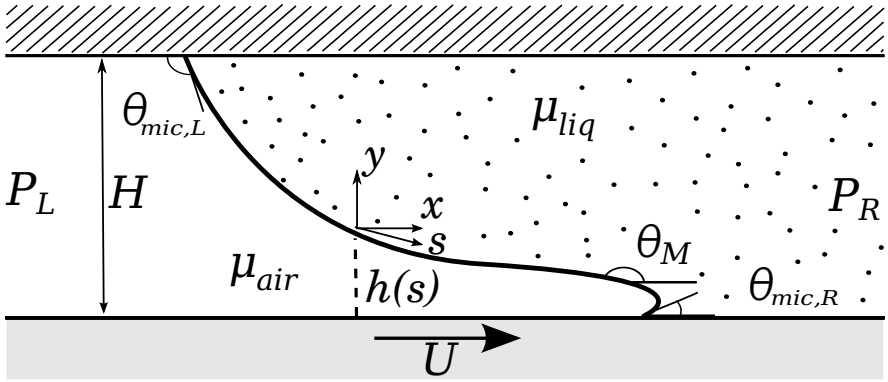

Figure 6.6: Idealization of the confined air-liquid dynamic wetting system. The fluid phases are separated by an impenetrable interface at $h(s)$ which is bound within the gap H formed between two parallel plates. The top plate is a stationary confinement surface and the bottom plate is the substrate moving with velocity U.

6.4 Theoretical Modeling

6.4.1 The Hydrodynamic Model

Our experimental results clearly demonstrate that the onset of wetting failure is influenced by the outer length scale associated with the wetting meniscus. This observation necessitates a theoretical description which emphasizes the role of hydrodynamic contributions in dynamic wetting. We postulate wetting failure to arise from a lack of 2D steady-state solutions past a critical capillary number. Beyond this critical point, the system must transition to transient or higher-dimensional flow, which is consistent with observations of wetting failure.

The model we adopt idealizes our system as two immiscible fluids contained between parallel plates. One plate moves at constant velocity, U, to represent our substrate, while the other is fixed to model the confinement-die surface. Feed flow is excluded from the model due to its negligible impact on Ca_c^{crit} values observed experimentally. Thus, a pressure drop ($\Delta P = P_L - P_R$) applied across the length of the channel acts to specify the position of the fluid interface as it balances with drag exerted from the moving plate. A schematic of our model is illustrated in figure 6.6.

The Navier-Stokes equations govern the velocity, $\boldsymbol{v}$, and pressure, p, within each fluid. Here we make a couple of simplifying assumptions:

(i) viscous stresses dominate over inertial contributions, which results in the creeping-flow equations (equations herein are shown in dimensionless form):

$$\boldsymbol{\nabla} \cdot \boldsymbol{v} = 0, \quad \boldsymbol{\nabla} p = \nabla^2 \boldsymbol{v}; \tag{6.1}$$

(ii) gravitational forces have negligible influence on confined wetting failure.

The characteristic dimensions of H, U, and $\mu U/H$ are used in the construction of (6.1) to scale length, velocity, and pressure, respectively.

Although creeping flow neglects the bulk Reynolds number ($Re = \rho U H/\mu$) associated with our experiments ($Re_{liq} \sim 1$, $Re_{air} \sim 10$), it captures the divergent wetting-line stress that characterizes hydrodynamic wetting models [65]. We assume that these steep viscous stresses play a significant role in the onset of wetting failure, making (6.1) a good starting point for our model. The second approximation follows from inspection of the characteristic Bond ($Bo = \rho g H^2/\sigma$) and Stokes numbers ($St = \rho g H^2/\mu U$) for our system, which are both significantly less than $O(1)$ within the data range that reflects a prominent confinement effect ($H < 1$ mm, $U > 0.4$ m s^{-1}). Gravity becomes important as the system becomes unconfined (as implied by our scaling of the experimental data with capillary length), but should not be needed to model the general confinement trend.

Interface curvature κ is governed by a balance of capillary and viscous stress:

$$\kappa = Ca \left[\boldsymbol{n} \cdot \boldsymbol{T} \cdot \boldsymbol{n}|_{air} - \boldsymbol{n} \cdot \boldsymbol{T} \cdot \boldsymbol{n}|_{liq} \right], \tag{6.2}$$

where $\boldsymbol{T}$ is the Newtonian stress tensor and $\boldsymbol{n}$ is the normal vector at the interface. In addition, the standard tangential stress balance and kinematic condition are applied along $h(s)$, which defines the interface height as a function of the arc-length coordinate s (see Section 2.1).

Terminal points of the interface take on special boundary conditions to account for the presence of wetting lines. At the fixed plate, the wetting line is static due to no-slip along the stationary surface:

$$\boldsymbol{v} = 0. \tag{6.3}$$

A slip condition must be applied along the moving substrate to avoid multi-valued velocity at the dynamic wetting line [66]. We choose to use a Navier condition [72]:

$$u - U = \beta[\boldsymbol{n} \cdot \boldsymbol{T} \cdot \boldsymbol{t}] \quad ; \quad v = 0. \tag{6.4}$$

$\chi = \mu_{air}/\mu_{liq}$	$\theta_{mic,R}$(deg.)	$\theta_{mic,L}$(deg.)
1.5×10^{-4}	70	90

Table 6.2: Material parameters used to model the air-glycerol system. Parameters are estimated from the measured data shown in table 6.1. Air viscosity (μ_{air}) is assumed to be 1.8×10^{-2} cP [154].

where $\beta = l_{slip}/H\mu$. The slip length, l_{slip}, characterizes the magnitude of slip behavior and serves as a fitting parameter. Although we apply (6.4) along the entire substrate, the fluid velocity rapidly approaches the no-slip limit ($u \to U$) at distances $\sim l_{slip}$ away from the wetting line. We assign the same fitted slip length to both fluids, and, therefore, the system geometry is described by a single length-scale ratio $\lambda = l_{slip}\ /H$.

The interface slope must also be prescribed as a boundary condition at each wetting line. We assume the microscopic interface angle, θ_{mic}, equals the static contact angle, θ_s [55]. Our assumption of constant θ_{mic} implies that the dynamic character of the contact angle arises from an *apparent* contact angle, θ_M, which is removed from the actual wetting line (and θ_{mic}) by some finite distance. For this study, we define θ_M as the maximum interface angle in proximity to the dynamic wetting line ($h(s) < H/2$). In section 6, we discuss the impact of θ_{mic} on our model predictions. Material parameters for the air-glycerol system, including microscopic angles, are listed in table 6.2.

The creeping-flow equations and associated boundary conditions generate a highly nonlinear free-boundary problem. We analyze the resulting equation set through two different approaches:

(i) a non-uniform finite-difference method to evaluate a 1D lubrication-type approximation of the governing equations,

(ii) a Galerkin finite element method (FEM) with elliptic mesh generation to evaluate the full 2D free-boundary problem.

6.4.2 QP Approach

Lubrication-theory-based models commonly provide insight into the mechanics of complex flows with a major reduction in computational effort in comparison to full 2D or 3D calculations [120]. For example, a quasi-parallel (QP) model was developed by [98]

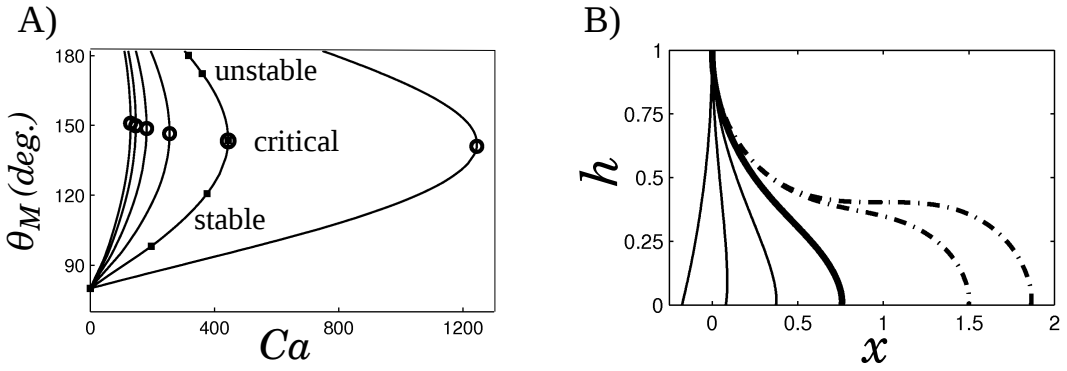

Figure 6.7: Steady-state solutions for the air-glycerol wetting system ($\chi = 1.5 \times 10^{-4}, \theta_{mic,R} = 70^o, \theta_{mic,L} = 90^o$) obtained with the QP approach. (A) Solution families show the change in θ_M with Ca for different values of λ. Going left to right, each curve increases in λ with values of $10^{-6}, 10^{-5}, 10^{-4}, 10^{-3}, 10^{-2}$, and 10^{-1}, respectively. Bold circles indicate the critical point for each curve. (B) Interface profiles correspond to square symbols along the $\lambda = 10^{-2}$ solution family in (A). The solid and dot-dashed lines represent stable and unstable steady-state profiles, respectively. The bold curve shows the critical interface.

to investigate wetting failure in equiviscous liquid-liquid systems. Results therein reveal the natural appearance of Ca^{crit} from turning points in families of steady-state solutions. The remainder of this section considers an adaptation of this lubrication-type model for our confined air-liquid system. Details of the model derivation and numerical methods are discussed in Section 2.2.

To model our experimental system we use air-glycerol material parameters listed in table 6.2. The appropriate range of the length-scale parameter, λ, is initially unknown because l_{slip} serves as a fitting parameter for our data. Therefore, our fitting process involves calculating Ca^{crit} for a wide range of length scale ratios ($\lambda \in [10^{-7}– 10^{-1}]$) and comparing against experimental values for the enhancement factor, Ca^*. Figure 6.7 shows the resulting solution families for the QP approach with an illustration of interface profiles obtained along one solution trajectory. Critical point data are listed in table 6.3.

The following definition is used for the computational data:

$$Ca^* = \frac{Ca^{crit}(\lambda)}{Ca^{crit}(\lambda_o)} \tag{6.5}$$

where $Ca^{crit}(\lambda)$ is the critical capillary number as a function of confinement ($\lambda =$

λ	$H(\mu\text{m})$	Ca^{crit}	$\theta_M^{crit}(deg.)$
10^{-1}	0.5	1245	142
10^{-2}	5	443.9	144
10^{-3}	50	255.3	147
10^{-4}	500	181.0	149
10^{-5}	5000	145.5	151

Table 6.3: Critical point data extracted from QP analysis of the air-glycerol system (see figure 6.7). Values for the confinement gap, H, are calculated from $\lambda = l_{slip}/H$ assuming l_{slip}= 50 nm.

l_{slip}/H), while $Ca^{crit}(\lambda_o)$ represents the critical speed at an unconfined limit corresponding to H_o. To gain insight into this unconfined limit, recall that the experimental data shows Ca^* to level off to unity when the confinement gap exceeds twice the capillary length; hence, $H_o \approx 5$ mm marks the "unconfined" limit where our simplified Stokes flow analysis is expected to break down due to the increased importance of body and inertial forces. Using this empirical value for H_o, we can extract l_{slip} from the best fit of λ_o for our data ($\lambda_o = l_{slip}/H_o$).

Results from the quasi-parallel model display a confinement trend consistent with the experimental Ca^* data for a wide range of selected λ_o, as shown in figure 6.8. The best quantitative agreement is obtained when selecting λ_o within a range of 5×10^{-6}– 2.5×10^{-5}, which places l_{slip} on the order of 50 nm. This fitted slip length seems reasonable in comparison to the magnitude of slip parameters tabulated from other wetting systems with similar material components, which typically report l_{slip} values between 1 nm and 100 nm [1, 74]. Figure 6.9 demonstrates the close agreement between the enhancement factor determined with the QP approach and the experimental values reported here.

Despite the QP approach's ability to match the experimental Ca^* trend, there is a notable discrepancy when considering the absolute value of the computed critical capillary numbers. Figure 6.9 reveals Ca^{crit} to be overestimated by multiple orders of magnitude by the QP approach. The magnitude of this error is shown to be fairly insensitive to the choice of fitting parameter λ_0, and is, instead, an inherent problem of the model. Further investigation reveals another peculiarity associated with the critical interface profiles predicted by the model. Figure 6.7 shows that apparent dynamic angles

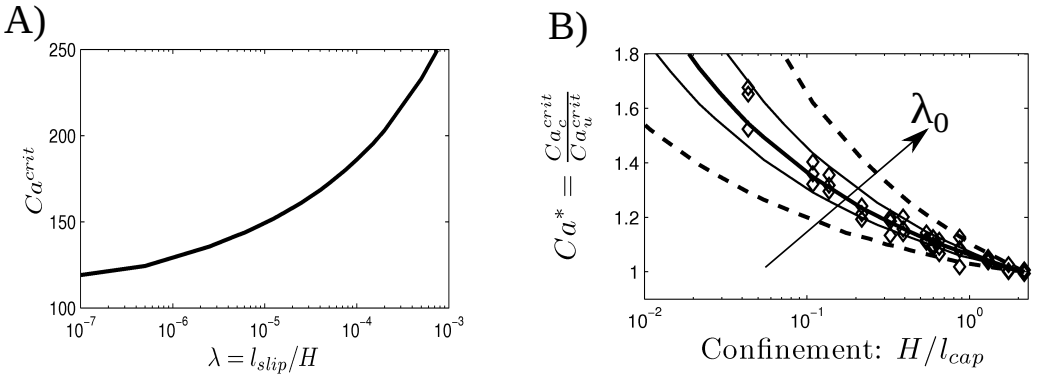

Figure 6.8: Critical capillary numbers as a function of confinement from QP analysis. Using data from figure 6.7, (a) the behavior of $Ca^{crit}(\lambda)$ is shown for $\lambda \in [10^{-7}, 10^{-3}]$. Equation (6.5) is used in (b) to plot Ca^* as a function of dimensionless confinement gap for various choices of λ_o, which increases along the inset arrow from 10^{-6} to 10^{-4} (dashed lines). Solid lines ($\lambda_o \in [5 \times 10^{-6}, 2.5 \times 10^{-5}]$) border the experimental data from figure 6.5 and the bold line ($\lambda_o = 10^{-5}$) provides the best fit.

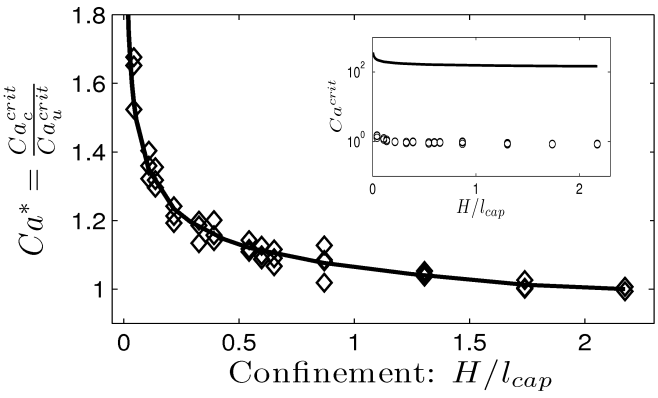

Figure 6.9: Comparison of critical speeds obtained from the QP approach and experimental data. The bold Ca^* curve represents QP data taken from figure 6.8B with $\lambda_o = 10^{-5}$ (l_{slip}= 50 nm). The inset curve includes QP data listed in table 6.3. Experimental data points (open symbols) are taken from figure 6.5.

associated with Ca^{crit} never advance beyond 155^o, which conflicts with a large body of experimental studies which report that air-liquid systems can achieve steady wetting up to angles very near 180^o. Although we did not postulate a critical dynamic angle associated with the onset of wetting failure, this conflict suggests that the quasi-parallel model lacks some of the key features necessary to model the regime just preceding wetting failure for our system.

6.4.3 2D Flow Model

Our second computational approach uses a Galerkin finite element method [128, 130] to evaluate the full 2D hydrdoynamic model established in Chapter 2. Since the interface position is coupled to the flow field, domain boundaries for the physical problem are unknown. Here, we map the system to a fictitious, computational domain where the dynamic boundary conditions are implemented. Within this computational domain, coordinates for the physical domain are retained as unknowns that are solved simultaneously with the flow variables. The free-boundaries (fluid interfaces) of the physical domain deform in response to the global flow field. Details of the FEM techniques used for this analysis are included in Section 2.3.

Figure 6.10 shows the mesh-independent solution families computed using our FEM approach for different values of λ. Qualitatively, each solution family depicts an increase in the apparent contact angle with capillary number until reaching a critical point near $\theta_M = 177^o$. The critical capillary numbers associated with these critical points increase as the wetting system becomes more confined (larger λ). Unstable solution branches exist for a narrow Ca range before the solution path reaches $\theta_M = 180^o$. Near the critical point ($Ca \approx Ca^{crit}$), the interface reveals characteristics of air-film entrainment, which is consistent with the experimental observations discussed in Section 6.3.

Critical capillary numbers and apparent angles extracted from the 2D flow model are tabulated as a function of λ in table 6.4. Unlike results from the QP approach (refer to table 6.3), the 2D flow data matches the experimental observation that $Ca^{crit} \sim 1$ and $\theta_M^{crit} \approx 180^o$ for air-liquid wetting failure. Moreover, FEM results show good quantitative agreement with our experimentally measured critical speeds when assuming a slip length of 10 nm. In figure 6.11 we compare the enhancement factor (Ca^*) and *absolute values* of critical capillary numbers to emphasize that the 2D flow model captures not

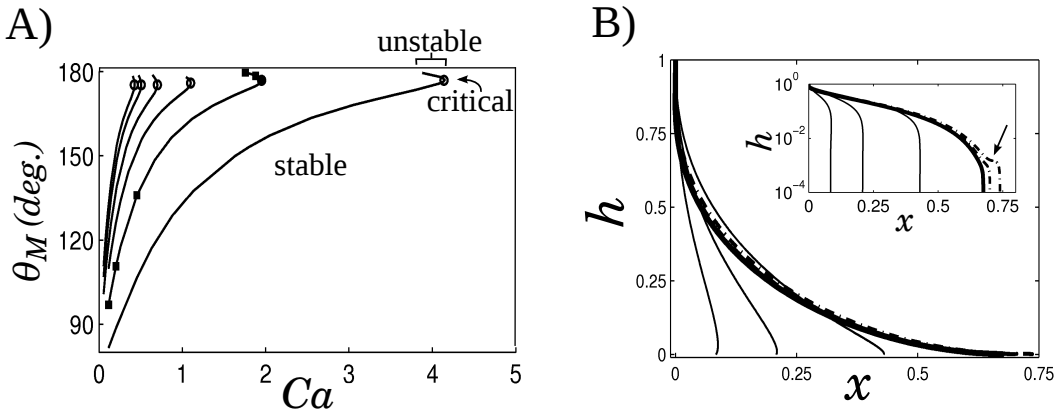

Figure 6.10: Steady-state solutions for the air-glycerol wetting system obtained with the 2D flow model. (A) Solution families show the change in θ_M with Ca for different values of λ. Going left to right, each curve increases in λ with values of $2 \times 10^{-6}, 10^{-5}, 10^{-4}, 10^{-3}, 10^{-2}$, and 10^{-1}, respectively. Bold circles indicate the critical point for each curve. (B) Interface profiles correspond to square symbols along the $\lambda = 10^{-2}$ solution family in (A). The solid and dot-dashed lines represent stable and unstable steady-state profiles, respectively. The inset figure shows profiles on semi-log axes to emphasize the difference in scale between macroscopic and microscopic interface behavior. An arrow denotes the location of microscopic air-film entrainment along the interface profile.

λ	$H(\mu\text{m})$	Ca^{crit}	$\theta_M^{crit}(deg.)$
10^{-1}	0.1	4.13	177
10^{-2}	1	1.95	177
10^{-3}	10	1.10	176
10^{-4}	100	0.700	175
10^{-5}	1000	0.507	175
2×10^{-6}	5000	0.424	175

Table 6.4: Critical point data extracted from the 2D flow model for the air-glycerol system (see figure 6.10). Values for the confinement gap, H, are calculated from $\lambda = l_{slip}/H$ assuming l_{slip}= 10 nm.

only the trend of increasing critical speed with confinement, but also provides accurate estimates (within a factor of 2) of the experimental Ca^{crit} values. The overall trend of increasing Ca^{crit} with λ is well-described by a scaling relationship obtained from asymptotic wetting theory (equation 6.8) , as will be discussed within the following section.

6.5 Discussion

Our experimental observations indicate that confined wetting failure can be characterized by the same sawtooth-meniscus transition that has previously been documented for unconfined systems (e.g., [91]). However, the critical speed that characterizes this transition increases as the wetting region is restricted to smaller gaps. To our knowledge, this study is the first to systematically demonstrate the ability to delay wetting failure to higher speeds through confinement of the wetting meniscus. Thus, meniscus confinement must be listed among the growing number of examples where macroscopic flow parameters influence high-speed wetting behavior.

Figure 6.5 shows a definitive trend of increasing critical speed as the wetting meniscus is confined to smaller gaps. In fact, the available data suggest that Ca^{crit} may achieve exceedingly high values as $H \to 0$. Despite the apparent divergence of the critical speed with decreasing gap widths, it is not surprising that this result has gone unnoticed in previous studies where system geometries are typically designed to have

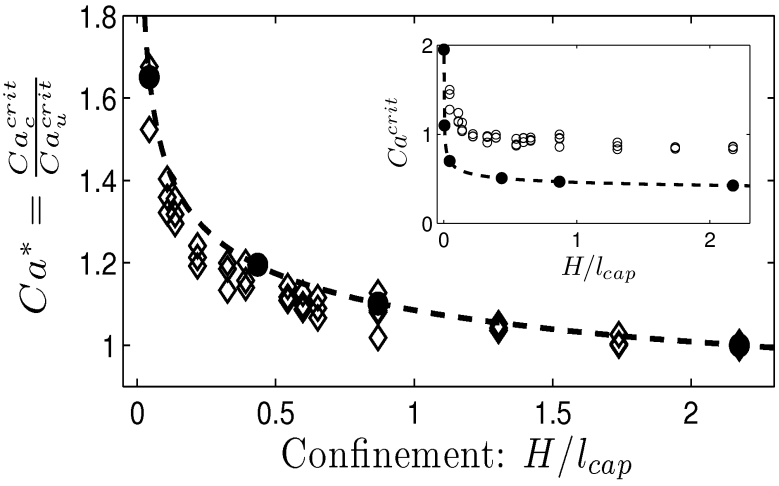

Figure 6.11: Comparison of critical speeds obtained from the 2D flow model and experimental data. Filled circles represent the model prediction taken from table 6.4. Ca^* values are calculated using (6.5) with $\lambda_0 = 2 \times 10^{-6}$ ($l_{slip} = 10$ nm). The dashed line, described by (6.8), provides a good fit for the data obtained from the model. Experimental data points (open symbols) are taken from figure 6.5.

dimensions larger than the capillary length ($l_{cap} \sim 1$ mm). Only when the confinement falls below 250 μm does our data reflect an 50% increase of Ca^{crit}, which would be easily distinguishable from routine experimental uncertainty. Our system design eliminates many of the difficulties associated with interpreting the impact of experimental uncertainty at larger gaps because the confined (variable) and unconfined (control) systems share the same substrate during each run. The qualitative increase in Ca^{crit} with confinement is readily apparent through direct comparison of the respective wetting regions while successively decreasing H. Furthermore, despite the limited precision of H, a smooth logarithmic curve is suggested by our Ca^* data in figure 6.5.

Within hydrodynamic theory, system geometry (λ) has a logarithmic influence on viscous bending. The degree of interface bending is dependent on the amount of viscous stress, F_μ, acting over the entire fluid interface:

$$\int_{l_{slip}}^{H} F_\mu \mathrm{d}h \sim \int_{l_{slip}}^{H} \frac{\mu U}{h} \mathrm{d}h = \mu U \ln(\lambda^{-1}). \tag{6.6}$$

As implied by (6.6), divergent viscous stresses near the wetting line are mitigated by

microscopic mechanisms (characterized by the Navier slip condition) that act to regulate viscous bending for $h < l_{slip}$. If the microscale remains relatively small ($\lambda << 1$), viscous stresses will be much larger near the wetting line than in the bulk fluid, promoting greater viscous bending.

The interface deforms unsteadily when the tendency for viscous bending overwhelms the resistance from surface tension. Therefore, the onset of wetting failure can be expressed by the following force balance (neglecting χ and θ_{mic}):

$$\mu U \ln(\lambda^{-1}) \sim \sigma. \tag{6.7}$$

Gravity resists interface deformation at scales greater than the capillary length, which limits viscous bending to the region $h < l_{cap}$. Therefore, l_{cap} becomes the upper bound for the integration of viscous stresses in (6.6) when $H > l_{cap}$. In this regime ($H > l_{cap}$), λ is effectively constant ($\lambda = l_{slip}/l_{cap}$) and, consequently, the magnitude of viscous bending becomes independent of H. This argument explains the insensitivity of wetting failure to geometric features in relatively unconfined systems (refer to figure 6.5).

As the system becomes more confined ($\lambda \to 1$ and $\ln(\lambda^{-1}) \to 0$), the interface deforms on length scales closer in size to the global domain. Consequently, the impact of $\ln(\lambda^{-1})$ is diminished and higher speeds are needed to promote wetting failure from viscous bending. Moreover, (6.7) simplifies to the following confinement scaling:

$$Ca^* \propto \frac{1}{\ln(\lambda^{-1})}. \tag{6.8}$$

This viscous-bending argument is shared by the asymptotic theories discussed in §2. For example, [45] describes how viscous forces influence the dynamic contact angle for a liquid-void system ($\chi = 0$):

$$\theta_M^3 - \theta_{mic}^3 = 9Ca \ln(\lambda^{-1}). \tag{6.9}$$

Similar to the preceding analysis, $\ln(\lambda^{-1})$ modifies the viscous forces that bend the interface and cause a difference between contact angles measured from the macroscopic and microscopic scale (θ_M^3 - $\theta_{mic}^3 > 0$). Additionally, (6.8) is recovered from (6.9) when assuming that θ_{mic} and θ_M associated with Ca^{crit} change very little in response to confinement.

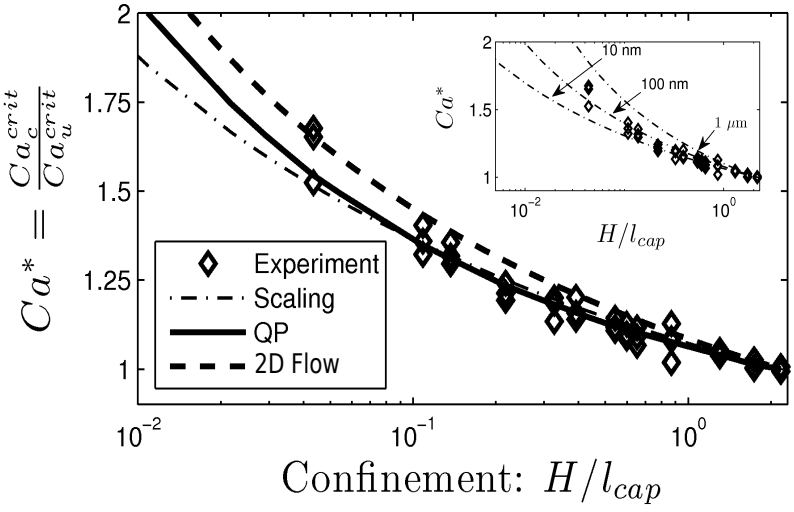

Figure 6.12: Comparison of experimental data and model predictions with the Ca^* scaling derived from asymptotic theory. Data comprising the experimental, QP, and FEM curves initially appear in figure 6.9 and figure 6.11. The scaling curve is described by (6.8) with $l_{slip} = 50$ nm. The inset plot demonstrates the performance of the scaling relationship for $l_{slip} = 10$ nm, 100 nm, and 1 μm.

As shown in figure 6.12, (6.8) agrees with the experimental confinement trend, and the fit is fairly insensitive to the choice of slip length ($l_{slip} \in$ [10 nm – 1 μm]). (Note: The prefactor in (6.8) is chosen so that $Ca^* \to 1$ as $H \to 5$ mm; this corresponds to a prefactor of $\ln(5 \text{ mm}/l_{slip})$.) Surprisingly, this simple scaling describes the data to the same degree as the more rigorous QP and 2D-flow models. [99] demonstrates the applicability of this scaling to a similar lubrication model through a range of the system parameters (i.e., θ_{mic}, χ, λ). This uniform quality between the models suggests that the confinement trend arises as a general consequence of the hydrodynamics of dynamic wetting. Furthermore, the agreement between (6.8) and the experimental data argues in favor of the viscous-bending mechanism for wetting failure.

Although the QP and 2D models agree on the hydrodynamic scaling of Ca^*, there exists a large discrepancy between Ca^{crit} values obtained between the two approaches. The QP approach over-predicts Ca^{crit} by several orders of magnitude (figure 6.9), whereas the 2D flow model estimates the experimental data within a factor of two (refer to figure 6.11). The agreement obtained with our 2D model suggests that the discrepancy of the

QP approach is not due to a inherent failure of our hydrodynamic framework. Instead, the lubrication approximations used to construct the simplified QP approach must be invalid for our system. This issue is discussed in more detail in Section 3.3.5.

Lastly, we comment on the sensitivity of our results to the choice of model parameters. As expected from (6.8), changes in l_{slip} have a logarithmically weak effect on Ca^{crit}; therefore, good agreement should be maintained between model predictions and experimental data for a wide range of fitted slip lengths. The scaling relationship suggests $l_{slip} \in [10\text{ nm}, 1\ \mu\text{m}]$ as an acceptable range (see figure 6.12). However, the lubrication approximation of the QP approach and (6.8) seem to overestimate l_{slip} relative to analysis from the 2D model. Therefore, we expect $l_{slip} \sim 10$ nm for the physical (air-glycerol-steel) system, which is consistent with experimentally measured slip lengths of similar materials [1, 74]. Due to computational limitations, we have been unable to investigate $l_{slip} < 10$ nm with our FEM approach and, consequently, the lower bound to l_{slip} remains unknown.

Our model idealizes the substrate as a perfectly smooth, homogeneous surface with wettability characterized by $\theta_{mic,R}$. Up to this point, we have implemented a microscopic angle equal to the static contact angle measured from our experimental system (i.e., $\theta_{mic,R} = 70^0$). Generally, $\theta_{mic,R}$ could depend on the flow field, which would require augmentation of the current model with some description of microscopic wetting physics [39, 83, 61, 18]. However, in the interest of constructing the simplest hydrodynamic wetting model (with the fewest fitting parameters), we focus on the impact of $\theta_{mic,R}$ as a material constant.

As illustrated by figure 6.13a, critical speeds calculated from the 2D model increase when prescribing smaller $\theta_{mic,R}$. Despite the dependence of Ca^{crit} on $\theta_{mic,R}$, figure 6.13b shows substrate wettability to have little impact on the Ca^* trend for $\theta_{mic,R} \in [50^0, 90^0]$. Thus, $\theta_{mic,R}$ may be decreased to bring the 2D flow results closer to experimental values for Ca^{crit} without yielding a dramatic disparity in the confinement trend. The use of a scraped-roll substrate made our experimental system prone to prewetted glycerol films, which would account for this change in the effective substrate wettability within our model ($\theta_{mic,R} \to 0^0$). This and other non-idealities of the substrate may be responsible for the under-predicted Ca^{crit} values shown by the 2D model in figure 6.11.

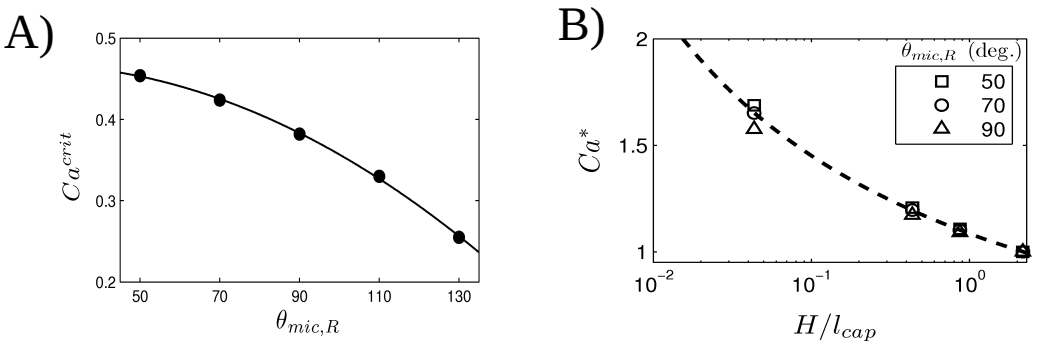

Figure 6.13: The influence of substrate contact angle on critical speeds predicted from the 2D flow model. (A) The dependence of Ca^{crit} on $\theta_{mic,R}$ for the air-glycerol system with $\lambda = 2 \times 10^{-6}$. Filled circles represent data extracted from FEM results. The solid line is generated with a quadratic fit of the data points. (B) The enhancement factor (Ca^*) as a function of confinement for different $\theta_{mic,R}$. Symbols represent data extracted from FEM results (l_{slip} = 10 nm) and the dotted line is the fit of (6.8) to the 2D model taken from figure 6.11.

6.6 Conclusion

In this work, we have investigated the effect of meniscus confinement on the onset of dynamic wetting failure. A novel experimental design is described, which allows for unconfined and confined wetting to be simultaneously viewed along a single moving substrate. Results from our experimental study demonstrate an increase in the critical capillary number, Ca^{crit}, associated with wetting failure through confinement of the wetting meniscus. When the meniscus is confined to gaps *smaller than the capillary length*, wetting failure occurs at higher speeds compared to that observed when the meniscus is unconfined. This relative increase in critical speed is expressed by an enhancement factor, Ca^*, which increases logarithmically as the gap width vanishes. To our knowledge, this work presents the first evidence that meniscus confinement can be used to delay wetting failure.

Additionally, a hydrodynamic model has been developed and analyzed using lubrication theory and 2D FEM. Both models match the experimental confinement trend shown by Ca^*, but only the full 2D analysis provided by FEM adequately models the stress field and provides accurate measures of Ca^{crit}. Agreement within a factor of two is reported in the range where 2D analysis and experiment overlap (100 μm $< H <$ 5

mm). This success of our 2D approach validates the choice of a hydrodynamic description for modeling wetting failure.

Collectively, our modeling results show confined wetting failure to be well-described by a hydrodynamic mechanism where the onset for wetting failure arises from the nonexistence of 2D steady states beyond Ca^{crit}. These steady states fail to exist when air is not pumped away from the wetting line rapidly enough. Although this view does not preclude the possibility of other failure mechanisms, our analysis suggests that viscous bending plays a key role in governing wetting failure in confined systems.

Currently, we are unable to comment in more depth about the nature of the hydrodynamic wetting-failure mechanism. Specifically, the transient process of air entrainment (via the sawtooth meniscus) is not directly addressed by this study. Recent works have made advances in visualizing the sawtooth meniscus [94] and providing a theoretical basis for air entrainment through free surfaces [108]. Further progress requires thorough experimental characterization of high-speed interface behavior. A needed improvement to our current experimental system would include the use of an initially dry substrate with well-characterized surface properties. Visualization of the interface profile or dynamic angle would also be necessary to make more detailed comparisons with theoretical predictions. Nevertheless, our work has shed light on the hydrodynamics of wetting failure and begins to provide a rational basis for the development of strategies to delay wetting failure in high-speed coating processes.

Chapter 7

Characteristics of Air Entrainment along a Planar Substrate

7.1 Introduction

Air entrainment occurs when a liquid mass fails to displace the surrounding air as it advances along a solid surface. In cases of air entrainment caused by dynamic wetting failure, air films originate at the three-phase contact line and release bubbles that are captured by the liquid flow. Air entrainment can be detrimental to industrial applications such as coating and printing processes, where bubbles lead to voids or surface irregularities in the final product [8, 34, 28]. The practical importance of this phenomenon has motivated prior experimental and theoretical studies, yet many questions remain regarding the fundamentals of air entrainment.

The enigmatic dynamic contact line (DCL) contributes many unknowns to the problem of air entrainment. Unlike a static contact line (SCL) found in a stationary system, the DCL necessarily involves transport of two fluid phases in contact with a substrate. The impact of macroscale and microscale mechanics near the DCL remains debated, as discussed in a number of recent reviews [50, 2, 25, 40, 51, 21, 48, 27]. This issue is further complicated near the limit of air entrainment, where DCL behavior is strongly

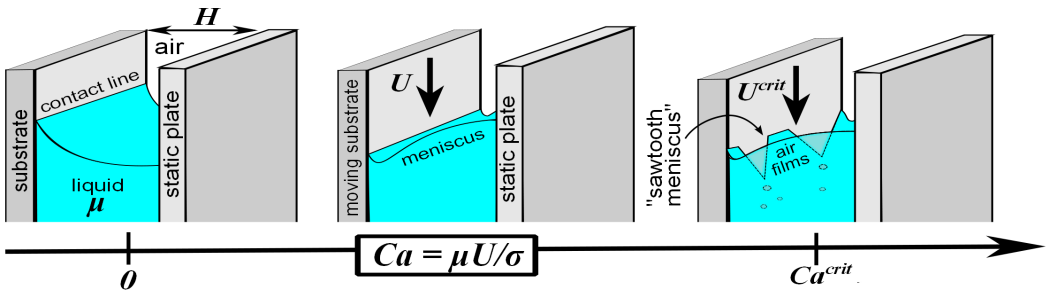

Figure 7.1: The stages of dynamic wetting illustrated as a function of Ca. The air/liquid meniscus is confined in a gap H between a moving substrate and a stationary plate. The meniscus becomes deformed as Ca increases, until a critical transition during the onset of air entrainment at Ca^{crit}. At this point, the contact line becomes jagged with triangular air films, yielding a "sawtooth" meniscus shape.

influenced by many system properties, including system geometry [138], flow-field effects [38, 141, 142], and electrostatic forces [155, 34].

For planar systems, air entrainment evolves from interface shapes similar to the illustration in Figure 7.1. In this example, the capillary number $Ca = \mu U/\sigma$ characterizes dynamic wetting of a substrate moving with speed U into a liquid with viscosity μ and surface tension σ. As speed increases (larger Ca), viscous effects deform the air/liquid meniscus and move the DCL in the direction of substrate motion. At a critical speed corresponding to Ca^{crit}, the DCL becomes unstable and air films elongate into the liquid. This onset of air entrainment is often identified by a "sawtooth" meniscus shape that results from the distribution of triangular air films along the width of the substrate [92]. Details of the sawtooth shape and scale depend on system parameters (e.g., liquid viscosity) in general, but descriptions within the literature have primarily been qualitative [104, 156, 106].

In a prior work, we investigated the influence of interface confinement on the critical speed associated with the onset of air entrainment [138]. Using an experimental apparatus in which a glycerol solution ($\mu \approx 120$ cP) is confined to gap H (see Figure 7.1) between a stationary surface and a rotating roll, we demonstrated that increasing confinement (smaller H) delays air entrainment to higher Ca^{crit} values. Results from a two-dimensional (2D) hydrodynamic model match the experimental observations and suggest a wetting-failure mechanism related to strong pressure gradients that pump air

away from the DCL [157]. Due to this mechanism, the model predicts that critical speeds are most strongly affected by parameters that alter the interface shape near the DCL.

This work yields a broader understanding for how the onset of wetting failure is influenced by the properties of planar wetting geometries. An experimental system is used in which polyethylene terephthalate (PET) tape is drawn through a glycerol/water solution at high speeds with close visualization of the DCL. Once again, confinement imposed with a stationary plate postpones air entrainment to higher Ca^{crit}. This work demonstrates the consistency of this confinement effect over a wide range of solution viscosity, expanding considerably upon prior findings [138]. Furthermore, liquid pressurization (using compressed air within the experimental apparatus) is found to significantly impact the dynamics of air entrainment when the meniscus is located near a sharp corner, leading to even higher critical speeds. Similar effects have been observed in high-speed fiber coating [115, 88], though, to the authors' knowledge, this work presents the first demonstration of air entrainment postponed via liquid pressurization in a planar geometry.

In addition, close visualization of the DCL provides new perspective on the dynamics of air entrainment. Image analysis techniques are used to quantify the size of air films formed at Ca^{crit} with data reflecting systematically smaller films at higher solution viscosities. Regardless of the specific operating conditions, visualizations reveal a dominant mechanism for air-film rupture, as illustrated in Figure 7.2. This sequence portrays air-film thickness variations that propagate across the meniscus, nucleating rupture sites that ultimately cause air-bubble entrainment. Recorded critical speeds and air-film sizes compare well against predictions from the computational model used within prior works [138, 157], further supporting the hydrodynamic mechanism for the onset of air entrainment.

Section 7.2 discusses details of the experimental apparatus and methods. Section 7.3 presents critical speeds measured with different system geometries and glycerol viscosities. Section 7.4 shows data from image analysis of the air films formed near the DCL under different operating conditions. Finally, Section 7.5 summarizes the dynamics observed at the onset of air entrainment and compares experimental data to predictions from the hydrodynamic model mentioned above.

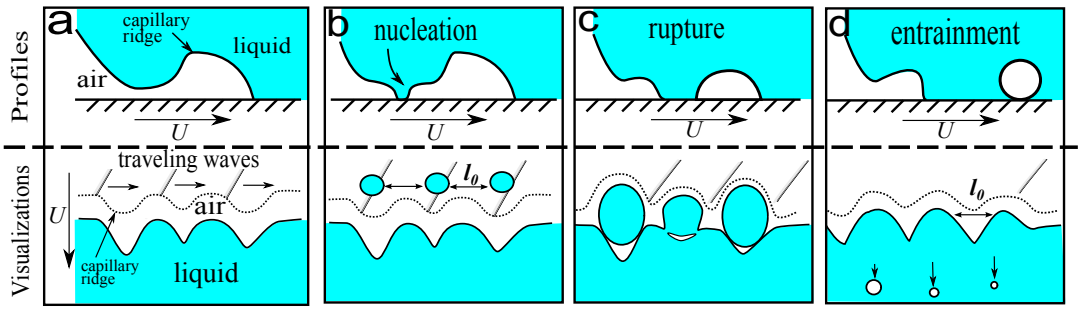

Figure 7.2: Idealization of the interface profiles corresponding to visualizations of air-film rupture. (a) Air films form with capillary ridges (shown by dashed line in visualization panels) near the DCL. (b) Traveling waves nucleate liquid contacts as the air films thin near the capillary ridge. Commonly, multiple nucleation sites appear simultaneously at distances matching the wavelength l_0. (c) Regions of liquid contact grow until reaching the DCL. (d) Discrete air films pinch off from the DCL and rapidly evolve into equilibrium bubble shapes.

7.2 Experimental Methods

The experimental apparatus shown in Figure 7.3. The apparatus features a transparent tape substrate that moves through the system as it transfers from the unwind roll to the rewind roll (see Figure 7.3a). A 125 μm thick polyethylene terephthalate (PET) tape is used for all of the data reported in this paper. A line-speed controller (Contrex® M-Drive) adjusts the rotational speed ω of the rewind roll to maintain a set linear speed U of the tape. Along its path, the tape enters a vessel designated as the "wetting box," where one side of the tape comes in contact with the wetting liquid and the opposite side runs along a glass support plate. Viewing through the support plate, a camera records wetting phenomena and projects real-time video to an external display.

The wetting box resembles a plunge-coating tank (approximately 10 cm in each dimension) in which the liquid reservoir is completely enclosed except for thin slots where the tape enters and exits the apparatus (see Figure 7.3b). Rubber gaskets seal the exit slot and all joining walls of the wetting box to minimize leaking. Within the wetting box, an interior plate is positioned with adjustable supports (not shown) that connect to the base of the apparatus. Shims (Precision Brand®) are used to set the distance between interior and support plates. The system is aligned such that the substrate's width narrowly fits between shims placed at opposite edges of the wetting

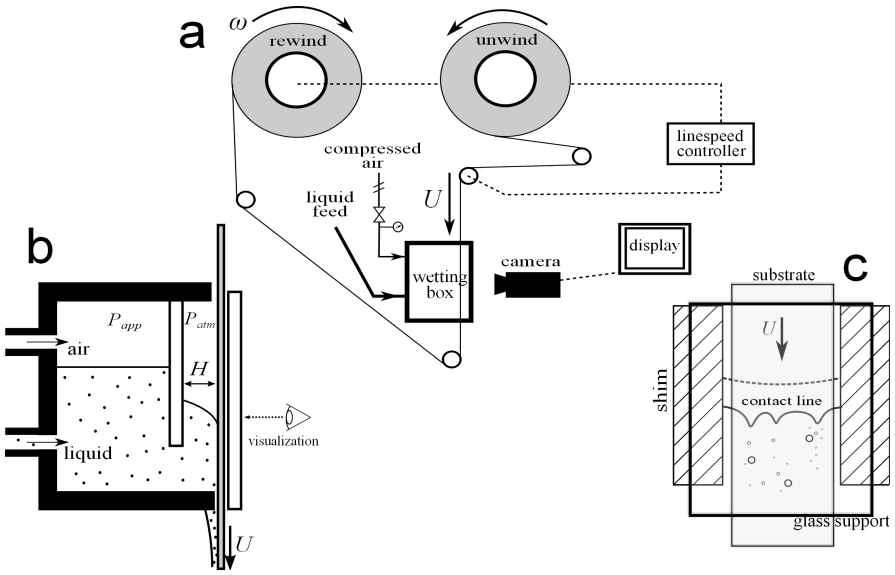

Figure 7.3: Schematic of the experimental apparatus. (a) Overview of the substrate's path driven by rotation of the rewind roll at angular speed ω. The line-speed controller adjusts ω through a feedback loop to maintain constant linear velocity U. (b) A glycerol/water solution wets the tape substrate as it passes through the wetting box. A stationary plate confines the air/liquid meniscus within a gap H. Compressed air controls the meniscus height and pressurizes the liquid (see Figure 7.5). (c) A high-speed camera allows visualization of contact-line behavior while viewing the meniscus through a glass support plate (located to the right of the substrate in panel b). The distance between the support and interior plates is set by shims that lie alongside the substrate. (Note that the shims are omitted from panel b to provide a clear view of the meniscus.)

box (see Figure 7.3c). The confinement gap H shown in Figure 7.3b results from the difference between the shim and tape thickness. The wetting region is left unconfined when the interior plate is completely removed from the system (this geometry will be denoted as $H \to \infty$).

The back wall of the wetting box includes liquid and air inlets. Liquid feed fills the vessel to a desired volume (usually 300 ml) prior to experimentation. During operation, compressed air enters the wetting box through the air inlet and pressurizes the liquid relative to atmospheric pressure P_{atm}. Liquid pressurization allows the meniscus to be positioned within the confinement gap, resisting the substrate's tendency to drag the meniscus toward the exit slot. The applied pressure P_{app} is controlled with a screw valve (Speedaire®) and measured by a manometer (Dwyer® Slack Tube) when $P_{app} < 10$

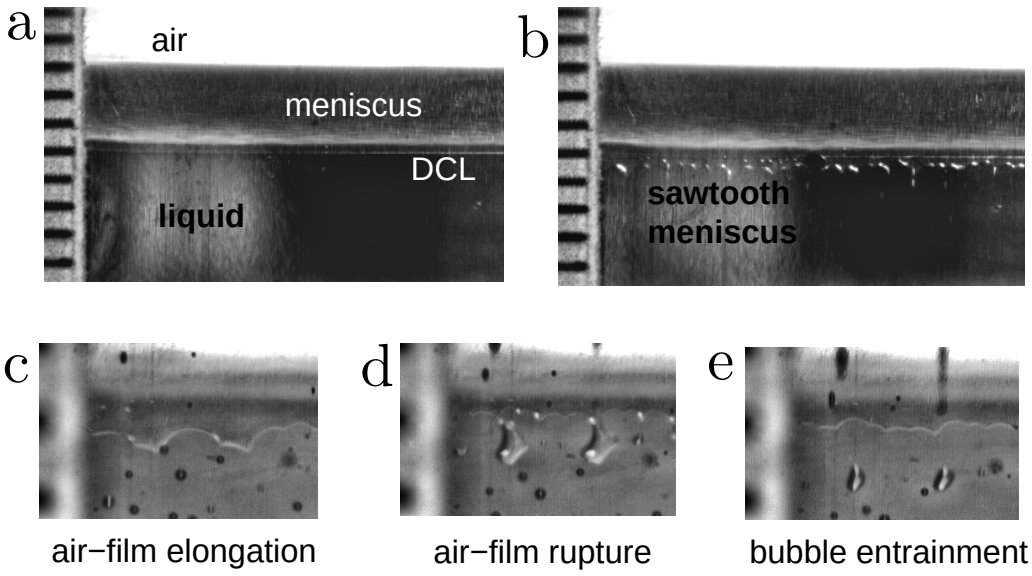

Figure 7.4: Visualizations of (a) steady wetting and (b - e) air entrainment recorded in the unconfined geometry ($H \to \infty$) with a high-viscosity glycerol/water solution ($\mu = 745$ cP). (a) The DCL appears smooth during steady wetting ($U \approx 0.055$ m/s), but (b) becomes serrated at the critical speed ($U^{crit} = 0.059$ m/s), forming a sawtooth meniscus. (c) Closer inspection reveals that air films of similar size and shape elongate from the DCL at U^{crit}. Over time, (d) air films become unstable and rupture, (e) leaving behind air bubbles that are entrained within the liquid flow. Note that ruler lines measure 1 mm distances in each image.

kPa and a pressure gauge (Binks®) for $P_{app} > 10$ kPa. Pressurization is not necessary for unconfined studies ($H \to \infty$) because gravitational forces maintain a constant liquid level away from the DCL, preventing any major changes in the meniscus position during a single run.

The critical speed U^{crit} associated with air entrainment is determined by gradually increasing the tape speed until triangular air films form at the DCL. These air films appear suddenly and uniformly along the entire width of web when $U \geq U^{crit}$, resembling the sawtooth meniscus discussed in Section 7.1. Figure 7.4 shows visualization of the transition from steady wetting (Figure 7.4a) to air entrainment (Figure 7.4b). Recorded images are analyzed with the MATLAB Image Processing Toolbox™ to improve contrast of the DCL and measure features associated with the air entrainment

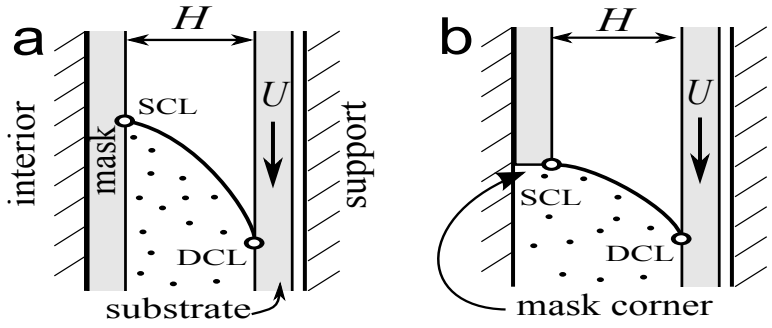

Figure 7.5: Illustration of the confined geometries used within this study. (a) The meniscus is confined within a parallel channel formed between interior and support plates. To prevent interaction with the substrate (see description in text), a PET mask covers the interior plate, forming a gap H between the mask and substrate surfaces. In this case, the SCL and DCL freely move in response to changing speed U or applied liquid pressure P_{app}. (b) In contrast, the meniscus remains effectively pinned when the SCL is located near the mask corner. Therefore, liquid pressurization alters the meniscus shape, as discussed in Section 7.3.3.

events illustrated in Figure 7.4c-e. These measurements are discussed in more detail in Section 7.4.

When imposing narrow confinement gaps ($H \leq 300$ μm), capillary forces cause the tape and interior plate to interact prior to start up of the substrate motion. It was found that a PET mask placed over the interior plate greatly reduces adhesive forces that otherwise result from this interaction. Figure 7.5 illustrates the mask system used for confinement studies. Similar to findings from our prior work [138], critical speeds appear to be independent of P_{app} when the meniscus is located in the gap formed between the mask and substrate (Figure 7.5a). Wetting characteristics, including U^{crit}, become sensitive to changes in P_{app} when the meniscus is positioned near the mask corner (Figure 7.5b). Due to an effective pinning of the SCL at the corner, liquid pressurization changes the interface shape rather than simply translating the meniscus, as discussed in Section 7.3.2.

Glycerol/water solutions were chosen for this study because of their Newtonian behavior and low vapor pressure at room temperature. Additionally, solution viscosity is easily adjusted through dilution with deionized water or concentration with 99.7% pure glycerin. For the cases presented here, solution viscosities span a range of 25 cP to

1000 cP, corresponding to compositions of approximately 75% and 99.7% glycerol (by weight), respectively [158]. (Note: we assume a density of $\rho \approx 1200$ kg m^{-3} for each solution when estimating the capillary length, $l_{cap} = \sqrt{\sigma/\rho g}$).

Experimental uncertainty arises from several different sources during each run. Viscosity measurements (DV-II Brookfield viscometer) typically show a standard deviation of 10% for each value of μ, while surface tension (Krüss K10ST digital tensiometer) remains within the bounds of $\sigma = 65 \pm 2$ mN m^{-1} for all of the air/glycerol systems used in this study. Contact angle hysteresis is observed on the PET substrate (Kruss DSA goniometer) with advancing and receding angles of approximately 80^o and 65^o, respectively. Substrate speed is held to within 0.005 m s^{-1} (Contrex® M-Drive controller) of the recorded set point U, producing relatively small errors in measured critical speeds ($U^{crit} > 0.05$ m s^{-1}) compared to the viscosity uncertainty. Confinement studies include uncertainty related to the reading of P_{app} (± 0.1 kPa and ± 2 kPa for the manometer and pressure gauge, respectively) and the measurement of the gap H. Misalignment of the wetting-box walls and interior/supporting plates contributes the most significant error to the system. Although this error is difficult to quantify, passing shims of varying thickness through the gap reveals that this uncertainty is less than 50 μm for the values of H reported here.

7.3 Critical Speeds

Air entrainment is observed at some critical substrate speed for all cases investigated in this study. As illustrated by Figure 7.4, the DCL becomes unsteady at U^{crit}, forming unstable air films that produce air bubbles upon rupture. Super-critical speeds ($U > U^{crit}$) tend to lengthen the air films and quicken rupture, though the dynamics depend strongly on the liquid viscosity, as discussed in Section 7.4. The critical capillary number $Ca^{crit} = \mu U^{crit}/\sigma$ marking the onset of air entrainment adopts different values depending on the operating conditions used in each experimental run. The following sections describe the dependence of Ca^{crit} on liquid viscosity (Section 4.4.1) and properties of the confined geometry, including the gap width (Section 7.3.2) and liquid pressure (Section 7.3.3).

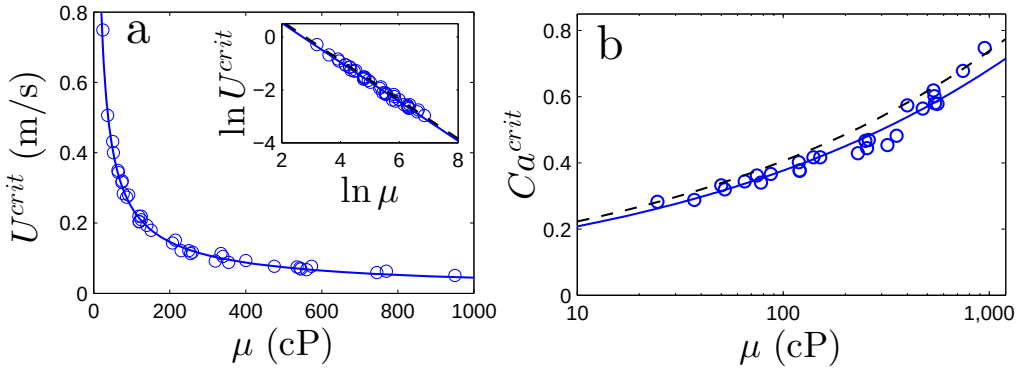

Figure 7.6: (a) Critical speeds measured as a function of glycerol viscosity in the unconfined geometry ($H \to \infty$). The inset demonstrates that critical speed data follow the weak-power law $U^{crit} \propto \mu^{-0.742}$ with the bold line denoting the best fit. (b) Critical capillary numbers corresponding to the data plotted in panel a. The fit from panel a (bold line) is rescaled with μ to match the definition of Ca^{crit}, as expressed by (7.1) with $K = 0.115$ cP$^{-0.258}$. The dashed line represents the correlation $Ca^{crit} = 0.123[\mu$ (cP)$]^{0.26}$, which is obtained from a collection of air-entrainment studies with unconfined geometries [2].

.

7.3.1 Liquid Viscosity

Critical speeds systematically decrease with higher liquid viscosities, similar to the findings of prior experimental works [2, 43]. Figure 7.6a plots the value of U^{crit} recorded for various glycerol viscosities ($\mu \in$ [25 cP 1000 cP]) using the unconfined geometry ($H \to \infty$) discussed in Section 7.2. The inverse relationship between critical speed and liquid viscosity (see inset of Figure 7.6a) suggests that the important parameter is the capillary number $Ca = \mu U/\sigma$, which measures the relative strength of viscous and surface-tension forces acting on the meniscus.

Figure 7.6b plots Ca^{crit} values corresponding to the critical-speed data in Figure 7.6a. Unlike U^{crit}, the critical capillary number increases with higher liquid viscosities, following the weak power-law relationship

$$Ca^{crit} \approx K\mu^{0.258}, \tag{7.1}$$

where the coefficient K depends on the value of H, as discussed in Section 7.3.2. The fit of (7.1) to the data closely resembles empirical correlations from similar studies of air entrainment in unconfined geometries [2] (e.g., see dashed line in Figure 7.6b).

7.3.2 Confinement

In a prior work, confinement was shown to delay the onset of air entrainment during dynamic wetting of a roll substrate with a single glycerol solution ($\mu \approx 120$ cP) [138]. The current study expands upon this result, demonstrating that narrow gaps increase the value of Ca^{crit} for glycerol/water solutions that span a wide viscosity range, as shown in Figure 7.7a. Furthermore, the tape substrate enters the wetting box completely dry, avoiding prewetting effects that may have influenced air entrainment in the previous system.

Despite differences in the experimental systems, Figure 7.7b demonstrates that critical speeds recorded from both the prior and current studies follow the scaling

$$Ca^* \propto [\ln(H/l_{slip})]^{-1}, \tag{7.2}$$

where Ca^* represents the fractional increase in the critical speed measured with a confined geometry (i.e., Ca_c^{crit}) relative to the unconfined case (i.e., Ca_u^{crit}) while holding all other parameters fixed. The slip length l_{slip} relates to the size of the region near the DCL where microscopic physics dominate the wetting mechanics. For the purposes of this study, the slip length acts as a fitting parameter in (7.2) [138], although there have been many experimental and theoretical investigations into the effect of l_{slip} on similar systems [72, 74, 1, 77]. Using $l_{slip} = 200$ nm, the scaling in (7.2) describes the trend of the current data set with fair accuracy as shown in Figure 7.7b.

Although critical speeds depend on the liquid viscosity, the relative effect of confinement (i.e., Ca^*) is nearly independent of μ. As a demonstration, Figure 7.8 plots data sets for each value of H with corresponding fits of (7.1). For each case, Ca^{crit} data show roughly the same power-law dependence on μ, but shift due to changes to the fitted coefficient K at different values of H. Consequently, the fractional increase in critical speed Ca^* is simply taken as the ratio of coefficient values from the confined (K_c) and unconfined (K_u) data sets. (Note that $Ca^* \approx K_c/K_u$ is plotted as the data symbols in Figure 7.7b.) Fitted values of K are listed in Table 7.1 for various values of the confinement gap.

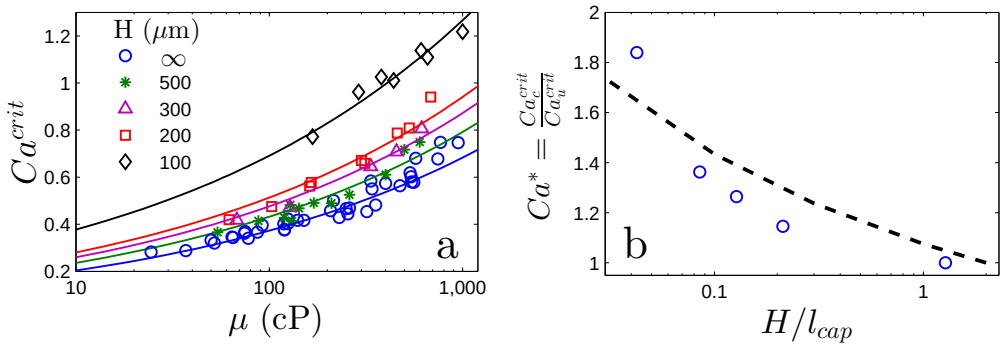

Figure 7.7: (a) Critical speeds plotted as function of μ for various confinement gaps H. Symbols and colors denote the value of H for each data point, as listed in the legend. Bold lines are fitted to data sets of corresponding color using (7.1) and K values listed in Table 7.1. (b) The fractional increase in critical speed Ca^* is plotted against the dimensionless gap where $l_{cap} = 2.5$ mm. As described in text, each data point represents the ratio $Ca^* = K_c/K_u$, where K_u and K_c are the coefficients in Table 7.1 for $H \to \infty$ and finite H, respectively. The dashed line denotes (7.2) with $l_{slip} = 200$ nm.

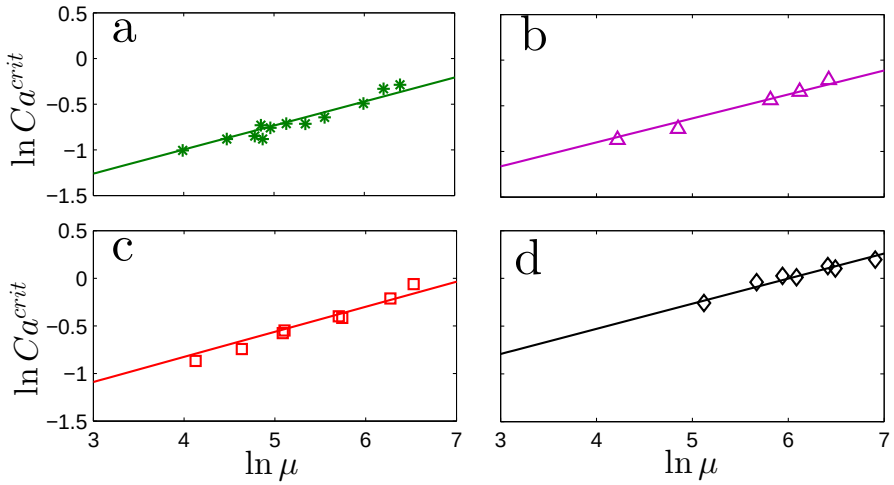

Figure 7.8: Fits of Ca^{crit} to the power-law relationship in (7.1) for H = (a) 500 μm , (b) 300 μm , (c) 200 μm , and (d) 100 μm . Fitted values of K are listed in Table 7.1.

H (μm)	K (cP)$^{-0.258}$
∞	0.115
500	0.132
300	0.146
200	0.157
100	0.212

Table 7.1: Coefficient values (K) used to fit (7.1) to Ca^{crit} data measured with various confinement gaps H.

7.3.3 Liquid Pressurization

Liquid pressurization positions the meniscus within the confinement gap during dynamic wetting. Higher applied pressures P_{app} are needed as speed increases in order to resist substrate drag on the meniscus. In fact, the data plotted in Figure 7.9 suggest that P_{app} must increase linearly with Ca to hold the meniscus position steady within the gap. At fixed Ca, P_{app} is weakly effected by changes to the liquid viscosity (see Figure 7.9a). In contrast, changes to the gap have a major impact on the required liquid pressure. Since the pressure gradient in channel flow is inversely dependent on the square of the channel height, the applied pressure must increase with smaller gaps as $P_{app} \propto H^{-2}$ (see Figure 7.9b). The wetting box becomes susceptible to liquid and compressed air leaks when $P_{app} > 10^4$ Pa. For this reason, high-speed wetting in gaps less than 100 μm could not be investigated in this study. Furthermore, only high-viscosity solutions ($\mu > 100$ cP) are used with the smallest gap ($H = 100$ μm) to limit the rate of liquid loss.

The onset of air entrainment appears insensitive to the magnitude of liquid pressurization when the meniscus is located within the gap (refer to Figure 7.5a). In this case, increasing P_{app} moves the meniscus further up the gap, but does not significantly alter Ca^{crit} or the behavior of the DCL. Consequently, critical speeds are reported as a single-valued function of liquid viscosity μ for each confinement gap H (see Figure 7.7a).

This picture becomes more complicated when the meniscus is located at the leading edge of the gap. In this case, the meniscus does not freely move with increasing liquid

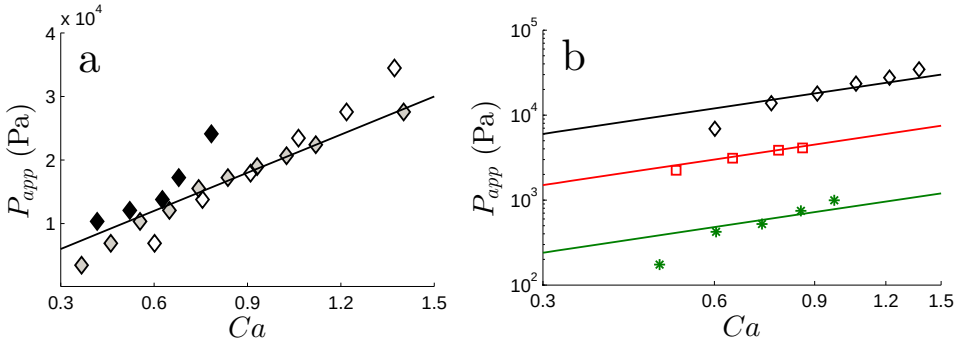

Figure 7.9: Applied pressure needed to hold meniscus position constant within the confinement gap while increasing Ca. (a) Data are plotted for $\mu = 1000$ cP (white), 600 cP (gray), and 170 cP (black) with $H = 100\mu$m. The solid line represents a linear fit of the $\mu = 500$ cP data. (b) Data are plotted for $H = 100$ μm (diamond), 200 μm (square), and 500 μm (asterisk) with $\mu = 600$ cP. For each data set, the linear fit from panel a is multiplied by the factor (100 μm $/H)^2$ to account for the influence of gap width on P_{app}.

pressures, but tends to remain fixed near the corner of the PET mask that covers the interior plate, as shown in Figure 7.5b. This effective pinning of the meniscus forces the air/liquid interface to change shape in response to pressurization.

Figure 7.10 demonstrates the effect of pressurization on the air film that forms near the DCL at Ca^{crit}. As a reference point, Figure 7.10a shows the serrated DCL shape that is characteristic of air entrainment in the unconfined geometry. Figure 7.10b reflects similar behavior when the meniscus is located within the gap, although confinement tends to produce a broader the air film with a less regular sawtooth shape. Figure 7.10c demonstrates a considerable change in the air film when the meniscus is located near the mask corner. While the meniscus remains effectively pinned, higher liquid pressures decreases the scale of interface deformation, significantly reducing the size of triangular air films (see Figure 7.10c) in comparison to the unconfined case (see Figure 7.10a). This influence of P_{app} on interface shape is also found at sub-critical speeds, where excessive pressurization shortens the meniscus similar to the observations of high-speed wetting during pressurized fiber coating [115].

While altering the interface shape, liquid pressurization also delays the onset of air entrainment, as illustrated in Figure 7.11. Data points in Figure 7.11a denote Ca^{crit} values recorded while pinning the meniscus at the mask corner. Under these conditions,

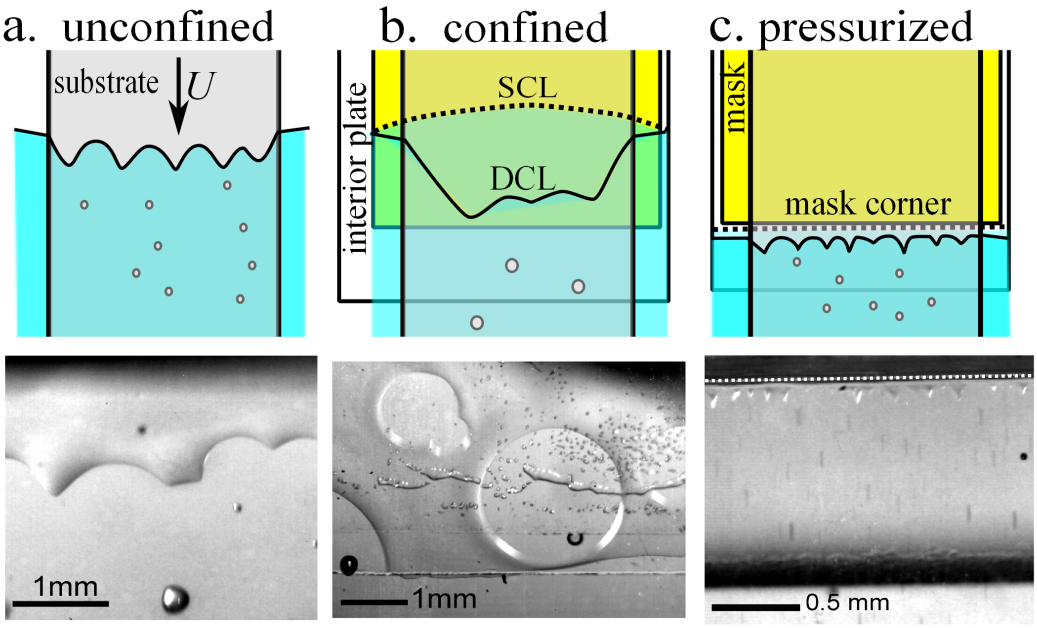

Figure 7.10: Visualization of the onset of air entrainment for (a) unconfined and (b-c) confined system geometries with $\mu = 400$ cP. Illustrations (top) idealize the system corresponding to each visualization image (bottom). (b) The SCL is located high above the DCL (outside of the visualization window) within the parallel channel of gap $H = 200$ μm ($P_{app} \approx 3$ kPa). (Note that the visualization shows bubbles trapped between the mask and interior glass plate.) (c) The SCL is pinned near the mask ridge with $H = 100$ μm and liquid pressurization ($P_{app} \approx 40$ kPa) reduces the size of the triangular air films. The mask ridge is marked with by the white dashed line. The scale bars denote lengths of (a-b) 1 mm and (c) 0.5 mm.

higher liquid pressures promote steady wetting at faster speeds, resulting in multiple Ca^{crit} values for each glycerol solution. This pressurization effect yields significantly faster critical speeds than are obtained when simply confining the meniscus within the gap (see bold curve in Figure 7.11a). Since pressurization ceases to postpone air entrainment once the meniscus moves away from the mask corner, P_{app} must be carefully balanced with substrate drag to prevent meniscus "depinning". (Achieving this balance is difficult in practice, resulting in an apparent variation in the pressurization effect at different values of μ shown in Figure 7.11a.) In fact, Figure 7.11b demonstrates

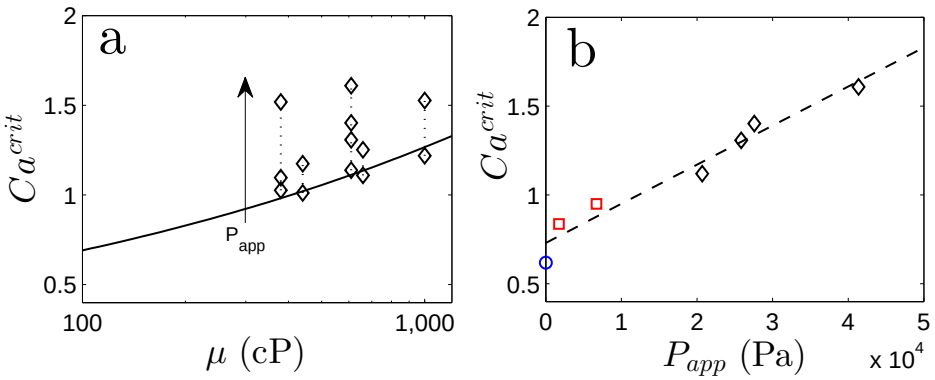

Figure 7.11: The effect of pressurization on Ca^{crit} when the meniscus is located at the mask corner (see Figure 7.5b). (a) Critical capillary numbers plotted for various glycerol solutions with $H = 100$ μm . Each solution shows a trend of increasing Ca^{crit} with larger P_{app}. The bold line represents the power-law (7.1) fit for the $H = 100$ μm data set plotted in Figure 7.7. (b) Critical speeds plotted as a function of P_{app} for $\mu = 600$ cP and $H = 200$ μm (square), 100 μm (diamond), and $H \to \infty$ (circle). (Recall that unconfined wetting $H \to \infty$ does not require liquid pressurization, making $P_{app} = 0$ in this case.

that Ca^{crit} increases linearly with P_{app} until excessive liquid pressure causes meniscus depinning. Larger gaps become prone to meniscus depinning at lower P_{app}, leading to less of an impact on the critical speed than the $H = 100$ μm case discussed above.

7.4 Air-film Characteristics

At the onset of air entrainment, thin air films elongate from the DCL, eventually rupturing and producing air bubbles that are captured within the wetting liquid. Figure 7.12 idealizes the three characteristic stages leading to air entrainment. First, the DCL adopts a serrated shape due to a periodic distribution of air films. Each air film resembles an isosceles triangle (Figure 7.12a) of characteristic angle ψ formed by a base and side of lengths W and L, respectively. Second, perturbations cause the interface to rupture locally (Figure 7.12b), releasing a portion of the air film with area A from the meniscus. Finally, surface-tension forces equilibrate the detached air patch, forming a spherical bubble with diameter D (Figure 7.12c). The following sections discuss characteristics of the air-film shape (Section 7.4.1), thickness (Section 7.4.2), and rupture mechanism (Section 7.4.3).

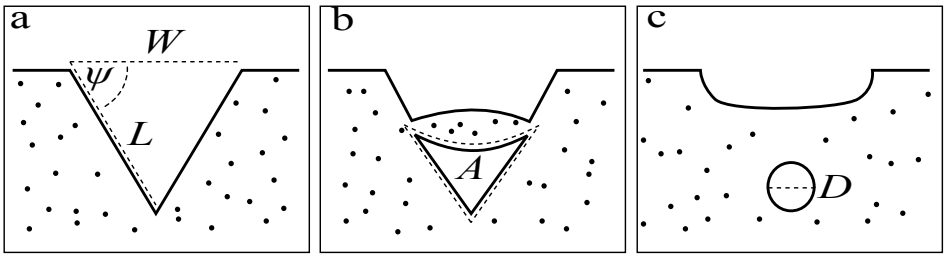

Figure 7.12: Idealization of the evolution of the air film during air entrainment. See description in text.

7.4.1 Shape

System parameters strongly influence air-film size at the onset of air entrainment. With low-viscosity solutions ($\mu < 40$ cP), a single air film extends across the width of the substrate, pinning on the edges of the tape. In this case W is fixed by the substrate width ($W \approx 5$ cm), making the triangular shape completely specified by the angle ψ. Figure 7.13 shows that the pinned air film elongates (see Figure 7.13a-b) as substrate speed exceeds U^{crit}, resulting in larger values of ψ as predicted by theory [92]:

$$\cos\psi = U^{max}/U. \tag{7.3}$$

Equation (7.3) requires that the DCL slope (ψ) increases to maintain a maximum velocity (U^{max}) normal to the DCL as the substrate moves at higher speeds ($U > U^{max}$). Figure 7.13c demonstrates that (7.3) matches experimental measurements for ψ as a function of U, although the fitted value of U^{max} underpredicts U^{crit} (measured at the onset of air-film growth) by approximately 10%, similar to the observations of Blake & Ruschak (1979) [92].

Air films become smaller with increasing liquid viscosity, as demonstrated in Figure 7.14. At relatively high viscosity ($\mu > 200$ cP), triangular air films are regularly distributed along the DCL forming the characteristic sawtooth meniscus. Fewer air films fit along the DCL (i.e., the width of the tape) in the moderate viscosity regime (200 cP $> \mu >$ 50 cP), resulting in relatively straight portions of the DCL (Figure 7.14c) in comparison to the air entrainment high-viscosity glycerol (Figure 7.14a-b).

Figure 7.15a plots the air-film width W (refer to Figure 7.12a) measured at the onset of air entrainment as a function of glycerol viscosity for the unconfined geometry. (Details regarding the processing of visualization images and measurement of W are

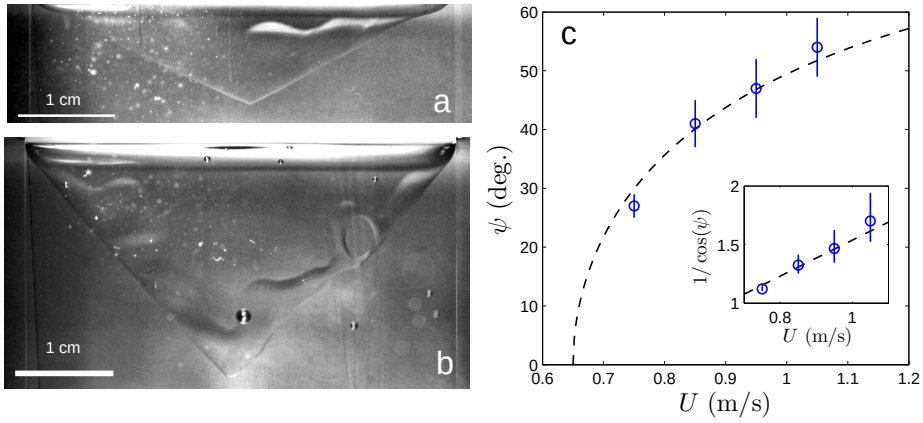

Figure 7.13: The effect of substrate speed on the air-film shape for $\mu = 25$ cP, where a single film spans the width of the substrate at super-critical speeds. The images show the elongation of the air film as speed increases from (a) $U \approx U^{crit}$ (0.75 m/s) to (b) $U > U^{crit}$ (1.05 m/s). (c) The angle ψ is measured as a function of U. *Inset*: The data plotted against the relationship (7.3). Dashed lines represent (7.3) using $U^{max} = 0.65$ m/s.

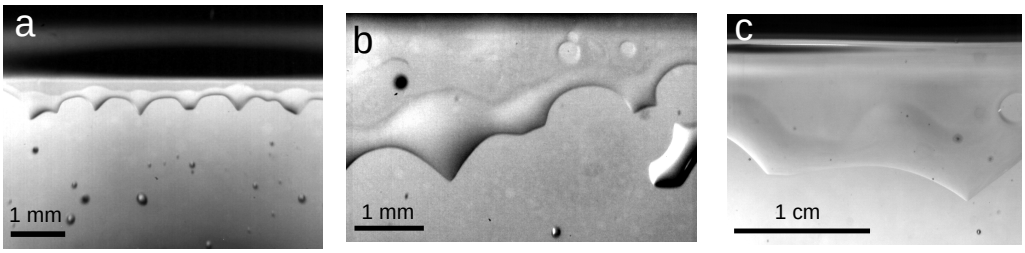

Figure 7.14: Visualization of triangular air films formed near the DCL at the onset of air entrainment with (a) $\mu = 1000$ cP, (b) 400 cP, and (c) 75 cP for the unconfined geometry ($H \to \infty$). Scale bars denote lengths of (a-b) 1 mm and (c) 1 cm.

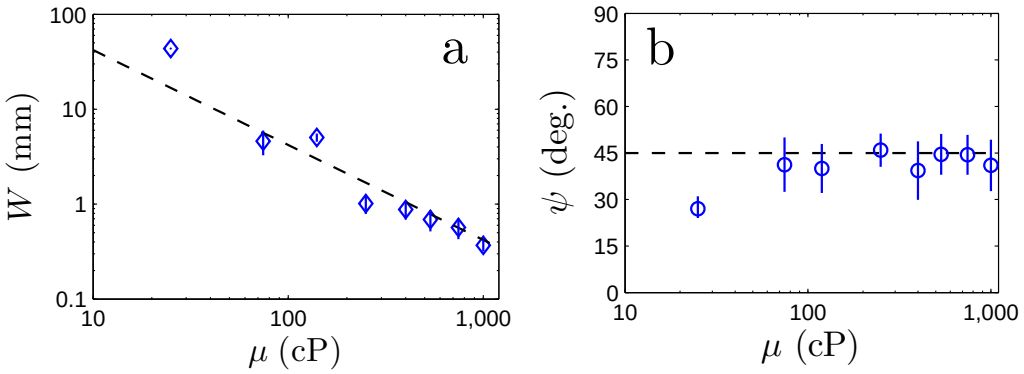

Figure 7.15: (a) The effect of liquid viscosity on air-film size as characterized by the width W of the triangular shapes formed at Ca^{crit}. (b) The angle ψ corresponding to the data points in panel a.

included in Appendix D.1.) The data reflect a systematic decrease in air-film size as glycerol viscosity increases, making W roughly proportional to $1/\mu$ (see dashed line in Figure 7.15a). As long as the air film remains small and avoids pinning against the tape edge, the angle ψ stays near 45^o on average, independent of solution viscosity. Super-critical substrate speeds ($U > U^{crit}$) generally lengthen the meniscus (including the air-film region), but also trigger faster rates of rupture and bubble entrainment. Qualitatively, air films appear to form sharper triangles as U increases beyond U^{crit}, but it is difficult to obtain meaningful measures of ψ due their rapid break up into air bubbles. In contrast, the $\mu = 25$ cP case yields a wide air film that pins against the substrate edges, effectively stabilizing the film and allowing ψ to be measured at super-critical speeds (refer to Figure 7.15c). This edge-pinning effect also causes ψ to deviate from 45^o at the onset of air entrainment, as shown in Figure 7.15b for $\mu = 25$ cP.

Confinement alters the dynamics of air entrainment. For example, Figure 7.10a and Figure 7.10b show the rupture of air films with 400 cP glycerol for unconfined and confined geometries, respectively. As reflected by these images, confinement typically yields broad, irregular air films in comparison to the triangular shapes formed during unconfined air entrainment. This difference is caused by the volume of liquid displaced away from the DCL during elongation of the air film. In the confined case, displaced glycerol enters the narrow gap, where even small increases in liquid volume force upward

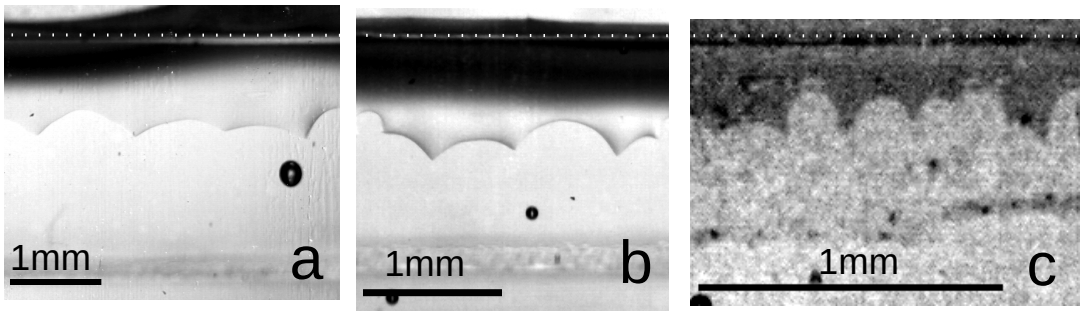

Figure 7.16: Visualization of DCL shapes at the onset of air entrainment for confined systems: (a) μ = 515 cP, H = 500μm, and P_{app} = 1.3 kPa; (b) μ = 460 cP, H = 200μm, and P_{app} = 6.9 kPa; (c) μ = 600 cP, H = 100μm, and P_{app} = 27.5 kPa;. In each case, the meniscus is positioned near the mask corner (white dotted line), allowing pressurization to reduce the size of air films relative to the unconfined system. Scale bars denote lengths of 1 mm for each figure.

movement of the SCL (see Figure 7.5a). (Note that this is consistent with observations from prior work where a glycerol film was deposited on a confining surface during air entrainment [138].) Through successive rupture and elongation of the air film, the SCL moves further away from the DCL, resulting in a broad air layer between the meniscus and substrate. Due to the relatively large reservoir, liquid displaced during unconfined air entrainment negligibly impacts the liquid level (i.e., SCL position), allowing triangular air films with consistent size to form along the DCL.

As illustrated in Figure 7.16, air entrainment is characterized by triangular air films when the meniscus is positioned near the mask corner. Although the meniscus is confined, the SCL remains fixed at the corner, preventing the formation of the broad air film discussed previously. Liquid pressurization tends to decrease the scale of air films that form at the onset of air entrainment. Since narrow gaps allow higher values of P_{app} before depinning the SCL (similar to observations of pressurized fiber coating [115]), much smaller air films are observed with $H = 100 \quad \mu$m (Figure 7.16c) than in the other geometries reported in this study (e.g., Figure 7.16a-b).

7.4.2 Thickness

Air-film thickness can be approximated from visualizations of the rupture events idealized in Figure 7.12. During rupture, a mass of air separates from the the DCL with volume $A \times h_f$, where h_f is the mean height of the air film defined by area A. The air mass forms a spherical bubble of diameter D as it becomes entrained within the liquid flow. Assuming that the volume of the air mass remains constant throughout this process, the film thickness can be found as

$$h_f = \frac{\pi D^3}{6A} \tag{7.4}$$

with A and D measured directly from visualization images. Previously, a similar method was used to estimate h_f with good precision during air entrainment in silicon oils [105].

Using (7.4), air-film thicknesses are estimated at the onset of air entrainment with different solution viscosities in the unconfined geometry ($H \to \infty$), as plotted in Figure 7.17 (see Appendix D.1 for more detail on the measurement of h_f). Similar to the trend of decreasing W with increasing μ (see Figure 7.15a), the data in Figure 7.17 shows that increasing liquid viscosity thins the entrained air film. The air-film thickness is approximated at $h_f \sim 10 \quad \mu$m for high-viscosity glycerol ($\mu \approx 1000$ cP) and increases by approximately an order of magnitude in the low-viscosity regime ($\mu < 50$ cP). Estimates from the glycerol system used in this study qualitatively match similar measurements made with silicon oils [105], suggesting that the trend may be a general feature of air-entrainment systems.

It should be noted that the method of estimating h_f using (7.4) does not necessarily accurately reflect the actual thickness of the triangular air films along the DCL (see Figure 7.12a). Prior to complete rupture, the interface enveloping the detaching air mass becomes more curved, making the thickness less uniform throughout the area A. Capillary forces resulting from the curved interface tend to squeeze air out of the mass and back into the continuous air phase above the meniscus. Furthermore, the triangular air films consistently show a thickness variation near the DCL resembling a capillary ridge (see Figure 7.14). Considering all of these factors, it is difficult to know how estimates from (7.4) map onto the true air-film thickness profile that extends from the DCL to the outer meniscus. Nevertheless, a clear trend arises from the data plotted in Figure 7.17, suggesting that this uncertainty does not obscure the dominant behavior

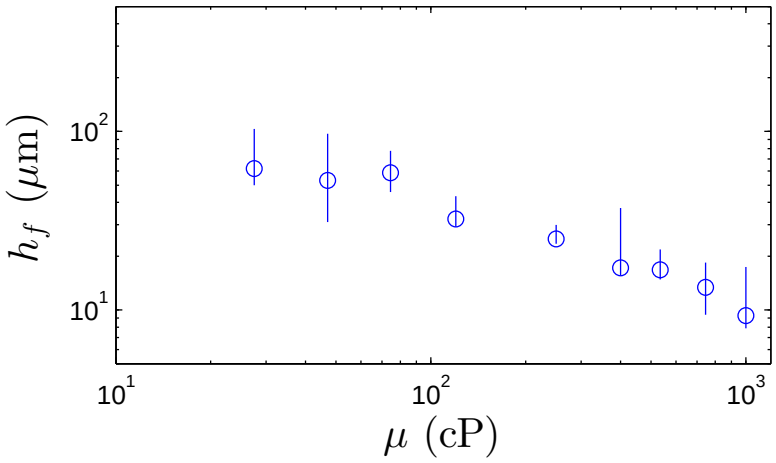

Figure 7.17: The effect of liquid viscosity on air-film thickness h_f measured at Ca^{crit} in the unconfined geometry ($H \to \infty$).

of air-film thickness as a function of μ.

7.4.3 Rupture

Rupture is initiated by a point of liquid-substrate contact that pierces through the air film. Figure 7.18a illustrates that multiple liquid contacts tend to simultaneously nucleate just above the triangular air films. The liquid sites increase in size as they are pulled with the substrate motion (Figure 7.18b). Upon intersection with the DCL, the liquid sites trap air bubbles that become entrained within the liquid flow (Figure 7.18c).

Variations in the air-film thickness are typically observed prior to the rupture events shown in Figure 7.18. These thickness variations resemble wave crests moving perpendicular to the substrate velocity. Figure 7.19 demonstrates typical behavior of these "traveling waves" as they traverse the triangular air films. In this example, two visible waves separated by a distance l_0 travel from left to right with speed V, which approximately matches the substrate speed U (further discussion below). Each wave remains inclined at an angle similar to ψ, suggesting that the initial thickness perturbation (that generates the traveling wave) arises during elongation of the triangular air film.

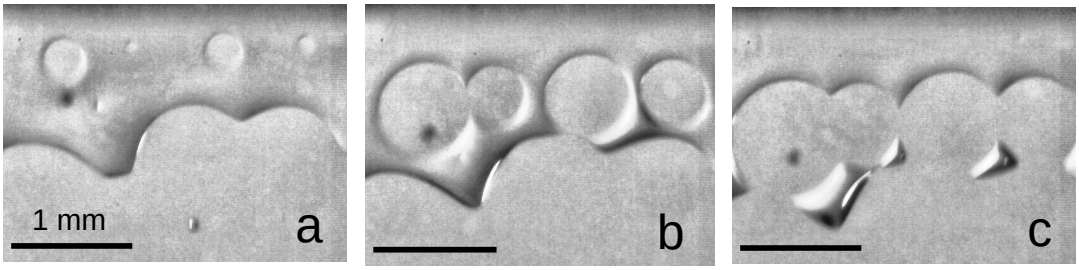

Figure 7.18: A sequence of visualizations showing the periodic nucleation of liquid contacts through the elongated air film, leading to film rupture and entrainment of air bubbles at Ca^{crit}. The images corresponds to (a) 2, (b) 5, and (c) 7 ms after the first point contact is observed. Scale bars denote lengths of 1 mm for each figure. System parameters: $\mu = 400$ cP and $H \to \infty$.

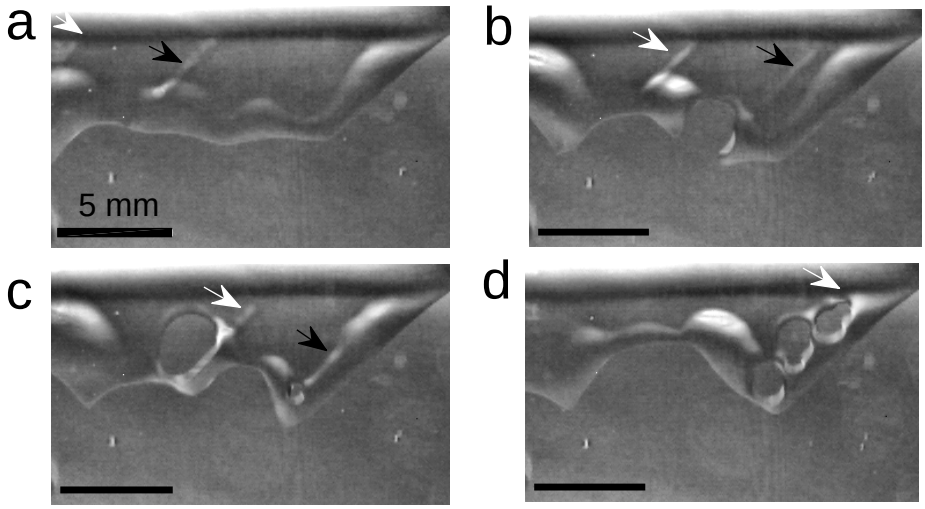

Figure 7.19: Visualization sequence illustrating thickness variations in air films leading to air-film rupture at Ca^{crit}. Two waves (denoted by white and black arrows) are shown moving from left to right at time (a) 0 ms, (b) 7.5 ms, (c) 10.0 ms , and (d) 17.5 ms. System parameters: $\mu = 25$ cP and $H \to \infty$.

Figure 7.2 illustrates the complete rupture mechanism suggested from the observations of Figure 7.18 and Figure 7.19. At the critical substrate speed, air films form that are characterized by a thin region connected to a thicker capillary ridge near the DCL. Traveling waves perturb the interface, making the thinnest portion susceptible to break-up as long-range molecular forces initiate liquid contact with the substrate. Since perturbations are distributed along intervals of the wavelength, multiple liquid contacts nucleate simultaneously with periodic spacing characterized by a distance l_0. Substrate motion drives liquid toward the rupture site, growing the liquid contact until air bubbles are released from the DCL.

Each system used in this study shows signs of the rupture mechanism discussed above. For instance, each glycerol solution exhibits a characteristic wavelength l_0 associated with rupture, as demonstrated in Figure 7.20 for the unconfined geometry. The data show that shorter wavelengths (smaller l_0) result during air entrainment in more viscous liquids. This trend reverses with decreasing μ until $l_0 \sim 5$ mm, at which point gravitational forces begin to level thickness variations along the interface (note that $l_{cap} \approx 2.5$ mm for glycerol), preventing further increase of l_0. Interestingly, the behavior of l_0 closely matches the trend of decreasing W as μ increases (refer to Section 7.4.1). Therefore, the size and distribution of triangular air films may be linked to the rupture mechanism that reshapes the DCL with periodic perturbations. The width W only significantly deviates from l_0 when a single air film spans the width of the substrate by pinning against the tape edges (see Figure 7.13). The abrupt change in W at $\mu = 25$ cP suggests that in addition to l_{cap} (which limits l_0 in the low-viscosity regime), some viscous length scale plays a significant role in determining the DCL shape. This viscous length scale is discussed in more detail in Section 7.5.

7.5 Discussion and Conclusions

This work focuses on the onset of air entrainment resulting when a planar (tape) substrate enters a glycerol bath at some super critical speed. Unlike steady wetting, which features a smooth air/liquid meniscus, air entrainment evolves from a jagged sawtooth meniscus that forms a serrated DCL at the substrate. Generally, system parameters influence the critical speed and DCL shape associated with this transition.

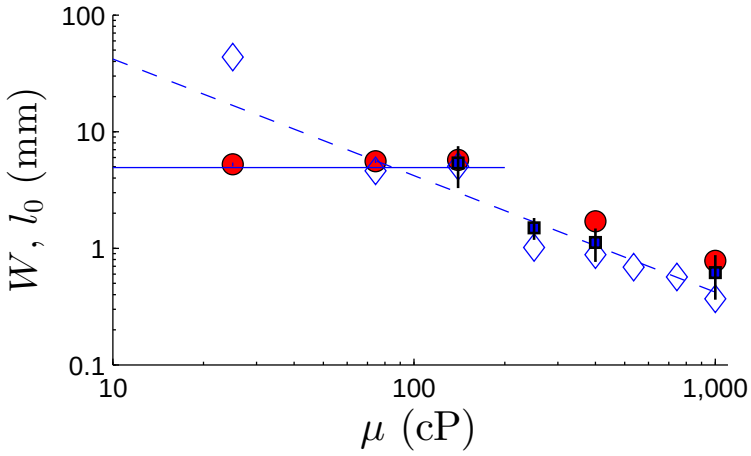

Figure 7.20: The perturbation wavelength l_0 observed at Ca^{crit} plotted against liquid viscosity. The distance l_0 is measured between traveling waves (circle) and nucleation sites (square) as illustrated in Figure 7.2b. The air-film width W (diamond) is also plotted for each case. The dashed line is taken from the fit of W in Figure 7.15a and the solid line denotes $l_0 \approx 2l_{cap}$, where $l_{cap} = 2.5$ mm. Note that error bars lie within symbol margins when not shown.

Similar to prior work, experiments conducted in this study demonstrate that higher liquid viscosities [2] and confined geometries [138] postpone air entrainment to higher substrate speeds. Critical capillary numbers Ca^{crit} associated with the onset of air entrainment closely match correlations from previous data sets, which validates the novel experimental apparatus used in this investigation. Furthermore, the current work expands upon past results by showing that the power-law dependence of Ca^{crit} on μ expressed in (7.1) is negligibly altered by meniscus confinement. In other words, confinement and viscosity effects independently influence the onset of air entrainment. As reflected by fits of the data listed in Table 7.1, smaller confinement gaps H increase Ca^{crit} through changes to the pre-factor in (7.1). Therefore, independent of viscosity, critical speeds increase logarithmically as H decreases, as captured by the scaling argument in (7.2).

The behavior of Ca^{crit} can be understood with insight gained from a hydrodynamic model for dynamic wetting failure that has been developed in our prior work [138, 157]. The model shows that strong pressure gradients pump the air flow away from the DCL during steady wetting. Liquid stresses deform the interface and restrict the air

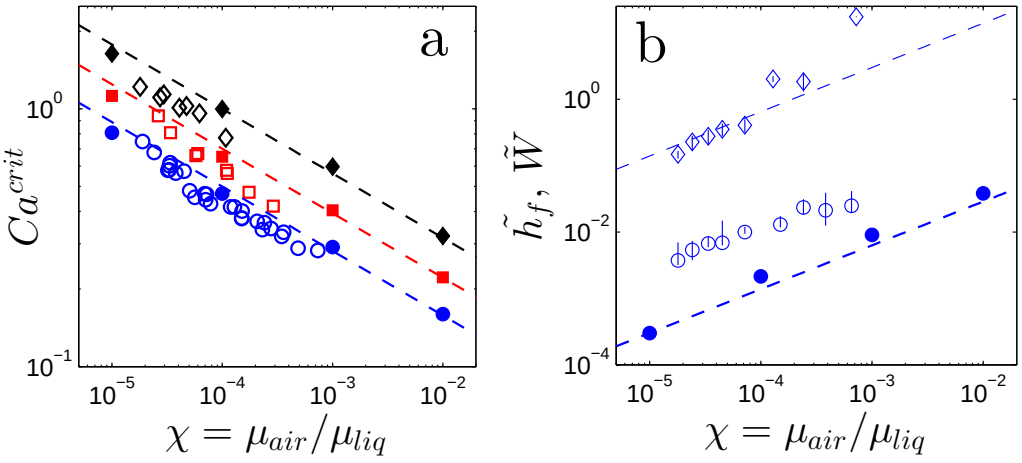

Figure 7.21: Comparison of experimental data with predictions from the 2D flow model. (a) Critical capillary numbers measured as a function of the viscosity ratio $\chi = \mu_{air}/\mu$ for various confinement gaps H. Open symbols denote experimental data taken from Figure 7.6a assuming $\mu_{air} = 0.018$ cP. Closed symbols are calculated with the 2D flow model for $\lambda = l_{slip}/H = 10^{-5}$ (circle), 10^{-4} (square), and 10^{-3} (diamond). Dashed lines represent $Ca^{crit} \propto \chi^{-0.258}$ (scaling from (7.1)) fitted to the model data for each λ. (b) Air-film thickness (circle) and air-film width (diamond) plotted against the viscosity ratio. Experimental data (open symbols) taken from Figure 7.15a and Figure 7.17 are non-dimensionalized using glycerol's capillary length $l_{cap} \approx 2.5$ mm. 2D flow results (closed symbols) are computed at Ca^{crit} with $\lambda = 10^{-5}$. Dashed lines represent $h_f \propto \chi^{2/3}$.

flow to a thin region between the interface and substrate until air stresses exceed the local capillary forces at some critical substrate speed, causing unsteady air entrainment. Decreasing the air viscosity μ_{air} relative to μ lessens the impact of the air stresses near the DCL, allowing for steady wetting at higher speeds. Figure 7.21a demonstrates that this trend of increase Ca^{crit} with decreasing $\chi = \mu_{air}/\mu$ matches the power-law behavior observed by experimentally varying the glycerol viscosity.

Similar to experimental observation, the model predicts that critical speeds increase when the air/liquid meniscus is confined to a narrow gap H. Confinement is modeled with the parameter $\lambda = l_{slip}/H$, where l_{slip} is a small length scale ($l_{slip} \ll H$) associated with the magnitude of fluid slip along the substrate near the DCL. This micro-scale slip plays a more significant role as λ increases, reducing viscous bending of the interface and allowing for steady wetting at higher speeds. Similar to the scaling relationship in (7.2),

predicted values of Ca^{crit} carry a logarithmic dependence on λ. Therefore, the choice of the l_{slip} slightly influences the absolute value of the predicted critical speed, but does not change the dominant trends shown in Figure 7.21a. Using $l_{slip} \sim 10$ nm, Ca^{crit} values predicted from the computational model come within 20 % of the experimentally measured critical speeds. (Note that similar to the findings of our prior work [138], the computational model predicts a lower l_{slip} values than is used with the scaling (7.2) in Figure 7.7b.)

In addition, experimental visualizations reveal interface characteristics at the onset of air entrainment that qualitatively match predictions from the model. Most notably, the elongated air films are thickest near the DCL (e.g., Figure 7.14), resembling capillary ridges (see Vandre *et al.* (2013) [157] for supporting data from the model). Although the steady-state model is unable to track the transient dynamics leading to air entrainment, the experimental system may proceed *quasi*-steadily along unstable solution branches, where the model predicts air-film elongation and subsequent capillary-ridge formation. This precise behavior is observed for the case of liquid-film withdrawal, in which a thick capillary wave forms at the dewetting contact line prior to complete entrainment [121], matching model predictions near steady-state bifurcation points [96]. However, liquid films eventually elongate to a state of steady deposition (i.e., Landau-Levich film) [93], whereas air films rapidly become unstable and rupture into bubbles.

The size of the air film may be determined by a local balance of capillary and viscous stresses. The hydrodynamic model shows that this visco-capillary balance crucially influences an interfacial inflection point in the vicinity of the DCL. The inflection-point height decreases exponentially with increasing Ca, sharpening interface curvature near the DCL to balance local capillary forces with the increasing viscous stress. Since Ca^{crit} increases with higher liquid viscosity, smaller inflection-point heights are computed at the onset of air entrainment with lower χ values. Figure 7.21b demonstrates that this trend resembles the behavior of the experimental air-film thickness h_f measured with different glycerol solutions. (Note that the overbar denotes dimensionless lengths, which are scaled with l_{cap} and H for the experimental and model data, respectively.) Both the experimental and computational data reflect weak power-law behavior (approximately $h_f \propto \mu^{-2/3}$), though the origin of such behavior is not yet completely understood. Figure 7.21b shows that this trend also describes the increase in air-film width W as viscosity

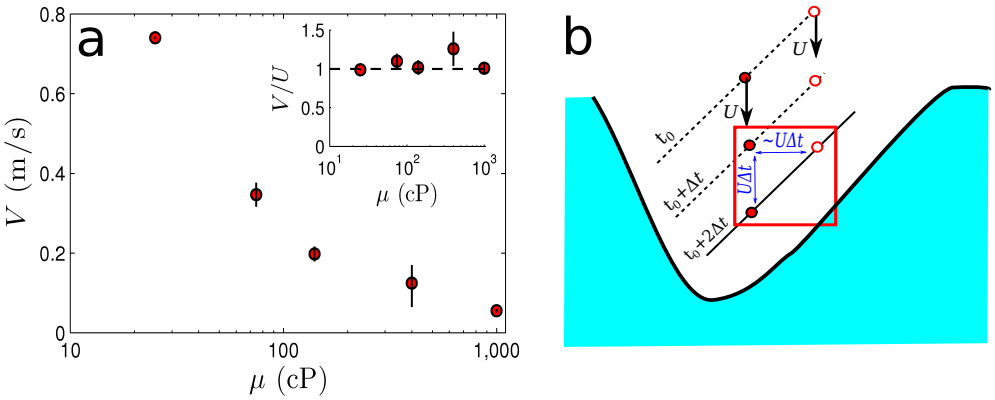

Figure 7.22: (a) Speed of wave propagation V measured at Ca^{crit} as a function of liquid viscosity for the unconfined geometry ($H \to \infty$). The inset shows V/U for each case and the dashed line marks $V/U = 1$. (b) Illustration of a wave moving with downward speed U at times t_0, $t_0 + \Delta t$, and $t_0 + 2\Delta t$. Due to the 45^o angle, a point along the wave may appear to move horizontally with speed $V \sim U$. However, this type of measurement actually accounts for two different points (closed vs. open symbols) that both propagate vertically toward the DCL.

decreases with the exception of the $\mu = 25$ cP case, where a single air film pins against the substrate edges. This suggests that the visco-capillary balance discussed above may influence the size of triangular air films in addition to film thickness. However, it is not yet clear how this effect interacts with the length scale arising from the traveling wave perturbations discussed in Section 7.4.3.

Fluid interfaces struggle to move around surfaces with corners due to contact-line pinning along the sharp edge. Such an obstruction is used in the current system to resist the tendency of the meniscus to rise into the confinement gap in response to higher applied pressure P_{app} (see Figure 7.5b). Due to the pinning of the meniscus against the corner, liquid pressurization changes the shape of the interface, resulting in steady wetting at faster speeds (e.g., Figure 7.11) and smaller air films at the onset of air entrainment (e.g., Figure 7.10). Similar effects have been observed in high-speed fiber coating [115, 88]. However, to the authors' knowledge, this work presents the first experimental demonstration of air entrainment postponed by liquid pressurization in confined planar systems.

Although this pressurization effect is not directly studied with the computational model, similar trends are observed when a large body force is numerically imposed on

a confined air/liquid meniscus (see Appendix D.2). The body force acts as a constant pressure gradient within the wetting liquid, pressurizing the liquid below the meniscus ($\sim P_{app}$) relative the air pressure ($\sim P_{atm}$) above. Higher liquid pressures force larger interface curvature, causing the meniscus to appear shorter as it only bends sharply on small scales close to the DCL. Due to the sharp curvature, the interface supports large capillary stresses that resist air entrainment to high substrate speeds. In reality, the cornered obstruction will generate a more complex pressure field than that modeled with a body force. However, qualitative agreement between the two cases suggests that hydrodynamic forces capture the essential mechanics of dynamic wetting near the onset of air entrainment.

Air entrainment ultimately occurs when elongated air films are perturbed and break into bubbles. In the current system, these transient events are linked to traveling waves that traverse the thin air layer (see Section 7.4.3). These waves appear to the translate laterally along the substrate (refer to Figure 7.2) with speed V, plotted as a function of μ in Figure 7.22a. The data show that V approximately matches the substrate speed U for each case (see inset of Figure 7.22a), suggesting that thickness variations originate above the triangular air film and follow the substrate motion toward the DCL. Despite the downwardly-directed velocity, a single wave may seem to move laterally through the air film, as illustrated by Figure 7.22b. Two images recorded at times separated by Δt appear to show the wave translating a horizontal distance $\sim U\Delta t$, whereas the material point (red symbol in Figure 7.22b) actually moves vertically through the air film. Since the waves remain inclined at approximately 45^o angles, horizontal and vertical components of velocity approximately match the substrate speed U. Further investigation of the local flow field and interface shape is required to gain insight into the mechanism governing the period l_0 (see Figure 7.2 and Figure 7.20) of the wave disturbances and subsequent interface rupture, leading to air-bubble entrainment.

Chapter 8

Curtain Coating

8.1 Introduction

Dynamic wetting is integral to a number of industrial systems where a liquid displaces another fluid along a solid surface. In particular, coating flows rely on steady dynamic wetting to smoothly and uniformly distribute liquid layers on moving substrates. This objective becomes more challenging to satisfy at higher process speeds, where a variety of defects may arise from disturbances to the wetting dynamics. At some critical speed, wetting catastrophically fails and air bubbles become entrained in the coating. Usually, this transition must be avoided to maintain coating integrity, leaving practitioners with the choice of operating at subcritical speeds or making significant system alterations to achieve higher production capacity. However, since the fundamentals of wetting failure remain poorly understood, relatively few system designs are known to postpone air entrainment.

Curtain coating is one system that is recognized for remarkably fast wetting, where speeds $\sim$10 m/s are typically achieved within the industry [114]. In this device, a coating liquid with viscosity μ_{adv} and density ρ is deposited from a hopper or die at a height h_{curt} above a solid surface [37]. Initially flowing with speed V, the liquid falls as a two-dimensional (2D) curtain that is accelerated by gravity until impacting a substrate moving with speed U. Hydrodynamic stresses from the impinging curtain are thought to assist fluid displacement at the dynamic contact line (DCL) [26]. When displacement is successful, the liquid steadily wets the substrate and forms a coating film of

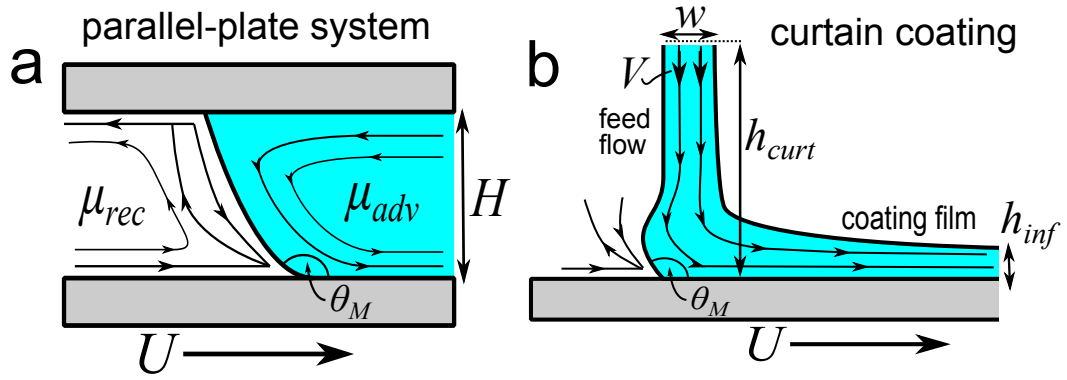

Figure 8.1: Illustration of (a) parallel-plate and (b) curtain-coating geometries.

thickness h_{inf} downstream. Wetting fails at some critical substrate speed U^{crit}, leading to air entrainment at the DCL. Typically the onset of wetting failure is influenced by the relative magnitude of viscous stresses and surface tension σ, making the capillary number $Ca = \mu_{adv}U/\sigma$ the primary dimensionless group describing high-speed wetting behavior. However, interface shapes and critical speeds are known to depend on other parameters in curtain-coating systems with particular sensitivity toward the feed flow rate [82, 25, 83]. Researchers have struggled to reproduce this behavior with hydrodynamic models, claiming that a more complicated description of the DCL mechanics may be needed to describe high-speed fluid displacement [39].

This chapter investigates the problem of fluid displacement in curtain coating using the hydrodynamic model developed in Chapter 2. Unlike prior works that neglect the air flow, we consider the interaction of *two* viscous fluids. Since curtain coating contains a challenging domain geometry with upstream and downstream air/liquid interfaces, we develop a new computational method that significantly reduces the computational cost associated solving for the two-fluid flow. In essence, we use a hybrid FEM technique to compute the 2D flow of the advancing fluid while approximating the receding flow (with viscosity μ_{rec}) with one-dimensional (1D) lubrication equations. Using the hybrid model, we find solution paths for curtain coating with a 25 cP liquid surrounded by air. As shown schematically in Figure 8.1, we compare curtain coating results to the parallel-plate case studied earlier in this thesis (e.g., Chapter 4) to demonstrate similar mechanisms for wetting failure. Furthermore, we find that many key characteristics of high-speed curtain coating are missed when neglecting the air flow, as is the current

convention in the literature.

The chapter is organized by the following sections. Section 8.2 develops the hybrid FEM model and compares solutions against results from the full 2D flow model. Section 8.3 discusses numerical details associated with implementation of the hybrid model in the curtain-coating system. Section 8.4 presents solution paths from the curtain-coating system and makes critical comparisons with parallel-plate results from previous chapters of this thesis. Lastly, Section 8.5 summarizes the findings and discusses their implications on the study of curtain coating and other complex wetting behavior.

8.2 Hybrid 1D/2D Method

In this section, a novel 1D/2D hybrid FEM model is developed using aspects of the quasi-parallel (QP) approach and the 2D flow model from Sections 2.2 and 2.3, respectively. Formulation of the hybrid model is motivated by the observation that the receding fluid becomes long and slender (especially in the case of air entrainment where $\chi \ll 1$) as the interface deforms near the onset of wetting failure. Consequently, the 1D lubrication-type approximation of the QP approach works well for the receding flow, but full 2D computations are needed for the advancing flow. In essence, the hybrid model accounts for complete hydrodynamics of the advancing flow, while approximating only viscous stresses that result from the receding flow.

Advantages of the hybrid model arise from its computational efficiency. Since the receding-fluid domain is not discretized, the hybrid model reduces the number of variables by nearly 50% in comparison to the 2D flow model. In addition, mesh quality is improved because computational nodes are not needed in half of the domain (i.e., mesh lines do not continue into the receding-fluid domain). These factors make the hybrid model an ideal candidate for studying fluid displacement in realistic coating systems that commonly include complicated geometries, complex liquid rheology, and the transport of surface-active agents. This section intends to only introduce the hybrid model and validate it against a few select cases from the 2D flow model. The hybrid model is applied to curtain coating in Section 8.3 with results presented in Section 8.4.

8.2.1 Governing Equations and Numerical Considerations

The hybrid model uses the foundation of the 2D flow model outlined in Section 2.3. The 2D governing equations (2.1) - (2.9) and FEM framework are applied to the advancing fluid phase, as shown in Figure 8.2. This includes the Navier-Stokes equations to govern the advancing-fluid velocity v and pressure p

$$\boldsymbol{\nabla \cdot v} = 0, \quad Re(\boldsymbol{v \cdot \nabla v}) = \nabla^2 \boldsymbol{v} - \boldsymbol{\nabla} p, \tag{8.1}$$

and a set of stress balances along the fluid interface $y = h$

$$\boldsymbol{n \cdot T \cdot t}|_{rec} = \boldsymbol{n \cdot T \cdot t}|_{adv}; \tag{8.2}$$

$$\kappa = Ca(\boldsymbol{n \cdot T \cdot n}|_{rec} - \boldsymbol{n \cdot T \cdot n}|_{adv}). \tag{8.3}$$

(See Section 2.1 for a complete description of the governing equations.) In the expressions above, $\boldsymbol{T}$ is the Newtonian stress tensor, κ is the interface curvature, and u and v are the horizontal (x-coordinate) and vertical (y-coordinate) velocity components, respectively. Normal ($\boldsymbol{n}$) and tangent ($\boldsymbol{t}$) vectors are defined by the interface profile at $y = h$. The stress tensor for the receding fluid contains the viscosity ratio, $\chi = \mu_{rec}/\mu_{adv}$, such that $\boldsymbol{T}|_{rec} = \frac{\chi}{2}[\boldsymbol{\nabla v} + (\boldsymbol{\nabla v})^T]$. Note that p includes the pressure head from gravity $\rho g x$ (the "modified pressure" in [119]).

The lubrication-type approximation of the QP approach (see derivation in Section 2.2) is applied to the receding-fluid flow, resulting in "loading" terms that augment the stress balances at the interface. Using lubrication theory [67], normal and tangential stresses in the receding flow are approximated by

$$\boldsymbol{n \cdot T \cdot t}|_{rec} \approx \chi \frac{\partial u}{\partial y} \; ; \quad \boldsymbol{n \cdot T \cdot n}|_{rec} \approx p. \tag{8.4}$$

Since FEM uses the weak form of the 2D governing equations [128] the normal and tangential stresses in (8.4) cannot be directly applied to a boundary condition, but must be converted into an effective traction vector:

$$\boldsymbol{n \cdot T}|_{rec} = \{\chi n_y \frac{\partial u}{\partial y} - n_x p \; , \; -\chi n_x \frac{\partial u}{\partial y} - n_y p\}, \tag{8.5}$$

where subscripts indicate the x and y components of the normal vector $\boldsymbol{n}$ at the interface. Note that (8.4) is recovered from normal and tangential projections of (8.5), confirming that $\boldsymbol{n \cdot T}|_{rec}$ contains the appropriate loading terms from the QP approach.

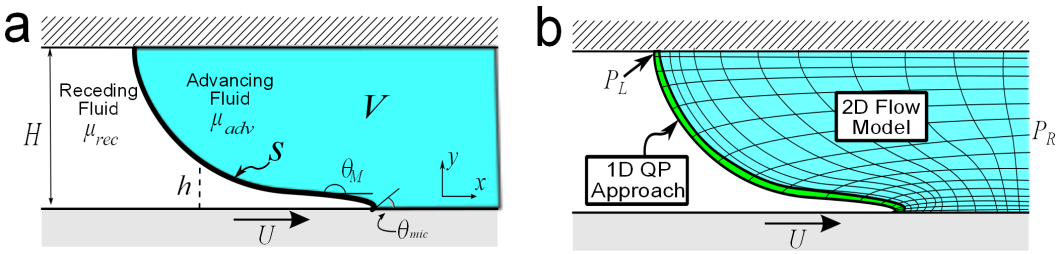

Figure 8.2: Schematic of the (a) 2D flow system and (b) the numerical scheme used in the hybrid FEM model. The advancing flow (volume V) is treated with the 2D flow model while the receding flow is approximated with the QP approach applied to 1D elements along the interface (surface S).

Expression (8.5) enters the hybrid FEM model through the following weak-form residual applied to the advancing phase along the fluid interface:

$$R_{hybrid} = \int_S \phi \left(\frac{1}{Ca} \frac{\mathrm{d}\boldsymbol{t}}{\mathrm{d}s} - \boldsymbol{n} \cdot \boldsymbol{T}|_{rec} \right) dS + \int_V \phi \left(Re\ \boldsymbol{v} \cdot \boldsymbol{\nabla} \boldsymbol{v} - \nabla^2 \boldsymbol{v} + \boldsymbol{\nabla} p \right) dV \qquad (8.6)$$

where ϕ is the basis function, s is the interfacial arc length, and V and S define the domain volume and interface-boundary curve, respectively (refer to Figure 8.2). With exception of the loading term ($\boldsymbol{n} \cdot \boldsymbol{T}|_{rec}$), all flow variables within (8.6) are referenced to the advancing fluid.

In order to solve (8.6), the receding fluid pressure p and velocity gradient $\frac{\partial u}{\partial y}$ (see (8.5)) must be described as functions of the interface height and flow variables in the advancing phase. Following the derivation of the QP approach (refer to Section 2.2.1), the expressions below define fluid pressure within the lubrication limit:

$$Ah + \frac{1}{2} B h^2 + \frac{1}{6} \frac{dp}{ds} h^3 = 0, \qquad (8.7)$$

$$\frac{\partial u}{\partial y} = B + \frac{dp}{ds} h \quad \text{where} \quad A = \frac{\chi U h + \chi \lambda u_{int} - \frac{1}{2} \frac{dp}{ds} h^2}{\lambda + h}\ ,\ B = \frac{-\chi U + A}{\lambda}. \qquad (8.8)$$

The expressions above reflect the fact that fluid must slip in the vicinity of the contact line to avoid an unphysical infinite-force singularity [65] (further discussion of slip can be found in Section 1.2.3). Here λ is the dimensionless slip length used in a Navier boundary condition (i.e., (2.9)) that is applied along the substrate. In the parallel-plate geometry (see Figure 8.2), $\lambda = l_{slip}/H$ where l_{slip} is the dimensional slip length and H is the gap, but the definition of λ depends on details of the system geometry in general (e.g., for curtain coating $\lambda = l_{slip}/w$ where w is the curtain width).

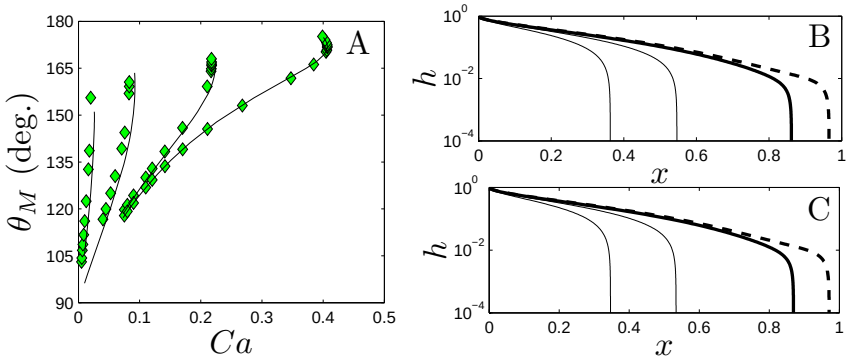

Figure 8.3: Comparison of steady-state solutions obtained with the 2D flow model and the hybrid FEM model. (a) Steady-state solution families are plotted for $\chi = 1, 10^{-1}, 10^{-2}$ and 10^{-3} (decreasing left to right). Solid lines and diamond symbols are obtained from the 2D flow model and hybrid model, respectively. (b) Air/liquid ($\chi = 10^{-3}$) interface profiles obtained from the hybrid model for (going left to right) $Ca = 0.110, 0.211, 0.407$ and 0.399. (c) Air/liquid ($\chi = 10^{-3}$) interface profiles calculated from the 2D flow model for $Ca = 0.104, 0.202, 0.407$ and 0.398. In both cases, the bold and dashed curves represent critical and unstable solutions, respectively. Additional parameters used with the models are listed in the following: $\lambda = 10^{-4}$, $\theta_{mic} = 90^o$, $Bo = 0$, $Re = 0$ and $H/D = 0$.

Equation(8.7) uses the approximation $dx \approx ds$ from the QP approach to express pressure gradients with respect to the arc-length coordinate s. This approximation allows direct integration of (8.6) along s (following substitution of (8.5), (8.7), and (8.8)). Integration proceeds in an analogous manner to 2D FEM, except that the pressure function in (8.7) only exists within nodes along the fluid interface. Thus, the interfacial nodes comprise "1D elements" of the receding fluid, where the pressure is approximated by biquadratic basis functions that span from the SCL (top plate in Figure 8.2) to the DCL (bottom plate).

One boundary condition is needed at $h = 1$ to specify the receding-fluid pressure from $\frac{dp}{ds}$ in (8.7) - (8.8):

$$p = P_L. \tag{8.9}$$

Similar to the 2D flow model, (8.9) imposes an arbitrary pressure drop $\Delta P = P_L - P_R$ (note that P_R remains the outflow pressure datum for the advancing fluid) that is used as an adjustable parameter to satisfy θ_{mic} while numerically fixing the DCL at x_o in the computational domain. This procedure directly follows the description in Section 2.3.

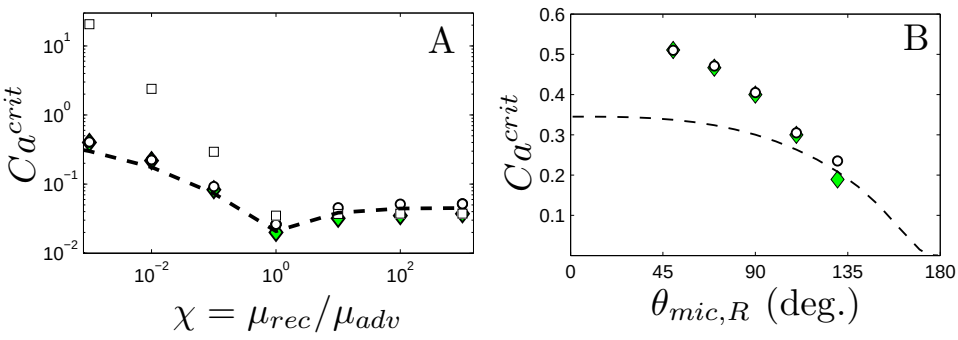

Figure 8.4: Validation of critical capillary numbers obtained from the hybrid model while varying (a) fluid viscosity ratio and (b) substrate wettability. The relevant system parameters are listed in the following: (a) $\lambda = 10^{-4}$ and $\theta_{mic} = 90^o$; (b) $\lambda = 10^{-4}$ and $\chi = 10^{-3}$. Data are shown for the 2D flow approach (circles), the QP approach (squares), the hybrid model (diamonds), and the asymptotic theory in equation (4.1) with $\lambda_{Cox} = \lambda = 10^{-4}$ (dashed line).

8.2.2 Numerical Validation

The 1D/2D hybrid model has been validated against 2D flow results over a fairly broad parameter range. Figure 8.3 illustrates that solution paths from the hybrid model, including the turning point at Ca^{crit}, match 2D flow result for various values of χ. In fact, the hybrid model appears to converge to the 2D flow model as χ decreases within the air/liquid displacement regime ($\chi \ll 1$). Comparing Figure 8.3B and Figure 8.3C, it can be seen that the predicted interface profiles are visually identical for air/liquid displacement, even along the unstable solution branch.

Figure 8.4 demonstrates the ability of the hybrid model to accurately predict critical capillary numbers associated with the onset of wetting failure. In Figure 8.4A, Ca^{crit} values are plotted for various viscosity ratios. Again, the hybrid model compares well with the 2D-flow model, especially in the air/liquid regime where the QP approach fails (refer to Section 2.2.4). Figure 8.4B shows that the agreement extends to various substrate wettabilities. (The data remains restricted to partially-wetting substrates where $50^o \leq \theta_{mic} \leq 130^o$ due to numerical limitations of the quadrilateral elements used within the advancing fluid as discussed in Section 2.3).

Collectively, the plots of Figure 8.3 and Figure 8.4 illustrate that the hybrid model accurately approximates steady 2D fluid displacement up to the onset of wetting failure

Dimensional	Values	Dimensionless	Values
μ_{adv}	1-1000 cP	$\chi = \mu_{rec}/\mu_{adv}$	$10^{-5} - 10^{-2}$
σ	30 - 70 mN/m	$Ca = \mu_{adv}U/\sigma$	$10^{-1} - 10^{1}$
U, V	$0.01 - 1$ m/s	$Re = \rho V w/\mu_{adv}$	$10^{-1} - 10^{1}$
ρ	~ 1000 kg/m^3	$Bo = (\rho g/\sigma)(wV/U)^2$	$10^{-4} - 10^{-1}$
w, h_{inf}	0.01 - 1 mm	$\lambda = l_{slip}/w$	$10^{-5} - 10^{-3}$
h_{curt}	1 - 25 cm	h_{curt}/w	$10^{1} - 10^{2}$
θ_{mic}	70^o (?)	$\lvert\partial h/\partial x\rvert = \lvert\tan\theta_{mic}\rvert$	> 1

Table 8.1: Liquid properties and operating conditions typical of curtain coating. The list attempts to summarize the range of values reported in the literature [26, 37, 82, 38, 83, 39]. Note that θ_{mic} has not been well characterized in general. The listed value reflects the static angle measured in [82].

for a variety of systems. Errors become negligible in the the case of air/liquid displacement because viscous effects from the air are only important near the DCL, where the air flow is restricted to a slender wedge between the substrate and fluid interface. Consequently, receding-air pressures are well-described by the lubrication approximation (QP approach) used in the hybrid model. This accuracy holds true up to the critical capillary number, which makes the hybrid model an ideal option for modeling the onset of air entrainment in complex coating systems (e.g., curtain coating in the following sections) where computational cost may be prohibitive for the 2D flow model. Although similar 1D/2D FEM methods have previously been used to study single-phase [159] and two-phase [160] flows, this is the first work, to the best of the authors' knowledge, that presents a hybrid model for fluid displacement with dynamic contact lines.

8.3 Curtain-coating Model

8.3.1 Fluid Properties and Operating Conditions

Curtain coating features a variety of material properties, flow controls, and geometric parameters that influence the state of operation. For example, the curtain height h_{curt}, width w and angle of intersection with the substrate have been altered to alter dynamic wetting behavior [26, 38]. To focus on the fluid-displacement mechanics, we fix the geometric parameters as follows: $w = 1$ mm, $h_{curt} = 10$ mm, and the curtain

falls perpendicular to the substrate. Even while fixing the device geometry, there is a broad range of system parameters to consider, as demonstrated by Table 8.1. It can be seen that the liquid properties influence a number of dimensionless groups, including the viscosity ratio χ, capillary number Ca, Reynolds number Re, and bond number Bo. (Note that the curtain width w is the characteristic length scale used for all dimensionless groups defined in Table 8.1). For simplicity, we analyze a single coating liquid with properties similar to prior experimental investigations [25, 39]: $\mu_{adv} = 25$ cP, $\sigma = 70$ mN/m, and $\rho = 1000$ kg/m^3. In addition, we assume an ideal, smooth substrate with wettability defined by a microscopic contact angle $\theta_{mic} = 90^o$ and dimensionless slip length $\lambda = l_{slip}/w = 10^{-2}$. (This relatively large values of λ is selected for numerical convenience, as mentioned in the following section.) Section 8.4 characterizes wetting effects generated from changes to the remaining curtain-coating parameters: the receding fluid viscosity μ_{rec} (in χ); the substrate speed U (in Ca and Bo); the feed-flow velocity V (in Re and Bo).

8.3.2 Implementation of Hybrid FEM

Figure 8.5 illustrates the model curtain-coating system. A curtain is formed with two free surfaces (see Figure 8.5a) as liquid is deposited from an elevated slot die (width w) with downward velocity V. The liquid curtain falls from a height h_{curt} above a substrate that moves with speed U. (Although not shown in Figure 8.5, gravity also points downward, parallel with the curtain.) The liquid impacts the substrate at the dynamic contact line (DCL), whose position x_{DCL} depends on parameters of the curtain flow (discussed in Section 8.4.1). During steady operation, curtain coating ultimately deposits a liquid coating film with height h_{inf} that is carried downstream with the substrate motion.

The hybrid FEM model developed in Section 8.2 is used to study the hydrodynamics of fluid displacement in curtain coating. Similar to the parallel-plate example explored above, viscous stresses from the air flow are approximated by 1D lubrication equations near the DCL (region 8 in Figure 8.5). The liquid curtain domain is partitioned into seven regions to comply with the meshing scheme (refer to Section 2.3). In essence, each region defines a separate rectangular subdomain in the computational coordinates (see

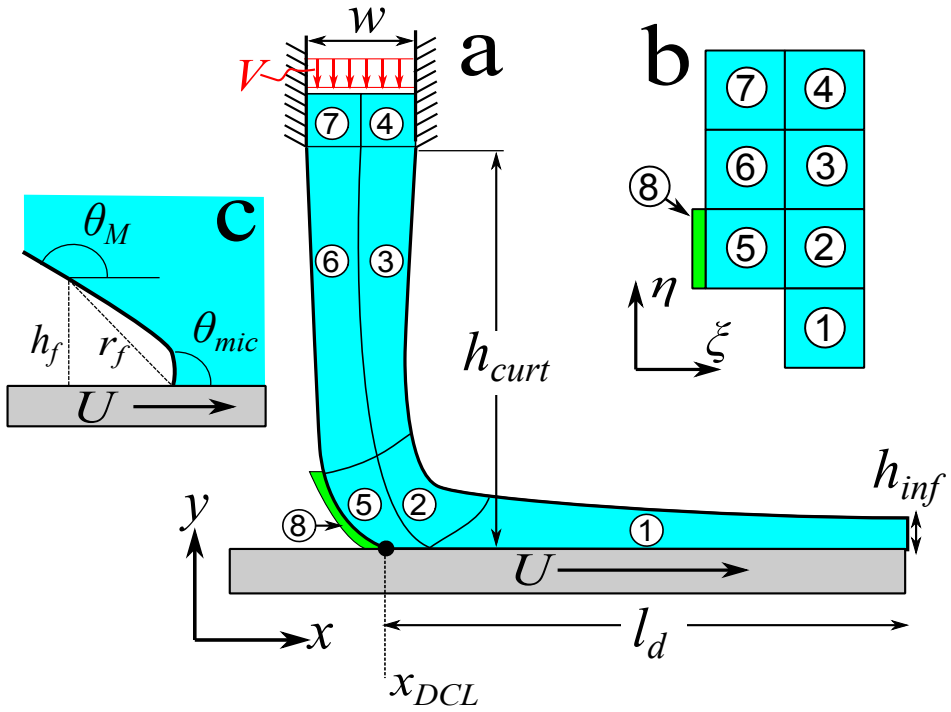

Figure 8.5: Schematic of the computational curtain-coating model. (a) Overview of the physical coating domain composed of seven liquid regions (1-7) and one air region (8) using hybrid FEM. (b) The computational domain used with FEM. (c) Illustration of interface characteristics close to the DCL.

Figure 8.5b) that is handled in a similar fashion to the liquid domain in the parallel-plate geometry. The interface bends sharply near the contact line (see Figure 8.5c), requiring a larger number of computational elements near the DCL (region 5) to resolve large gradients in interface curvature. It should be noted that this region contains an interface inflection point (IP) at a small distance (vertical h_f and radial r_f) from the contact line. This marks the location of a local ($h < 0.1$) maximum in the interface angle that represents the apparent contact angle θ_M in this study. The domain length l_d extends to approximately $5 \times h_{curt}$ downstream in order to obtain well-developed flow in the coating film of height h_{inf}.

Figure 8.6 shows typical computational mesh used for the curtain coating model. The liquid domain is composed of elements with smallest size near the DCL in order to resolve strong velocity and pressure gradients associated with fluid slip. Even when imposing a relatively large slip length (i.e., $\lambda = 10^{-2}$), element sizes near the DCL had

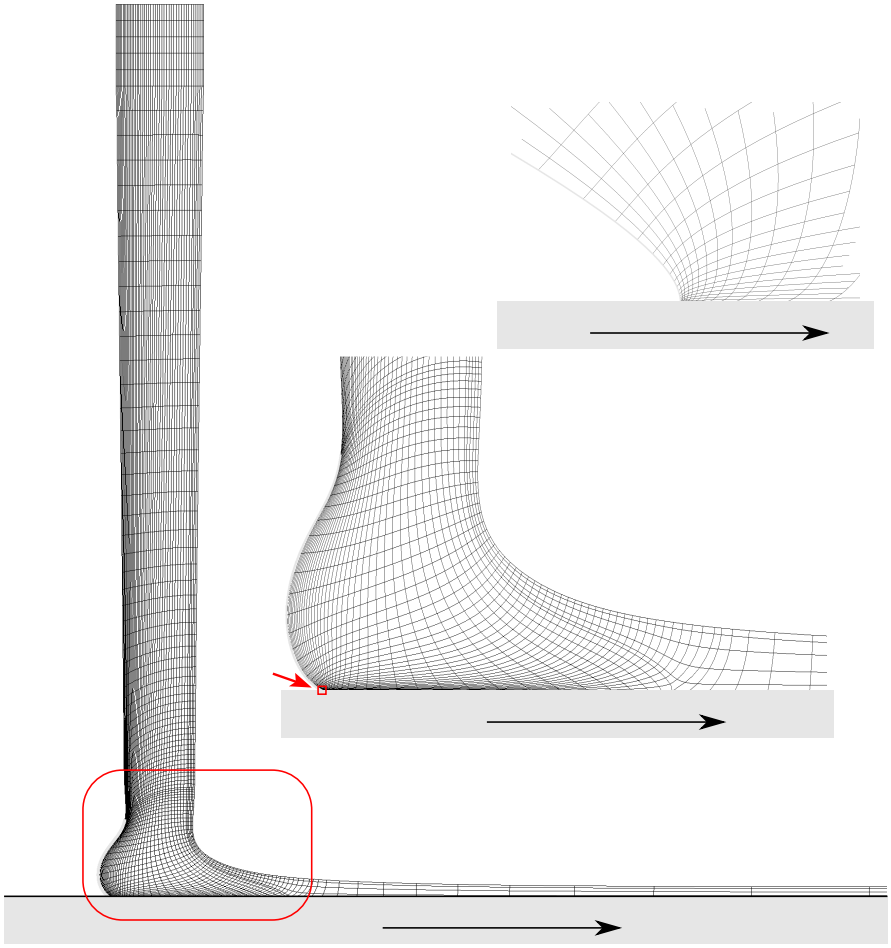

Figure 8.6: Mesh used with the curtain-coating system. Moving toward the upper right corner, images show approximately 10× and 1000× zoom near the DCL.

to be less than $w \times 10^{-4}$ ($\sim$ 10 nm) to avoid significant numerical errors. Mesh quality was tested by systematically varying global and local element properties to verify that solutions reported here are practically mesh independent (e.g., less than 2% variation solution paths in Section 8.4). Figure 8.6 includes close-up views of the DCL to illustrate the exceptionally fine mesh needed to resolve interface curvature in this region.

Mesh quality changes in response to global distortion of the liquid curtain. This is most strongly a function of the contact-line position x_{DCL}. For instance, the curtain elongates, stretching and skewing elements, when the DCL moves downstream ($x_{DCL} >$

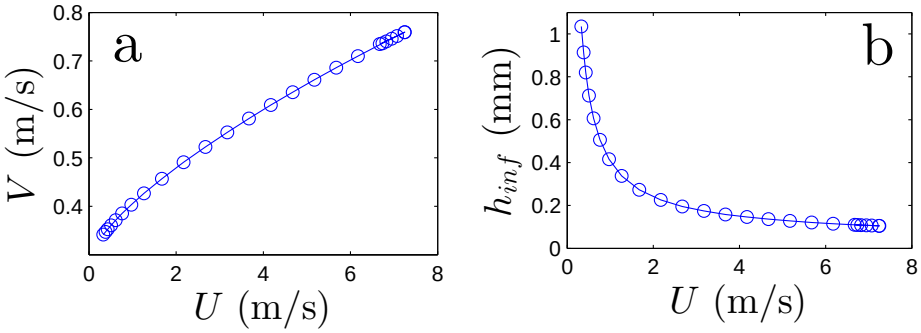

Figure 8.7: (a)Dependence of feed-flow velocity V on substrate substrate speed U needed to hold curtain position fixed at $x_{DCL} = 0$. (b) The coating-film thickness h_{inf} resulting from the balance of rates shown in (a). Parameter values: $\mu_{adv} = 25$ cP, $\mu_{rec} = 0.02$ cP, $\sigma = 70$ mN/m, $\theta_{mic} = 90^o$ and $\rho = 1000$ kg/m^3. (This corresponds with the $x_{DCL} = 0$ solution path shown below in Figure 8.8.)

0). On the other hand, movement of the DCL in the opposite direction($x_{DCL} < 0$) typically forms a "heel" along the upstream interface, which poses a different set of meshing problems. (The effect of contact-line position is discussed in Section 8.4.1.) To mitigate numerical error from mesh distortion, we fix the x_{DCL} while tracing solution paths to higher substrate speeds U. This is very similar to the procedure described in Section 2.3, only here we iteratively adjust the feed-flow velocity V to satisfy θ_{mic} at a given speed. Figure 8.7a demonstrates that V must increase with faster substrate speeds U while holding the DCL position fixed. However, V does not grow as quickly as U, leading to thinner liquid coating layers ($h_{inf} = wV/U$) as U increases, as shown by Figure 8.7b. Note that Figure 8.7 provides insight into the dimensional values of predicted speeds and coating thicknesses, whereas the following discussion focuses on the dimensionless properties of curtain coating.

The lubrication equations describing viscous air stresses are only valid near the contact line, where the air flow typically becomes long and slender as substrate speed increases (refer to Section 8.2). For theoretical and computational considerations, it is preferable to restrict the air-flow calculation (region 8 in Figure 8.5) to the portion of the interface close to the DCL. As specified by lubrication theory, air pressure gradients decay like $\sim 1/h^2$ away from the DCL, which makes the air flow have marginal impact when the upper bound moves to $h > 0.1$ mm (e.g., $\sim 10\%$ variation in the solution paths shown in Section 8.4 when region 8 extends to $h = 2$ mm). In contrast, reducing

the air-flow region to $h < 0.1$ mm yields significant differences in the calculations (e.g., $\sim 40\%$ variation in the solution paths shown in Section 8.4 when $h = 0.05$ mm is the upper bound of region 8). To avoid truncacting the air stress, we fix the upper bound of the air-flow calculation (region 8) to $h = 1$ mm for the results reported herein.

8.4 Curtain-coating Results

8.4.1 Solution Paths and Comparisons with the Parallel-plate System

In this section, air/liquid displacement ($\chi = 7.2 \times 10^{-4}$) in curtain coating is compared to the parallel-plate case that has been investigated earlier in this thesis (e.g., Section 3.6). Figure 8.13 plots solution paths from our curtain-coating model corresponding to the different contact-line positions, x_{DCL}. For each solution path, the liquid feed velocity V is treated as an free parameter that is iteratively adjusted in order to hold x_{DCL} constant while substrate speed (i.e., Ca) increases, as described in Section 8.3.2. Solution paths appear similar to the parallel-plate case (see Section 3.6), where the apparent contact angle θ_M increases with Ca until reaching a turning point at some critical capillary number Ca^{crit}. In fact, the parallel-plate solution (see dashed curve in Figure 8.8) nearly matches the curtain-coating curve for $x_{DCL} = 3$ with the same air/liquid system ($\chi = 7.2 \times 10^{-4}$). This similarity suggests that despite differences in flow geometry, curtain coating contains the same features of viscous fluid displacement that have been exposed earlier in this thesis for the confined (parallel-plate) geometry (e.g. Chapter 4).

Curtain-coating solutions are strongly influenced by the DCL position x_{DCL}. Figure 8.8 shows that for a fixed substrate speed, θ_M increases as the DCL moves downstream ($x_{DCL} > 0$). In a real curtain-coating system, x_{DCL} is usually controlled with the feed-flow rate V. Decreasing V reduces the hydrodynamic pressure associated with the impinging curtain, allowing substrate motion to drag the contact line downstream ($\uparrow x_{DCL}$). The inset of Figure 8.8 shows this effect with a substrate speed of $U = 2.4$ m/s ($Ca \approx 0.85$), where low feed flow causes θ_M to advance rapidly toward 180^o. Consequently, turning points occur at lower values of Ca^{crit} for solution paths associated with low feed flow (larger values of x_{DCL}).

In addition to the DCL position, feed flow impacts the overall shape of the liquid

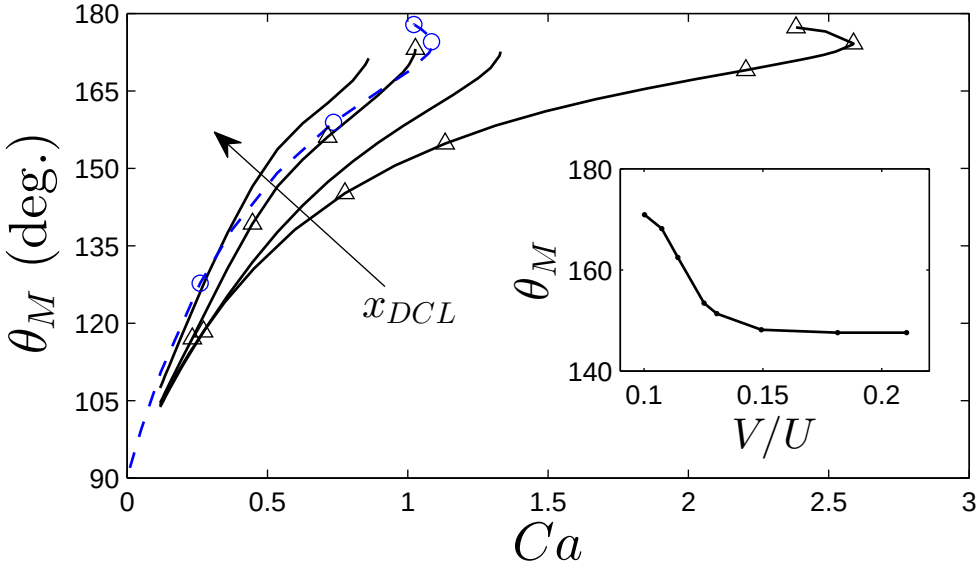

Figure 8.8: Solution paths for curtain coating with various positions of the DCL. Each solid curve represents a different DCL position: $x_{DCL} = 0, 1, 3, 7$. The dashed curve denotes the parallel-plate solution with $Re = 0$ and $Bo = 0$. Additional parameters (both systems): $\chi = 7.2 \times 10^{-4}$ and $\lambda = 10^{-2}$. *Inset*: The apparent contact angle θ_M as a function of feed flow V at fixed substrate speed $U = 2.4$ m/s ($Ca \approx 0.85$). Note that decreasing V/U corresponds to solution curves with higher values of x_{DCL} in the main panel of this figure.

curtain. Since low feed flow causes x_{DCL} to move downstream, the fluid interface must elongate as the curtain is pulled in the direction of substrate motion. Figure 8.9 plots curtain shapes and streamlines for different values of x_{DCL}, demonstrating that the interface becomes more deformed as x_{DCL} moves away from the curtain feed slot ($x_{DCL} = 0$ in Figure 8.5). In contrast, the curtain remains nearly perpendicular to the substrate when $x_{DCL} = 0$ with only a small upstream "heel" resulting from viscous bending of the interface very close to the DCL.

Figure 8.10 compares liquid flow fields from curtain coating with $x_{DCL} = 0$ and $x_{DCL} = 3$ to the case of fluid displacement in a parallel-plate geometry. (Substrate speed is fixed such that $Ca \approx 1.0$ for the comparison.) In each system, liquid moves slowly along the outer interface and rapidly gains speed near the DCL in order to match the substrate velocity. Consequently, liquid pressures decrease sharply near the DCL, providing suction forces that draw liquid toward the moving substrate. When

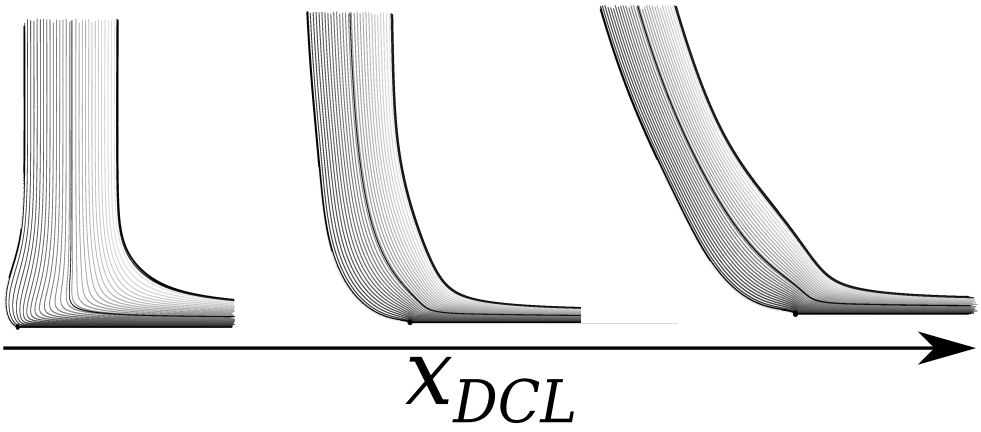

Figure 8.9: The change in curtain shape and streamlines at Ca^{crit} as a function of contact-line position: $x_{DCL} = 0, 1, 3$. Additional system parameters: $\chi = 7.2 \times 10^{-4}$ and $\lambda = 10^{-2}$.

$x_{DCL} = 0$, momentum from the impinging liquid pressurizes the flow underneath the curtain, creating pressure gradients that assist in directing liquid toward the moving substrate. This "hydrodynamic assist" paired with suction forces near the DCL allows the $x_{DCL} = 0$ case to achieve fast steady wetting, doubling the critical speed of the equivalent parallel-plate system (refer to solution paths in Figure 8.8). In parallel-plate system, strong downstream pressures drive liquid flow through the parallel channel, but do not assist flow toward the substrate (pressures remains nearly constant along the interface). Consequently, curtain coating with the appropriate operating conditions (e.g., feed-flow rate) can postpone wetting failure relative to confined coating geometries.

Ultimately, air stresses near the DCL trigger the onset of wetting failure at some critical substrate speed corresponding to Ca^{crit}. Chapter 4 reveals that local stresses depend on the interface inflection point (IP) position $\{h_f, r_f\}$ relative to the DCL (refer to Figure 8.5c). Specifically, the magnitude of local gradients in capillary stress and air pressure scale roughly as $\sim 1/r_f$ and $\sim 1/h_f^2$, respectively (see Section 4.3 for a more complete derivation). As Ca increases, the IP migrates closer to the DCL, increasing the local interface curvature in order to balance capillary forces with increasing viscous stresses. This IP migration forms stronger fluid stresses, especially the local air pressure gradient, at faster substrate speeds.

Figure 8.11 demonstrates that air stresses eventually exceed the local capillary forces (note that $1/h_f^2$ grows faster than $1/r_f$ as the DCL is approached), causing the loss of

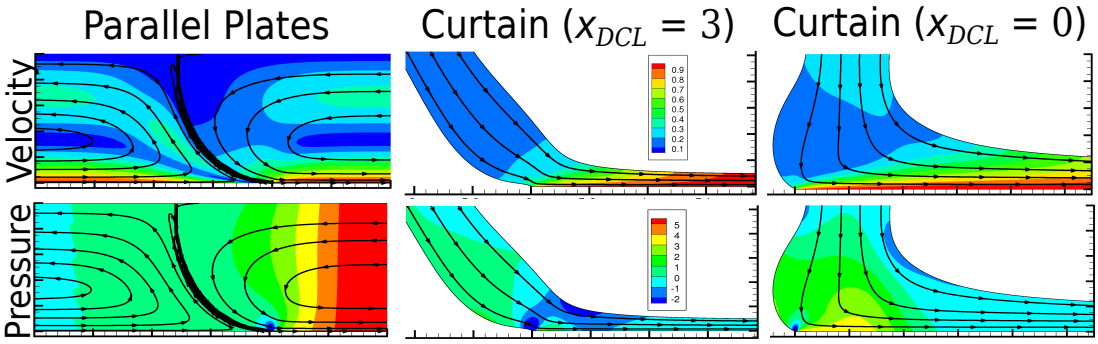

Figure 8.10: Comparison of flow fields in parallel-plate and curtain-coating geometries. Curtain coating results are shown for $x_{DCL} = 3$ and 0. Velocity and pressure fields are plotted for each case. Additional system parameters: $Ca \approx 1$, $\chi = 7.2 \times 10^{-4}$, and $\lambda = 10^{-2}$.

steady 2D wetting at Ca^{crit}. This wetting-failure mechanism holds for both the parallel-plate case (Figure 8.11a) and curtain coating (Figure 8.11b); however, capillary stresses are different due to the flow field associated with the falling curtain. Figure 8.11 shows that capillary-stress gradients have a stronger dependence on the IP location in curtain coating ($\sim 1/r_f^{1.5}$) than in parallel-plate systems ($\sim 1/r_f$). This can be interpreted as "hydrodynamic assist" resulting from pressure gradients in the impinging curtain flow near the DCL (see Figure 8.10 and discussion above). Consequently, higher capillary forces resist the growing air stress to faster speeds, yielding larger values of Ca^{crit} in curtain coating (when $x_{DCL} \approx 0$) in comparison to the parallel-plate case. (Note that the Ca ranges differ by a factor of two in the axes of Figure 8.11a and 8.11b.)

As discussed above, the curtain shape deforms in response to changes in the feed-flow speed V, or equivalently, differences in the DCL location along the substrate x_{DCL}. Since interface shape affects the IP position, these flow controls can greatly impact Ca^{crit}. For instance, Figure 8.12 plots interface shapes from curtain coating at $Ca \approx 1$ with $x_{DCL} = 0$ and $x_{DCL} = 3$. Due to interface elongation when the curtain moves downstream ($x_{DCL} = 3$), the IP is pulled away from the DCL, primarily increasing the radial distance as illustrated in the inset of Figure 8.12. This effectively weakens the local capillary forces ($\sim 1/r_f$), causing wetting failure at lower substrate speeds. In fact, $Ca^{crit} \approx 1$ for $x_{DCL} = 3$, whereas steady wetting continues to $Ca > 2$ when the DCL is located underneath the curtain (refer to solution paths in Figure 8.8).

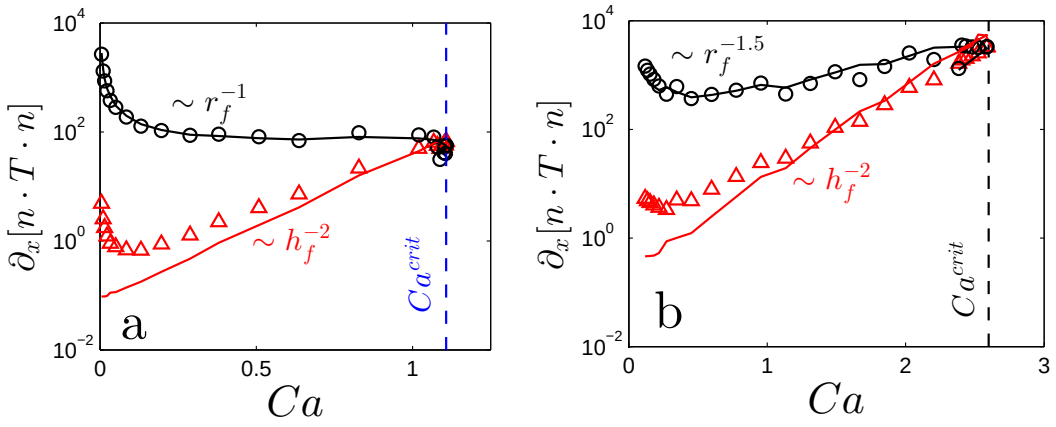

Figure 8.11: The magnitude of normal-stress gradients near the DCL in (a) parallel-plate and (b) curtain-coating geometries. Capillary stress (circles) and air stress (triangle) contributions are shown for each case. System parameters: $\chi = 7.2 \times 10^{-4}$, $\lambda = 10^{-2}$ and $x_{DCL} = 0$.

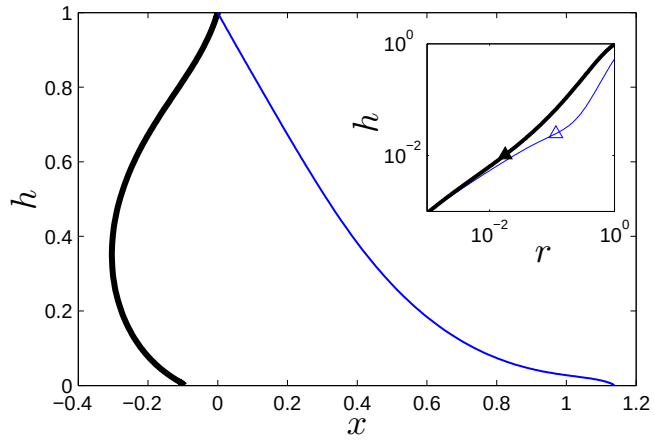

Figure 8.12: Interface shapes near the DCL for curtain coating with $x_{DCL} = 0$ and 3. (Note that the $x_{DCL} = 3$ curve is shifted along the x-coordinate for the purpose of comparison.) Additional system parameters: $Ca \approx 1$, $\chi = 7.2 \times 10^{-4}$, and $\lambda = 10^{-2}$. *Inset*: Interface profiles replotted against the radial distance r from the DCL. The IP position is denoted with a closed and open triangle for $x_{DCL} = 0$ and 3, respectively.

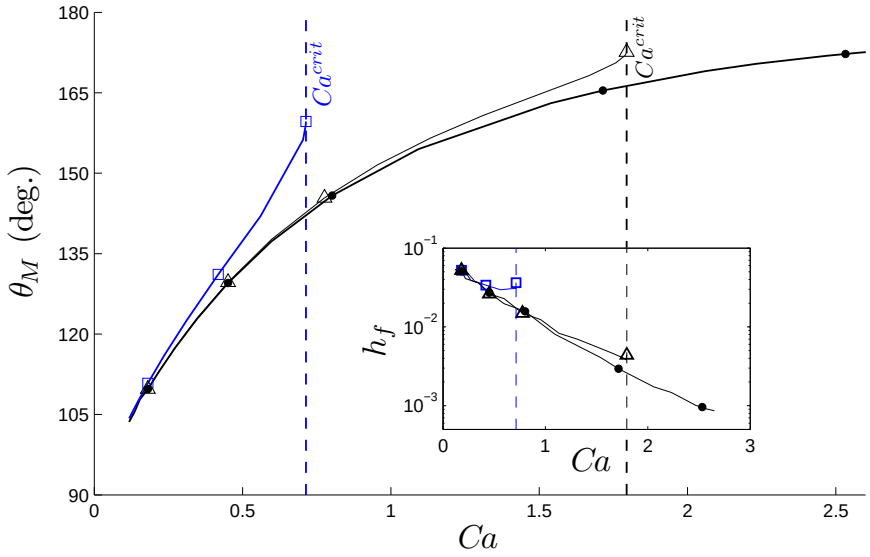

Figure 8.13: Solution paths for curtain coating with various values of the viscosity ratio: $\chi = 10^{-2}$ (open squares), 7.2×10^{-4} (open triangles), and 0 (filled circles). *Inset*: Plot of the IP position h_f as a function of Ca.

8.4.2 The Impact of the Receding Flow

To demonstrate the impact of the receding flow, solutions are computed for various values of the viscosity ratio χ in the curtain coating system described in Section 8.3. To compare against the case of air/liquid displacement ($\chi = 7.2 \times 10^{-4}$), systems are considered in which the receding fluid is a high-viscosity gas ($\chi = 10^{-2}$), or completely lacking viscosity ($\chi = 0$). The latter example of void/liquid displacement is practically the only case that has been modeled within the curtain-coating literature prior to the current work [36, 37, 39].

Figure 8.13 plots solution paths from our curtain-coating model corresponding to the different fluid systems mentioned above. In each case the contact-line position is fixed underneath the curtain at $x_{DCL} = 0.5$ by adjusting the feed rate (V) as substrate speed increases (U), as described in Section 8.3.2. The impact of the receding flow is very similar to the parallel-plate case (see Section 3.6), where a receding fluid of higher viscosity ($\chi \to 1$) causes solutions to diverge from the void/liquid solution path ($\chi = 0$) at lower Ca. Turning points are located in solution paths corresponding to

systems with finite receding-fluid viscosity, whereas the $\chi = 0$ case appears to maintain steady 2D wetting at infinite substrate speeds with $\theta_M \rightarrow 180^o$ as $Ca \rightarrow \infty$ in an analogous manner to void/liquid displacement in parallel-plate geometries (e.g. Figure 3.3c). Furthermore, the inset of Figure 8.13 demonstrates that the interface inflection point (IP) migrates closer to the contact line as substrate speed increases. The IP height h_f decays exponentially with Ca, once again matching trends from parallel-plate results (for example, see Figure 3.5). A more thorough comparison between curtain coating and fluid displacement in a parallel-plate system is presented in the preceding section.

It should be emphasized that Figure 8.13 clearly demonstrates that the receding flow influences the apparent contact angle θ_M during curtain coating. Moreover, the onset of wetting failure is completely missed when neglecting stresses from the viscous receding flow (i.e., $Ca^{crit} \rightarrow \infty$ for $\chi = 0$). Therefore, it is crucial to include the appropriate two-fluid displacement mechanics when modeling high-speed curtain coating flows.

Further support for this statement is found in pressure and velocity fields plotted in Figure 8.14 and 8.15, respectively. These figures show that a viscous receding fluid alters the liquid flow field as substrate speed approaches the critical value ($Ca^{crit} \approx 0.75$ for $\chi = 10^{-2}$ and $Ca^{crit} \approx 1.75$ for $\chi = 7.2 \times 10^{-4}$). Receding-fluid stresses cause θ_M to increase (refer to Figure 8.13), which forces higher liquid pressures to support the increase in interface concavity (e.g., Figure 8.14). These high pressures slow the liquid flow along the upstream meniscus (e.g., Figure 8.15), which may contribute to flow recirculation that commonly coincides with heel formation when the dynamic contact line moves upstream ($x_{DCL} < 0$) [37, 83]. Even when avoiding air entrainment, flow recirculation can lead to undesirable effects such as nonuniform thickness and uneven particle distribution within the final coating layer [161]. Unfortunately, the $x_{DCL} < 0$ regime presents numerical challenges associated with mesh distortion following gross heel formation and, consequently, has been omitted from this analysis. However, the results discussed above suggest that the receding flow also impacts this regime of high-speed curtain coating.

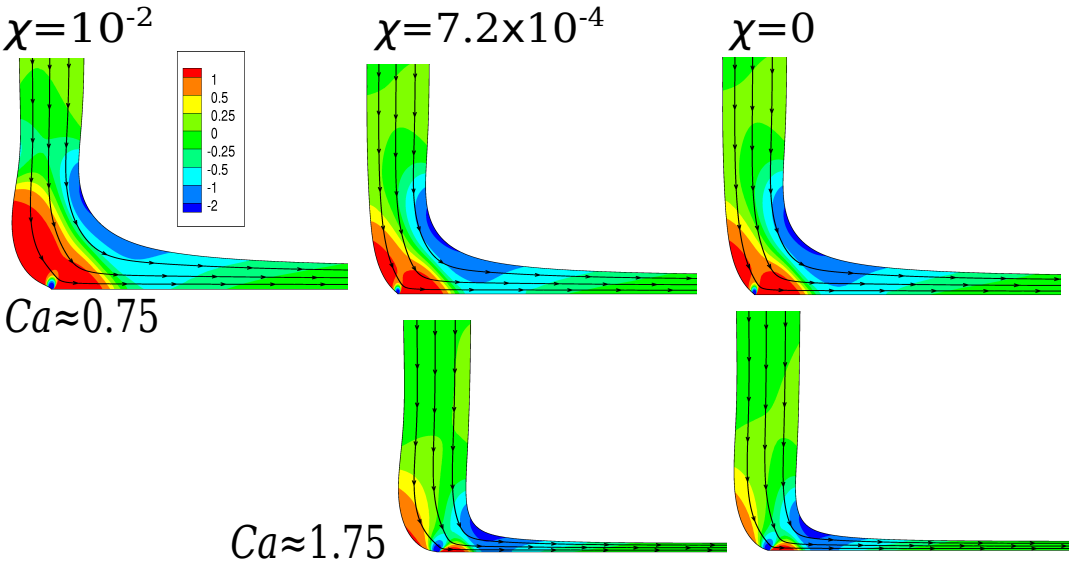

Figure 8.14: Pressure fields produced in curtain coating with various values of the viscosity ratio. Values for χ are listed above each column. Columns represent solutions for different values of Ca (note that there is not solution for $Ca \approx 1.75$ and $\chi = 10^{-2}$). Each solution corresponds to a data point plotted in Figure 8.13.

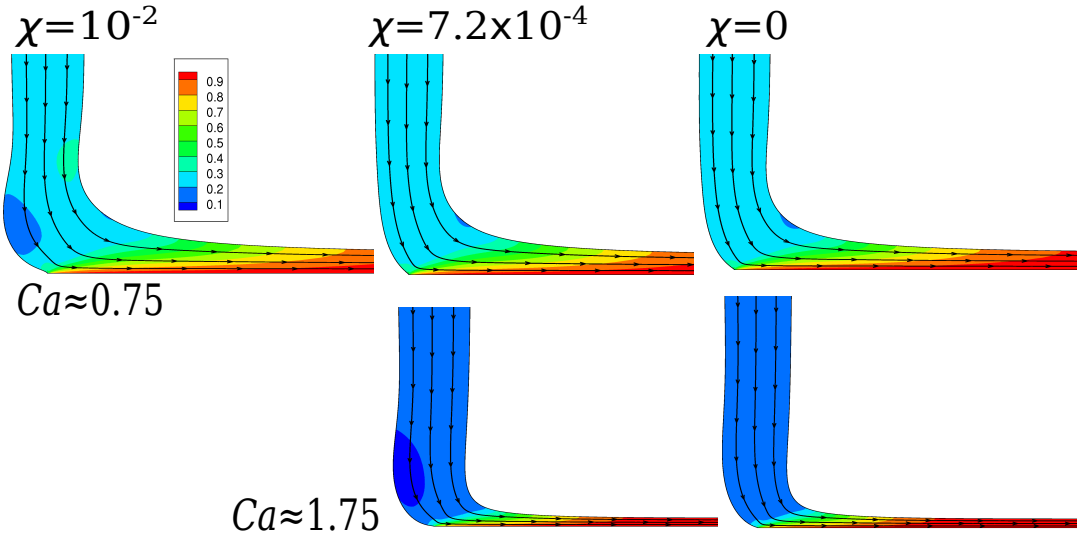

Figure 8.15: Velocity fields produced in curtain coating with various values of the viscosity ratio. Values for χ are listed above each column. Columns represent solutions for different values of Ca (note that there is not solution for $Ca \approx 1.75$ and $\chi = 10^{-2}$). Each solution corresponds to a data point plotted in Figure 8.13.

8.5 Conclusions

In this chapter, a novel fluid displacement model was developed using a hybrid FEM technique to compute the 2D flow of the advancing fluid while approximating receding-flow stresses with 1D lubrication equations. To the best of the authors' knowledge, this is the only time that such a model has been developed for dynamic wetting systems. The hybrid model performs particularly well in the regime of air/liquid displacement because 2D liquid stresses dominate most of the interface behavior. The air flow only contributes significant viscous stresses near the dynamic contact line (DCL) during high-speed wetting ($Ca \approx Ca^{crit}$). Under these conditions, the air flow is typically long and slender and, therefore, can be accurately approximated by 1D lubrication theory. Section 8.2 demonstrates that solutions from the hybrid model converge to results from the full 2D flow model when the viscosity ratio $\chi \ll 1$ for fluid displacement in a parallel-plate geometry.

Using the hybrid model, two-fluid displacement was modeled in a curtain-coating system for the first time. Similar to fluid displacement in parallel-plate systems, the receding flow crucially impacts high-speed curtain coating, contributing viscous stresses that trigger the onset of wetting failure. Pressure gradients developed from the impinging liquid curtain aid the fluid displacement process, delaying wetting failure to faster substrate speeds relative to the parallel-plate case. However, feed-flow rate strongly influences the curtain properties through control of the DCL position. Low feed rates tend to move the DCL downstream with the substrate drag, elongating the interface and weakening the influence of the impinging liquid flow. Consequently, wetting failure results at lower critical speeds when the DCL is positioned further downstream.

Ultimately, our analysis shows that careful control of the operating conditions in curtain coating can yield the "hydrodynamic assist of dynamic wetting" that has been observed in past experimental studies [26]. Specifically, the fastest steady wetting speeds are achieved when the feed rate is adjusted to keep the dynamic contact line (DCL) underneath the impinging curtain [38]. While maintaining this optimum DCL position, our model predicts that critical speeds increase by more than a factor of two in comparison to a situation where the DCL drifts downstream (refer to Figure 8.8). These predictions closely resemble experimental measurements made with a similar curtain system (i.e.,

μ_{adv} = 25 cP, $w \sim 1$ mm, and $h_{curt} \sim 1$ cm) [82]. Furthermore, our computations reflect a maximum steady wetting speed of approximately 8 m/s, which is close to line speeds (~ 10 m/s) achieved in real curtain-coating processes [114]. However, the effects of several parameters (e.g., λ, θ_{mic}, and h_{curt}) still need to be systematically studied with the model before making a strict comparison with the operability limits found in the curtain-coating industry.

Previously, the effects of curtain parameters on wetting characteristics have stood as an argument against hydrodynamic wetting theory [82, 39]. However, one problem with this assessment is that past theoretical studies neglect the air flow when modeling dynamic wetting in curtain coating. The current work demonstrates that air stresses do, in fact, play a crucial role in high-speed curtain coating behavior, such as the sensitivity of the apparent contact angle θ_M to the liquid feed rate V. While considering viscous effects from the air flow, our model predicts that θ_M can change by over 20^o in response to reducing V at fixed substrate speed (refer to the inset of Figure 8.8), matching the range of contact-angle values measured experimentally [83, 82]. In contrast, prior calculations using the conventional void/liquid curtain-coating model ($\chi = \mu_{rec}/\mu_{adv} = 0$) predict that the apparent contact angle varies by a mere 5^o in response to different feed rates [39]. Although numerical issues currently limit us to a qualitative comparison with prior work, it is apparent that nonlocal hydrodynamic effects (e.g., V) have a weaker impact on θ_M when the air flow is neglected, which explains the prior discrepancy between theoretical predictions and experimental data. In order to improve upon this analysis with quantitative comparisons, future studies will need to address problems associated with numerical resolution during heel formation ($x_{DCL} < 0$) and when implementing smaller slip lengths. (Recall that here we have selected $\lambda = 10^{-2}$ for numerical convenience, but $\lambda \sim 10^{-5}$ is likely in physical systems). Nevertheless, our preliminary results clearly demonstrate the importance of two-fluid displacement in curtain coating that merits further investigation with the hybrid FEM model.

Beyond curtain coating, the hybrid model could provide a useful tool for the study of various wetting phenomena that have been plagued with computational challenges in the past. For instance, complex rheology or surfactant effects can be incorporated into the systems studied in this thesis with relative ease (see Section 9.2.1 for further discussion). In other cases, transient flows typically require many costly computations that

become impractical when considering 2D flow mechanics in an expansive air domain. The hybrid model offers an efficient alternative for the study of fluid displacement in transient systems that may be affected by viscous air stresses, such as the impact and fast spreading of liquid droplets on a solid surface [17, 16, 20]. Lastly, the hybrid model could be extended to a three-dimensional system (i.e., 2D/3D hybrid FEM). Given the challenges associated with computing 3D free-surface flows [162, 163], this hybrid technique may be the only feasible way to account for air stresses while accurately resolving the outer ($\sim$ 1 mm) liquid flow and inner ($\sim$ 1 nm) mechanics near the DCL. In total, this push toward 3D transient simulation would considerably advance the study of fluid displacement in real-world coatings and engineering problems.

Chapter 9

Conclusion

9.1 Thesis Summary

The objective of this thesis was to understand the role of two-fluid displacement in high-speed coating flows. In particular, experimental and theoretical methods were sought to characterize air entrainment arising from dynamic wetting failure, which commonly limits process speed in the coatings industry. Many times, the appropriate techniques for this research were not readily available or did not yet exist. Consequently, novel theoretical (Chapter 5), experimental (Chapter 6 and 7), and computational (Chapter 8) methods were developed in the course of this thesis. New insight into high-speed dynamic wetting emerged with practical implications for a broad range of applications, such as microfluidic flows [13], oil-recovery systems [15], splashing droplets [16], and printing and coating processes [8]. Ultimately, the findings presented in this thesis advance the fundamental understanding of fluid displacement in systems with moving contact lines, which have challenged researchers for several decades (e.g., see references in [2, 21]).

Three primary conclusions can be drawn as a summary of the results presented in the preceding chapters. First, the findings presented throughout this work clearly demonstrate the importance of the air flow in high-speed wetting systems. In the face of highly viscous coating liquids, it appears convenient to neglect the dynamics of low-viscosity gases when considering interface behavior. However, Chapter 3 shows that viscous air

flow generates large pressure gradients in order to pump air mass away from the dynamic contact line. Since air flow and interface shape are coupled, pressure gradients become stronger as the interface deforms at faster wetting speeds, until triggering the onset of wetting failure when air stresses exceed local capillary forces (see Chapter 4). Therefore, a lack of consideration for the air mechanics leads to the misinterpretation of phenomena in high-speed coating flows, including air entrainment.

Second, the collective results in this thesis strongly support a hydrodynamic mechanism for dynamic wetting behavior. Unlike prior experimental works that are plagued with ambiguous interface metrics, this study focuses on the readily apparent transition between steady and unsteady states in order to understand wetting fundamentals. For example, Chapters 6 and 7 report two completely distinct experimental studies that both demonstrate that system geometry influences the critical speed associated with the onset of wetting failure. Data clearly show that meniscus confinement delays air entrainment to faster substrate speeds, matching predictions from hydrodynamic theory. Furthermore, results from the hydrodynamic model used in this work quantitatively match experimentally measured critical speeds for a variety of different parameter studies. In addition, the model predicts curtain-coating behavior that had previously stood as an argument *against* hydrodynamic wetting theories. As mentioned above, air flow is found to crucially impact interface shapes (Chapter 8), explaining the failure of previous curtain-coating models that have neglect the essential air mechanics.

Lastly, this thesis has demonstrated that two-dimensional, two-fluid displacement mechanics can be accurately approximated with a reduced-order computational technique. In Chapter 8, a hybrid FEM model is presented that treats the receding fluid as a one-dimensional flow while solving the full two-dimensional fluid mechanics for the advancing fluid. The hybrid model makes use of lubrication theory, which generally fails to describe two-fluid displacement, but sufficiently accounts for fluid stresses in the receding flow (see Section 3.3.5). Therefore, the hybrid technique represents the optimal computational efficiency for an accurate model of general two-fluid displacement. Although this finding alone does not impact the fundamental understanding of dynamic wetting, the hybrid model will be an important tool for future studies of fluid-displacement behavior. In particular, upcoming investigations will need to address issues involving complex liquid rheology, surfactant effects, and non-ideal substrate properties

that will demand significantly higher computational costs. The computational efficiency of the hybrid model places these objectives within aim.

9.2 Future Directions

As with any research of this magnitude, each conclusion appears to be replaced with more questions. Fortunately, the methods developed in this thesis provide a framework for tackling many of these open problems. The following briefly introduces several future directions for this work.

9.2.1 Surfactants and Rheology

Real coating flows often include solutions with non-Newtonian characteristics and surface-active components [30]. However, few systematic studies have investigated high-speed wetting behavior with complex liquids [27]. From the available literature, there are conflicting reports about the sensitivity of fluid displacement to solvent and solute properties [164]. In some cases, it appears that wetting only depends on solute characteristics, acting independent of the non-Newtonian characteristics of the solution [54]. However, prior experiments only consider simple flow geometries, so it is not clear how these results relate to complex coating flows.

This thesis has established a baseline by investigating the onset of wetting failure for ideal displacement systems (i.e., Newtonian fluids, constant surface tension, and smooth substrate). However, both experimental and computational methods can be augmented with relatively low effort in order to study more complex behavior. For example, the hybrid model allows for non-Newtonian constitutive equations to be incorporated into the two-dimensional fluid mechanics of the advancing liquid flow. In addition, one-dimensional surface-transport equations can be added to the lubrication "loading" terms (refer to Chapter 8) along the interface to model surfactant effects. Experimentally, the wetting-box apparatus could be used to visualize air entrainment with complex fluids in confined and unconfined geometries. In tandem, these experiments and computations would drive toward a deeper understanding of dynamic wetting with realistic coating liquids.

9.2.2 Substrate Properties

Another open issue in dynamic wetting centers around the effects of substrate properties. Coating flows often occur on deformable, heterogeneous surfaces that do not well match the idealized substrates used and modeled in this work. Although not studied systematically, a thin substrate ($\sim$ 25 μm) was briefly tested in the wetting-box apparatus, demonstrating very different dynamic wetting characteristics when compared against the thick tape ($\sim$ 125 μm) that was used for the results in Chapter 7. Both substrates had the same chemistry (polyethylene teraphthalate) and yielded nearly identical static contact angles, however the thin tape revealed small-scale wrinkles in response to non-uniform contact line forces. Apparently, even these small surface irregularities strongly influence macroscopic properties of fluid-displacement and air entrainment. This effect is likely amplified by porous media (e.g., paper), where liquid may penetrate the surface to different depths depending on the operating conditions. Recently, advances have been made in the modeling of displacement flows with complex substrate interactions [165, 166], however incorporation of these effects with the two-fluid hydrodynamic model presented in this work (Chapter 2) would produce significant computational hurdles. This problem would likely be more tractable by approximating the substrate dynamics with a set of one-dimensional differential equations, similar to the treatment of air flow in hybrid model (Section 8.2). Comparable numerical analysis has been conducted to model deformable substrates used in tensioned-web-over slot die coating flows [167]. A more general inspection of substrate effects would have a great impact on a broad spectrum of high-speed coating processes.

9.3 Final Remarks

Upon beginning this thesis research, the field of dynamic wetting appeared to swell with observations of unusual wetting behavior [17, 168, 83, 39, 20] and new models with increasingly complex mechanics to fit each phenomenon [82, 169, 40, 18]. Taking a step back from the forward push, it became clear that the hydrodynamics of simple two-fluid displacement needed to be reconsidered in these problems. Following years of method development and painstaking analysis, this final document demonstrates that *careful* consideration of viscous flow effects does, in fact, account for complex wetting behavior

that was previously thought to lie outside of the scope of conventional hydrodynamic theories [25, 39]. In particular, newly found descriptions for the mechanisms of dynamic wetting failure represent a breakthrough in the science of interfacial phenomena that impacts numerous real-world applications, including the engineering of industrial coating processes. The author hopes that the foundations established here will propagate to shed light on the abundance of unresolved wetting behavior mentioned above and yet to be characterized in high-speed coating flows.

References

[1] E. Lauga, M. P. Brenner, and H. A. Stone. Microfluidics: The no-slip boundary condition. In C. Tropea, J.F. Foss, and A. Yarin, editors, *Handbook of Experimental Fluid Dynamics*. Springer, 2005.

[2] S. F. Kistler. Hydrodynamics of wetting. In John C. Berg, editor, *Wettability*, pages 311–429. Marcel Dekker, Inc., 1993.

[3] M. Tanaka, F. Rehfeldt, M. F. Schneider, G. Mathe, A. Albersdorfer, K. R. Neumaier, O. Purrucker, and E. Sackmann. Wetting and dewetting of extracellular matrix and glycocalix models. *Journal of Physics: Condensed Matter*, 17:S649–S663, 2005.

[4] M. H. Al-Dahhan and M. P. Dudukovic. Catalyst wetting efficiency in trickle-bed reactors at high pressure. *Chemical Engineering Science*, 50:2377 – 2389, 1995.

[5] S. Roy, A. K. Heibel, W. Liu, and T. Boger. Design of monolithic catalysts for multiphase reactions. *Chemical Engineering Science*, 59:957 – 966, 2004.

[6] A. Marmur. The lotus effect: superhydrophobicity and metastability. *Langmuir*, 20:3517–3519, 2004.

[7] R. Blossey. Self-cleaning surfaces - virtual realities. *Nature Materials*, 2:301–306, 2003.

[8] S. J. Weinstein and K. J. Ruschak. Coating flows. *Annual Review of Fluid Mechanics*, 36:29–53, 2004.

[9] H. Benkreira and M. I. Khan. Air entrainment in dip coating under reduced air pressures. *Chemical Engineering Science*, 63:448 – 459, 2008.

[10] X. Casadevall i Solvas and A. deMello. Droplet microfluidics: recent developments and future applications. *Chem. Commun.*, 47:1936–1942, 2011.

[11] Adam R. Abate and David A. Weitz. Air-bubble-triggered drop formation in microfluidics. *Lab Chip*, 11:1713–1716, 2011.

[12] J. G. Kralj, H. R. Sahoo, and K. F. Jensen. Integrated continuous microfluidic liquid-liquid extraction. *Lab Chip*, 7:256–263, 2007.

[13] H. A. Stone, A. D. Stroock, and A. Ajdari. Engineering flows in small devices: Microfluidics toward a lab-on-a-chip. *Annual Review of Fluid Mechanics*, 36:381–411, 2004.

[14] J. Bear. *Dynamics of Fluids in Porous Media*. American Elsevier Publishing Company, Inc., 1972.

[15] M. G. Gerritsen and L. J. Durlofsky. Modeling fluid flow in oil reservoirs. *Annual Review of Fluid Mechanics*, 37:211–238, 2005.

[16] M. M. Driscoll and S. R. Nagel. Ultrafast interference imaging of air in splashing dynamics. *Physical Review Letters*, 107:154502, 2011.

[17] J. C. Bird, S. Mandre, and H. A. Stone. Short-time dynamics of partial wetting. *Physical Review Letters*, 100:234501, 2008.

[18] A. Carlson, M. Do-Quang, and G. Amberg. Dissipation in rapid dynamic wetting. *Journal of Fluid Mechanics*, 682:213–240, 2011.

[19] A. Latka, A. Strandburg-Peshkin, M. M. Driscoll, C. S. Stevens, and S. R. Nagel. Creation of prompt and thin-sheet splashing by varying surface roughness or increasing air pressure. *Physical Review Letters*, 109:054501, 2012.

[20] J. M. Kolinski, S. M. Rubinstein, S. Mandre, M. P. Brenner, D. A. Weitz, and L. Mahadevan. Skating on a film of air: Drops impacting on a surface. *Physical Review Letters*, 108:074503, 2012.

[21] D. Bonn, J. Eggers, J. Indekeu, J. Meunier, and E. Rolley. Wetting and spreading. *Reviews of Modern Physics*, 81:739–805, 2009.

[22] T. D. Blake and Y. D. Shikhmurzaev. Dynamic wetting by liquids of different viscosity. *Journal of Colloid and Interface Science*, 253:196–202, 2002.

[23] J. Eggers and R. Evans. Comment on "dynamic wetting by liquids of different viscosity" by t. d. blake and y. d. shikhmurzaev. *Journal of Colloid and Interface Science*, 280:537–538, 2004.

[24] Y. D. Shikhmurzaev and T. D. Blake. Response to the comment on [j. colloind interface sci. 253 (2002) 196] by j. eggers and r. evans. *Journal of Colloid and Interface Science*, 280:539–541, 2004.

[25] T. D. Blake. The physics of moving wetting lines. *Journal of Colloid and Interface Science*, 299:1 – 13, 2006.

[26] T. D. Blake, A. Clarke, and K. J. Ruschak. Hydrodynamic assist of dynamic wetting. *AIChE Journal*, 40:229–242, 1994.

[27] J. H. Snoeijer and B. Andreotti. Moving contact lines: Scales, regimes, and dynamical transitions. *Annual Review of Fluid Mechanics*, 45:269–92, 2013.

[28] T. D. Blake and K. J. Ruschak. Wetting: Static and dynamic contact lines. In S.F. Kistler and P.M. Schweizer, editors, *Liquid Flim Coating*, pages 63–97. Chapman & Hall, 1997.

[29] K. J. Ruschak. Coating flows. *Annual Review of Fluid Mechanics*, 17:65–89, 1985.

[30] S. F. Kistler and P. M. Schweizer. Coating science and technology: An overview. In S. F. Kistler and P. M. Schweizer, editors, *Liquid film coating*. Chapman & Hall, 1997.

[31] P.M. Martin. *Handbook of deposition technologes for films and coatings: science, applications and technology*. William Andrew, 2009.

[32] L. E. Scriven. Fine-structured materials by continuous coating and drying or curing of liquid precursors. In *Chemical Engineering: Trends and Developments*, page 229. Wiley, 2005.

[33] K. Miyamoto. On the mechanism of air entrainment. *Industrial Coating Research*, 1:71–88, 1991.

[34] M. Yamamura. Assisted dynamic wetting in liquid coatings. *Colloids and Surfaces A: Physicochemical and Engineering Aspects*, 311:55 – 60, 2007.

[35] S. F. Kistler. *The fluid mechanics of curtain coating and related viscous free surface flows with contact lines*. PhD thesis, University of Minnesota, 1983.

[36] S. F. Kistler and L. E. Scriven. Coating flow theory by finite element and asymptotic analysis of the navier-stokes system. *International Journal for Numerical Methods in Fluids*, 4:207–229, 1984.

[37] K. Miyamoto and Y. Katagiri. Curtain coating. In S.F. Kistler and P. M. Schweizer, editors, *Liquid Film Coating*, pages 461–494. Chapman & Hall, 1997.

[38] T. D. Blake, R. A. Dobson, and K. J. Ruschak. Wetting at high capillary numbers. *Journal of Colloid and Interface Science*, 279:198 – 205, 2004.

[39] M. C. T. Wilson, J. L. Summers, Y. D. Shikhmurzaev, A. Clarke, and T. D. Blake. Nonlocal hydrodynamic influence on the dynamic contact angle: Slip models versus experiment. *Physical Review E*, 73:041606, 2006.

[40] Y. D. Shikhmurzaev. *Capillary flows with forming interfaces*. Chapman & Hall/CRC, 2008.

[41] E. B. Dussan V. On the spreading of liquids on solid surfaces: Static and dynamic contact lines. *Annual Review of Fluid Mechanics*, 11:371–400, 1979.

[42] R. L. Hoffman. A study of the advancing interface. i. interface shape in liquid–gas systems. *Journal of Colloid and Interface Science*, 50:228 – 241, 1975.

[43] E. B. Gutoff and C. E. Kendrick. Dynamic contact angles. *AIChE Journal*, 28:459–466, 1982.

[44] R. G. Cox. The dynamics of the spreading of liquids on a solid surface. part 1. viscous flow. *Journal of Fluid Mechanics*, 168:169–194, 1986.

[45] O. V. Voinov. Hydrodynamics of wetting. *Fluid Dynamics*, 11:714–721, 1976.

[46] T. D. Blake. Dynamic contact angles and wetting kinetics. In John C. Berg, editor, *Wettability*, pages 249–309. Marcel Dekker, Inc., 1993.

[47] P. G. de Gennes, X. Hua, and P. Levinson. Dynamics of wetting: local contact angles. *Journal of Fluid Mechanics*, 212:55–63, 1990.

[48] P. Yue and J. J. Feng. Can diffuse-interface models quantitatively describe moving contact lines? *The European Physical Journal - Special Topics*, 197:37–46, 2011.

[49] Y. D. Shikhmurzaev. The moving contact line on a solid surface. *International Journal of Multiphase Flow*, 19:589–610, 1993.

[50] P. G. de Gennes. Wetting: statics and dynamics. *Reviews of Modern Physics*, 57:827–863, 1985.

[51] J. De Coninck and T.D. Blake. Wetting and molecular dynamics simulations of simple liquids. *Annual Review of Materials Research*, 38:1–22, 2008.

[52] C. G. Ngan and E. B. Dussan V. On the dynamics of liquid spreading on solid surfaces. *Journal of Fluid Mechanics*, 209:191–226, 1989.

[53] J. Eggers. Toward a description of contact line motion at higher capillary numbers. *Physics of Fluids*, 16:3491 – 3494, 2004.

[54] Y. Wei, E. Ramé, L. M. Walker, and S. Garoff. Dynamic wetting with viscous newtonian and non-newtonian fluids. *Journal of Physics: Condensed Matter*, 21:464126 (12pp), 2009.

[55] J. Eggers. Existence of receding and advancing contact lines. *Physics of Fluids*, 17:082106, 2005.

[56] R. E. Johnson and R. H. Dettre. Contact angle hysteresis. In F. M. Fowkes, editor, *Contact Angle, Wettability, and Adhesion*. American Chemical Society, 1964.

[57] L. Gao and T. J. McCarthy. Contact angle hysteresis explained. *Langmuir*, 22:6234–6237, 2006.

[58] C. N. C. Lam, N. Kim, D. Hui, D. Y. Kwok, M. L. Hair, and A. W. Neumann. The effect of liquid properties to contact angle hysteresis. *Colloids and Surfaces A: Physicochemical and Engineering Aspects*, 189:265–278, 2001.

[59] T. D. Blake and J. M. Haynes. Kinetics of liquid/liquid displacement. *Journal of Colloid and Interface Science*, 30:421–423, 1969.

[60] J. G. Petrov, J. Ralston, M. Schneemilch, and R. A. Hayes. Dynamics of partial wetting and dewetting in well-defined systems. *Journal of Physical Chemistry B*, 107:1634–1645, 2003.

[61] J. H. Snoeijer and B. Andreotti. A microscopic view on contact angle selection. *Physics of Fluids*, 20:057101, 2008.

[62] E. B. Dussan V., E. Ramé, and S. Garoff. On identifying the appropriate boundary conditions at a moving contact line: an experimental investigation. *Journal of Fluid Mechanics*, 230:97–116, 1991.

[63] J. A. Marsh, S. Garoff, and E. B. Dussan V. Dynamic contact angles and hydrodynamics near a moving contact line. *Physical Review Letters*, 70:2778–2781, 1993.

[64] Q. Chen, E. Rame, and S. Garoff. The breakdown of asymptotic hydrodynamic models of liquid spreading at increasing capillary numbers. *Physics of Fluids*, 7:2631 – 2639, 1995.

[65] C. Huh and L. E. Scriven. Hydrodynamic model of steady movement of a solid/liquid/fluid contact line. *Journal of Colloid and Interface Science*, 35:85 – 101, 1971.

[66] E. B. Dussan V. and S. H. Davis. On the motion of a fluid-fluid interface along a solid surface. *Journal of Fluid Mechanics*, 65:71–95, 1974.

[67] A. Oron, S. H. Davis, and S. G. Bankoff. Long-scale evolution of thin liquid films. *Reviews of Modern Physics*, 69:931–980, 1997.

[68] J. H. Snoeijer, B. Andreotti, G. Delon, and M. Fermigier. Relaxation of a dewetting contact line. part 1. a full-scale hydrodynamic calculation. *Journal of Fluid Mechanics*, 579:63–83, 2007.

[69] J. Eggers. Hydrodynamic theory of forced dewetting. *Physical Review Letters*, 93:094502, 2004.

[70] C. Huh and S. G. Mason. The steady movement of a liquid meniscus in a capillary tube. *Journal of Fluid Mechanics*, 81:401–419, 1977.

[71] Y. D. Shikhmurzaev. Singularities at the moving contact line. mathematical, physical and computational aspects. *Physica D*, 217:121–133, 2006.

[72] E. B. Dussan V. The moving contact line: the slip boundary condition. *Journal of Fluid Mechanics*, 77:665–684, 1976.

[73] J. N. Tilton. The steady motion of an interface between two viscous liquids in a capillary tube. *Chemical Engineering Science*, 43:1371 – 1384, 1988.

[74] C. Neto, D. R. Evan, E. Bonaccurso, H.-J. Butt, and V. S. J. Craig. Boundary slip in newtonian liquids: a review of experimental studies. *Reports on Progress in Physics*, 68:2859–2897, 2005.

[75] L. M. Hocking. A moving fluid interface on a rough surface. *Journal of Fluid Mechanics*, 76:801–817, 1976.

[76] T. D. Blake. Slip between a liquid and a solid: D.m. tolstoi's (1952) theory reconsidered. *Colloids and Surfaces*, 47:135 – 145, 1990.

[77] H. B. van Lengerich and P. H. Steen. Energy dissipation and the contact-line region of a spreading bridge. *Journal of Fluid Mechanics*, 703:111–141, 2012.

[78] P. A. Thompson and M. O. Robbins. Simulations of contact-line motion: slip and the dynamic contact angle. *Physical Review Letters*, 63:766–769, 1989.

[79] E. Kirkinis and S. H. Davis. Hydrodynamic theory of liquid slippage on a solid substrate near a moving contact line. *Physical Review Letters*, 110:234503, 2013.

[80] Y. D. Shikhmurzaev. Some dry facts about dynamic wetting. *The European Physical Journal - Special Topics*, 197:47–60, 2011.

[81] D. N. Sibley, N. Savva, and S. Kalliadasis. Slip or not slip? a methodical examination of the interface formation model using two-dimensional droplet spreading on a horizontal planar substrate as a prototype system. *Physics of Fluids*, 24:082105, 2012.

[82] T. D. Blake, M. Bracke, and Y. D. Shikhmurzaev. Experimental evidence of nonlocal hydrodynamic influence on the dynamic contact angle. *Physics of Fluids*, 11:1995, 1999.

[83] A. Clarke and E. Stattersfield. Direct evidence supporting nonlocal hydrodynamic influence on the dynamic contact angle. *Physics of Fluids*, 18:048106, 2006.

[84] Q. Min, Y.-Y. Duan, X.-D. Wang, Z.-P. Liang, and C. Si. Does macroscopic flow geometry influence wetting dynamic? *Journal of Colloid and Interface Science*, 362:221–227, 2011.

[85] C. G. Ngan and E. B. Dussan V. On the nature of the dynamic contact angle: an experimental study. *Journal of Fluid Mechanics*, 118:27–40, 1982.

[86] B. Legait and P. Sourieau. Effect of geometry on advancing contact angles in fine capillaries. *Journal of Colloid and Interface Science*, 107:14 – 20, 1985.

[87] A. V. Lukyanov and Y. D. Shikhmurzaev. Curtain coating in microfluidics and the phenomenon of nonlocality in dynamic wetting. *Physics Letters A*, 358:426–430, 2006.

[88] P. G. Simpkins and V. J. Kuck. On air entrainment in coatings. *Journal of Colloid and Interface Science*, 263:562 – 571, 2003.

[89] M. T. Ghannam and M. N. Esmail. Effect of substrate entry angle on air entrainment in liquid coating. *AIChE Journal*, 36:1283–1286, 1990.

[90] R. Burley and R. P. S. Jolly. Entrainment of air into liquids by a high speed continuous solid surface. *Chemical Engineering Science*, 39:1357 – 1372, 1984.

[91] W. L. Wilkinson. Entrainment of air by a solid surface entering a liquid/air interface. *Chemical Engineering Science*, 30:1227 – 1230, 1975.

[92] T. D. Blake and K. J. Ruschak. A maximum speed of wetting. *Nature*, 282:489–491, 1979.

[93] Maniya Maleki, Etienne Reyssat, David Quéré, and Ramin Golestanian. On the landau-levich transition. *Langmuir*, 23:10116 – 10122, 2007.

[94] H. Benkreira and J. B. Ikin. Dissolution and growth of entrained bubbles when dip coating in a gas under reduced pressure. *Chemical Engineering Science*, 65:5821 – 5829, 2010.

[95] S. D. Wilson. The drag-out problem in film coating theory. *Journal of Engineering Mathematics*, 16:209–221, 1982.

[96] G. Delon, M. Fermigier, J. H. Snoeijer, and B. Androtti. Relaxation of a dewetting contact line. part 2. experiments. *Journal of Fluid Mechanics*, 604:55–75, 2008.

[97] L. M. Hocking. Meniscus draw-up and draining. *European Journal of Applied Mathematics*, 12:195–208, 2001.

[98] D. Jacqmin. Onset of wetting failure in liquid-liquid systems. *Journal of Fluid Mechanics*, 517:209–228, 2004.

[99] M. Sbragaglia, K. Sugiyama, and L. Biferale. Wetting failure and contact line dynamics in a couette flow. *Journal of Fluid Mechanics*, 614:471–493, 2008.

[100] J. H. Snoeijer, G. Delon, M. Fermigier, and B. Andreotti. Avoided critical behavior in dynamically forced wetting. *Physical Review Letters*, 96:174504, 2006.

[101] L. Limat and H. A. Stone. Three-dimensional lubrication model of a contact line corner singularity. *EPL (Europhysics Letters)*, 65:365–371, 2004.

[102] J. H. Snoeijer, E. Rio, N. Le Grand, and L. Limat. Self-similar flow and contact line geometry at the rear of cornered drops. *Physics of Fluids*, 17:072101, 2005.

[103] J. H. Snoeijer, N. Le Grand-Piteira, L. Limat, H. A. Stone, and J. Eggers. Cornered drops and rivulets. *Physics of Fluids*, 19:042104, 2007.

[104] R. Burley and B. S. Kennedy. An experimental study of air entrainment at a solid/liquid/gas interface. *Chemical Engineering Science*, 31:901 – 911, 1976.

[105] A. Marchand, T. S. Chan, J. H. Snoeijer, and B. Andreotti. Air entrainment by contact lines of a solid plate plunged into a viscous fluid. *Physical Review Letters*, 108:204501, 2012.

[106] Y. C. Severtson and C. K. Aidun. Stability of two-layer stratified flow in inclined channels: applications to air entrainment in coating systems. *Journal of Fluid Mechanics*, 312:173–200, 1996.

[107] P. G. Simpkins and V. J. Kuck. Air entrapment in coatings by way of tip-streaming meniscus. *Nature*, 403:641–643, 2000.

[108] J. Eggers. Air entrainment through free-surface cusps. *Physical Review Letters*, 86:4290–4293, 2001.

[109] R. T. Perry. *Fluid Mechanics of Entrainment Through Liquid-Liquid and Liquid-Solid Junction*. PhD thesis, University of Minnesota, 1967.

[110] E. B. Gutoff and C. E. Kendrick. Low flow limits of coatability on a slide coater. *AIChE Journal*, 33:141–145, 1987.

[111] J. Hens and W. V. Abbenyen. Slide coating. In S.F. Kistler and P. M. Schweizer, editors, *Liquid Film Coating*, pages 427–462. Chapman & Hall, 1997.

[112] R. R. Quiel, A. E. Gros, D. S. Finnicum, and F. M. Joos. Slide bead coating method. *U.S. Patent no. 6511711 B2*, 2003.

[113] A. Clarke, C. L. Bower, and K. E. Goppert. Apparatus and method of coating a web. *U.S. Patent no. 6638576 B2*, 2003.

[114] T. D. Blake, R. Dobson, G. B. Batts, and W. J. Harrison. Coating processes. *U.S. Patent no. 5391401*, 1995.

[115] S. Ravinutala and C. Polymeropoulos. Entrance meniscus in a pressurized optical fiber coating applicator. *Experimental Thermal and Fluid Science*, 26:573 – 580, 2002.

[116] V. J. Kuck and P. G. Simpkins. Bubble prevention in coating of filaments. *U.S. Patent no. 6131416*, 2000.

[117] W. Mues, J. Hens, and L. Boiy. Observation of a dynamic wetting process using laser-doppler velocimetry. *AIChE Journal*, 35:1521–1526, 1989.

[118] J. Lowndes. The numerical simulation of the steady movement of a fluid meniscus in a capillary tube. *Journal of Fluid Mechanics*, 101:631–646, 1980.

[119] G. K. Batchelor. *An Introduction to Fluid Dynamics*. Cambridge University Press, 1967.

[120] R. Krechetnikov. On application of lubrication approximations to nonunidirectional coating flows with clean and surfactant interfaces. *Physics of Fluids*, 22:092102, 2010.

[121] J. H. Snoeijer. Free-surface flows with large slopes: Beyond lubrication theory. *Physics of Fluids*, 18:021701, 2006.

[122] Eugenia Kálnay de Rivas. On the use of nonuniform grids in finite-difference equations. *Journal of Computational Physics*, 10:202–210, 1972.

[123] J. F. Thompson, Z. U. A. Warsi, and C. W. Mastin. *Numerical Grid Generation: Foundations and Applications*. North-holland Amsterdam, 1985.

[124] J. H. Bolstad and H. B. Keller. A multigrid continuation method for elliptic problems with folds. *SIAM Journal on Scientific Computing*, 7:1081–1104, 1986.

[125] K. N. Christodoulou and L. E. Scriven. Discretization of free surface flows and other moving boundary problems. *Journal of Computational Physics*, 99:39–55, 1992.

[126] P. M. Gresho and R. L. Sani. *Incompressible Flow and the Finite Element Method. Volume Two: Isothermal Laminar Flow*. John Wiley & Sons, Inc., 1998.

[127] J. E. Sprittles and Y. D. Shikhmurzaev. Finite element framework for describing dynamic wetting phenomena. *International Journal for Numerical Methods in Fluids*, 68:1257–1298, 2012.

[128] K. N. Christodoulou, S. F. Kistler, and P. R. Schunk. Advances in computational methods for free-surface flows. In S.F. Kistler and P. M. Schweizer, editors, *Liquid Film Coating*, pages 297–367. Chapman & Hall, 1997.

[129] S. Dodds, M. S. Carvalho, and S. Kumar. Stretching and slipping of liquid bridges near plates and cavities. *Physics of Fluids*, 21:092103, 2009.

[130] J. Nam and M. S. Carvalho. Mid-gap invasion in two-layer slot coating. *Journal of Fluid Mechanics*, 631:397–417, 2009.

[131] L. M. Hocking. The spreading of a drop by capillary action. *Journal of Fluid Mechanics*, 121:425–442, 1982.

[132] Y. Sui and P. D. M. Spelt. Validation and modification of asymptotic analysis of slow and rapid droplet spreading by numerical simulation. *Journal of Fluid Mechanics*, 715:283–313, 2013.

[133] M. Zhou and P. Sheng. Dynamics of immiscible-fluid displacement in a capillary tube. *Physical Review Letters*, 64:882–885, 1990.

[134] M. Fermigier and P. Jenffer. An experimental investigation of the dynamic contact angle in liquid-liquid systems. *Journal of Colloid and Interface Science*, 146:226–241, 1991.

[135] P. G. Petrov and J. G. Petrov. A combined molecular-hydrodynamic approach to wetting kinetics. *Langmuir*, 8:1762–1767, 1992.

[136] E. Ramé, S. Garoff, and K. R. Willson. Characterizing the microscopic physics near moving contact lines using dynamic contact angle data. *Physical Review E*, 70:031608, 2004.

[137] M. J. Savelski, S. A. Shetty, W. B. Kolb, and R. L. Cerro. Flow patterns associated with the steady movement of a solid/liquid/fluid contact line. *Journal of Colloid and Interface Science*, 176:117 – 127, 1995.

[138] E. Vandre, M. S. Carvalho, and S. Kumar. Delaying the onset of dynamic wetting failure through meniscus confinement. *Journal of Fluid Mechanics*, 707:496–520, 2012.

[139] T. S. Chan, G. Thomas, and J. H. Snoeijer. Maximum speed of dewetting on a fiber. *Physics of Fluids*, 23:112103, 2011.

[140] T. S. Chan, J. H. Snoeijer, and J. Eggers. Theory of the forced wetting transition. *Physics of Fluids*, 24:072104, 2012.

[141] D. Jacqmin. Very, very fast wetting. *Journal of Fluid Mechanics*, 455:347–358, 2002.

[142] H. Benkreira and J. B. Ikin. Dynamic wetting and gas viscosity effects. *Chemical Engineering Science*, 65:1790–1796, 2010.

[143] S. M. Troian, E. Herbolzheimer, S. A. Safran, and J. F. Joanny. Fingering instabilities of driven spreading films. *Europhysics Letters*, 10:25–30, 1989.

[144] M. A. Spaid and G. M. Homsy. Viscoelastic free surface flows: spin coating and dynamic contact lines. *Journal of Non-Newtonian Fluid Mechanics*, 55:249–281, 1994.

[145] A. L. Bertozzi and M. P. Brenner. Linear stability and transient growth in driven contact lines. *Physics of Fluids*, 9:530 – 539, 1997.

[146] M. A. Spaid and G. M. Homsy. Stability of newtonian and viscoelastic dynamic contact lines. *Physics of Fluids*, 8:460–478, 1995.

[147] M. D. Davis, D. E. Kataoka, and S. M. Troian. Transient dynamics and structure of optimal excitations in thermocapillary spreading: Precursor film model. *Physics of Fluids*, 18:092101, 2006.

[148] T-. S Lin, L. Kondic, and A. Filippov. Thin films flowing down inverted substrates: Three-dimensional flow. *Physics of Fluids*, 24:022105, 2012.

[149] B. Bradie. *A Friendly Introduction to Numerical Analysis*. Pearson Prentice Hall, 2006.

[150] M. S. Carvalho and L. E. Scriven. Three-dimensional stability analysis of free surface flows: Application to forward deformable roll coating. *Journal of Computational Physics*, 151:534–562, 1999.

[151] M. S. Carvalho and H. S. Kheshgi. Low-flow limit in slot coating: Theory and experiments. *AIChE Journal*, 46:1907–1917, 2000.

[152] R. C. Ernst, C. H. Watkins, and H. H. Ruwe. The physical properties of the ternary system ethyl alcohol-glycerin-water. *The Journal of Physical Chemistry*, 40:627–635, 1936.

[153] M. D. Abramoff, P. J. Magalhaes, and S. J. Ram. Image processing with imagej. *Biophotonics International*, 11:36–42, 2004.

[154] S. G. Jennings. The mean free path in air. *Journal of Aerosol Science*, 19:159–166, 1988.

[155] T. D. Blake, A. Clarke, and E. H. Stattersfield. An investigation of electrostatic assist in dynamic wetting. *Langmuir*, 16:2928–2935, 2000.

[156] O. Cohu and H. Benkreira. Air entrainment in angled dip coating. *Chemical Engineering Science*, 53:533 – 540, 1998.

[157] E. Vandre, M. S. Carvalho, and S. Kumar. On the mechanism of wetting faluire during fluid displacement along a moving substrate. *Physics of Fluids*, (submitted), 2013.

[158] M. L. Sheely. Glycerol viscosity tables. *Industrial & Engineering Chemistry*, 24:1060–1064, 1932.

[159] M. S. Stay and V. H. Barocas. Coupled lubrication and stokes flow finite elements. *International Journal for Numerical Methods in Fluids*, 43:129–146, 2003.

[160] M. K. Smith and G. P. Neitzel. Multiscale modelling in the numerical computation of isothermal non-wetting. *Journal of Fluid Mechanics*, 554:67–83, 2006.

[161] J. Nam, L. E. Scriven, and M. S. Carvalho. Tracking birth of vortex in flows. *Journal of Computational Physics*, 228:4549 – 4567, 2009.

[162] T. A. Baer, R. A. Cairncross, P. R. Schunk, R. R. Rao, and P. A. Sackinger. A finite element method for free surface flows of incompressible fluids in three

dimensions. part ii. dynamic wetting lines. *International Journal for Numerical Methods in Fluids*, 33:405–427, 2000.

[163] S. Dodds, M. S. Carvalho, and S. Kumar. The dynamics of three-dimensional liquid bridges with pinned and moving contact lines. *Journal of Fluid Mechanics*, 707:521–540, 2012.

[164] O. Cohu and H. Benkreira. Entrainment of air by a solid surface plunging into a non-newtonian liquid. *AIChE Journal*, 44:2360–2368, 1998.

[165] J. B. Dupont and D. Legendre. Numerical simulation of static and sliding drop with contact angle hysteresis. *Journal of Computational Physics*, 229:2453–2478, 2010.

[166] Y. D. Shikhmurzaev and J. E. Sprittles. Dynamic contact angle of a liquid spreading on an unsaturated wettable porous substrate. *Journal of Fluid Mechanics*, 715:273–282, 2013.

[167] J. Nam and M. S. Carvalho. Flow visualization and operating limits of tensioned-web-over slot die coating process. *Chemical Engineering and Processing: Process Intensification*, 50.5:471–477, 2011.

[168] L. Courbin, J. C. Bird, M. Reyssat, and H. A. Stone. Dynamics of wetting: from inertial spreading to viscous imbibition. *Journal of Physics: Condensed Matter*, 21:464127, 2009.

[169] W. Ren and W. E. Boundary conditions for the moving contact line problem. *Physics of Fluids*, 19:022101, 2007.

[170] J. E. Sprittles and Y. D. Shikhmurzaev. Viscous flow in domains with corners: numerical artifacts, their origin and removal. *Computer Methods in Applied Mechanics and Engineering*, 200:1087–1099, 2011.

[171] J. E. Sprittles and Y. D. Shikhmurzaev. Viscous flows in corner regions: Singularities and hidden eigensolutions. *International Journal for Numerical Methods in Fluids*, 65:372–382, 2011.

[172] I. Peters, J. H. Snoeijer, A. Daerr, and L. Limat. Coexistence of two singularities in dewetting flows: Regularizing the corner tip. *Physical Review Letters*, 103:114501, 2009.

Appendix A

Glossary and Acronyms

A.1 Glossary

- **Static Contact Line** (**SCL**) – The three-phase junction between a fluid interface and a solid surface at equilibrium.
- **Dynamic Contact Line** (**DCL**) – Same as above, except in a system out of equilibrium (e.g., a contact line along a moving solid surface)
- **Quasi-Parallel approach** (**QP approach**) – Specific numerical method that assumes one-dimensional flow using a lubrication-type approximation for fluid-displacement systems
- **Finite Element Method** (**FEM**) – General numerical method used to approximate solutions differential equations associated with continuum mechanics (e.g., Navier-Stokes equations)
- **Two-dimensional flow model** (**2D flow model**) – Specific numerical model using FEM to solve for the two-dimensional flow fields in fluid-displacement systems
- **Linear Stability model** (**LS model**) – Numerical model that predicts the stability of solutions from the QP approach (see above) using conventional linear stability analysis

- **Inflection Point** (**IP**) – A point of zero curvature marking the maximum interface angle near the DCL

A.2 Nomenclature

Table A.1: Nomenclature

Symbol	Definition
θ_M	apparent contact angle or maximum interface angle
θ_{mic}	microscopic contact angle
U	substrate speed
U_T	top-plate speed (usually stationary; $U_T = 0$)
ρ	fluid density
σ	surface tension
μ	fluid viscosity
μ_{adv}, μ_{rec}	advancing and receding fluid viscosity, respectively
H	confinement gap or other characteristic length scale
L	interface length measured in x coordinate (parallel to substrate)
l_{slip}	fluid slip length
l_{mic}	microscopic length scale near the DCL; usually $l_{mic} \sim l_{slip}$
$l_{cap} = \sqrt{\sigma/(\rho g)}$	capillary length
$\boldsymbol{v}$	fluid velocity vector
$\boldsymbol{T}$	Newtonian stress tensor
$\boldsymbol{n}$, $\boldsymbol{t}$	normal and tangent vectors to the fluid interface
P_L, P_R	computational pressure values at ends of parallel-plate channel
x, y, z	Cartesian coordinates
u, v, w	components of the fluid velocity vector corresponding to the Cartesian coordinates above
η, ξ	computational coordinates
s	arc-length coordinate
r	coordinate marking radial distance from the DCL

Continued on next page

Table A.1 – continued from previous page

Symbol	Definition
h	interface height function (measured in y coordinate)
κ	interface curvature
h_f, r_f	vertical and radial position of the IP
x_{SCL}	position of the static contact line
x_{DCL}	position of the dynamic contact line
α	perturabation growth rate
k	perturbation wavenumber
W	air-film width
ψ	angle formed by triangular air film
V	wave speeed (Chapter 7 only)
P_{app}	applied liquid pressure
P_{atm}	atmospheric air pressure
h_{curt}	curtain-coating height
h_{inf}	curtain-coating film thickness
w	liquid curtain width (Chapter 8 only)
V	curtain feed-flow velocity (Chapter 8 only)
l_d	length of curtain-coating domain

Table A.2: Dimensionless groups

Symbol	Definition
$Ca = \mu U/\sigma$	capillary number
$Re = \rho U H/\mu$	Reynolds number
$Bo = \rho U H^2/\sigma$	Bond number
$\chi = \mu_{rec}/\mu_{adv}$	viscosity ratio
$\lambda = l_{slip}/H$	dimensionless slip length or confinement ratio
$\omega = U_T/U$	plate speed ratio

Appendix B

Finite Element Method

This appendix illustrates mesh-independence within our two-dimensional (2D) flow model using the Galerkin finite element method (FEM) described in Section 2.3.

B.1 Mesh-Independent FEM Solutions

Contact-line resolution presents the primary hurdle to numerical analysis of 2D wetting flows. Recent works [39, 127, 170] have identified some factors which hinder FEM simulations of wetting systems from converging to mesh-independent solutions. For instance, strongly imposed boundary conditions at the wetting line (i.e., slip velocity and contact angle) appear to cause larger global errors than the weak form of these conditions (see [127] for further discussion). Our FEM study is vulnerable to these errors because we strongly impose velocity and mesh boundary conditions along the interface and substrate. To ensure that we acquire mesh-independent solutions, we have extensively studied the effect of mesh refinement on our reported FEM results.

In this section, we demonstrate the convergence to a mesh-independent solution for the air/glycerol system ($\chi = 1.5 \times 10^{-4}$) used in Chapter 6 with $\lambda = 0.1$. We focus on the effect of contact-line resolution achieved by concentrating the mesh while holding the total number of elements constant ($N_{ele} = 4000$). Resolution is characterized by the element height (Δy_{cl}) at the wetting line. We include one case with a 300% increase in N_{ele} to show the insensitivity of our solution to the global element count. The selected studies are listed in Table B.1 with relevant mesh parameters and resulting Ca^{crit} values.

Mesh	N_{ele}	Δy_{cl}	$\widetilde{Ca}^{crit}$	Error %
A	4000	7.7×10^{-3}	1.81	57
B	4000	3.3×10^{-3}	2.09	50
C	4000	1.2×10^{-3}	2.50	40
D	4000	3.3×10^{-4}	3.27	21
E	4000	1.7×10^{-4}	4.08	1.7
F	4000	1.6×10^{-5}	4.14	0.2
G	16000	7.7×10^{-6}	4.13	–

Table B.1: FEM mesh studies for the air/glycerol system ($\chi = 1.5 \times 10^{-4}$, $\theta_{mic,R} = 70^o$, $\theta_{mic,L} = 90^o$) with $\lambda = 0.1$. Error percents are determined by comparing $\widetilde{Ca}^{crit}$ values to the true critical capillary number found with Mesh G ($Ca^{crit} = 4.13$).

Solution families are plotted for each mesh study in Figure B.1. The plot shows that computations with a coarser mesh converge to the refined result at low Ca, but then deviate at some finite capillary number, $\widetilde{Ca}^{crit}$. Unfortunately, artificial turning points are produced at $\widetilde{Ca}^{crit}$ as a consequence of poor mesh quality. Therefore, one cannot simply rely on the presence of a "critical point" to identify the true Ca^{crit}, but must successively refine the computational mesh until converging to a single value for $\widetilde{Ca}^{crit}$.

As we illustrate in Figure B.2, failure to sufficiently resolve the wetting line can lead to grossly inaccurate estimates for Ca^{crit}. For example, even a 10-fold refinement of the slip length ($\Delta y_{cl} = \lambda \times 10^{-1}$) yields over 50 % error in Ca^{crit}. For the parameters of interest to our air/glycerol system we have achieved mesh independence when the wetting line is resolved three orders of magnitude below the length scale ratio ($\Delta y_{cl} = \lambda \times 10^{-3}$). This heuristic seems to remain valid for the entire range of λ examined within this study ($\lambda \in [2 \times 10^{-6}, 10^{-1}]$). However, the necessary mesh conditions for a general wetting system depend on θ_{mic} and factors set by the macroscopic flow field. The mesh conditions needed to guarentee convergence in general wetting systems remains under investigation.

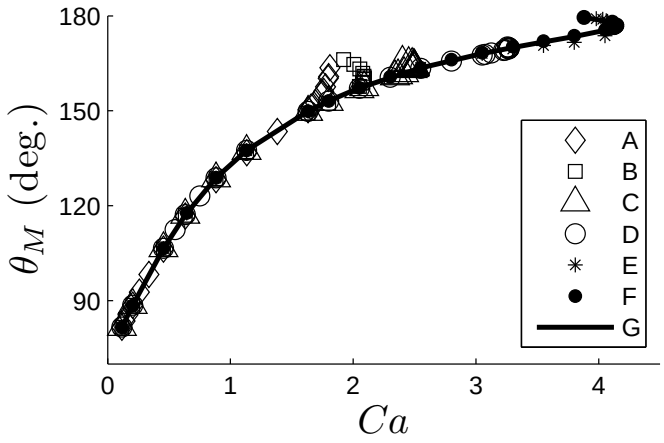

Figure B.1: Solution paths for the FEM mesh studies listed in Table B.1.

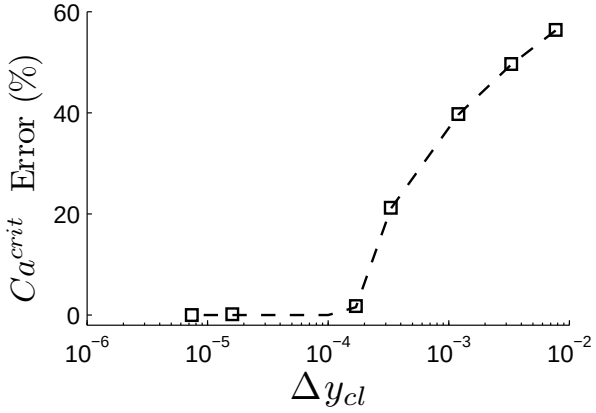

Figure B.2: The convergence of Ca^{crit} with increasing mesh resolution near the contact line.

Appendix C

Steady Wetting

C.1 Void/Liquid Notes

The Low-Speed Regime

Although the interface deforms to angles as high as 140^o in the low-speed regime ($Ca < 0.5$ in the case studied in Section 3.5 where $\lambda = 0.01$ and $\theta_{mic} = 90^o$), the flow field does not change significantly. As visualized in Figure 3.12c, dimensionless velocity profiles are qualitatively similar along the outer portion of the interface for all Ca. Therefore, the liquid pressure increases with substrate speed ($p \sim \mu U/H$), but maintains the same functional form. In dimensionless terms, this amounts to an interfacial pressure drop that is only a weak function of Ca, as demonstrated by Figure C.1 (note that normal stress is nearly constant for $r > r_f$ for all curves in Figure 3.12d). This effectively simplifies the normal stress balance in (2.6) to $\kappa = Ca$ for low substrate speeds. As speed increases and $\theta_M \to 180^o$, velocity slows along the outer interface (see Figure 3.9) and the substrate has a weaker impact on viscous stresses in this region. In addition, the macroscopic interface curvature approaches unity at high speeds, leading to a second approximation of the normal-stress balance: $\Delta P_{int} \sim 1/Ca$ (where ΔP_{int} is the pressure drop across the interface $p|_{adv} - p|_{rec}$). Figure C.1 shows the predicted pressure-drop decay when $Ca \sim 1$.

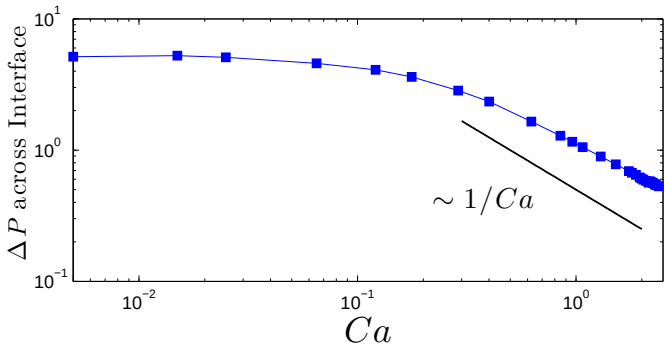

Figure C.1: Normal stress difference across the interface at $h = 0.5$ as a function of Ca for the void/liquid system.

C.1.1 Normal Stress and Flow in a Corner

Pressure typically diverges as $p \sim r^{-1}$ for flow in a corner bounded by solid surfaces. Figure 3.12d demonstrates that the normal stress associated with corner flow near a contact line has stronger radial dependence as Ca increases. This may be due to contributions from an eigensolution that appears in free-surface flows with obtuse angles [171]. Pressure from the eigensolution typically diverges as $p \sim r^{-0.5}$ for angles near 180^o. Thus, a composite of the eigensolution and the traditional flow-in-a-corner result may explain the $r^{-1.5}$ dependence as Ca increases and $\theta_M \to 180^o$. However, sharp interface curvature near the contact line invalidates a strict comparison with rigid corner flow.

Another intriguing aspect of flow in a corner with an obtuse angle is the appearance of multi-valued pressure near the corner [170, 171]. Numerically, this pressure pole may appear as a region of extremely high pressure directly adjacent to a region of low pressure. Most numerical schemes cannot handle singularities within field equations. As a result, this pressure "pole" will appear to have a finite (though very large) derivative. The value of the pressure gradients in this region depend entirely on the spacing of the nodes that try to "resolve" the pressure pole. Therefore, the large-angled corner flow problem can never be mesh independent in this form.

A couple methods have been suggested for removing this type of pressure singularity from contact line problems. One method is to first solve for the eigensolution (high

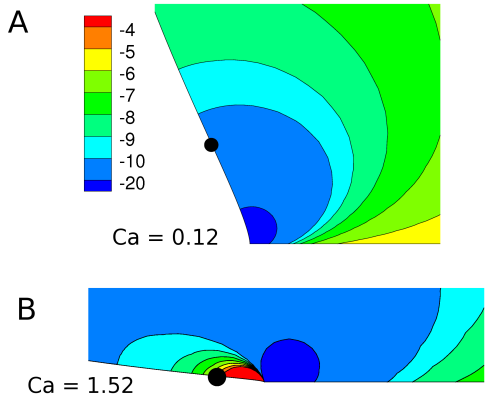

Figure C.2: Pressure contours for the void/liquid system at (A) $Ca = 0.12$ and (B) $Ca = 1.52$ with $10\times$ and $100\times$ magnification of the contact-line region, respectively.

pressure) to the homogeneous corner-flow problem and then subtract this solution from the entire problem domain [170]. The second option is similar to the first, only an *approximate* eigensolution is removed in a local region near the contact line region instead of the entire fluid domain [171]. The resulting problem (minus the eigensolution) should be well posed for numerical analysis with the weak pressure divergence ($p \sim \log r$) at the contact line, just as in the acute-angle corner flow case.

Although this problem has not been characterized for a free-surface corner with curvature (i.e., a realistic contact line problem), some of the numerical solutions reported in this thesis appear to show the characteristics of a pressure pole within the liquid near the contact line. As shown in Figure C.2, a region of high liquid pressure resides adjacent to the low-pressure (suction) zone near the contact line. This high pressure region appears at high speeds due to the increase in the apparent contact angle ($\theta_M > 135^o$) and continues to intensify as $\theta_M \rightarrow 180^o$. Despite this numerical artifact, the FEM model used in this report appears to converge to mesh-independent solution paths with error of $\sim 1\%$ near the turning point and negligible error at lower speeds. Further investigation is needed with more advanced meshing tools to identify how mesh distribution and properties of the basis functions influence the numerical error associated with pressure singularities.

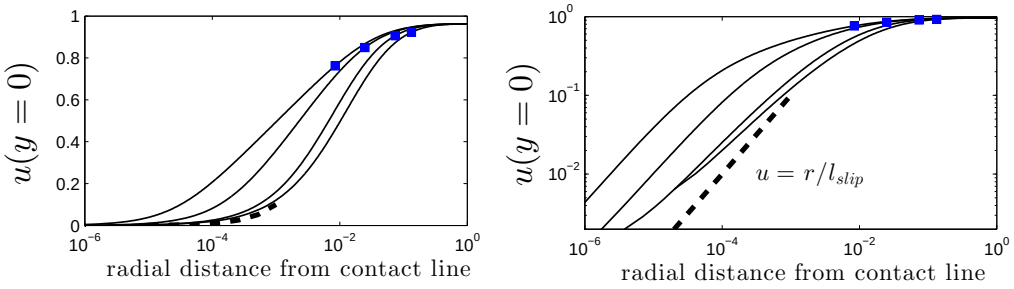

Figure C.3: Fluid velocity along the substrate for various Ca. Curves are shown for $Ca = 0.12, 0.40, 1.07,$ and 1.52 with values increasing from right to left. Square symbols mark the radial position associated with the inflection point along the interface. The dashed line approximates the velocity decay near the contact line as r/l_{slip}. The same data points are plotted on semi-log (left) and log-log (right) axes to highlight different portions of the profiles.

C.1.2 Slip Velocity along the Substrate

As shown in Figure C.3, fluid velocity along the liquid/solid interface behaves similarly to the velocity magnitude along the air/liquid interface (refer to Figure 3.12c). Namely, the inner region near the contact line experiences rapid deceleration due to high tangential stresses that activate fluid slip through (2.9). The velocity within this slip region goes as $u \sim r$ (this is also true for velocity along the air/liquid interface). As expected, the liquid recovers no-slip velocity ($u \to U$) when moving along the substrates at distances greater than l_{slip} away from the contact line.

Surprisingly, slip along the substrate is very sensitive to the air/liquid interface shape. This is because the interface is responsible for directing fluid particles toward the moving substrate. For instance, a vertical air/liquid interface (perpendicular to the substrate) imparts high shear on fluids particles due to the sharp change in flow direction near the contact line. This is why the low-speed curves in Figure C.3 exhibit more slip and lower velocities as $x \to 0$. As speed increases, the air/liquid interface tends toward parallel alignment with the substrate ($\theta_M \to 180^o$), which creates a much gentler transition for fluid near the contact line. Therefore, fluid slip weakens as substrate speed increases. This causes the inner region of interface dynamics to migrate closer to the contact line, as reflected by the decrease of r_f with increasing Ca.

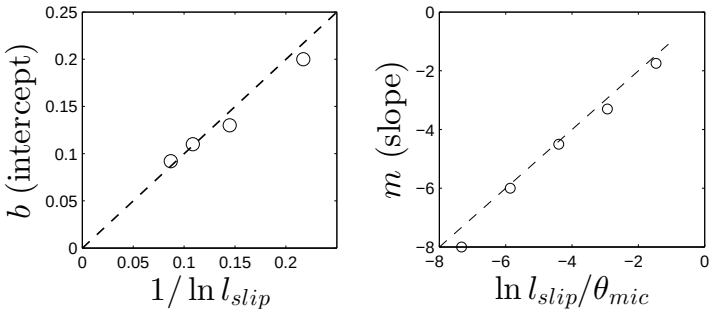

Figure C.4: Fitting parameters used for (C.1). Values for the intercept (left) and slope (right) are obtained from the data in Figure 3.13.

C.1.3 Cox Theory and the Inflection along the Interface

Slopes and intercepts are extracted from the data plotted in Figure 3.13 by a simple linear fit:

$$\log h_f = m \times Ca + \log b. \tag{C.1}$$

The resulting fitting parameters (m and b) provide insight into the effect of the slip length on the inflection point h_f. Figure C.4 plots the fitting parameters against functions of the (dimensionless) slip length. Each plot reflects proportionality between the ordinate and abscissa. Thus, the full functional form of the h_f becomes:

$$\log h_f - \log\left[(\log|l_{slip}|)^{-1}\right] \propto \frac{Ca \log l_{slip}}{\theta_{mic}} \tag{C.2}$$

Equation (C.2) can be derived from asymptotic theory using a matching procedure [44]. In the double limit where $Ca \to 0$ and $Ca \log l_{slip} \to 0$, one must match interface profiles (curvature) between an inner and outer region where the interface angle changes like $\theta(r) \sim \log r$ and $\theta(r) \sim \log l_{slip}$, respectively. One may recognize that the inner solution must dominate close to the contact ($r < r_f$). Therefore, the following must true near the contact line for $\theta(r)$ to match onto the inner solution:

$$\frac{\log l_{slip}}{\log r} > 1. \tag{C.3}$$

Taylor expanding (C.3) around $r = 1$ yields $r < (\log|l_{slip}|)^{-1}$ for $l_{slip} << 1$. Since the inflection point marks the beginning of the inner region, one expects $r_f \sim (\log|l_{slip}|)^{-1}$. This scaling agrees with the intercept for $\log h_f$ shown in (C.2).

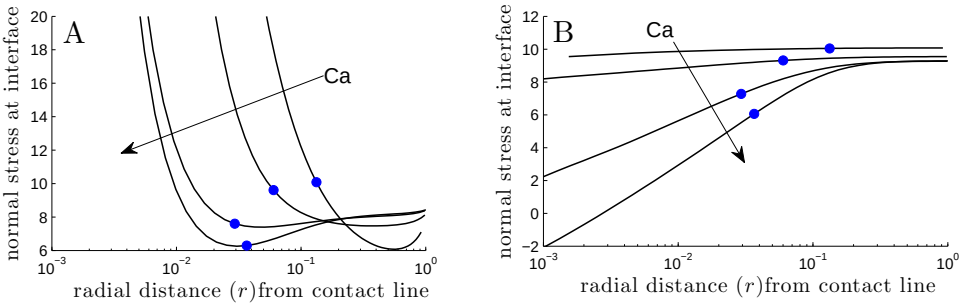

Figure C.5: Normal stress along air/liquid interface for $\chi = \mu_{air}/\mu_{liq} = 0.001$. Profiles for the advancing liquid (A) and receding air (B) are shown for $Ca = 0.1, 0.5, 1.02$ and 1.107 (on the stable solution branch). Circles denote the stress values at the inflection point along the interface.

For larger Ca, one must consider an intermediate region where the interface angle varies as $\theta(r) \sim Ca \log l_{slip}$. Rigorous matching this region with the outer interface proves to be very challenging [44]. However, it can readily be seen that the scaling of the intermediate region matches the capillary number dependence in (C.2). The geometric influence from θ_{mic} requires further investigation.

C.2 Air/Liquid Notes

Fluid Pressures Near the Inflection Point

Figure C.5 shows the liquid and air normal stresses along the interface at increasing Ca. It can be seen that the liquid stress grows rapidly as one moves from inflection point toward the contact line. The diverging liquid stress is due suction from the flow in a corner ($p \sim 1/r$) near the contact line. In contrast, the air pressure remains fairly level at low to moderate Ca. The change in air pressure only becomes comparable to the liquid-stress divergence at high substrate speeds (near Ca^{crit}). The magnitude of air pressure is dictated by adverse pressure gradients near the contact line that grow as $1/h^2$. Sharp curvature of the interface in this region converts these strong pressure gradients to a weaker divergence of air-pressure: $p \sim \log r$. However, the prefactor in this relationship is a strong function of Ca, which explains why the air pressure near r_f increases dramatically at high speeds.

So what is it that makes the liquid-stress divergence so strong near the contact

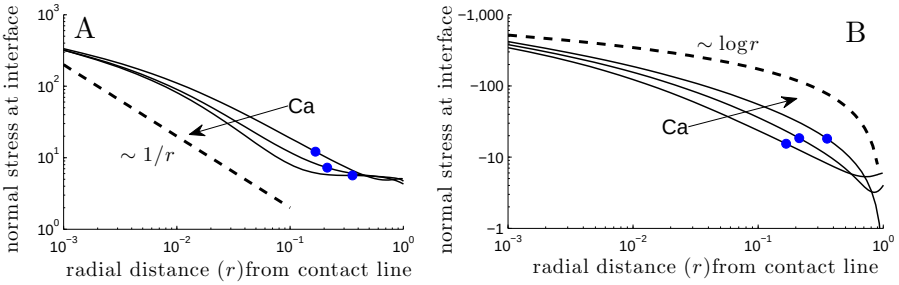

Figure C.6: Normal stress along liquid/liquid interface for $\chi = \mu_{air}/\mu_{liq} = 1$. Profiles for the advancing liquid (A) and receding liquid (B) are shown for $Ca = 0.01, 0.05$ and 0.0653 (on the stable solution branch). Normal stress for the air are shifted by -25 dimensionless stress units (vertical axis on B) for the purpose of maintaining a consistent sign for the logarithmic plot. Circles denote the stress values at the inflection point along the interface.

line? From a modeling standpoint, the pressure divergence arises from the microscopic contact angle condition in (2.9). The interface must bend sharply from the apparent contact angle to meet the contact line at the prescribed θ_{mic}. Due to the low air viscosity, the liquid carries most of the burden of matching the capillary stress in region, which explains the steep increase in normal stress shown in Figure C.5. Physically, this can be interpreted as the influence of microscopic forces that favor liquid-solid adhesion (contact). Although this may not be apparent from the dynamic-wetting model, the microscopic contact angles describe the three-phase molecular interaction in an equilibrium setting. (Note: θ_{mic} represents the Young's angle for the air/liquid/substrate system at $Ca = 0$.) Therefore, the strength of the liquid stress in this region would appear to be influenced by long-range molecular forces. It would be interesting to probe this idea by measuring the response of liquid stresses to $\theta_{mic} \to 180^o$ or imposed disjoining pressures.

Figure C.6 shows the stresses along an interface between two equiviscous fluids at increase Ca. The advancing and receding fluid pressures retain the same spatial dependence discussed in the preceding paragraph ($p \sim 1/r$ and $p \sim \log r$, respectively). Unlike the air/liquid case, the receding phase in the equiviscous system has pressure gradients that are comparable to the advancing phase for all Ca. This means that stresses within the receding phase impact the interface shape for all speeds. Due to interface bending, normal stress in the receding fluid becomes emphasized as Ca increases. Eventually, the

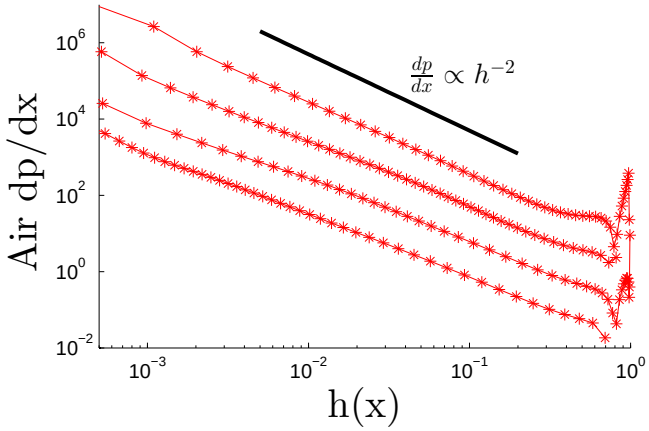

Figure C.7: Air pressure gradients along the air/liquid interface for $\chi = 0.001$ at various Ca. Pressure-gradient profiles are shown for $Ca = 0.1, 0.5, 1.02$ and 1.107 where Ca increases when jumping to a higher red curve. Each profile exhibits the lubrication scaling for wedge flow (3.10).

equiviscous system achieves a critical pressure gradient near h_f, which motivates the system to a transient state of fluid entrainment. These dynamics are very similar to the case of liquid entrainment where a receding liquid completely dominates the interface behavior [55, 172].

C.3 Air Wedge Flow

Figure C.7 demonstrates that air pressure gradients scale as $1/h^2$ for various values of Ca. Consequently air flow in the interface wedge near the contact line is well approximated by lubrication theory.

Appendix D

Wetting Box Apparatus

This appendix clarifies methods and results mentioned in Chapter 7. Section D.1 discusses the method used to measure air-film dimensions from visualzations made with the wetting box apparatus. Section D.2 compares the effect of pressurization between experimental data and model predictions.

D.1 Air-film Measurements

Visualizations are analyzed with software from the MATLAB Image Processing Toolbox™ in order to measure the dimensions of entrained air films. First, recorded images are converted to greyscale and contrast is enhanced using the *imadjust* function in MATLAB®. Figure D.1a demonstrates that this contrast filter is typically sufficient to clearly expose the triangular air films that form at the onset of air entrainment (i.e., Ca^{crit}). Second, an edge-detection algorithm (the *edge* function with the "Canny" method) is used to segment the image, as shown in Figure D.1b. Lastly, the pixels bounding a single triangular air film (i.e., the dynamic contact line) are used to fit two distinct lines that intersect near the vertex of the air film. These linear fits are used to define the two equal sides of an isosceles triangle. The base of the isosceles triangle is positioned at the point where the fitted triangle width deviates by approximately 25% from the width of the true air-film shape. As shown by Figure D.1, this procedure does a fairly good job of capturing the air-film shape and provides a reproducible method for measuring the width W and angle ψ associated with the triangular air films.

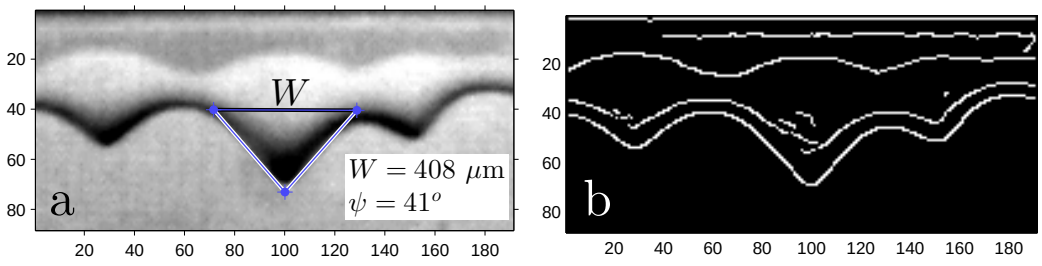

Figure D.1: Measurement of air-film width for $\mu = 1000$ cP at Ca^{crit} in the unconfined geometry ($H \to \infty$). (a) The greyscale visualization image (contrast filter applied) with an isoscelese triangle of base width W and angle ψ fit to the triangular air film. (b) Rendered image of the air film using the edge-detection method described in text. In each visualization image, 140 pixels (number on axes) corresponds with a distance of approximately 1 mm.

Using the procedure above, at least six distinct air films were analyzed to obtain statistical samples of W for each glycerol/water solution that was visualized during this study. Figure D.2 plots the distribution of air-film widths measured for three different values of μ. Each data set resembles a normal distribution with a standard deviation of less than 25%, which seems to be a reasonable uncertainty considering the somewhat crude measurement method.

Image processing is also used to estimate the thickness h_f of air films. In this case, a sequence of frames is analyzed to capture air-film rupture, which releases a discrete film of air that rapidly evolves into a spherical bubble. (See Section 7.4 for further discussion of this event.) The mean air-film thickness h_f is approximated by

$$h_f = \frac{\pi D^3}{6A} \tag{D.1}$$

where A is the area of the ruptured air film and D is the resulting bubble diameter.

Image segmentation is achieved using the contrast filters and edge-detection algorithms discussed above. Following this procedure, regions associated with the air domain can be isolated in order to measure A and D in the case of the film and bubble, respectively. Figures D.3 and D.4 demonstrate this procedure, where region "1" denotes the initial air-film area and region "2" marks the resulting air bubble. The air-film height h_f is calculated by substituting the measurements for A and D into (D.1).

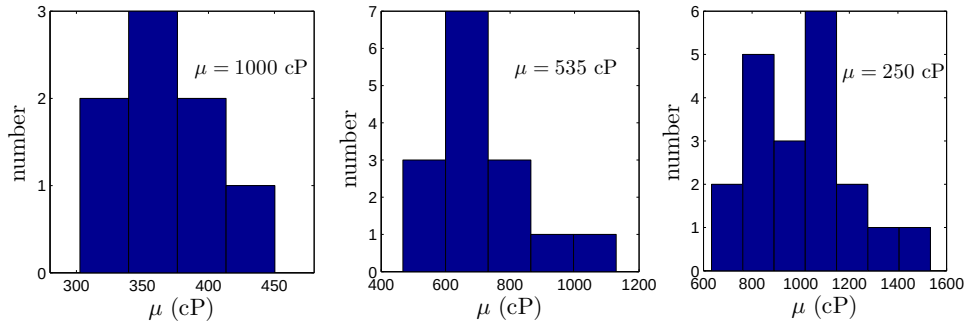

Figure D.2: The distribution of air-film widths W for different liquid viscosities (μ values listed in each panel) measured at Ca^{crit} in the unconfined geometry ($H \to \infty$). Refer to Figure D.1 for the measurement technique.

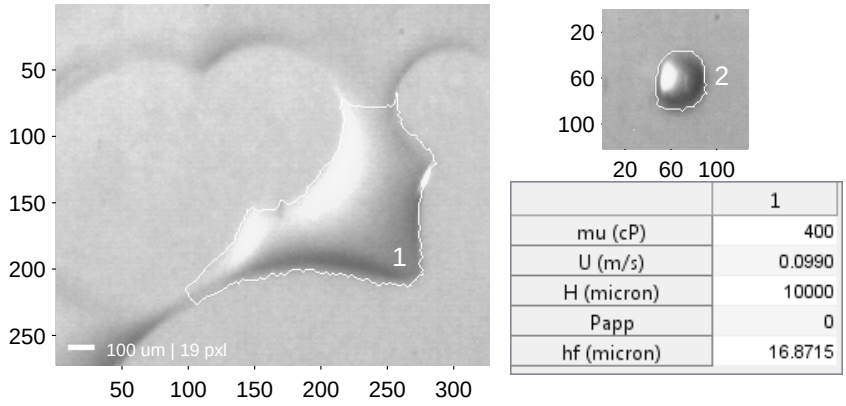

Figure D.3: Measurements associated with the calculation of air-film thickness h_f for $\mu = 400$ cP at Ca^{crit} in the unconfined geometry ($H \to \infty$). In each image, 190 pixels (values on axes) corresponds to approximately 1 mm.

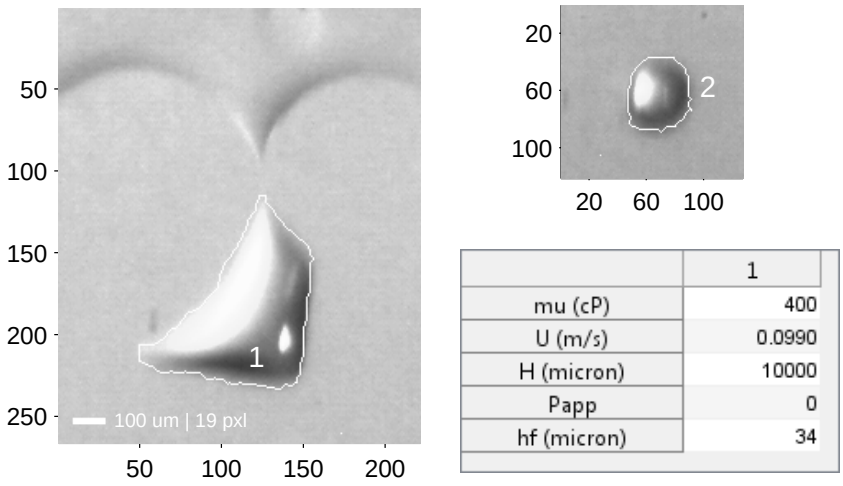

Figure D.4: The same procedure as shown above, only the air film is analyzed at approximately 1 ms later than the image in Figure D.3.

Unfortunately, this measurement is fairly sensitive to the time (i.e., the frame) at which the air-film area is analyzed. This is because the air film only remains relatively flat and two dimensional at early times in the rupture process (Figure D.3). As rupture proceeds, capillary forces cause the air pocket to become more compact and curved (Figure D.4), resulting in higher mean thickness than would be present in the original air film. For example, h_f values differ by approximately a factor of two when comparing the images in Figures D.3 and D.4 (the frames separated by approximately 1 ms). Values of h_f reported in Chapter 7 correspond to measurements made early in the rupture sequence (similar to Figure D.3) since the air film remains nearly flat during these times. The increase in h_f at later times is accounted for in the reported uncertainty.

D.2 Hydrodynamic Model

This section explores the effect of liquid pressurization using a hydrodynamic model for dynamic wetting that we have developed in a prior work [138]. A single geometry is considered in which the air/liquid meniscus is confined to a gap $H = 100$ μm in a parallel channel. Since this simplified geometry does not include the mask corner used

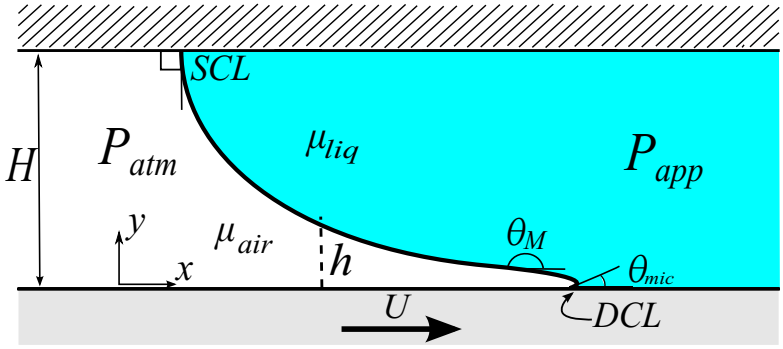

Figure D.5: Schematic of the hydrodynamic model.

to experimentally pin the meniscus (refer to Figure 7.5), pressurization is controlled with an imposed pressure gradients that is similar in form to a body force acting on the liquid. Model predictions are compared against experimental data for an equivalent gap with liquid viscosity $\mu = 600$ cP.

The two-dimensional model system is illustrated in Figure D.5, where an impenetrable air/liquid interface with surface tension σ resides within a gap H between a stationary plate (top) and a substrate (bottom) that moves at speed U. Since we consider a confined interface ($H = 100$ μm), inertial effects are neglected, resulting in the creeping-flow equations for the fluid velocities $\boldsymbol{v}$ and pressures p:

$$\boldsymbol{\nabla} \cdot \boldsymbol{v} = 0, \quad \boldsymbol{\nabla} p = \mu \nabla^2 \boldsymbol{v}, \tag{D.2}$$

where the fluid viscosity μ adopts values μ_{liq} and μ_{air} for the liquid and air, respectively.

Standard normal-stress, tangential-stress, and kinematic conditions are imposed at the fluid interface $y = h$. Velocity and interface angle conditions are prescribed at the static contact line (SCL) and the dynamic contact line (DCL). For simplicity, microscopic contact angles are fixed to $\theta_{mic} = 90^o$ at both the SCL and the DCL. The no-slip condition ($\boldsymbol{v} = 0$) is assumed at the stationary plate, whereas a Navier-slip condition is applied along the substrate with slip length $l_{slip} = 100$ nm. The governing equations are solved with the Galerkin finite element method (FEM) with elliptic mesh generation [125]. A more complete description of the governing equations and numerical technique can be found in Section 2.3.

Solutions to the model discussed above describe steady-state wetting in a parallel channel, similar to the confinement system used experimentally (refer to Figure 7.5b).

As discussed in Section 7.3.3, substrate drag is balanced by pressure P_{app} applied to the liquid flow downstream from the meniscus. The applied pressure P_{app} can be used to adjust the meniscus position along the substrate, but does not affect the interface shape or wetting state. In order to hold meniscus position constant, P_{app} must increase nearly linearly with Ca, similar to the experimental data plotted in Figure 7.9.

Pressurization effects arise from changes to the pressure *gradients* in the liquid flow. Experimentally, pressure gradients can be influenced when the meniscus is pinned against a corner as shown in Figure 7.5c. Since the corner obstructs meniscus motion, changes to P_{app} affect the liquid flow and interface shape. In order to model pressurization without considering this complicated domain geometry (refer Figure 7.5c) we modify the x-component of (D.2) for the liquid:

$$\frac{\partial p}{\partial x} = \mu_{liq}\frac{\partial^2 u}{\partial y^2} + \frac{\Delta P_{app}}{H}. \tag{D.3}$$

Here, u is the x-component of the liquid velocity and ΔP_{app} represents an increase in the applied liquid pressure ($\Delta P_{app} \geq 0$). Similar to a body force, $\Delta P_{app}/H$ contributes a constant pressure gradient in (D.3) that augments liquid pressures downstream from the fluid interface. This effectively pressurizes the liquid flow while keeping the meniscus position fixed, similar to that which is achieved with the cornered geometry in the experimental system.

The onset of air entrainment is determined by tracing steady-state solution paths to faster substrate speeds (larger capillary numbers $Ca = \mu_{liq}U/\sigma$) until locating a turning point at a critical capillary number Ca^{crit}. Since two-dimensional steady states cease to exist at higher speeds, Ca^{crit} denotes the transition to unsteady or three-dimensional flow, consistent with our experimental observations of air entrainment. Our prior work contains details about solution paths and flow fields predicted from the hydrodynamic model [157].

Similar to our experimental findings, the model shows that liquid pressurization delays air entrainment to faster substrate speeds. As plotted in Figure D.6a, the model predicts that the critical capillary number increases by a percentage ΔCa^{crit} that grows with ΔP_{app}. Direct comparison with experimental data is challenging since we do not model the identical system geometry. Specifically, the value of the applied liquid pressure P_{app} depends on the domain shape and the location of the measurement. (Recall

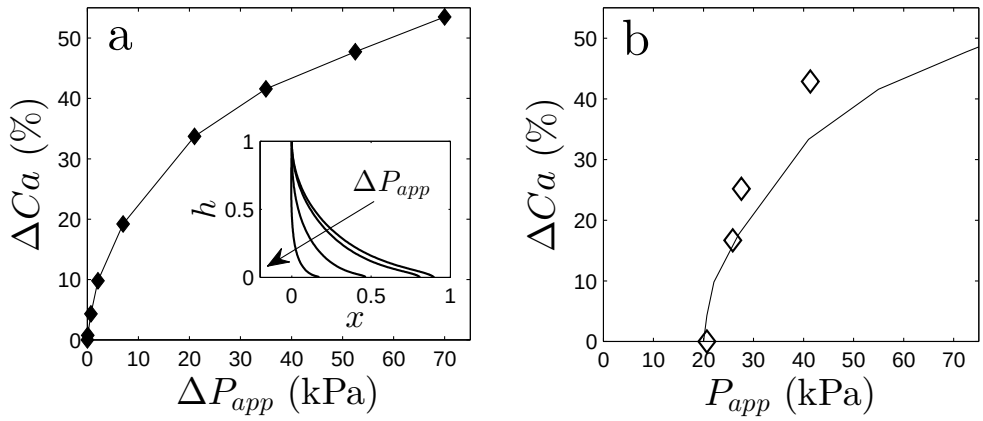

Figure D.6: Comparison of pressurization effects from model predictions and experimental measurements. (a) Model predictions for the percent change in the critical speed as a function of ΔP_{app} in (D.3). *Inset*: Interface profiles at Ca^{crit} for ΔP_{app} =0 kPa, 0.7 kPa, 7 kPa, and 70 kPa. (b) Comparison with experimental measurements (open symbols) of the change in critical speed at various P_{app}. Note that the model prediction (line) is simply taken from panel (a) using $P_{app} = \Delta P_{app} + p_0$, where $p_0 \approx 2$ kPa, as described in the text. Parameters for experimental system: $H = 100$ μm, $\mu_{liq} = 600$ cP, $\sigma = 65$ mN/m; model parameters: $H = 100$ μm, $\mu_{liq} = 1$ cP, $\sigma = 70$ mN/m, and $l_{slip} = 100$ nm. (See Sections 1.2.3 and 2.1 for description of the slip length l_{slip} used in the model.)

that in the experimental system P_{app} is measured in the liquid reservoir, outside of the confinement channel.) As an approximation, the applied liquid pressure can be computed from the model with the value of a pressure datum p_0 that is fitted to the experimental data, such that $P_{app} = \Delta P_{app} + p_0$. Figure D.6b shows that model predictions qualitatively match the trend of experimental results when $p_0 \approx 2$ kPa. Here, p_0 is selected to match the experimental value of P_{app} needed to position the meniscus at the corner during the first signs of wetting failure (corresponding to $Ca^{crit} \approx 1.12$ and $\Delta Ca^{crit} \approx 0$). Any further increase in P_{app} pressurizes the liquid ($\Delta P_{app} > 0$), leading to higher critical speeds, in agreement with the model predictions.

Furthermore, the hydrodynamic model predicts that liquid pressurization shortens the meniscus, qualitatively matching experimental visualizations (e.g. Figure 7.16). The inset of Figure D.6a illustrates that the interface length decreases by nearly an order of magnitude when ΔP_{app} increases to 70 kPa. This change in scale roughly approximates the effect of pressurization on the size of triangular air films that are experimentally observed at the onset of wetting failure (see Figure 7.10 in Chapter 7).